

UNIVERSITY OF OXFORD

ULTRA-SMALL OPEN ACCESS
MICROCAVITIES FOR ENHANCEMENT OF THE
LIGHT-MATTER INTERACTION

DPhil Thesis by

Philip Dolan

Wolfson College

January 2013

Declaration of Authorship

I, Philip Dolan, declare that this thesis titled, ‘ULTRA-SMALL OPEN ACCESS MICRO-CAVITIES FOR ENHANCEMENT OF THE LIGHT-MATTER INTERACTION’ and the work presented in it are my own. I confirm that:

- This work was done wholly or mainly while in candidature for a research degree at this University.
- Where any part of this thesis has previously been submitted for a degree or any other qualification at this University or any other institution, this has been clearly stated.
- Where I have consulted the published work of others, this is always clearly attributed.
- Where I have quoted from the work of others, the source is always given. With the exception of such quotations, this thesis is entirely my own work.
- I have acknowledged all main sources of help.
- Where the thesis is based on work done by myself jointly with others, I have made clear exactly what was done by others and what I have contributed myself.

“Nothing in the world can take the place of Persistence. Talent will not; nothing is more common than unsuccessful men with talent. Genius will not; unrewarded genius is almost a proverb. Education will not; the world is full of educated derelicts. Persistence and determination alone are omnipotent.”

Calvin Coolidge, 30th President of the US

UNIVERSITY OF OXFORD

Abstract

Mathematical, Physical and Life Sciences

Department of Materials

Doctor of Philosophy

by *Philip Dolan*

The design, construction and characterisation of a novel, arrayed, open-access optical microcavity is described. Included in this thesis are the precise fabrication details, making use of the focused ion beam. A technique for analysing and optimising the microcavities constructed, making use of an atomic force microscope is also included. Results from the optical characterisation of the fabricated microcavities are presented, including quality factors of around 10^4 , and finessees of around 400. The optical analysis then progressed onto coupling colloidal semiconductor nanocrystals to the microcavity modes. This yielded room temperature Purcell enhancements, single particle sensing, and also allowed for the characterisation of a second iteration of cavities. This improved set was shown to achieve finessees in excess of 1800 and quality factors with a lower limit of 15000. The optical identification of single NV centres in nanodiamond is discussed, along with the development of an optical apparatus to couple them to microcavities at cryogenic temperatures. Finally several results from finite difference time domain simulations will be presented, showing ultimate mode volumes of less than $0.5\lambda^3$ are possible for this approach.

Acknowledgements

My time at Oxford has left me indebted to many. Extraneous to the direct progress of my thesis initial thanks have to go to my family and friends for their unceasing support. Without them my time at Oxford would have been less content, and much less productive. As for the department, I have learned many things from many people here, and to everyone who has assisted, taught or simply listened I am truly grateful. As far as the technical details of the project go, specific mention must go to Steve Lett, Sverre Myhra and Gareth Hughes for their patient instruction. Pete Flaxman has been invaluable for his dexterity in machining components, as well as his advice, also Richard Cripps for his steady soldering hand. Turning to the group that has provided such an enjoyable working environment there is, without exception not one of the members past and present that I have not valued my time with, and enjoyed working alongside greatly. From Fabio, Ed, Benny and particularly Brian (who contributed massively to my hands-on optics tuition) to Matthew, Johnny, the two Alexes, Sam and Zi Yun (and Ben, a surrogate member), they have all made the lab and office brighter places to spend time. Special thanks have to go to Simon who has been a great colleague and friend throughout all of my time studying alongside him. The final and greatest thanks have to go to the architect of this fantastic group, my supervisor Jason. It is simply an impossible task to list all the ways he has helped with his constant direction and guidance for the project. In addition all the advice and encouragement for my teaching experiences, and my general appreciation for the scientific method are similarly unquantifiable. Heartfelt thanks will have to do in place of an exhaustive list.

Contents

Declaration of Authorship	i
Abstract	iii
Acknowledgements	iv
List of Figures	viii
List of Tables	xvii
Abbreviations	xviii
Physical Constants	xix
Symbols	xx
1 Introduction and Literature Review	1
1.1 Thesis Outline	1
1.2 Project Goals	2
1.3 Optical Microcavities	3
1.3.1 Open Access Microcavities	4
1.3.2 High Q Factor Fabry-Pérot Cavities	7
1.3.3 Micropillars	8
1.3.4 Microdisks	11
1.3.5 Microspheres	12
1.3.6 Microtoroids	14
1.3.7 Photonic Crystal Microcavities	16
1.4 Summary and Conclusions	21
2 Theoretical Background	24
2.1 Introduction	24
2.2 The Purcell Factor	24
2.2.1 Optical Density of States	26
2.2.2 Perturbing Hamiltonian	29

2.2.3	The Wigner-Weisskopf Theory of Spontaneous Emission and the Strong Coupling Regime	33
2.3	Distributed Bragg Reflectors and Cavity Metrics	37
2.3.1	DBRs and the 1D Transfer Matrix	37
2.3.2	A Few Cavity Metrics	45
2.4	Gaussian Beams	47
2.4.1	Gaussian Modes	49
2.4.2	Hermite-Gaussian and Laguerre-Gaussian Beams	53
2.5	Finite Difference Time Domain Simulations	56
2.5.1	Physical Background of Simulations	56
2.5.2	General Model Details	58
2.5.3	Mode Volume Calculations	60
2.6	Summary and Conclusions	62
3	Cavity Construction	63
3.1	Introduction	63
3.2	The Focused Ion Beam Milling	63
3.2.1	The Focused Ion Beam System	63
3.2.2	Sample Patterning	65
3.2.3	Substrate Preparation and Imaging Details	69
3.3	Atomic Force Microscopy	71
3.3.1	AFM Introduction	71
3.3.2	One dimensional curve fitting	72
3.3.3	AFM Image reconstruction	73
3.3.4	Two dimensional surface fitting	75
3.4	Substrate Development	80
3.5	Summary and Conclusions	81
4	Cavity Characterisation	83
4.1	Introduction	83
4.2	Room Temperature Transmission Set-Up	83
4.3	Fabry-Pérot etalons	85
4.4	Preliminary Microcavity Analysis	86
4.5	Length Dependent Measurements	89
4.6	Summary and Conclusions	98
5	Nanocrystals in Cavities	100
5.1	Introduction	100
5.2	Experimental Setup	101
5.3	Modified Emission Spectra	102
5.4	Modified Lifetimes	107
5.5	Decay Rate Analysis	110
5.6	Single Particle Sensing	114
5.7	Characterisation of the Second Cavity Iteration	114
5.8	Summary and Conclusions	120
6	Nanodiamonds in Cavities	122
6.1	Introduction	122

6.2	The Diamond and the Nitrogen Vacancy Defect	122
6.3	Experimental Set-up	124
6.4	Scanning Confocal Imaging of Microcavities	126
6.5	Preliminary NV Centre Studies	127
6.6	Room Temperature NV Centre Couping	133
6.7	Design and Construction of Low Temperature Set-up	137
6.8	Summary and Conclusions	140
7	Conclusions and Outlook	142
7.1	Introduction	142
7.2	Conclusions	142
7.3	Outlook	143
7.3.1	Ultra Small Volumes	143
7.3.2	The Future	145
	Bibliography	147

List of Figures

1.1	Reproduced from reference [1].	5
1.2	Imaged Hermite-Gauss (00,01,11) and Laguerre-Gauss (01) modes from left to right, reproduced from [2].	6
1.3	A high finesse cavity situated below a magneto optical trap (MOT) to allow single atom detection. Reproduced from reference [3].	7
1.4	An SEM image of GaAs/AlAs micropillar, diameter 1.3 μm . Reproduced from reference [4].	9
1.5	(a) A typical PL spectrum of coupled InAs QDs. (b) SEM micrograph of a 1 μm pillar with the inset showing the location of the InAs QDs. Reproduced from reference [5].	10
1.6	Reproduced from reference [5].	10
1.7	SEM of a 5 μm radius laser diode microdisk. Reproduced from reference [6].	11
1.8	Reproduced from reference [7].	12
1.9	Illustration (photo inset is of a rare earth doped sphere) of a microsphere equatorial WGM using a fiber taper delivery system for the pump. Reproduced from reference [8].	13
1.10	Solid line - Calculated propagation constants for the fibre tip as a function of radius (top y axis). Points - The same constants for the first few n modes of the sphere, as a function of sphere radius (bottom y axis). Reproduced from reference [9].	14
1.11	(a) Schematic of the experimental setup. (b) Spectrum showing 72% efficiency coupling light into a WGM, Q factor 2×10^6 (sphere size $\alpha \approx 85 \mu\text{m}$, fibre taper size $\rho \approx 1.7 \mu\text{m}$). Inset shows the highest Q achieved, 5×10^7 with 37% collection efficiency ($\alpha \approx 210 \mu\text{m}$, $\rho \approx 2.25 \mu\text{m}$) Reproduced from reference [9].	15
1.12	SEM image of a microdisk with Q of 1.00×10^8 . Reproduced from reference [?].	15
1.13	Reproduced from reference [?].	16
1.14	Optical images of micro tori before and after liberation from the plinth used during the growth. Reproduced from reference [10].	17
1.15	Cross section of a photonic crystal cavity. The defect region is shaded in green and the inset shows an SEM of the same structure. Reproduced from reference [8].	17
1.16	(a) FDTD simulation of the resonant cavity modes for an M1 PC with periodicity $a = 0.27\lambda_{cav}$, hole radius $r = 0.3a$ and crystal thickness $d = 0.65a$. (b) A SEM of the cavity. Reproduced from reference [11].	18
1.17	(a) Spectrum for structure 1 shows strongly pumped dipole mode with a Q of ~ 5000 although no emission peaks match the crystal resonances in this case. (b) Structure 2, the inset shows the high pump power, revealing a Q factor of 250, with the low power spectrum shows a coupled exciton line that matches the cavity polarisation. Reproduced from reference [11].	19

1.18	(c) The equivalent plot to 1.17(b) for structure 3 with a Q of 200. Peak B mentioned in the passage is not shown. (d) Inset shows line coupled to the cavity mode with $Q \approx 1600$. Temperature is used to tune the QDs into resonance. Reproduced from reference [11].	19
1.19	Time resolved spontaneous emission modification because cavity coupling (a) shows the suppression and enhancement of emission in structure 2. (b) shows a shortening of the lifetime to just 210 ps, with the inset showing the antibunching for a single emitter. Reproduced from reference [11].	20
1.20	A surface illustration of the effect of misalignment spectrally and spatially on the spontaneous emission rate. The points observed experimentally are marked. Reproduced from reference [11].	21
1.21	Schematics and approximate estimates of the capacities of some of the various approaches to microcavitation.	23
2.1	(a) Conceptual cubic volume to facilitate optical state counting. (b) An example \mathbf{k} vector, $L/2\pi(1, 0, 1)$ plotted within the volume. (c) colormaps of field associated with plane wave with the same \mathbf{k} vector.	27
2.2	(a) Positive octant of allowed modes plotted in k -space, with volume of an individual mode highlighted in red. (b) shows the integrating sphere octant associated with the \mathbf{k} vectors plotted. (c) shows both modes and integrating volume.	28
2.3	Density of states, $g(\omega)$, plotted against angular frequency, ω for free space (red) and for a \mathbf{k} vector resonant with a cavity mode (blue).	29
2.4	a) shows three density of states available to an emitter with an emission frequency of ω_0 , b) shows the effect each of these situations has on the FWHM of the emitter (in the bad cavity limit).	31
2.5	Pictorial representation of the directional dependence of the DoS. In this case the cavity mode emission is shown in blue, with some of the available leaky modes shown in red.	32
2.6	Sketched plots of the excited state population against time an emitting dipole to various Q factor cavities. This type of plot might be obtained in a time-resolved photoluminescence experiment.	33
2.7	The hypothetically observed spectra for each of the emission decay plots shown in figure 2.6.	36
2.8	Pictorial representation of the three rates important to consider in CQED.	37
2.9	A single dielectric boundary under consideration. In this scheme material with refractive index n_1 precedes the material with n_2 for light propagating in the positive z direction.	39
2.10	Notation scheme adaptation for the same situation as that shown in figure 2.9, where the superscript denotes direct (+/- z) and the subscript denotes the refractive index of the medium ($1/2$).	40
2.11	Field distribution of light of wavelength $\lambda \sim 650$ nm incident on a mirror consisting of 10 pairs of silica ($n_1 = 1.46$) and zirconia ($n_2 = 2.1$) with thicknesses of $\lambda/(4 \times n_i)$ where $i = 1, 2$, where $\lambda_0 = 650$ nm.	41
2.12	Reflectivity spectrum obtained for the mirror depicted in figure 2.11 showing a reflection band around 150 nm wide.	42
2.13	Plot of transmissivity against wavelength for a 1 dimensional 2 micron long microcavity formed from 2 DBR stacks identical to the mirror characterised in figures 2.12 and 2.11.	42

2.14	A graphical plot showing the distribution of modes for a one dimensional cavities with lengths $2\ \mu\text{m}$ (red) and $650\ \text{nm}$ (blue). The grey region is the portion of the spectrum over which the dielectric mirrors are usefully reflective.	43
2.15	Transmission spectrum of a $325\ \text{nm}$ long cavity identical in all other respects to that shown in figure 2.13.	44
2.16	Field distribution for the cavity resonance visible close to $650\ \text{nm}$ in figure 2.15.	44
2.17	A sketched plot to indicate the modification of the optical density of states which occurs due to the presence of an optical microcavity. The important point is that strong suppression and enhancement only occur within the reflectivity band of the mirrors. Outside of this region the density of states may be unaltered (as shown) or impacted by other mechanisms.	45
2.18	Cavity modes for cavities of lengths $1/2, 5, 10, 20\ \lambda_{\text{res}}$. The modes clearly show a redshift, as field penetration into the mirrors becomes less significant, and narrowing width corresponding to increasing Q factors.	46
2.19	The beam waist w_0 and the Rayleigh length z_R shown schematically on an arbitrary Gaussian beam profile.	49
2.20	Field distributions for 2 different beam waists plotted using 2.50, highlighting the impact a reduction in the beam waist has on the divergence of the stable cavity mode.	50
2.21	A visual accompaniment to the condition that the hemispherical feature width needs to be considerably larger than the beam waist incident on in (case 1) rather than smaller, where no optical confinement would take place (case 2).	51
2.22	Lower plot shows the mode locations for a $1\ \mu\text{m}$ long planar-planar cavity (blue) and a planar-hemispherical cavity with radius of curvature $5\ \mu\text{m}$ (red), showing a marked divergence for the lower order longitudinal modes. The upper plot shows that for higher order longitudinal modes this divergence becomes less prominent.	52
2.23	The electric field lying on the $1\ \mu\text{m}$ wide beam waist for the first ten Hermite-Gauss modes. The white text indicates the labelling subscripts and each image is $4\ \mu\text{m} \times 4\ \mu\text{m}$	54
2.24	Resonant modes plotted for $q = 1, 2, 3$ and $m + n = 6$ from equation 2.62. Degenerate modes have been separated slightly and reduced in height in proportion to the degeneracy for ease of viewing.	55
2.25	Lower plot shows the mode locations for a $1\ \mu\text{m}$ long planar-planar cavity (blue) and a planar-hemispherical cavity with radius of curvature $5\ \mu\text{m}$ (red), showing a marked divergence for the lower order longitudinal modes. The upper plot shows that for higher order longitudinal modes this divergence becomes less prominent.	56
2.26	A diagram of a single cuboid Yee Cell in a 3D mesh comprised of several such cells. Components of the electric field (\mathcal{E}_{xyz}) are calculated along the edges and the magnetic field strength (\mathcal{H}_{xyz}) in the faces midpoints.	57
2.27	The leftmost diagram indicates the most relevant cavity properties. The DBRs are then constructed layer-by-layer in both the planar and featured case by the automated design script.	59
2.28	The modeled dipole location and refractive index cross sections shown within the cuboid simulation region (the outer wireframe box).	59
2.29	Depiction of the volume calculation by partial analytic integration (over ϕ) and numerical integration (over r and z).	61
3.1	Exploded diagram of single FIB column, with diagram of focal region.	64

3.2	a) An example image taken with a mid-range beam current, b) zoomed out image including the region imaged in a), showing mild damage incurred, c) further drops in magnification revealing octopole objective lens silhouette and severe aberrations around the edges.	65
3.3	A visualisation of the effect of increasing the magnification (above) and the beam current (below) on the overlap of adjacent pixels during stream file milling. . . .	66
3.4	An example surface generated by a simple MATLAB code, (inset) shows the grey scale bitmap to be read by the FIB system.	67
3.5	a) A single feature milled into silicon, b) An array of 100 features milled from an arrayed stream file, c) Several arrays of features stenciled together by moving the sample stage between mills. Scale bar 20 μm	68
3.6	Arrays of cavities milled into silicon next to a single hair. Scale bar 20 μm	68
3.7	A variety of other features milled into substrates. a) A sinusoidal curve, b) elliptical microcavities, c) arrayed SILs. Scale bar 2 μm	69
3.8	Arrays of features imaged optically. Scale bar 80 μm	70
3.9	Identical features milled into silicon a), and silica b). Scale bar 50 μm	71
3.10	AFM topography of identical features milled into silicon a), and silica b). Scale bar 5 μm	71
3.11	Optical and SEM images of the AFM tips used in this project.	72
3.12	a) SEM image of a feature milled into silicon, scale bar 3 μm and b) An AFM scan of a comparable area.	73
3.13	Single line profile of the central micrometer of a hemispherical cavity.	73
3.14	Blue - Single column of data depicted in figure 3.12b), Green - Average of first twenty columns from figure 3.12b), Red - Gaussian blur applied to an average of the first twenty columns.	74
3.15	Mesh plot of AFM data shown in figure 3.12b) with artifact digitally removed. . .	75
3.16	Complete removal of non-linear AFM tip response in x and 're-zeroing' artifact in y	75
3.17	AFM topography of features before, a), and after, b), optimising mill parameters. Scale bar 5 μm	76
3.18	A surface fit of equation 3.2 to a complete set of AFM data.	76
3.19	The residuals from the fit performed in figure 3.18.	77
3.20	Here increasing beam currents of 500, 3000, 7000 and 20000 pA (L to R) were used to mill in identical patterns.	77
3.21	The beam widths of Gaussian modes with radii of curvature 25 (blue) and 5 (red) μm for a variety of cavity lengths.	78
3.22	Mesh plot of a complete data set alongside three smaller samples of the same data. .	79
3.23	Plots of the 'square' mode diameter (from sampling square regions of AFM data) against fitted surface radii of curvature for 9 identical cavities.	79
3.24	Nine identical cavities showing almost all residuals < 1 nm for the central 1 μm of the feature.	80
3.25	Comparison of the most relevant metrics for the first (black outlined circles squares and triangles) and second (filled red diamonds and triangles) iteration of cavity features.	80
3.26	Optical microscope images at various magnifications of cavity arrays milled into plinth like structures arrayed onto a single fused silica substrate. Each plinth is approximately 200 $\mu\text{m} \times 600 \mu\text{m}$	81

3.27	SEM images of the second iteration of features milled onto plinth like projections from a fused silica substrate which has been gold coated a second time to facilitate FIB imaging. As in figure 3.26 the plinths are approximately $200 \mu\text{m} \times 600 \mu\text{m}$ in size.	82
4.1	Schematic of the bench top confocal microscope designed and constructed for interrogation of individual cavity modes.	83
4.2	Transmission spectrum for a dielectric mirror consisting of 10 pairs of $\text{SiO}_2/\text{ZrO}_2$ capped with a final layer of $\lambda/2$ SiO_2 (blue). A one dimensional model of these mirrors based on the transfer matrix approach is also plotted (red). Inset shows central region plotted logarithmically.	84
4.3	Transmission spectra from a Fabry-Pérot etalon formed of two of the mirrors characterised above, for cavity lengths decreasing from black to red to blue. In each case a mode was settled close to 637 nm	85
4.4	Transmission spectrum from the shortest cavity shown in figure 4.3 plotted with the results from a one dimensional transfer matrix model. The modeled data in red is for a cavity length of $10 \times \lambda/2$, or $q = 10$ using the labeling system of section 2.4, with the pink and blue plots above showing the cases where $q = 11, 9$ for $\lambda_q = 637 \text{ nm}$ for comparison.	86
4.5	Exploded view showing the arrangement of the substrates and manual actuators on a cage rod set-up.	87
4.6	Images of illumination spots generated by multimode and single mode fibres. In order to see the cavity arrays diffuse white light was coupled into the setup between lens 9 and fibre coupler 10 on the optical schematic shown in figure 4.1. Scale bar $50 \mu\text{m}$	87
4.7	Transmission spectrum from a relatively long cavity with RoC nominally $25 \mu\text{m}$ in blue. The red plot is given by an appropriate transfer matrix model with cavity length of $10.05 \mu\text{m}$, or a longitudinal mode of $q = 33$	88
4.8	Diagram showing that when aligned to the centre of the cavity, white light illumination excites only the TEM_{00} mode (upper). Upon mis-alignment towards the edge of the feature, higher order lateral modes are excited by the illumination (lower).	89
4.9	Spectrum obtained for a cavity with length almost identical to that of figure 4.7, however now the spot has been misaligned towards the edge of the feature, allowing increased coupling of light into the transverse modes.	89
4.10	A series of 10 spectra stacked with the longest cavity length at the top. In the uppermost spectrum the mode at approximately 637 nm (closest to the central grey arrow) corresponds to the 43rd longitudinal mode and a cavity length of $13.378 \mu\text{m}$. Each spectrum below was acquired after $\approx 318 \text{ nm}$ decrease in cavity length, so that the longitudinal modes situated at 637 nm correspond to the 42nd, 41st, 40th, . . . 34th longitudinal mode.	90
4.11	Transfer matrix model of transmission spectrum for the 42nd mode, plotted with the experimental data showing good agreement.	91
4.12	A similar set of spectra as those shown in figure 4.10. In the uppermost spectrum the mode closest to 637 nm is the 17th longitudinal mode of the cavity. Each spectrum below is taken after a reduction in cavity length of $\approx 318 \text{ nm}$ so that the 16th, 15th, . . . 5th longitudinal mode is situated at 637 nm. The very shortest of these cavities (the lowermost spectrum) corresponds to a gap between the mirrors of around $1.593 \mu\text{m}$ or with single distinct mode with longitudinal number $q = 5$	92

4.13	The spectra of the shortest cavities for all three cavity types investigated. The uppermost plot (blue) shows the transmission spectrum for the smallest (nominal) $\beta = 5 \mu\text{m}$ cavities, the red is the intermediate $\beta = 12 \mu\text{m}$ with the black is a re-plot of the lowermost curve in figure 4.12, with $\beta = 25 \mu\text{m}$	93
4.14	A high resolution spectrum of the narrowest cavity mode measured (black squares) with a Lorentzian function fitted yielding a Q factor of 14000.	93
4.15	The finesses and Q factors for every mode at 637 nm in sequences running from the shortest possible cavity to the point at which the cavity becomes to long to support stable modes (for the $\beta = 5 \mu\text{m}$ blue triangles, and $\beta = 12 \mu\text{m}$ red squares) or when drift prohibited alignment (for $\beta = 25 \mu\text{m}$ black disks).	94
4.16	The normalised numerical inverse of the mode width on the featured mirror, plotted against cavity length. The feature of note is the relative decreases in value for the three radii of curvature, suggestive of the role this plays in the drop in finesse shown in figure 4.15.	95
4.17	Plots of several higher order transverse modes once the cavities have been misaligned with respect to the illumination (blue), and the locations of the modes predicted by equation 2.62.	95
4.18	Spectrum obtained from cavity displaying pronounced splitting of the TEM_{01} and TEM_{10} transverse modes.	96
4.19	Radii of curvature determined from the relative positions of the first order transverse modes ($TEM_{01\&10}$) plotted against cavity length.	97
4.20	Plots of the numerical aperture of each of the modes formed calculated from figure 4.19, against cavity length.	97
4.21	The hypothetical maximum Purcell factors achievable for the cavities characterised.	98
4.22	Histogram of the frequency of occurrence of various Q factors from 1000 up to 5000 for an entire array of 100 features.	98
5.1	Schematic of the optical set-up used to obtain the photoluminescence from colloidal nanocrystals coupled the the open access optical microcavities.	101
5.2	Diagram of the sample mounting approach to allow coarse and fine adjustment of the cavity length. In addition a lower spacer was added to allow for white light illumination to aid in alignment.	103
5.3	Upper plot - Emission spectra from reservoir of colloidal nanocrystals away from cavity plinth, showing ~ 20 nm width Gaussian profile centred on 640 nm as expected for the free space emission of these nanocrystals. Lower plot - Emission spectra from colloidal nanocrystals for a cavity of $L = 5.5 \mu\text{m}$, $\beta = 25 \mu\text{m}$. Data obtained by Dr. ZiYun Di.	104
5.4	An image taken by the spectrograph without next to the same figure with a graded overlay to highlight the Fabry-Pérot etaloning visible. Data obtained by Dr. ZiYun Di, scale bar $10 \mu\text{m}$	104
5.5	Spectra taken from the two cavities marked in figure 5.4(a), the upper plot from a central bright region within the cavity, and the lower plot taken from the doughnut shaped mode visible in the red circle on figure 5.4(a). Data obtained by Dr. ZiYun Di.	105
5.6	Spectra taken from cavities of $L = 1.6 \mu\text{m}$ and $\beta = 25$ and $7 \mu\text{m}$ for the upper and lower plots respectively. Data obtained by Dr. ZiYun Di.	106

5.7	Schematic of the experimental set-up designed to facilitate easy switching of spectral, spacial and temporal interrogation of sample photoluminescence. The light path within the monochromator is expanded slightly and several of the optical elements inconsequential to the overall picture have been removed to simplify the diagram.	108
5.8	Time resolved photoluminescence histograms for free space emission (open squares) and cavity coupled emission (filled squares), with counts plotted logarithmically. Red lines of best fit are for the first 20 ns only to exclude poorly coupled PL. Data obtained by Dr. ZiYun Di.	109
5.9	Intensity plots for the normalised electric field distribution of a resonant TEM_{00} mode.	110
5.10	Plot of measured decay rate enhancement (as a multiple of the free space rate) plotted against cavity volume. The open squares are for $\beta = 25 \mu\text{m}$ cavities, and the open circles for $\beta = 7 \mu\text{m}$ cavities. The stars represent results obtained by FDTD analysis. Experimental data obtained by Dr. ZiYun Di.	110
5.11	Graphical representation of the multi-mode coupling and off-resonant suppression of emitter coupled to cavities in the bad cavity regime.	112
5.12	The distribution of power transmitted out of the simulation region for the case of without (a) and with a cavity (b). With no cavity in place the symmetry of the simulation means opposite faces of the cube are identical. With the cavity in place the symmetry is broken along the optical (z) axis (out of the page). The cavity parameters used match the smallest cavity achieved experimentally ($\beta = 7 \mu\text{m}$, $L = 1.6 \mu\text{m}$).	113
5.13	Time series of spectra showing the intermittency of the nanocrystal photoluminescence suggestive of single dot detection (above). The lower plot shows the total PL over the same time period, with background subtraction. Data taken by Helene Jones.	115
5.14	Emission spectrum of a Lorentzian shaped, narrower emission profile suggestive of single dot emission (blue) plotted about the mode distribution for a highly diluted colloidal nanocrystal solution exhibiting comparable spectral extent. Data taken by Dr ZiYun Di.	115
5.15	A stack of NC emission spectra coupled to the second iteration of microcavities produced. The upper plot is taken with a cavity length of $3.25 \mu\text{m}$. Each spectra below is taken after reducing the cavity length by a further 325 nm , so that a primary (TEM_{00}) mode is located at 650 nm . The lowermost spectrum corresponds to a cavity length of $\approx 1.25 \mu\text{m}$	116
5.16	Comparison of the data series shown in figure 5.15 (black disks) with several of the results obtained from the first iteration of cavities (red disks). Also plotted is a the result of a single spectrum obtained once additional care was taken to remove vibration and drift (blue star). The arrow emphasises this Q-value is a lower limit.	117
5.17	Spectral plots of nanocrystal PL populating cavity modes in the second iteration of cavities constructed (blue plots).	118
5.18	Emission spectrum obtained showing coupling of PL to transverse modes right up to the $m + n = 10$ case. This spectrum also clearly shows the degradation of the nanocrystal solution, redshifting past 675 nm	119
5.19	Expanded view of the $m + n = [0, 1, 2, 3]$ TEM_{mn} shown in figure 5.18. Note the additional degeneracy which has been lifted for the TEM_{01} and TEM_{10} modes.	119

5.20	Data series obtained by placing a linear polariser in the collection beam path and collecting nanocrystal photoluminescence for a variety of orientational arrangements. The central arrows indicate the orientation of the polariser whilst the mode distributions shown on either side provide a visualisation for a possible arrangement of polarisation with respect to the major and minor axis of the elliptical feature.	120
6.1	Schematic of the scanning head used to control the location of the focus of the collection optics (marked 4 and 5) and the excitation beam (marked 1 and 2). The dichroic mirror is selected so that it reflects red photoluminescence and transmits green excitation light. This light is then directed through a 4-f system via a fast steering mirror, allowing the confocal spot at the sample to be scanned by the distal scanning optics.	125
6.2	Diffraction limited spot obtained by the home built scanning confocal microscope by imaging the PL of an isolated NV centre in bulk diamond. Image taken by Dr Brian Patton.	126
6.3	Scanning imaging of the white light illuminated cavities. This can be performed with diffuse (a) or focused (b) illumination, scale bar 10 μm	127
6.4	Schematic indicating the method for imaging the higher order modes. The spectra show the alignment of the higher order mode with the 637 nm illumination. The cavity schematics show the required length tuning, and the images the anticipated mode structure.	128
6.5	Two sequences of higher order modes obtained by tuning the length to allow successive cavity modes to become resonant with the 637 nm laser illumination. Scale bar 2 μm	128
6.6	Spectra for the NV^- colour centre obtained at room (grey) and liquid nitrogen (black) temperatures. Also marked on the spectrum are the first and second order Raman peaks generated by the non-linear response of the diamond crystal.	129
6.7	Optical and PL images of the FIB marked dielectric mirrors.	130
6.8	Schematic of the optical set-up for obtaining the experimental HBT results and the theoretical results for results obeying Bose-Einstein (blue) and Poissonian (red) statistics, and a single emitter (black).	131
6.9	PL map of marked substrate with the locations of three emitters highlighted for photon statistical analysis.	131
6.10	HBT data for the three marked emitters in figure 6.9. The first shows clear single emitter statistics, whilst the second show a partial anti-bunching. The third has only the slightest of anti-bunching dips visible.	132
6.11	Linear and logarithmic y-axis plots for various illumination intensities of the same emitter. There is clear bunching around the central anti-bunching dip, indicating the presence of a third, metastable ‘dark’ state.	132
6.12	Schematic of the optical set-up used to obtain room temperature coupling of NV centres to optical microcavities.	133
6.13	An illustration to clarify the emitter and microcavity arrangement.	134
6.14	Consecutive images taken to ascertain the relative positions of the NV centres on the front planar mirror and microcavities on the back featured mirror.	134
6.15	The images in figure 6.14 superimposed on one another to clearly show the relative locations of the NV centres and the optical microcavities	135
6.16	Spectra obtained from the 3 microcavities labeled in figure 6.15.	136

6.17	Comparison of the white light transmission spectrum obtained from the cavity close to the NV1. This shows identical mode locations, with the NV centre showing increased coupling to the transverse modes.	136
6.18	a) - Schematic of the scanning confocal head arranged above a large cryogenic dewar to allow for low temperature measurements to be taken b) An expanded view of the sample region, b) Expanded view of the piezo positioners.	138
6.19	Room temperature PL measurements taken showing the ability to traverse an emitting object into spatial resonance with an optical microcavity.	139
6.20	Room temperature PL measurements taken showing the ability to traverse an emitting object into spacial resonance with an optical microcavity.	140
7.1	Series of resonant field cross sections plotted with linear and logarithmic color scales. The series forms a subset of the results presented in figure 7.2, showing the numerical values for the calculated volumes.	144
7.2	Plot showing the decrease in mode volume as the radius of curvature of the feature is lowered, such that a TEM_{00} is situated close to the maximum reflectivity. Black squares show the modeled volumes, with blue triangles showing the unaltered formula (7.1), and red disks with a penetration depth of 0.3λ included in the formulas length parameter.	145

List of Tables

1.1	Currently achieved figures of merit for open access optical microcavities. .	7
3.1	Summary of the main characteristics of the cavities produced using FIB milling. Figures 3.25(b) and 3.25(a) depict their measured radii of curvature and RMS residuals.	82

Abbreviations

AFM	A tomic F orce M icroscope
APD	A valanche P hoto D iode
CQED	C avity Q uantum E lectro D ynamics
DBR	D istributed B ragg R eflectors
DoS	D ensity of S tates
FDTD	F inite D ifference T ime D omain
FIB	F ocussed I on B eam
FSR	F ree S pectral R ange
FWHM	F ull W idth H alf M aximum
HBT	H anbury B rown T wiss
NV	N itrogen V acancy
PCC	P hotonic C rystal C avity
PL	P hoto L uminescence
QED	Q uantum E lectro D ynamics
RoC	R adius of C urvature
SCM	S canning C onfocal M icroscope
SEM	S canning E lectron M icroscope
SIL	S olid I mmersion L ens
SPAD	S ingle P hoton A valanche D iode
TRPL	T ime R esolved P hoto L uminescence
WGM	W hispering G allery M ode
ZPL	Z ero P honon L ine

Physical Constants

Speed of Light	c	$=$	$2.997\,924\,58 \times 10^8 \text{ ms}^{-1}$
Planck's constant	h	$=$	$6.626 \times 10^{-34} \text{ Js}$
Planck's reduced constant	$\hbar = h/2\pi$	$=$	$1.055 \times 10^{-34} \text{ Js}$
Electric permittivity	ϵ_0	$=$	$8.854 \times 10^{-12} \text{ Fm}^{-1}$
Permeability of free space	μ_0	$=$	$4\pi \times 10^{-7} \text{ NA}^{-2}$

Symbols

a	distance	m
E	energy	J
$g_{\omega}(\omega)$	density of states (ang. freq. space)	
$g_{\mathbf{k}}(\mathbf{k})$	density of states (k space)	
\mathcal{F}	Finesse	
n	refractive index	
P	power	W (Js^{-1})
Q	Q factor	
R	Radius of curvature	μm
t	time	s
V	volume	m^3
x	displacement	m
\mathcal{E}	electric field	Vm^{-1}
\mathcal{B}	magnetic field	T
\mathcal{D}	electric displacement	Cm^{-2}
\mathcal{H}	magnetic field strength	Am^{-1}
ω	angular frequency	rads^{-1}
λ	wavelength	nm

For Amelia and my Parents, for my future and my past,

Chapter 1

Introduction and Literature Review

1.1 Thesis Outline

In this thesis I aim to discuss my contribution to the field of optical microcavitation. As with any discussion, context is vital and to provide (an admittedly restricted) vista of the state of this particular art I will discuss some of the literature published to date. I am fortunate in that this field is constantly and rapidly developing but for this reason a strong caveat has to be attached to this literature review, in that there is a wealth of fantastically ingenious work that I will unfortunately overlook. Once some degree of context has been developed by this review the next chapter will deal with some theoretical details. This will include a variety of physics ranging from the fundamental to a few more esoteric topics. After this chapter I will describe in detail how the primary subject of my thesis, the novel hemispherical microcavities, are constructed. This will include technical notes and many of the more mundane aspects which were crucial to perfect in order to achieve some measure of success. I will proceed to discuss the optical characterisation of these cavities, presenting results that formed the basis of a publication [12]. After this, results from several photo-luminescence (PL) experiments will be presented. These will include results that were taken by myself with no direct assistance, and some that were taken taken as part of a collaborative effort. Finally I will end with chapter to conclude the achievements of this thesis, and present a look to the future with the assistance of some finite difference time domain simulations to estimate the limitations of this approach.

1.2 Project Goals

In the task of optically integrating a single quantum emitter there is often one main goal: to collect as much light as possible. Passively collecting light as efficiently as possible by using ever higher numerical aperture objective lenses, such as oil or solid immersion lenses [13, 14] or near field fibre optic constructions [15, 16] is limited by only ever being able to collect 100% of the light. There is a much more elegant approach which can potentially out-perform even a perfect collection system. During the 1940s investigations in a very different field, that of nuclear magnetic resonance led Edward Purcell to show that by coupling the sample to a resonator it was possible to alter its spontaneous emission rate [17]. Since then it has been understood that cavitation effects can drastically alter the emission properties of any emitter well coupled to them. The potential of this insight is worth restating. By altering the environment in which we place our emitter we can potentially tailor it to have drastically altered emission properties. It is a method of enhancing one of the most relevant interactions, that of a dipole with the electromagnetic field. Since then progress in this area has been unceasing, and these effects have been utilised in experiments and devices for lower frequency interactions, in the microwave spectral region with fantastic results. The challenge now is to construct optical resonators, or cavities of a high enough quality and a small enough volume to be able to take advantage of these effects in the optical regime. If done well enough this approach can not only encourage photon emission towards the collection optics, but emit *more* photons than it normally would in free space. A technique that achieves this will always outperform any clever collection scheme. That is the goal of this project. For the most part, this has been based around the emission of a NV defect in diamond. This defect has a lot of potential as a candidate for a quantum bit (a ‘qubit’) in a scalable quantum computer. Despite many properties which have attracted considerable interest from the global research community one of the big drawbacks for its implementation in a scalable quantum computer via some type of path erasure entanglement system is the fact that a relatively small amount of light is emitted in its zero phonon line. The microcavities described in this thesis are designed to be able to enhance this zero phonon line emission whilst suppressing the majority of its phonon assisted decay. In addition to NV centres, semiconductor nanocrystals were also analysed, indeed it is their incorporation into these microcavities at room temperature which form the basis of the most recent journal submission, [18].

1.3 Optical Microcavities

In their essence optical cavities are a means to confine light for as long as possible within a particular region, thus enhancing its interaction with any system also contained in the cavity. In recent years developments in microcavities, optical cavities with dimensions on the micron length scale, have allowed scientists to observe certain effects that can no longer be described with a classical theory of light. These cavity structures come in a plethora of forms and offer rich insights into a variety of fundamentally new phenomena, and could form the basis of potentially revolutionary technologies. Enhancements of this interaction can potentially impact many devices or processes which involve light and matter. For example flow cytometry involves exposing large numbers of cells to laser radiation in order to detect fluorescent marker molecules. Low laser powers often have to be used to avoid killing the cells under examination. The use of microcavities would allow the fluorescent molecules to interact more strongly with the incident light whilst leaving the cells unharmed. Many other sensing technologies also stand to be enhanced, from superconducting single photon infra-red detectors to biomedical assaying. Improved control of this interaction could also play a pivotal role in the further development of new ‘quantum’ technologies such as single photon generation for quantum cryptography and measurement based entanglement procedures for quantum information processing. These technologies often have stringent requirements on efficiencies of photon generation, collection and detection, all of which stand to be improved upon with the development and application of optical microcavities. In addition, microcavities are vital tools in studying the physics of the interaction between light and matter, allowing the stunning accuracy of quantum electrodynamics (QED) to be extended into what has developed into an entire field in its own right, that of cavity quantum electrodynamics (CQED). This review will begin with a detailed examination of progress in the specific type of microcavity this thesis is associated with. After this several of the alternative methods of microcavitation will be presented via a brief analysis of fewer, more major publications. Amongst these experiments are approaches involving micropillars, microspheres, microdisks and microtoroids. The impact of photonic crystals cavities (PCCs) on this field will also be covered. Before introducing any cavities however some initial definitions and descriptions will be provided. Many of these will be expanded upon in subsequent chapters and their purpose here is to facilitate the appreciation of some achievements in the literature to come.

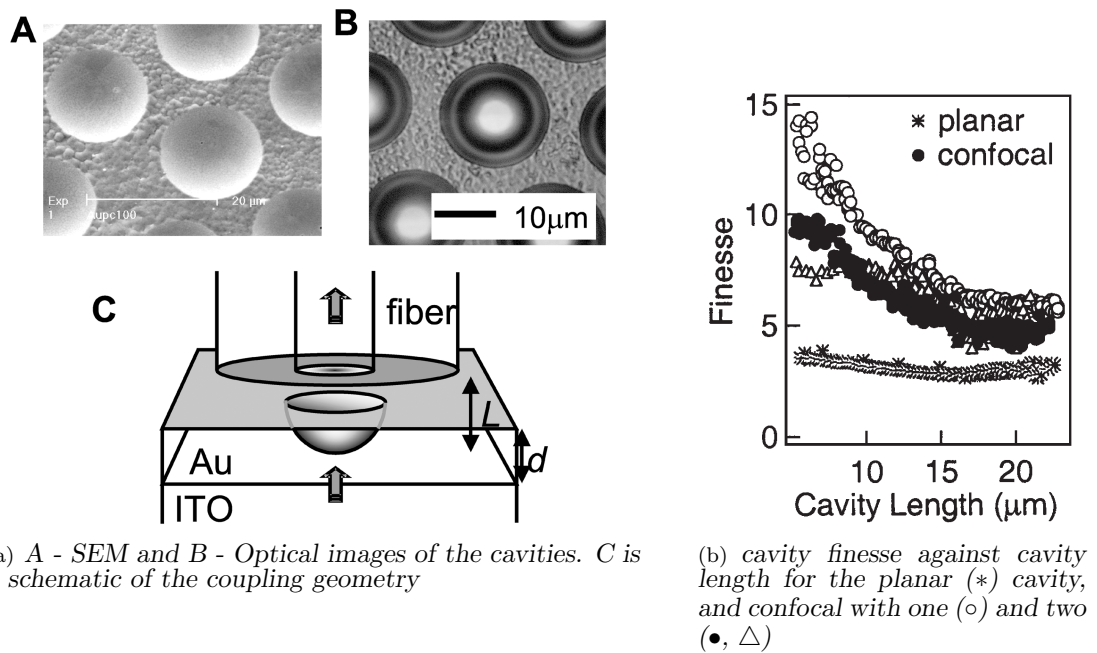
The first metric to be mentioned here is the cavity finesse, represented algebraically as \mathcal{F} . Physically this represents loss of photons per round trip within the cavity. In the field of microcavitation it is desirable for the value of this quantity to be maximised, as increasing the number of passes a photon on average makes within a cavity increases

its chances of interacting with any system contained within the cavity. This often takes values between 50 and 100, in exceptional circumstances exceeding values of 10^5 . A second metric of the cavity is the Q factor. Physically it represents the number of oscillations a resonant photon can make before being scattered out of the cavity, and is proportional to the time a photon spends inside the cavity. A good Q factor for a microcavity would generally exceed 10^3 with some of the very best achieving the order of 10^8 . Although the Q factor of a cavity should also be maximised, it is not as directly related to an enhancement of the light matter interaction as the finesse. This can be understood by considering the example of a simple cavity constructed by arranging two mirrors to be perfectly parallel and separated by a small gap. The number of round trips made by photons within this cavity (the finesse) can only be improved by increasing the mirrors' reflectivity. The amount of time spent within the cavity (the Q factor) can be increased by either improving the reflectivity of the mirrors, or increasing the distance between the mirrors. By increasing the reflectivity the finesse also increases, and the interaction would be enhanced. However, for increases in the length of the cavity the finesse and the potential interaction strength remain constant, although the Q factor has increased. Both of these metrics are discussed in much more detail in section 2.3.2. The section preceding this one (section 2.3.1) contains a detailed description of dielectric mirrors, or distributed Bragg reflectors (DBRs) which can achieve reflectivities in excess of 99.999% in the visible region (compared with metallic mirrors $< 98\%$). Finally, in the 'strong coupling regime' (mentioned at the end of section 2.2.2) the interaction between an emitter and a cavity is completely described by three rates. These are γ , the free space decay rate of emitter, κ , the cavity decay rate (inversely proportional to the Q factor) and g , the cavity - emitter coupling rate.

1.3.1 Open Access Microcavities

I will begin the review of relevant literature with several approaches very similar to the one implemented in this thesis. As stated above, in their essence cavities aim to contain light within a three dimensional region. A straight forward way of confining light is to arrange two mirrors opposite one another. If they are perfectly parallel then resonant light is restricted to the entirety of the planar region in between them and is then confined in one out of three dimensions. In fact even this partial confinement is sufficient to enhance the collection efficiency of light by a factor 2, as shown by Dumiege *et al* in 2011 with their thorough consideration of experimental results and theoretical extrapolations [19]. Here an NV centre in diamond was coupled to a moderate finesse ($\mathcal{F} \sim 60$) planar Fabry-Pérot cavity formed by two unbalanced distributed Bragg reflectors (DBRs), collecting photons through the less reflective of the mirrors.

A modification to this situation, by creating a hemispherical feature on the surface of one of the mirrors can further contain light in the other two dimensions, opening the door to true microcavitation effects. The details of why and how this allows for light to be contained in all three spatial dimensions will be discussed in chapter 2, but essentially the challenge of this approach is how to make a sufficiently small hemispherical feature on a very reflective surface. The first approach to be discussed here is based on work carried out at the University of Southampton [1, 20]. In this investigation, latex microspheres were used to template the electrochemical deposition of gold onto an indium tin oxide (ITO) surface. The end of a cleaved, striped single mode fibre was coated with a 28 nm



(a) A - SEM and B - Optical images of the cavities. C is a schematic of the coupling geometry

(b) cavity finesse against cavity length for the planar (*) cavity, and confocal with one (○) and two (●, △)

FIGURE 1.1: Reproduced from reference [1].

Au film and positioned above the concave spherical feature (figure 1.1(a)). The cavity was illuminated from below the ITO, and the transverse modes were mapped. The results were in good agreement for cavities with a larger radius of curvature than that of the spheres used as templates, highlighting a minor issue with the method of production, specifically that the spherical template method leaves a small completely flat (radius of curvature, $R = \infty$) area in the base of the microcavity. In addition it was found, as expected, that the lateral confinement provided by the microcavity improved the finesse ($\mathcal{F} > 15$), compared to the planar cavity equivalent ($\mathcal{F} < 5$). Trupke *et al* in 2005 constructed this type of microcavity with a wet etching technique. This scheme was designed to be implemented for atom optics experiments, and so the open access was a key feature [21]. With this approach cavity finesse of around 6000 were achieved for cavities with radius of curvature ≈ 185 , making use of highly reflective distributed Bragg

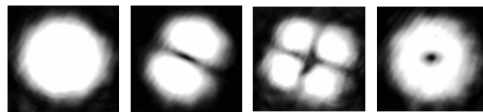


FIGURE 1.2: *Imaged Hermite-Gauss (00,01,11) and Laguerre-Gauss (01) modes from left to right, reproduced from [2].*

reflector (DBR) stacks. The planar substrate in this case was actually formed from the tip of an optical fibre, to facilitate light collection.

About a year later hemispherical features were also coated with DBR mirrors by Cui *et al* [2]. In this paper the production method involves creating the features out of bubbles formed in molten silica. This method only allows for cavity lengths and radii of curvature down to $40\ \mu\text{m}$, and no Q factors are quoted, but finesses of up to 200 are achieved and stand to be improved upon with mirror contamination being the limiting factor. Figure 1.2 shows some of the Hermite-Gauss and Laguerre-Gauss modes formed from these cavities. Also in this year another method involving direct fibre coupling was developed [22]. This involved using a convex stamp to pattern the core of the fibre prior to coating with the radius of curvature getting as low as $100\ \mu\text{m}$ with finesses of around 1000. This technique was further developed, and in 2009 Muller *et al* achieved a much lower radius of curvature, as low as $34\ \mu\text{m}$ [23].

More recently a pulsed CO_2 laser has been used to ablate a concave feature in a fused silica substrate [24–26]. Once again, as with the approach used in [2] this did achieve radii of curvature as small as $40\ \mu\text{m}$, which is approaching the limit that this particular laser ablation technique can achieve. A shorter wavelength of light could potentially push this limit back, however to achieve ultra low volumes operating below the diffraction limit of light is a considerable advantage in terms of achievable mode volumes. All three papers do however show that the smoothness of the features and their sphericity allow for highly reflective coatings of up to 0.999997. This meant that they achieved finesses in excess of 150,000 with cavity lengths $\sim 10\ \mu\text{m}$, giving Q factors of the order 10^6 . Achieving these kinds of values for smaller volumes is the ultimate goal of this project.

As these approaches are so similar to the one that this thesis proposes the achievements of the current state of the art of open access hemispherical microcavities is summarised in table 1.1.

In this table italicised entries are estimates based on the other values given in each publication. The conclusion to draw from this is that as it stands laser ablation gives sufficiently smooth surfaces to achieve excellent cavity finesses. It does seem that this approach will struggle to fabricate features with radius of curvature less than 30 or 40

TABLE 1.1: Currently achieved figures of merit for open access optical microcavities.

1st author	RoC (μm)	Finesse	Technique	Year	Volume (μm^3)
Prakash [1]	10	30	Latex sphere templating	2004	< 5
Trupke [21]	185	6000	Wet HF + acid etch	2005	> 50
Cui [2]	50	50	Bubbled glass	2006	> 50
Steinmetz [22]	100	1000	Convex template	2006	600
Muller [23]	34	1000	Convex template	2009	44
Muller [25]	30	$> 150,000$	Laser ablation	2010	40
Hunger [24]	45	$> 130,000$	Laser ablation	2010	> 5
Barbour [26]	80	900	Laser ablation	2011	> 7

μm , unless the application of adaptive optics or some other advancement brings it much closer to the diffraction limit of the CO_2 laser used is approximately half the wavelength used, of $\lambda \sim 10 \mu\text{m}$. The requirements that this places on a technique to supplant these approaches are that it will need to maintain a comparable surface roughness to the laser ablation approach, whilst producing features with radius of curvature less than $5 \mu\text{m}$.

In addition, an alternative to the spherical shape, specifically a parabolic dome cavity, has also been considered [27], in which a very complete analysis of the mode structure concludes that deformations corresponding to even small deviations from confocality result in chaotic ray patterns.

1.3.2 High Q Factor Fabry-Pérot Cavities

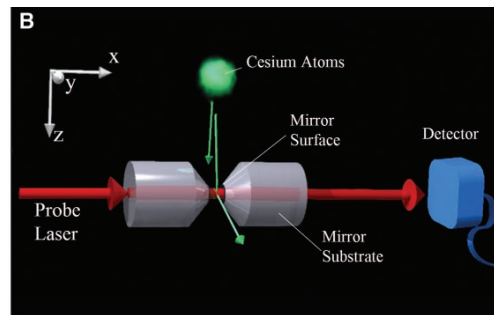


FIGURE 1.3: A high finesse cavity situated below a magneto optical trap (MOT) to allow single atom detection. Reproduced from reference [3].

Although they do not entirely qualify as microcavities due to the large path lengths of the light being held in the cavity (often of the order of centimetres), high finesse Fabry-Pérot cavities have achieved much in terms of observing atom-light interactions. Here we will discuss those advances made in the optical region of the spectrum, as opposed to the microwave region. Recently optical cavities have achieved a remarkable level of stability, which can allow for an atom cavity system to enter into the so called ‘strong

coupling' regime of CQED. This is where the coupling strength between the emitter and cavity dominate the cavity leakage and the spontaneous decay of the emitter. Such high finesses are unattainable when using metallic mirrors (which can achieve exceedingly high finesses in the microwave region), but by making use of periodic changes in refractive index, very large reflectivities (and therefore finesses in cavities) can be achieved. In 1996 such cavities were able to detect in real time the presence of an individual atom within the cavity [28]. This is no mean feat considering the scale of the atom, in the order of Angstroms is several orders of magnitude below the diffraction limit optics is normally constrained by. In this set up a high finesse ($\mathcal{F} = 2 \times 10^5$) Fabry-Pérot resonator is made from two super polished spherical mirrors (radius of curvature 1m) with highly reflective dielectric coatings. The finesse of a cavity can be calculated from the free spectral range (FSR) of the spectral mode distribution, and the full width half maximum of the modes. It can be thought of as an alternative to the Q factor as a way of quantifying cavity perfection.

If the atomic, cavity and probe laser frequencies are all equal ($\omega_A = \omega_C = \omega_L$), both the Jaynes-Cummings Hamiltonian [3, 29–31], and the optical bistability state equation predict that the presence of an atom within the cavity should drop its transmission. This drop depends on the atom-cavity coupling constant, g , and is a function of position with the cavity. For an atom dropped through a cavity this then becomes a function of time, $g[\mathbf{r}(t)]$. In this setup the cavity is large enough and the coupling strong enough that the atom dwell times are relatively long, allowing for the atom to cycle through a variety of equilibrium states during its transit. This has been extended in [32], to such a level that the trajectory of a single atom can be inferred from the master equation governing the atom cavity interaction and the fluctuations in the transmission of a probe laser. Results taken in this manner showed atoms orbiting the cavity mode several times before falling out of the cavity. This optical detection of single atoms hints at some of the potential the precise control of available light modes can offer. A year later the same group led by Kimble produced a full characterisation of the mirrors used to get such high finesses [33]. These papers are framed in the language of the strong coupling regime, and have been included to give insights into just how sensitive devices based on optical microcavities could become.

1.3.3 Micropillars

A further application of DBR mirrors [34], used in conjunction with self assembled quantum dots, is shown when a layer of such dots was embedded between two Bragg stacks, separated by a deposited layer only a few wavelengths of light thick. Micropillars (see fig 1.4) can then be constructed by etching away regions of the stacks leaving pillar

structures. This approach has been used for vertical cavity surface emitting lasers as the reduced volume allows for a very low lasing threshold, and is also used for all optical switching devices. The pillar in figure 1.4 is a representative sample, reproduced from a

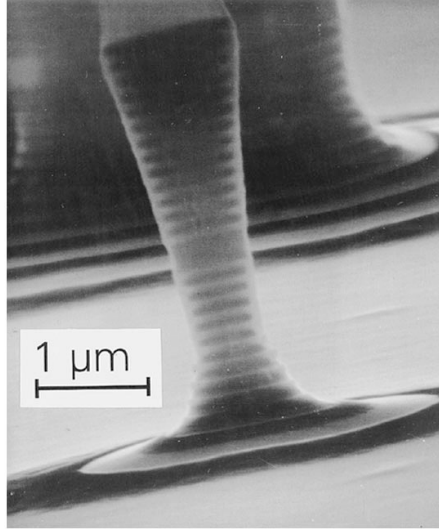


FIGURE 1.4: An SEM image of GaAs/AlAs micropillar, diameter $1.3 \mu\text{m}$. Reproduced from reference [4].

paper by Gerard *et al*, published in 1996 [4] and consists of InAs quantum dots (QDs) with an areal density of $4 \times 10^{10} \text{ cm}^{-2}$ sandwiched between a top GaAs/AlAs quarter wave DBR of 13 periods, and a bottom one with 23. The pillar shape was obtained using a reactive ion etch. This arrangement in extended planar form (prior to etching) allows for cavities with Q factors of 1600. Q factors can be thought of as a way of quantifying how good the cavity is at trapping light. The lateral confinement caused by the etching process (essentially introducing a cylindrical dielectric boundary) increased this to $Q \approx 2700$ for pillar radii $> 2 \mu\text{m}$, although this dropped to $Q \approx 400$ for the thinnest $r = 0.35 \mu\text{m}$. This is probably due to diffraction losses through the side walls. Two years after this initial investigation into the nature of mode formation in micropillar structures, in 1998, the same group published a five-fold enhancement of the spontaneous emission from InAs QDs [5]. In this case the QDs were positioned at the anti-nodes of the standing wave resonant mode formed between a stack of 15 (top) and 25 (bottom) GaAs/AlAs DBR stacks. The fundamental mode of the pillar is calculated to be as small as $\sim 5(\lambda_c/n)^3$, which, combined with Q factors in excess of 2000 in $1 \mu\text{m}$ diameter pillars, yielded a Purcell factor of $F_p = 32$, a record at the time for such structures. The Purcell factor is determined by the ratio of cavity modes to free space modes, but can be written in terms of the cavity volume, V and the Q factor of the cavity, as in equation 1.1.

$$F_p \equiv \frac{3Q(\lambda/n)^3}{4\pi^2V} \quad (1.1)$$

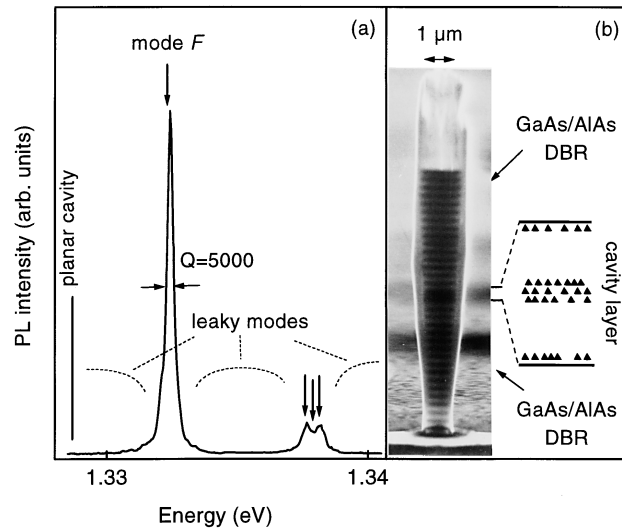
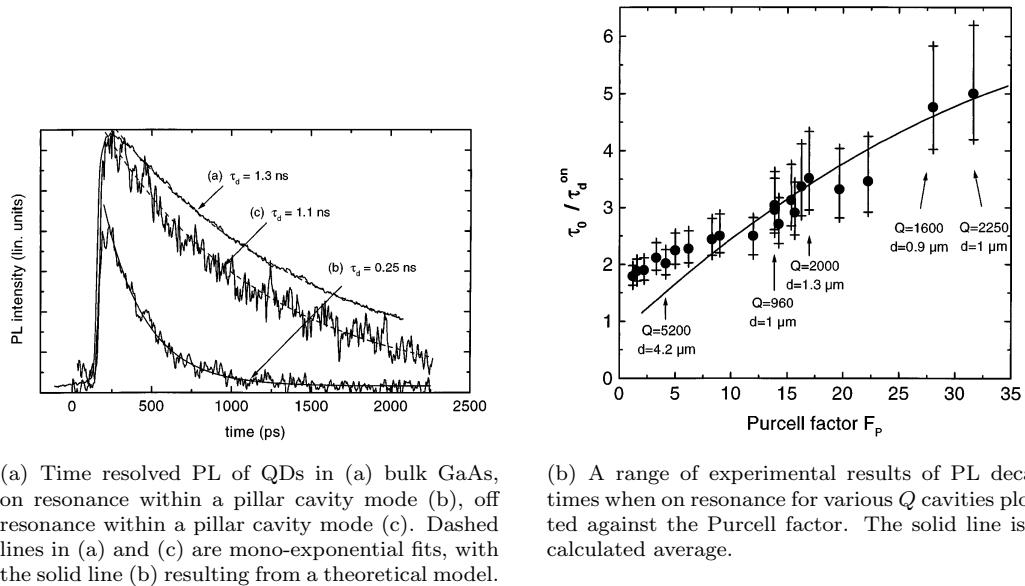


FIGURE 1.5: (a) A typical PL spectrum of coupled InAs QDs. (b) SEM micrograph of a $1\mu\text{m}$ pillar with the inset showing the location of the InAs QDs. Reproduced from reference [5].



(a) Time resolved PL of QDs in (a) bulk GaAs, on resonance within a pillar cavity mode (b), off resonance within a pillar cavity mode (c). Dashed lines in (a) and (c) are mono-exponential fits, with the solid line (b) resulting from a theoretical model.

(b) A range of experimental results of PL decay times when on resonance for various Q cavities plotted against the Purcell factor. The solid line is a calculated average.

FIGURE 1.6: Reproduced from reference [5].

More recent developments, and a shift to the use of $\text{TiO}_2/\text{SiO}_2$ as the dielectrics for the DBR stacks has led to much higher Q factors ($\sim 3 \times 10^6$) in much smaller volumes ($\sim 0.1(\lambda/n)^3$) being theoretically demonstrated [35] incorporating a “tapered DBR” design to mode match the localised cavity mode to the evanescent Bloch mode inside the DBR. With these high Q factors, along with calculated values of κ (the cavity loss rate) and γ (the spontaneous emission lifetime), it is shown that this system is no longer in the weak coupling regime, and has entered well into the strong coupling regime [31].

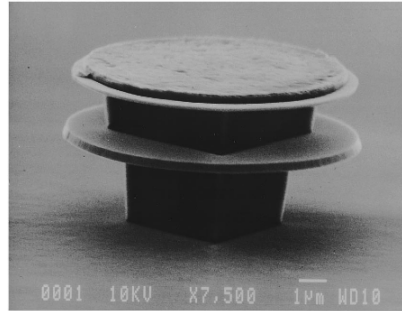


FIGURE 1.7: SEM of a $5 \mu\text{m}$ radius laser diode microdisk. Reproduced from reference [6].

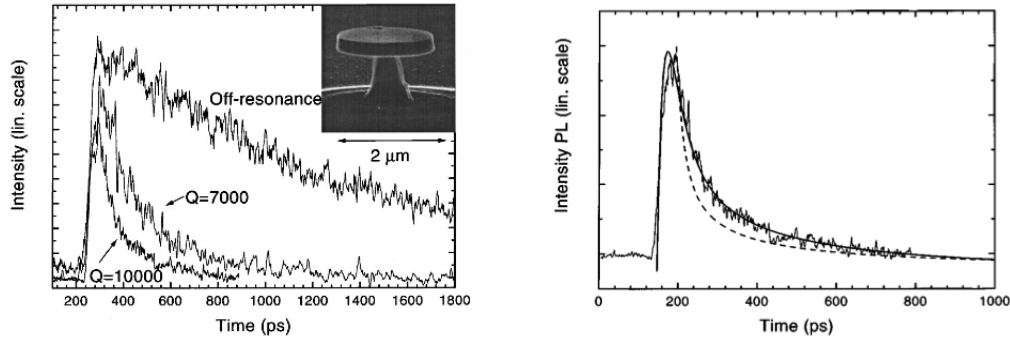
This is where the coupling constant, g is much greater than γ and κ , and so a coherent oscillation of energy between the cavity and emitter can occur.

1.3.4 Microdisks

Microdisks will be the first of several structures in this discussion that make use of an alternative confinement effect described as ‘whispering gallery modes’ [36] (WGMs) in reference to a particular acoustic effect in St. Paul’s Cathedral. In this form the photons propagate around the perimeter, being constantly constrained by total internal reflection occurring at a dielectric interface. Structures that achieve these sort of modes normally (but not necessarily [37]) have some sort of circular symmetry (i.e. disks, toroids, spheres) and have been used, amongst other things, to make microdisk laser diodes (figure 1.7) [6].

In one instance utilising this method of mode confinement [7] InAs QDs were shown to experience a Purcell Factor of up to 155 when coupled to the WGMs of a GaAs microdisk. The InAs/GaAs QDs were fabricated via self organised growth. When cooled their emission linewidth (less than $30 \mu\text{eV}$) is smaller than that of high quality ($Q > 20000$) microdisk cavities. Such high Q factors are obtainable since the primary leakage mechanism comes only from scattering due to defects on the wall of the disk, or the unavoidable tunnelling of light upon total internal reflection. By minimising scattering sites these high Q factors can be combined with small cavity volumes (as small as $1.8 \mu\text{m}$ diameter) and have shown that impressive Purcell factors are achievable. Figure 1.8(a) from [7] shows the Purcell effect appearing in several real-time photoluminescence (PL) measurements of QDs off resonance as well as those on resonance in microdisks with $Q = 7000$ and 10000 . The decay time of the off resonance case, at 1.2 ns is comparable to InAs QDs in bulk GaAs. Interestingly whilst the off resonance case can be described with a mono exponential, figure 1.8(b) shows that a such a simple monoexponential

model is insufficient for the Purcell enhanced emission. Indeed even the necessary steps of summing all the monoexponential decays with a variety of characteristic lifetimes and incorporating the spread of spectral and spatial overlaps of the QDs with the WGM is still inadequate (this gives the dotted line in 1.8(b)). The Purcell enhancement for the QDs best coupled to the mode drops their spontaneous lifetime below 10 ps, that is, shorter than the capture/relaxation time of the carriers in the QD. The addition of a 20 ps capture/relaxation time gives a good agreement to the time-resolved PL recorded.



(a) Time resolved PL for the off resonant case, and for two micro disks with Q s of 7000 and 10000.

(b) Time resolved PL for the $Q = 10000$ disk with mono-exponential fitting (dashed line) and with the addition of 20ps capture/relaxation time (solid line).

FIGURE 1.8: *Reproduced from reference [7].*

1.3.5 Microspheres

Carrying on with the WGM confinement method, fused-silica microspheres [9, 38] offer one route to get to the strong coupling regime. In this case the spheres can be made with surfaces so smooth that light can be confined within the structure for appreciable amounts of time, which is equivalent to saying that they can achieve some remarkably high Q factors. In fact with these WGMs, especially the ones with low radial mode numbers, the problem is less how to contain the light and more how to achieve an efficient, stable, controllable coupling to free space modes. Initially this has been done using a prism to couple light into and out of the cavity [38]. By matching the angle of incidence on the internal surface of the prism to the propagation constant of the desired mode to be excited, and making use of frustrated total internal reflection, specific modes can be addressed. An alternative method uses a side polished fibre as an excitation source [39, 40], but this can only achieve efficiencies of 20% for relatively large spheres with diameters ~ 1 mm and much less for smaller spheres. However, a novel and very efficient solution to the problem of coupling light into such spheres was offered in a paper in 1997 [9] in which an optical fibre taper is used. In the tapered region of the fibre the

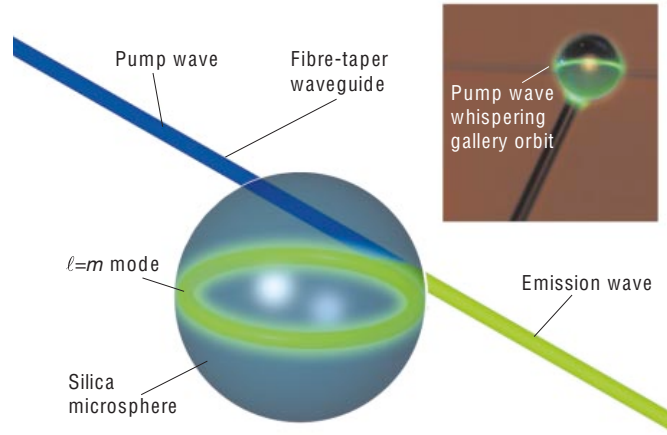


FIGURE 1.9: *Illustration (photo inset is of a rare earth doped sphere) of a microsphere equatorial WGM using a fiber taper delivery system for the pump. Reproduced from reference [8].*

diameter, ρ is reduced to $1.4 < \rho < 3 \mu\text{m}$. With such a small diameter the evanescent part of the light propagating in the fibre mode is reasonably extensive. The propagation constant of this mode, β then depends on the wave vector of the light k and the refractive index N as one would expect, as well as the fibre diameter. This propagation constant has to be matched with that of the mode confined within the sphere which depends on several parameters of the particular mode being considered. These modes are labelled by l , m and n which are the polar, azimuthal and radial mode numbers respectively. The propagation constant can be approximated to be dependant only on l , x_{nlm} , which is the size parameter of the mode and k , the is the wave vector in free space. This is a reasonable approximation to assert, as the modes of interest are those of low n and $m \simeq l$. These equate to modes propagating close to the surface (low n) and around the equator of the sphere ($|m| = l$). The results of matching these two parameters is shown in figure 1.10, in which the solid curve is a plot of the propagation constant of the fibre mode, β_{fibre} against the fibre diameter, ρ . The dots are the propagation constants for first few radial orders (lowest few n values) and a variety of microsphere sizes (equivalent to l). The experimental setup then employed is shown in figure 1.11a, with the resulting transmission profile shown in figure 1.11b. The main trace shows the transmission of a sphere with $a \simeq 85 \mu\text{m}$, corresponding to $x \simeq 350$ coupled with a delivery fibre taper of $\rho \simeq 1.7 \mu\text{m}$ which has a coupling efficiency of 72% and a Q factor of 2×10^6 . The inset shows a higher Q in a larger sphere with $a \simeq 210 \mu\text{m}$, $\rho \simeq 2.25 \mu\text{m}$, $Q = 5 \times 10^7$ and coupling efficiency 37%. In this case the resonance linewidth was due entirely to the acoustic linewidth of the laser source, and so higher Q factors could have been observed. One year after the tapered fibre approach was published, as predicted in [9] a $Q \approx 8 \times 10^9$ corresponding to a finesse of $\mathcal{F} \approx 2.2 \times 10^6$ in the near infra-red was

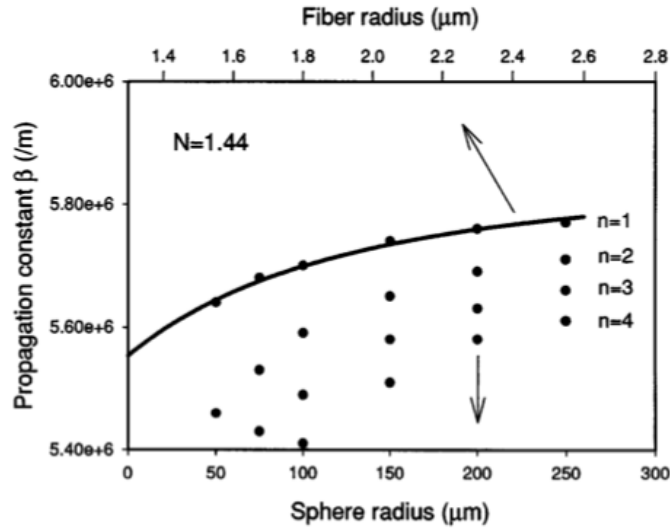


FIGURE 1.10: Solid line - Calculated propagation constants for the fibre tip as a function of radius (top y axis). Points - The same constants for the first few n modes of the sphere, as a function of sphere radius (bottom y axis). Reproduced from reference [9].

achieved [41]. In this paper efforts were made to quantify the limiting factors. Atomic force microscopy (AFM) gave a value for the rms roughness of $\sigma \sim 2$ nm and the time dependent reduction in Q suggested that both surface scattering and the absorption of water into the surface of the sphere, rather than bulk absorption of silica limits the maximum achievable Q factor. More recently these experiments have been used as the basis for low threshold Raman lasers [42].

1.3.6 Microtoroids

The WGM method of confinement has since been developed to the microtoroid case (figure 1.12)[?]. This progression of the microdisk takes a step towards implementing a microchip based solution to the problem of micro-optical cavitation. A silicon substrate with a $2 \mu\text{m}$ thick layer of SiO_2 grown on its surface undergoes an initial photolithographic patterning step to create circular photo-resist regions. This is followed by HF and XeF_2 etches and finally some IR laser illumination ($10.6 \mu\text{m}$, 10 MWm^{-2}) leaves a toroid. Figure 1.12 shows the final result, with the inset showing the disk prior to the laser melting. The final toroid can be addressed by the same tapered fibre method as used in the microsphere case. As an aside, the Q factor of the cavity prior to the laser illumination was found to be of the order 10^5 . Figure 1.13(a) shows the transmission spectrum of such a cavity. Geometrical considerations lead to the conclusion that the free spectral range corresponds to adjacent equatorial modes (l and $l + 1$) as inspection of the dimensions of the toroid show it will support very few radial (n) or azimuthal

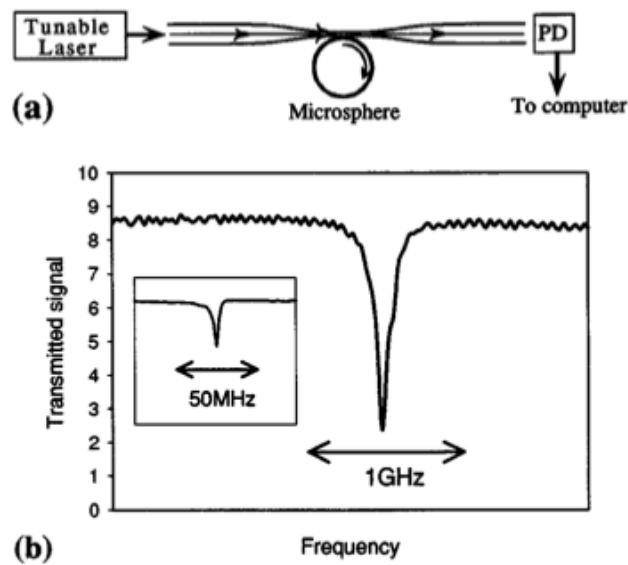


FIGURE 1.11: (a) Schematic of the experimental setup. (b) Spectrum showing 72% efficiency coupling light into a WGM, Q factor 2×10^6 (sphere size $\alpha \approx 85 \mu\text{m}$, fibre taper size $\rho \approx 1.7 \mu\text{m}$). Inset shows the highest Q achieved, 5×10^7 with 37% collection efficiency ($\alpha \approx 210 \mu\text{m}$, $\rho \approx 2.25 \mu\text{m}$) Reproduced from reference [9].

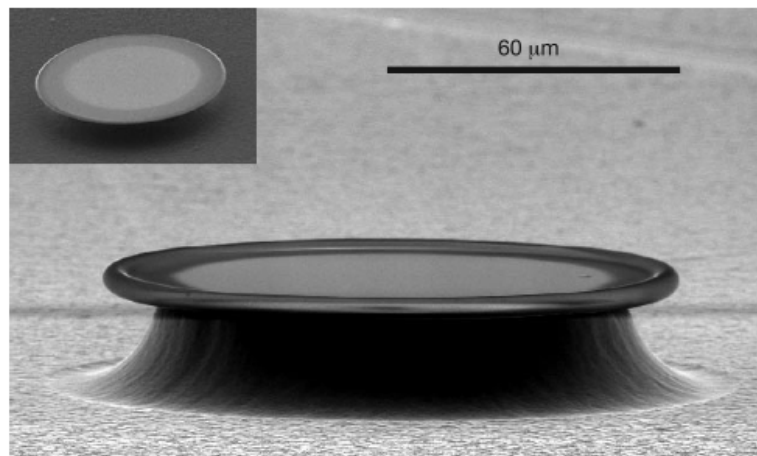
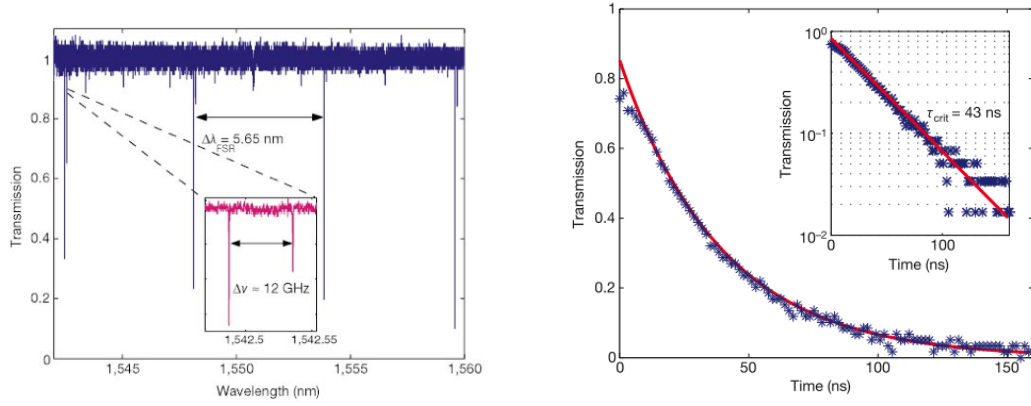


FIGURE 1.12: SEM image of a microdisk with Q of 1.00×10^8 . Reproduced from reference [?].

(m) modes. The Q factor of this system can be obtained in two ways, both of which were performed. The first approach is to use a single mode laser (short term linewidth ~ 300 kHz) to spectrally scan over the sample (figure 1.13(a)) and take the FWHM of the Lorentzian shaped resonance. This yielded Q factors consistently in excess of 10^8 for a variety of torii radii and thicknesses. The second method of finding the Q factor is essentially to completely load the cavity with light, then switch the light off and measure the ringdown of the signal. This result is shown in figure 1.13(b) and indicates the cavity has a lifetime of τ_{crit} 43 ns. This result as it stands will give the ‘loaded’ Q



(a) Resonant frequency transmission dips, the FSR of 5.65 nm between successive azimuthal modes suggests a $94\mu\text{m}$ toroid. Inset shows the two lowest order radial modes.

(b) The ringdown of a $90\mu\text{m}$ toroid giving a lifetime, τ_{crit} of 43 ns corresponding to a Q of 1.25×10^8 .

FIGURE 1.13: *Reproduced from reference [?].*

factor of the cavity, which is distinct from the ‘intrinsic’ Q factor (used in this review thus far). In order to obtain the intrinsic Q factor the intermode coupling parameter, Γ , which quantifies the coupling between the modes loaded by the fibre and some counter propagating modes populated by intrinsic scatterers in the disk has to be found (see [43]). The loading by the taper waveguide also has to be accounted for (exactly why is not fully explained). The value of Γ was found to be 1 which is equivalent to 17% of the field being stored in counter propagating modes, and is put into equation 1.2 to give the intrinsic Q factor.

$$Q \equiv \omega\tau_0 = \omega\tau_{crit}(1 + \sqrt{1 + \Gamma^2}) \quad (1.2)$$

This equation yields $Q = 1.25 \times 10^8$ which is in good agreement with the spectral approach. This technique has since been developed, and although it has seen no substantial improvement in the Q factors obtained, in 2007 the toroids began to be lifted off their plinths (see figure 1.14) [10], with only marginal decreases in their Q factors occurring due to damage incurred during the lift off. These free toroids can now be coupled more easily to a variety of photonic devices. Arrays of this type of microresonator have also been successfully coupled to cold caesium atoms by allowing the laser cooled atoms to drop through evanescent fields protruding beyond the physical extent of the disks [44].

1.3.7 Photonic Crystal Microcavities

Photonic crystals (PCs) work due to multiple photon scattering within dielectrics that have periodic interfaces. It is analogous to the way the periodicity of semiconductor crystals effects the motion of electrons. Photonic crystal cavities [45–49] can be formed by a missing hole in the periodic crystal (often cavities are denoted M1, referring to 1 missing hole in an M type array, M2 is two missing, etc.). In principle, the highest

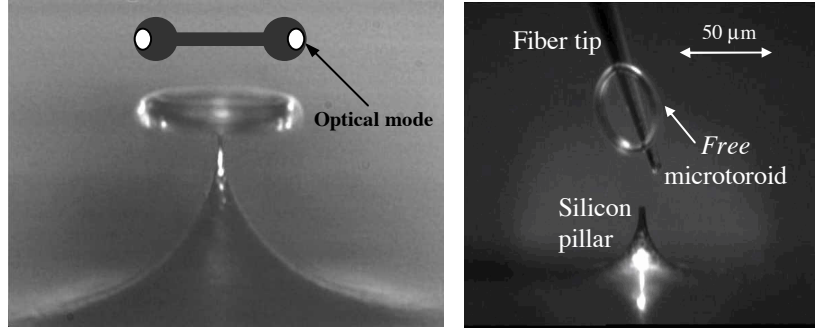


FIGURE 1.14: Optical images of micro tori before and after liberation from the plinth used during the growth. Reproduced from reference [10].

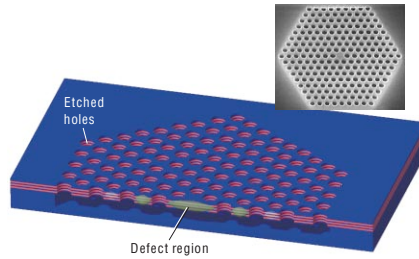


FIGURE 1.15: Cross section of a photonic crystal cavity. The defect region is shaded in green and the inset shows an SEM of the same structure. Reproduced from reference [8].

possible enhancements are achievable using a three dimensional arrangement of two materials with high refractive index contrast [50]. Currently, however the most progress has been made in coupling emitters two dimensional crystal cavities [51–53] using some other mechanism to constrain the light in the third dimension (often total internal reflection). It has been shown [11] that spontaneous emission can be either enhanced or suppressed depending on whether the emitter is coupled or decoupled to the photonic crystal. This suppression or enhancement is attributed to, in the Wigner-Weisskopf approximation, a change in the local density of optical states (LDOS). The Wigner-Weisskopf approximation is that the excited state of a two level system has a spontaneous emission that is an exponential decay [54]. In agreement with intuition, the enhancement occurs with an increase in the LDOS, and suppression with a decrease.

In more detail, the spontaneous emission rate is the sum of the emission rate into the cavity modes, plus all other modes, $\Gamma = \Gamma_{cavity} + \Gamma_{other}$. Here the density of states of the cavity modes follows a Lorentzian line shape, as expected for a lightly damped oscillator, and the density of the other states is reduced in photonic crystal, compared to bulk material. The emitter is at position \mathbf{r}_A and is spectrally detuned from the cavity's resonant wavelength by $\lambda - \lambda_{cavity}$. Here we are considering the weak regime [31] where the cavity decay rate $\kappa = \frac{\pi c}{\lambda Q}$ is greater than the coupling strength of the emitter to

the cavity $|g_{cavity}(\mathbf{r}_A)|$ which is dependent on the position of the emitter, as in [28, 32]. The spontaneous emission rate can then be calculated using Fermi's golden rule. The enhancement factor is given by equation 1.3, which is the ratio the system emission rate in the cavity crystal system to the emission rate in bulk material.

$$\frac{\Gamma}{\Gamma_0} = F_{cavity} \left(\frac{\mathbf{E}(\mathbf{r}_A) \cdot \boldsymbol{\mu}}{|\mathbf{E}||\boldsymbol{\mu}|} \right)^2 \frac{1}{1 + 4Q^2 \left(\frac{\lambda}{\lambda_{cavity}} - 1 \right)^2} + F_{PC} \quad (1.3)$$

Here $\left(\frac{\mathbf{E}(\mathbf{r}_A) \cdot \boldsymbol{\mu}}{|\mathbf{E}||\boldsymbol{\mu}|} \right)^2$ and $\frac{1}{1 + 4Q^2 \left(\frac{\lambda}{\lambda_{cavity}} - 1 \right)^2}$ account for the spatial, orientational and spectral mismatch of the emitter dipole $\boldsymbol{\mu}$ to the cavity field, \mathbf{E} and F_{PC} is the spontaneous emission rate in the equivalent photonic crystal without the cavity incorporated (i.e. $F_{PC} \neq \Gamma_{PC}/\Gamma_0$). The Purcell factor of the cavity is given in identity 1.1, where n is the refractive index and V is the volume of the mode in the cavity. These considerations can allow a finite difference time domain (FDTD) approach to yield a photonic crystal design that will maximally couple an emitter with the cavity, achieving as high a Q factor and as low a V as possible. According to this design the cavity will have a predicted Q factor of 45000 and V of $0.5 \left(\frac{\lambda}{n} \right)^3$. Self assembled InAs quantum dots (QDs) are coupled to a single defect cavity in photonic crystal. The crystal structure was patterned onto membranes of 160 nm thick GaAs with a single central layer of self assembled InAs QDs. These dots emit with a 50nm line width inhomogeneously distributed around 920 nm. Figure 1.16 (a) shows the FDTD assisted design of the photonic crystal cavity

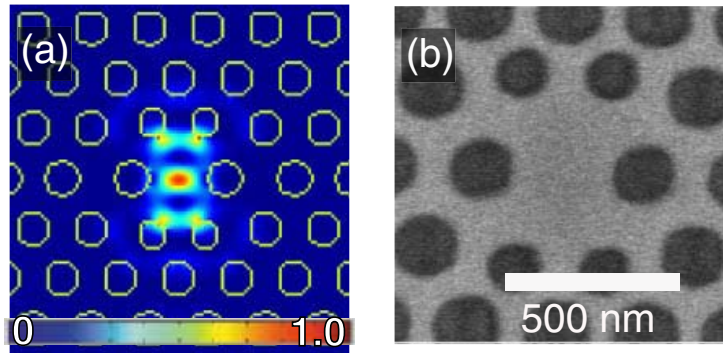


FIGURE 1.16: (a) FDTD simulation of the resonant cavity modes for an M1 PC with periodicity $a = 0.27\lambda_{cav}$, hole radius $r = 0.3a$ and crystal thickness $d = 0.65a$. (b) A SEM of the cavity. Reproduced from reference [11].

with the calculated electric field intensity of an x -dipole resonance. The resonances were quantified by photoluminescence (PL) measurements performed with a confocal microscope set up, simultaneously taking spectral and photon coincidence information by means of a beam splitter, a spectrometer and two photon counters. The 0.6 NA objective lens gives a $0.6 \mu\text{m}$ spot size (wavelength 750 nm) exciting QDs only in the cavity, or in very close proximity. The spectrum for QDs in the bulk material is shown

in the inset of figure 1.17 (a). The Q factor for the cavity is calculated by using a high

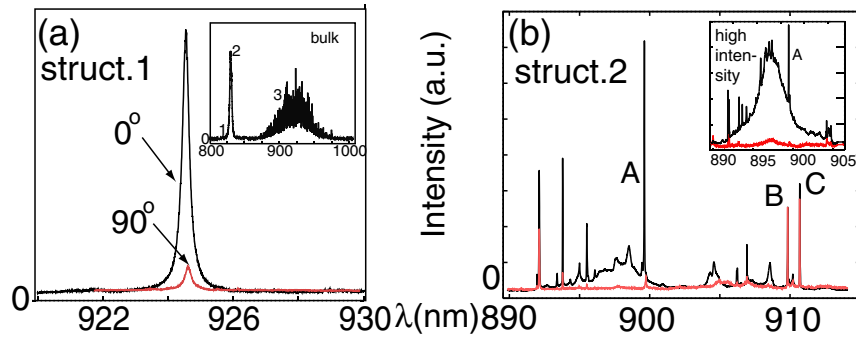


FIGURE 1.17: (a) Spectrum for structure 1 shows strongly pumped dipole mode with a Q of ~ 5000 although no emission peaks match the crystal resonances in this case. (b) Structure 2, the inset shows the high pump power, revealing a Q factor of 250, with the low power spectrum shows a coupled exciton line that matches the cavity polarisation. Reproduced from reference [11].

pump intensity (1.5 kW/cm^2) and fitting a Lorentzian curve to the spectrum. Four such cavity structures were analysed. A typical example is shown in the main plot 1.17 (a). In this case no single exciton emission lines matched the cavity so no coupling took place, and the Q factor was calculated to be $Q \approx 5000$. This is an order less than intended by the FDTD pattern, and is attributed to fabrication inaccuracies. An additional consideration is that whilst a high Q means strong enhancement or suppression, the narrow spectral linewidth of a high Q means the cavity requires a much closer spectral agreement with a QD if they are to be effectively coupled. This necessitates the focus to be shifted to more modest Q s. The next three structures (struct.2, struct.3 and struct.4) whose spectra are shown in 1.17 (b), and 1.18 (c) and (d), have Q factors of 200, 250 and 1600 respectively, calculated from the high intensity line widths shown in the insets, and have the same design as that shown in figure 1.16. The low intensity plots for these

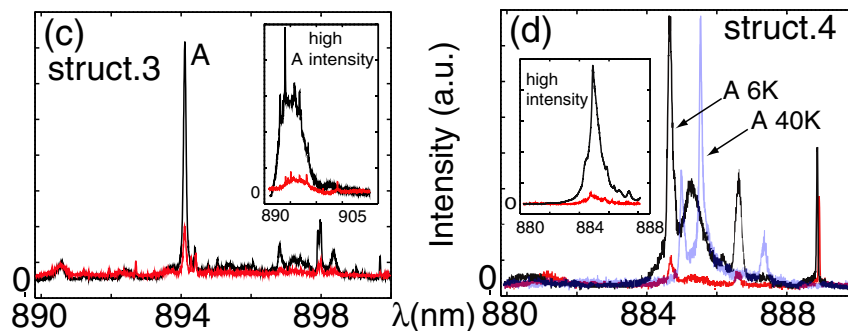


FIGURE 1.18: (c) The equivalent plot to 1.17(b) for structure 3 with a Q of 200. Peak B mentioned in the passage is not shown. (d) Inset shows line coupled to the cavity mode with $Q \approx 1600$. Temperature is used to tune the QDs into resonance. Reproduced from reference [11].

structures show single exciton lines coupled the cavity modes. In figure 1.18 (d) the light QDs have been tuned using the dot's temperature dependence, from 6K to 40K. The line marked A from structure 2 in figure 1.18 (b) indicates some coupling to the cavity mode, confirmed by the polarisation dependence [55] when only one of the two near-degenerate orthogonal emission lines of the dot is enhanced. The enhancement of the decay rate, Γ can be observed as a decrease in the lifetime, τ of the exciton since $\tau_A = \frac{1}{\Gamma}$. A streak camera was used to obtain values for all the emission peaks labelled in figure 1.17 (b). $\tau_A = 650$ ps, $\tau_B = 3.8$ ns and $\tau_C = 4.2$, as well as the lifetime of τ_A when excited by a pulse polarised at 90° and are shown in figure 1.19 (a). Considering

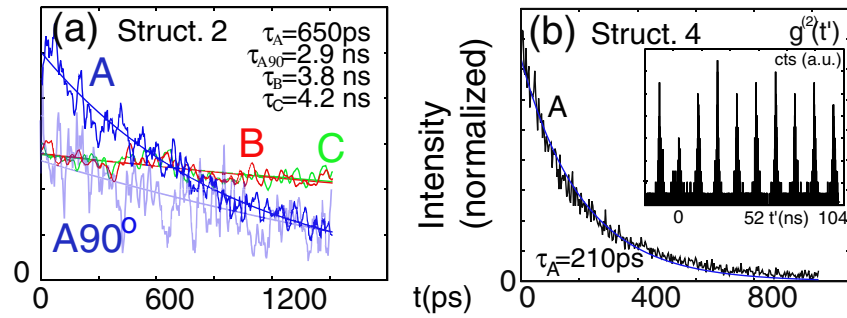


FIGURE 1.19: Time resolved spontaneous emission modification because cavity coupling (a) shows the suppression and enhancement of emission in structure 2. (b) shows a shortening of the lifetime to just 210 ps, with the inset showing the antibunching for a single emitter. Reproduced from reference [11].

that the excitonic lifetime for a layer of QDs in bulk GaAs (with no photonic crystal structure) has distribution of $\tau_0 = 1.7 \pm 0.3$ ns this indicates an enhancement for line A of $F_A = 2.6 \pm 0.5$ and suppressions for lines B and C. A similar coupled-enhancement /decoupled-suppression occurs for the spectrum in figure 1.18 (c), with the line A once again being enhanced and line B (not shown) at 932nm being suppressed. All of these lines were confirmed to be from single emitters using the photon counting statistics autocorrelation function and the results from the Hanbury Brown-Twiss interferometer.

Equation 1.3 casts some light onto the suppression of emitters, as the spectral detuning $\frac{\lambda}{\lambda_{cavity}}$ effectively removes the first term, leaving the second term F_{PC} which is below one due to the diminished local density of states. Figure 1.20 is a surface plot of exactly how these detunings (spectral and spatial) can either enhance or suppress lifetimes, note that the red rim is the unaltered decay, where $\frac{\Gamma}{\Gamma_0} = 1$. In conclusion, this paper has shown enhancement and suppression of single emitters. Whilst it is technically possible to achieve enhancements in the order of up to ~ 400 according to equation 1.3 the inability to either spectrally or spatially align these QDs to the cavity or visa versa limits enhancements to an 8 fold faster spontaneous emission rate. It is this type of combined enhancement (of the defect in diamond's zero phonon line) and suppression

(of the phonon assisted side band) that this DPhil project aims to achieve. In addition to

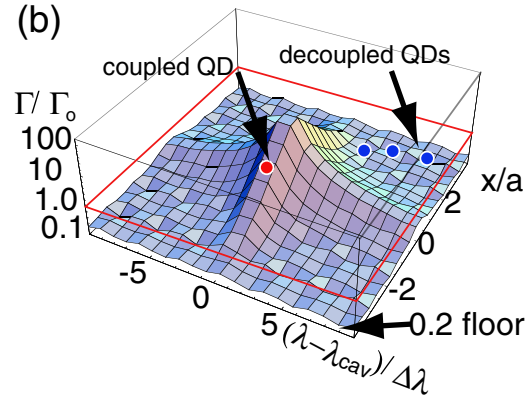


FIGURE 1.20: A surface illustration of the effect of misalignment spectrally and spatially on the spontaneous emission rate. The points observed experimentally are marked. Reproduced from reference [11].

altering aspects of the spontaneous emission of radiation the fabrication of this form of cavity is being constantly honed, with notable improvements being devised in [46, 56–58], especially in the later two where fine tuning features of the air holes close to the cavity allows for up to a 20 fold increase in achievable Q factors. Work has also been carried out exploring the possibilities of replacing the air with an alternative material, to further improved the versatility of this approach [59]. In fact photonic crystals have also been designed to reproduce the WGMs more often associated with microspheres or microdisks [60], as well as being extended into 3 dimensions, by stacking multiple layers of periodic GaAs around a single defect layer [61]. InAsSb QDs were generated in some of the basic GaAs layers to provide a light source, and a peak Q factor of 2,300 was recorded. This versatility has been further emphasised by coupling together large numbers ($N > 100$) of photonic cavities whilst still maintaining very large Qs, concomitantly also achieving very slow group velocities for spectral experiments and pulse propagation experiments ($c/1000$ and $c/170$ respectively) [62].

1.4 Summary and Conclusions

The above discussion is really a summary in its own right. With the possible exception of the first section, any one of the approaches briefly mentioned could be vastly expanded upon. As there is such a wealth of diverse literature, in this section I will attempt to further summarise the strengths and weaknesses of the myriad of approaches covered and so finish this chapter with a more concise perspective on the various routes to microcavitation. To facilitate the comparisons I will initially mention the factors that

are important in considering what makes a good microcavity. The most frequently touted figures of merit are the Q factor (or finesse) and the cavity volume which need to be as large and as small as possible, respectively. As well as this there needs to be some method of ensuring the emitter is perfectly coupled in terms of both resonance energy and spatial positioning. Another factor that may be vital to some applications is how well the confined cavity mode is coupled to free space optics.

In terms of maximising the confinement of the light, whilst minimising the volume theoretically at least, the clear winner is a full 3D PCC. These can achieve volumes a fraction of the size of the wavelength cubed, and can achieve exceptionally large Q factors. At this stage however full 3D PCCs are still very much in their infancy. That said, 2D PCCs still boast the smallest volumes and achieve respectable Q factors, and are routinely incorporated into the structures in which QDs are grown. Micropillars can achieve good Q factors and can generate single photons well [63, 64], but seem to have reached their limit in terms of mode size, as leakage through the pillar sides begins to unavoidably contribute to a drop in Q factor below pillar diameters of a few microns. Similar size constraints plague any of the WGM approaches, although they have achieved some of the highest Q factors observed.

In order to address the perfect spatial and spectral coupling, one key feature that every realistic cavity coupling system cannot do without is some method of resonance tuning. Because the resonances of any particular confinement system are determined by the geometry, and often the line widths of the emitters being considered are very narrow, the conditions placed on the precision with which one constructs the cavity are beyond stringent. It is not realistic to design a cavity to be precisely resonant with most narrow line width emitters. In this aspect the open access microcavities have a clear advantage over WGM, PCC and micropillar approaches, as they can physically be tuned over a broad spectrum in environments ranging from cryogenic to ambient. Temperature tuning is an established method for varying the position of resonance of PCCs and in addition a ‘digital’ etch has been developed [65], although referring to it as a tuning technique is slightly misleading as it is irreversible. A similarly irreversible method exists for tuning WGMs of microdisks, by introducing a noble gas into the environment at low temperatures and pressures [66, 67]. The gas then condenses on the surface of the structure, altering the resonances properties. However this both shifts the location of the resonance and degrades the Q factors achieved, and so is also not an ideal tuning method.

Assuring good spatial overlap is another challenge which for many of these approaches is somewhat unresolved. For the decoupled substrates of an open access cavity, once again this optimisation is straightforward, well within the capacity of modern piezo positioners.

For the PCC approach, either by registering the emitter's position and constructing the cavity around them [68], or relying on an average density [69], consistently coupling quantum dots to these kinds of cavity is now possible. WGM appear to have the most trouble coupling to quantum emitters. Placing a nanocrystal on the surface degrades the Q factor considerably [70] and also requires 'pick and place' nanotechnology [71, 72] which adds a non-negligible level of technical difficulty to production.

Finally in terms of coupling to free space optics, once again the WGM approaches suffer having to rely on evanescent field coupling and remains a considerable engineering challenge. For photonic crystals, it is possible to directly incorporate waveguides into the PCC structure and this can improve the light collection dramatically [48, 69, 73]. Once again it is straightforward for the open access approach to couple to free space optics or fibre optics, since the Gaussian modes formed from the hemispherical mirror are perfectly matched to the modes collected by an objective lens.

Figure 1.21 shows the four categories of approaches and approximate volumes and Q factors achieved by each.

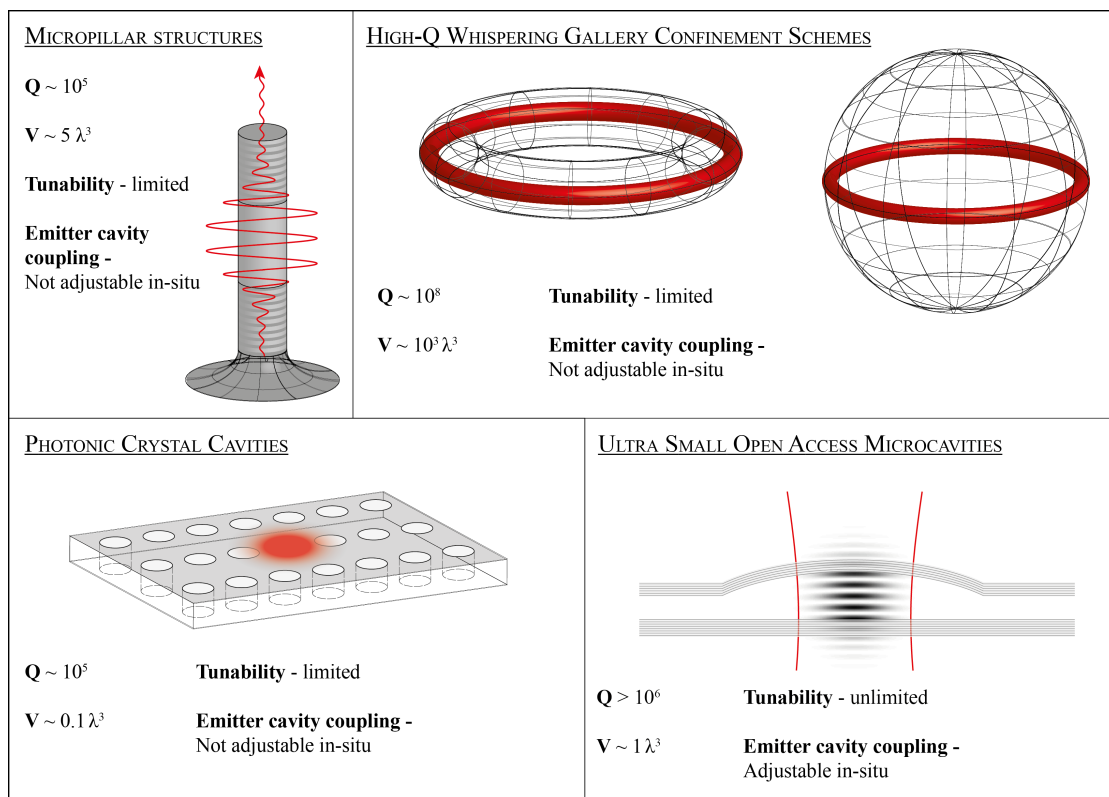


FIGURE 1.21: Schematics and approximate estimates of the capacities of some of the various approaches to microcavitation.

Chapter 2

Theoretical Background

2.1 Introduction

This chapter will be comprised of three sections. First will be a derivation of the often quoted Purcell factor, F_p . This will be framed in a general discussion of several aspects of atom-field coupling. The second section will then discuss a few specific details of the types of modes that will turn up in the open access hemispherical cavities of this thesis. The final section will discuss some of calculations performed whilst simulating the microcavities with a finite difference time domain engine. This will also include a brief description of the simulation procedure itself.

2.2 The Purcell Factor

As mentioned in chapter 1, in April 1946 Edward Purcell found an increase in spontaneous emission probability as the expression in equation 2.1.

$$F_p \equiv \frac{3Q(\lambda/n)^3}{4\pi^2V} \quad (2.1)$$

Although the paper in which this expression was introduced pertained to the field of nuclear magnetic resonances, and in this case it was small metal particles that played the role that the optical cavity does in this thesis, the effect observed was a fundamental one. In order to adequately explain this effect it is useful to gain a thorough understanding of spontaneous emission. One of the first attempts to incorporate spontaneous emission into quantum theory was made by Einstein, who listed it as one of his three coefficients [74]. This is defined in the straightforward rate equation 2.2 where N is the number of

light sources prepared in their excited state.

$$\frac{\partial N}{\partial t} = -A_{21}N \quad (2.2)$$

This equation can be solved to show A_{21} as the decay constant in an exponential decay. At this stage quantum theory was not sufficiently developed to offer a more thorough explanation as it was still only quantising the energy of the atom, but remaining with a classical description of radiation. Shortly after this Einstein turned his attention to general relativity, and so this effect was more completely described a decade later [75]. In a seminal text book later published [76] to consolidate developments in quantum theory spontaneous emission was described in a fundamental equation that would later be referred to as ‘Fermi’s golden rule’, and is shown in equation 2.3.

$$\Gamma_{i \rightarrow f} = \frac{2\pi}{\hbar^2} \left| \langle f | \hat{H}' | i \rangle \right|^2 g_{\omega f} \quad (2.3)$$

In this equation $\Gamma_{i \rightarrow f}$ is the transition rate from an initial to a final state $|i\rangle$ and $|f\rangle$ are initial and final energy eigenstates, $g_{\omega f}$ is the density of final states and π & \hbar have their usual meanings. This equation can be derived by making use of perturbation theory. This theory was implemented in an effort to aid the application of quantum mechanics to anything more complex than the most basic, symmetric systems. In its essence it assumes that the system being dealt with is very similar to a ‘nice’ symmetric system upon which the standard approaches of functional analysis can be brought to bear. As quantum mechanics is primarily involved with Hamiltonian mechanics, this can be expressed as

$$\hat{H}_{total} = \hat{H} + \hat{H}' \quad (2.4)$$

where \hat{H}' is the perturbing Hamiltonian and is small compared to \hat{H} , the Hamiltonian of the unperturbed system which in practice has to be a time independent system with equations possessing analytic solutions. This powerful approach can be implemented to accurately take into account static perturbations of a system’s energy eigenvalues, for example in the Stark effect. If the perturbation considered is time dependent then it can cause the system to change its energy state from an initial eigenstate $|i\rangle$ to a final one $|f\rangle$, via the emission of a single photon of energy corresponding to the energy difference between the two states. Through Planck’s relation [77] we can assign angular frequency ω_0 to the photon corresponding to this energy. The rate of this transition can be shown to be equal to the right hand side of 2.3 if the density of final states for the photon is assumed to form a continuum, and the dipole has discrete energy eigenvalues. It is important to note that the application of Fermi’s golden rule is appropriate for transitions where no further interaction occurs between the atom and the field final states. Specifically this means that it cannot accommodate the possibility of the photon and the ground state

interacting again, after the emission process. For this a much more complete quantum description of the field is required [29, 30, 78].

Since the Purcell factor represents a rate enhancement, we can work it out by applying Fermi's Golden rule to a dipole in both free space, and also within a cavity. Then by taking the ratio of these rates, we can arrive back at the expression discovered by Purcell 2.1.

2.2.1 Optical Density of States

In order to begin this process we need a method to quantify the optical density of states (DoS). These optical states are also referred to as 'modes' especially in the context of optical cavitation, as resonances often form a harmonic series, or harmonic modes. To begin with it is useful to set up a clear way of counting the modes. The method taken here is based on approaches that can be found in [79, 80]. A volume V can be defined as a cube with sides length L . A cube is a convenient choice as much of this work will be conducted in a Cartesian coordinate system, but the geometrical shape chosen does not effect the final result. We can then represent any electric field distribution present in this region as a sum of traveling waves, as in equation 2.5.

$$\mathcal{E}_{total}(\mathbf{r}, t) = \sum_{\mathbf{k}} \mathcal{E}_{\mathbf{k}} e^{i(\mathbf{k} \cdot \mathbf{r} - \omega t)} \quad (2.5)$$

Here the summation is over all the possible \mathbf{k} vectors of the traveling waves, each with an angular frequency of ω . Gauss's law of electrostatics (2.31b) applied to the vacuum gives us the divergence of the field, which must be zero ($\nabla \cdot \mathcal{E} = 0$). Applying this to our electric field distribution in equation 2.5 gives us the expression shown in equation 2.6,

$$\nabla \cdot \mathcal{E}_{total}(\mathbf{r}, t) = \sum_{\mathbf{k}} \mathbf{k} \cdot \mathcal{E}_{\mathbf{k}} e^{i(\mathbf{k} \cdot \mathbf{r} - \omega t)} = 0 \quad (2.6)$$

Which is only true for the case when $\mathbf{k} \perp \mathcal{E}_{\mathbf{k}}$, so the electric field is then always pointing perpendicularly to the direction of motion of the wave, as one expects for the transverse nature of light. This does mean however that for each \mathbf{k} vector of light we can have some combination of 2 orthogonal polarisations, which can be taken into account by multiplying any total number of \mathbf{k} vectors by 2. We can then arrive at a sensible method for counting the possible \mathbf{k} vectors by making the stipulation shown in equations 2.7,

where $n_x, n_y, n_z \in \mathbb{Z}$.

$$k_x = 2\pi n_x / L \quad (2.7a)$$

$$k_y = 2\pi n_y / L \quad (2.7b)$$

$$k_z = 2\pi n_z / L \quad (2.7c)$$

This means that every possible \mathbf{k} can be written in the form shown in equation 2.8, and are easily counted by the use of the rational set of numbers \mathbb{Z} .

$$\mathbf{k} \equiv (k_x, k_y, k_z) = \frac{2\pi}{L} (n_x, n_y, n_z) \quad (2.8)$$

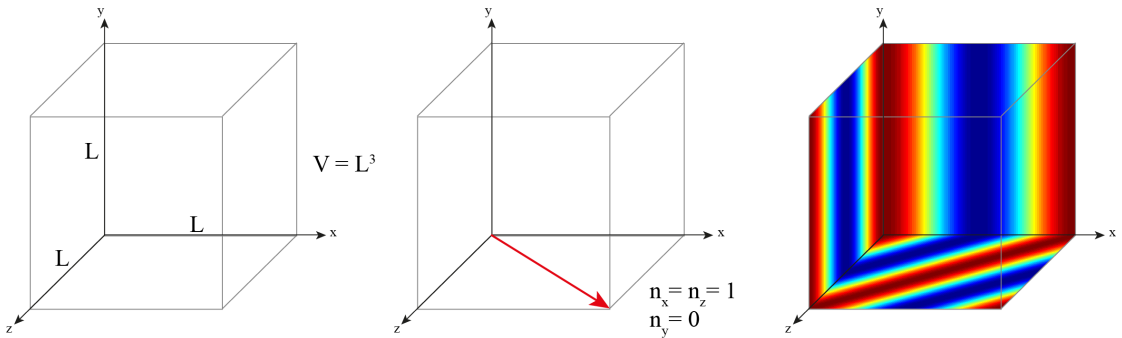


FIGURE 2.1: (a) Conceptual cubic volume to facilitate optical state counting. (b) An example \mathbf{k} vector, $L/2\pi(1,0,1)$ plotted within the volume. (c) colormaps of field associated with plane wave with the same \mathbf{k} vector.

Figure 2.1 (a) shows the volume being considered, with (b) showing an example \mathbf{k} vector where $n_x = n_z = 1$ and $n_y = 0$. The planar wave for this vector is plotted in colormaps on the three of the cube's faces to aid visualisation in Figure 2.1 (c). If rather than plotting these modes in the normal x, y, z coordinate system, we plot them in 'k' space, with the axis markings taking the values of k_x, k_y and k_z we find that the allowed modes form a three dimensional array. The first 125 positive allowed modes are plotted in Figure 2.2 and can be seen to be dispersed evenly over the interior of a cube. Each mode is a distance $2\pi/L$ from the next, and can be thought of as occupying a volume of $(2\pi/L)^3$. We can then work out how many allowed modes are contained in the volume element of the sphere between k and $k + dk$, where k carries the normal value as the magnitude of the vector \mathbf{k} , calculated as $k = \sqrt{k_x^2 + k_y^2 + k_z^2}$. By dividing the number of modes allowed within this volume by the effective volume a single mode occupies we can arrive at an expression for the DoS in k-space. This is shown in equation 2.9.

$$g_k(k)dk = \frac{4\pi k^2 dk}{(2\pi/L)^3} = \frac{V k^2 dk}{2\pi} \quad (2.9)$$

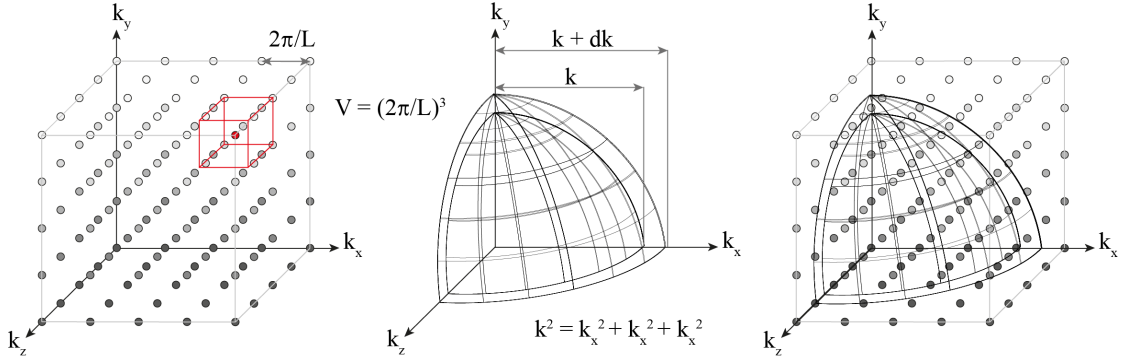


FIGURE 2.2: (a) Positive octant of allowed modes plotted in k -space, with volume of an individual mode highlighted in red. (b) shows the integrating sphere octant associated with the \mathbf{k} vectors plotted. (c) shows both modes and integrating volume.

Normalising this to the cubic volume that we chose we arrive at the final expression for the DoS in k -space as equation 2.10.

$$g_k(k) = \frac{k^2}{2\pi^2} \quad (2.10)$$

This density in k -space can be converted to the more useful units of angular frequency, ω by making use of the relation $\omega = ck$. These are given in equations 2.11, at this stage including the factor of 2 for the different polarisations.

$$g_\omega(\omega) = \frac{\omega^2}{\pi^2 c^3} \quad (2.11)$$

For the case of a cavity we can begin with the assumption that there is a single cavity mode, ω_0 available (this may or may not be a realistic assumption - if not the theory can be adjusted, see chapter 5). From the fact that a cavity mode will decay away at an exponential rate we can take the Fourier transform of a negative exponential function and arrive at equation 2.12 for the DoS for an emitter in a cavity g_ω^c in terms of ω .

$$g_\omega^c(\omega) = \frac{\Delta\omega}{2\pi(\omega - \omega_0)^2 + (\Delta\omega/2)^2} \quad (2.12)$$

Here $\Delta\omega$ is the full-width half-max of the Lorentzian peak, and is related to the Q factor by $\Delta\omega = \omega_0/Q$. These two functions are plotted in figure 2.3, to begin to give a qualitative appreciation for how the cavities alter the density of optical states. These axis are arbitrarily chosen to give a good graphical representation of the different functional shapes. At this juncture expressions for the density of states both in and out of the cavity have been derived. The next step is then to work out expressions for the matrix element of the perturbing Hamiltonian in each case.

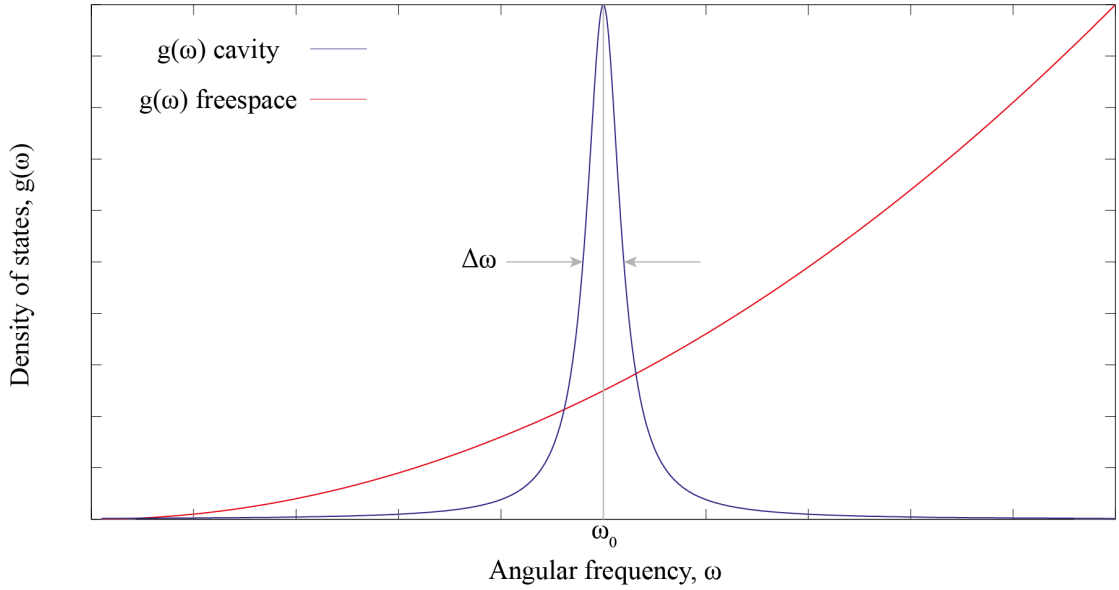


FIGURE 2.3: Density of states, $g(\omega)$, plotted against angular frequency, ω for free space (red) and for a \mathbf{k} vector resonant with a cavity mode (blue).

2.2.2 Perturbing Hamiltonian

For this section several results will be assumed, but thorough explanations exist in a variety of texts [79–81]. The perturbing Hamiltonian which appears in equation 2.3 can be simply written as the dot product of the electric dipole, \mathbf{p} and the electric field \mathcal{E} . The electric dipole can be restricted to include only the electronic response to the electric field as it is oscillating at optical frequencies, and only the electron can respond. We can then define the dipole moment of the transition depicted by the slightly ungainly $\mu_{i \rightarrow f}$ to be the inner product the initial state's bra, and the final state's ket, as shown in equation 2.13, where \mathbf{r} is the position of the electron in the dipole. The subscript is in place to emphasize that is a dipole moment for a transition between states. This simplification is appropriate since the field fluctuations are large ($\sim 10^{-7}$ m) compared with a normal atomic or exciton dipole moment ($\sim 10^{-10}$ m & $\sim 10^{-9}$ m respectively), and so the spatial integration implied by closing Dirac's bra-kets will depend little on the field variation on these scales.

$$\langle f | \hat{H}' | i \rangle = -e \langle f | \mathbf{r} | i \rangle \cdot \mathcal{E} = \mu_{i \rightarrow f} \cdot \mathcal{E} \quad (2.13)$$

It is at this stage that classically one would assume in a vacuum the electric field has a value of 0. This is avoided by the application of quantum operators to a simple harmonic oscillator, which is equivalent to the oscillations of the EM field. Actually this approach can form the basis of the formal quantisation of light, however in order to do this properly one must re-write Maxwell's equations in a form which uses scalar and vector potentials

and then perform a gauge transformation which is excessively protracted for this thesis. Suffice it to say that the electric field of light can be thought of as a quantum harmonic oscillation, and crucially, no longer has a ground state energy of 0, but rather $1/2 \hbar\omega$. If reassurance is required, the application of Heisenberg's uncertainty principle using time and energy as the conjugate variables to an empty field will lead to the same conclusion. This vacuum energy or zero point energy, E can be equated to the vacuum electric field and the vacuum magnetic field, \mathcal{E}_{vac} & \mathcal{B}_{vac} through the equation 2.14.

$$E = \frac{1}{2} \iiint \epsilon_0 \mathcal{E}_{vac}^2 + \mu_0^{-1} \mathcal{B}_{vac}^2 dV = \iiint \epsilon_0 \mathcal{E}_{vac}^2 dV = \frac{1}{2} \hbar\omega \quad (2.14)$$

Here we make use of the fact that the electric and magnetic field both contribute equally to the time averaged energy. This integral can be performed and the expression for the vacuum field energy is yielded (2.15).

$$\mathcal{E}_{vac} = \left(\frac{\hbar\omega}{2\epsilon_0 V} \right)^{1/2} \quad (2.15)$$

We are now in a position to solve equation 2.3 for both the free space and cavity coupled spontaneous emission making use of the DoS expressions 2.12, 2.11. These transition rates are given in equation 2.16 as $\Gamma_{i \rightarrow f}^c$ and $\Gamma_{i \rightarrow f}^{fs}$ for emission within a cavity of volume V_c and in free space, ω is the emission frequency and ω_0 is the cavity resonance.

$$\Gamma_{i \rightarrow f}^c = \frac{2\pi}{\hbar^2} \xi^2 \mu_{i \rightarrow f}^2 \left(\frac{\hbar\omega_0}{2\epsilon_0 V_c} \right) \frac{\Delta\omega}{2\pi(\omega - \omega_0)^2 + (\Delta\omega/2)^2} \quad (2.16a)$$

$$\Gamma_{i \rightarrow f}^{fs} = \frac{2\pi}{\hbar^2} \frac{1}{3} \mu_{i \rightarrow f}^2 \left(\frac{\hbar\omega_0}{2\epsilon_0 V} \right) \frac{\omega_0^2 V}{\pi^2 c^3} = \frac{\mu_{i \rightarrow f}^2 \omega_0^3}{3\pi\epsilon_0 \hbar c^3} \quad (2.16b)$$

The dipole's orientation has been treated slightly differently in these two cases. For free space the dipole's orientation can be averaged completely out, in effect giving the value of ξ^2 to be 1/3. In the cavity case although still dealing with a vacuum field the dipole's orientation should not be averaged, and we retain ξ , which is defined to be

$$\xi = \frac{|\mathbf{p} \cdot \mathcal{E}|}{|\mathbf{p}| |\mathcal{E}|} \quad (2.17)$$

where as previously mentioned \mathbf{p} is the electric dipole and \mathcal{E} is the electric field. It is then straight forward to divide the cavity transition rate by the free space transition rate, and by replacing c/ω with $\lambda/2\pi n$ where n is the refractive index, and recalling that Q is $\omega_0/\Delta\omega$ we finally arrive at the expression given in equation 2.18.

$$F_p \equiv \frac{3Q(\lambda/n)^3}{4\pi^2 V_c} \xi^2 \frac{\Delta\omega^2}{4(\omega - \omega_0)^2 + \Delta\omega^2} \quad (2.18)$$

From this derivation it can be seen that it is a combination of the alteration of the density of states, and the vacuum field fluctuations within the cavity volume V_c that result in the shorter expression for the Purcell Factor given in equation 2.1. Within this derivation it has been assumed that the vacuum field distribution within the cavity is uniform, or at least the spatial coupling between the dipole and the field has been assumed to be maximal. In order to allow for the possibility of the emitting species to be spatially off-resonance we can include the additional term, to give a slightly more complete expression in 2.19

$$F_p \equiv \frac{3Q(\lambda/n)^3}{4\pi^2 V_c} \xi^2 \frac{\Delta\omega^2}{4(\omega - \omega_0)^2 + \Delta\omega^2} \frac{|\mathcal{E}(\mathbf{r})|^2}{|\mathcal{E}_{max}|^2} \quad (2.19)$$

This expression now includes all the possible variables. In some ways the contraction of the full Purcell expression into the more often quoted one in 2.1 allows one to ignore the importance of the ability to both spatially and spectrally tune the cavity into resonance. Having looked into the derivation of the Purcell effect we will consider a few of the implications this can have on our emitter.

One of the first observations to make is that clearly from expression 2.19 there are many ways this factor can be less than 1. Figure 2.4 shows the effect of coupling to a resonant cavity mode, an off-resonant cavity mode, and free space emission. These plots show

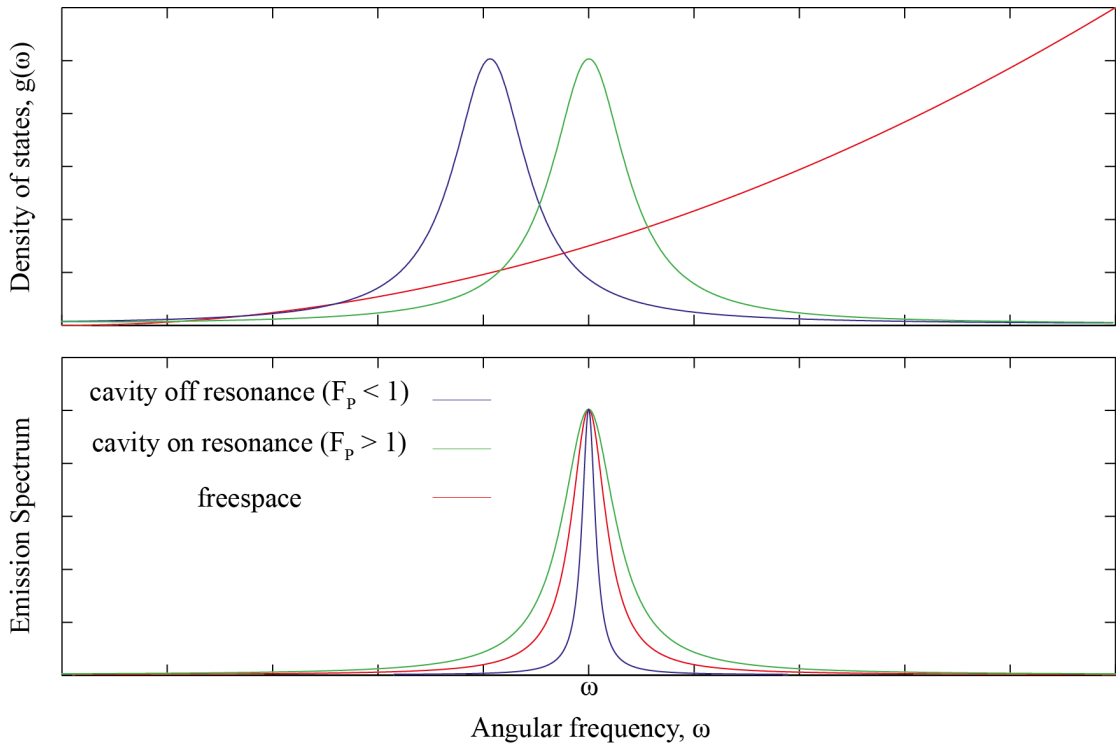


FIGURE 2.4: a) shows three density of states available to an emitter with an emission frequency of ω_0 , b) shows the effect each of these situations has on the FWHM of the emitter (in the bad cavity limit).

that the emission line width (if it is lifetime limited) will broaden corresponding to a decrease in the emitter's lifetime if it is tuned to be on resonance with a microcavity and narrowed if off resonance. These are compared to the free space case. The plot also draws attention to the relative line widths of the cavity and the emitter. Throughout this entire section it has been assumed that the line width of the cavity is much larger than the line width of the emitter, and in fact this is crucial for the theory to produce results consistent with experiments. This is referred to as the bad cavity regime, as opposed to the bad emitter regime which will be discussed in chapter 5.

Another important point to note is that the inclusion of the Lorentzian function as the total cavity DoS does not correspond to physical reality. As the derivation of the density of free space modes shows, it is important to be able to consider the DoS of \mathbf{k} vectors in any particular direction. During the Purcell factor derivation it has been assumed that the entirety of k -space has the same density of states - that of a cavity mode. In reality an emitter in a cavity can couple to many 'leaky modes' as well as the cavity modes. This is shown schematically for the case of the open access cavities in figure 2.5. In order to perfectly accurately determine the overall effect that the cavity will have on the emitter it would be necessary to consider the spectral density of states over the whole of the 4π sr available to the emitter. Although this can be approximated with the application of a full FDTD model (see chapter 6) often it can be assumed that apart from those \mathbf{k} vectors that are included in the cavity mode the rest of the emission is into an unaltered free space DoS. When the solid angle taken up by the cavity mode is small, this allows the total to be taken as simply the sum of the cavity enhanced emission plus the normal free space emission rate. This approach was previously mentioned in section 1.3.7 where the overall decay rate is the sum of all of the various decay rate contributions. One might expect that by increasing the Q factor of a cavity one might

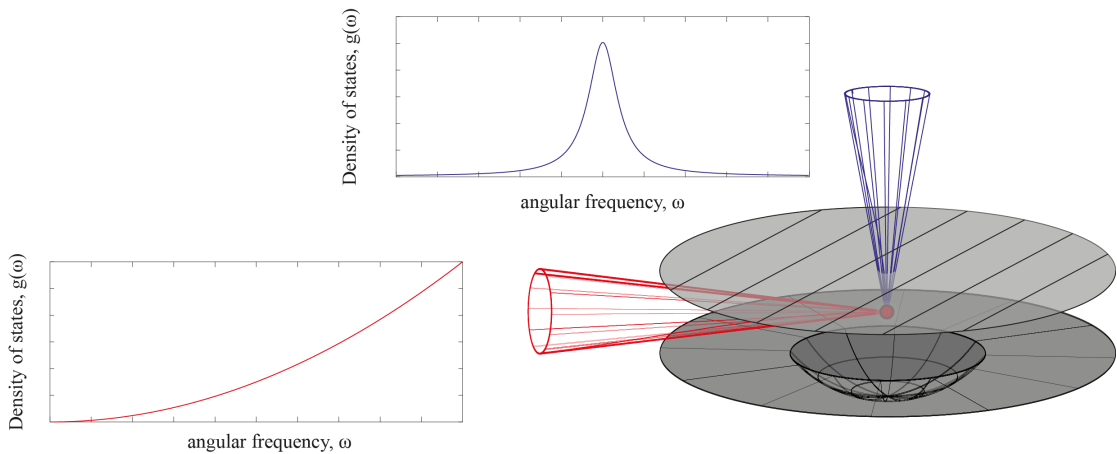


FIGURE 2.5: Pictorial representation of the directional dependence of the DoS. In this case the cavity mode emission is shown in blue, with some of the available leaky modes shown in red.

be able to enhance the decay rate to arbitrarily fast timescales. The effect of increasing the Q factor of the cavity on both the temporal and spectral emission is shown in figures 2.6 and 2.7. Clearly the appearance of an oscillatory term in the temporal decay, and the splitting of the emission peak in the spectral emission are not predicted by this theory. This is because as one increases the Q factor of the cavity one increases the amount of time that a photon spends within the cavity. This means that there is an

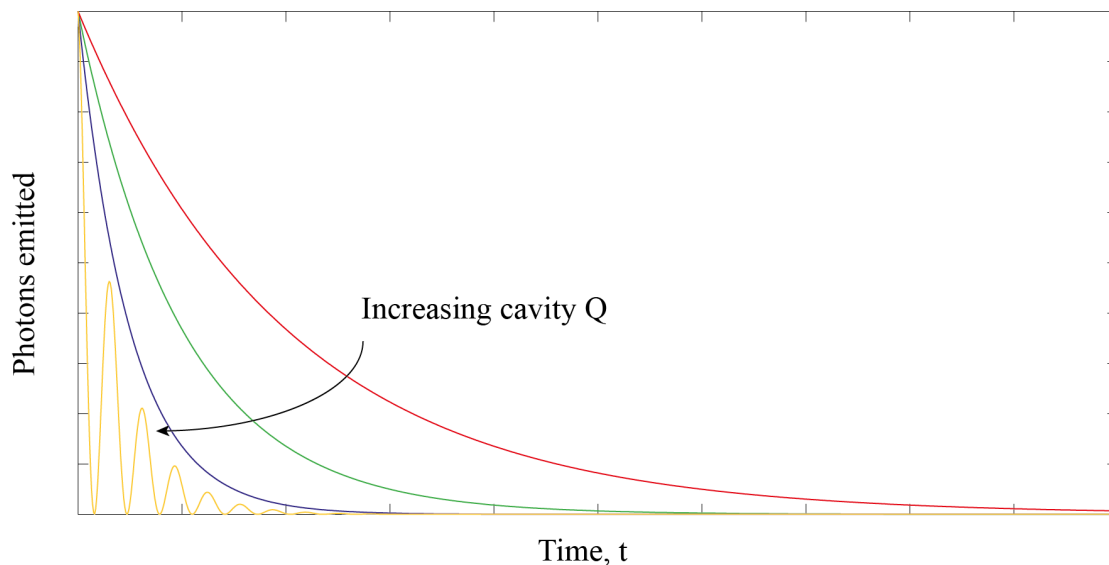


FIGURE 2.6: *Sketched plots of the excited state population against time an emitting dipole to various Q factor cavities. This type of plot might be obtained in a time-resolved photoluminescence experiment.*

increased chance of a photon emitted by the dipole being re-absorbed after circulating in the cavity. This extra interaction is where we move out of the ‘weak coupling’ regime, and into the ‘strong coupling’ regime.

2.2.3 The Wigner-Weisskopf Theory of Spontaneous Emission and the Strong Coupling Regime

The previous discussion began with Einstein’s basic picture of spontaneous emission as an exponential decay, and making use of perturbation theory (specifically Fermi’s golden rule) arrived at the formula for Purcell enhancement. The first complete solution to the problem of spontaneous emission was demonstrated in 1930 [82] and is a slightly more general formalism. This approach does not assume a short temporal perturbation (see [83]) and is phrased to a greater extent in Dirac’s notation and will be outlined roughly here. This will also set the scene for a brief discussion of the strong coupling regime features apparent in figures 2.6 and 2.7. More complete descriptions of the steps mentioned here can be found in a variety of texts [76, 79, 80, 83], and the discussion

presented here is based on the relevant chapters in [84]. The equations in 2.20 show the full Hamiltonian for an atom with many energy levels (labeled by i) interacting with a number of field modes (labeled by \mathbf{k} as in section 2.2.1) and includes terms for energy contributions from the atom, the field and their interaction.

$$H_{total} = H_{atom} + H_{field} + H_{interaction} \quad (2.20a)$$

$$= \sum_i E_i \sigma_{ii} + \sum_{\mathbf{k}} \hbar \omega_{\mathbf{k}} a_{\mathbf{k}}^\dagger a_{\mathbf{k}} + \sum_{ij} \sum_{\mathbf{k}} \hbar g_{\mathbf{k}}^{ij} \sigma_{ij} (a_{\mathbf{k}} + a_{\mathbf{k}}^\dagger) \quad (2.20b)$$

Here σ_{ij} is the atom transition operator defined as the outer product of the states i and j , $\sigma_{ij} = |i\rangle \langle j|$. As E_i is the energy eigenvalue of the i^{th} state, the first summation in 2.20b is the energy contributed by the atom itself. The second term accounts for all of the energy present in the field. Here $a_{\mathbf{k}}$ and $a_{\mathbf{k}}^\dagger$ are the annihilation and creation operators for photons in the optical mode labeled by \mathbf{k} . In the second summation they appear together as $a_{\mathbf{k}}^\dagger a_{\mathbf{k}}$, which means they act as a number operator, counting the number of photons present in mode \mathbf{k} with energy $\hbar \omega_{\mathbf{k}}$. With the exception of the vacuum field, the second terms counts up all of the energy contributed by photons in every mode. The final term is the interaction Hamiltonian. Here $g_{\mathbf{k}}^{ij}$ is the coupling strength of the \mathbf{k}^{th} field mode to the atomic transition between the i^{th} and j^{th} states, and is given by equation 2.21 and $\mathcal{E}_{\mathbf{k}}$ is the vacuum energy contribution of the \mathbf{k}^{th} field mode given by equation 2.15.

$$g_{\mathbf{k}}^{ij} = -\frac{\boldsymbol{\mu}_{i \rightarrow j} \cdot \boldsymbol{\mathcal{E}}_{\mathbf{k}}}{\hbar} \quad (2.21)$$

The next step is to reduce the many levels of the atom to two levels, denoted a and b . We will define $|a\rangle$ and $|b\rangle$ to be the excited and ground states of the atom (or generally any electronic dipole). If we assume $\boldsymbol{\mu}_{a \rightarrow b} = \boldsymbol{\mu}_{b \rightarrow a}$ then the coupling strength loses its i, j dependence and $g_{\mathbf{k}}^{ab} = g_{\mathbf{k}}^{ba} = g_{\mathbf{k}}$ (not to be confused with the optical density of states $g_{\mathbf{k}}(k)$ appearing in equations 2.10 and 2.9). Next we define three more operators which act on the atomic states, shown in equations 2.22.

$$\sigma_z = \sigma_{aa} - \sigma_{bb} = |a\rangle \langle a| - |b\rangle \langle b| \quad (2.22a)$$

$$\sigma_+ = \sigma_{ab} = |a\rangle \langle b| \quad (2.22b)$$

$$\sigma_- = \sigma_{ba} = |b\rangle \langle a| \quad (2.22c)$$

The first operator, σ_z is incorporated into the atomic Hamiltonian (where $E_a - E_b = \hbar \omega$) and the σ_+ and σ_- (representing the excitation and relaxation of the atomic state) are incorporated into the interaction Hamiltonian to give the total Hamiltonian in the form given in equation 2.23.

$$H_{total} = \hbar \omega \sigma_z + \sum_{\mathbf{k}} \hbar \omega_{\mathbf{k}} a_{\mathbf{k}}^\dagger a_{\mathbf{k}} + \sum_{\mathbf{k}} \hbar g_{\mathbf{k}} (\sigma_+ + \sigma_-) (a_{\mathbf{k}} + a_{\mathbf{k}}^\dagger) \quad (2.23)$$

Finally we expand out the brackets in the interaction term and ignore the $a_{\mathbf{k}}\sigma_-$ and $a_{\mathbf{k}}^\dagger\sigma_+$ terms as energy nonconserving terms, equivalent to applying the rotating-wave approximation. This leaves us with a time independent (or static) H_s and a dynamic interaction Hamiltonian, which is also known as the Jaynes-Cummings Hamiltonian H_{JC} [29, 30], shown in equation 2.24.

$$H_s = \hbar\omega\sigma_z + \sum_{\mathbf{k}} \hbar\omega_{\mathbf{k}} a_{\mathbf{k}}^\dagger a_{\mathbf{k}} \quad (2.24a)$$

$$H_{JC} = \sum_{\mathbf{k}} \hbar g_{\mathbf{k}} (\sigma_+ a + \sigma_- a_{\mathbf{k}}^\dagger) \quad (2.24b)$$

Having laid the groundwork for the Wigner-Weisskopf theory, the main results of the actual derivation will be explored. The first necessary step is to take the situation into the so called interaction picture of quantum mechanics (as opposed to the Schrödinger or Heisenberg pictures). This involves adding an explicitly time varying term to the Jaynes-Cummings Hamiltonian, $e^{i(\omega-\omega_{\mathbf{k}})t}$ which comes from the static Hamiltonian. The general state vector is given in equation 2.25 with initial values of $c_a(0) = 1$ and $c_{b,\mathbf{k}}(0) = 0$.

$$|\psi(t)\rangle = c_a(t) |a, 0\rangle + \sum_{\mathbf{k}} c_{b,\mathbf{k}}(t) |b, 1\rangle \quad (2.25)$$

Equations for the time evolution of the probability amplitudes c_a and c_b can be found by applying the time dependent Schrödinger equation $|\dot{\psi}(t)\rangle = -(i/\hbar)H_{JC}|\psi(t)\rangle$, and are shown in equation 2.26.

$$\dot{c}_a(t) = -i \sum_{\mathbf{k}} g_{\mathbf{k}} e^{i(\omega-\omega_{\mathbf{k}})t} c_{b,\mathbf{k}}(t) \quad (2.26a)$$

$$\dot{c}_{b,\mathbf{k}}(t) = -i g_{\mathbf{k}} e^{i(\omega-\omega_{\mathbf{k}})t} c_a(t) \quad (2.26b)$$

From here equation 2.26b can be integrated to yield an expression for $c_{b,\mathbf{k}}$ and inserted into equation 2.26a. This expression is shown in equation 2.27.

$$\dot{c}_a(t) = - \sum_{\mathbf{k}} |g_{\mathbf{k}}|^2 \int_0^t e^{i(\omega-\omega_{\mathbf{k}})(t-t')} c_a(t') dt' \quad (2.27)$$

Next we draw on a result from complex analysis, shown in 2.28

$$\lim_{t \rightarrow \infty} \int_0^t e^{-i(\omega-\omega_{\mathbf{k}})(t-t')} dt' = \pi \delta(\omega - \omega_{\mathbf{k}}) - \mathcal{P} \frac{i}{\omega - \omega_{\mathbf{k}}} \quad (2.28)$$

where \mathcal{P} is the principle value of the integral over t' . This gives us the final expression for the probability amplitude of the excited state of the atom to be

$$\dot{c}_a(t) = -\frac{\gamma}{2} c_a(t) \quad (2.29)$$

where

$$\gamma = 2\pi \sum_{\mathbf{k}} |g_{\mathbf{k}}|^2 \quad (2.30)$$

giving the excited state an exponential decay the precise rate of which depends on the summation (which in many cases may be replaced with an integral) of the coupling constants to all the available optical modes. In arriving at final solution imaginary part of the integral, associated with the principle value. Physically it is reassuring that this shift is accounted for experimentally as the Lamb shift and was observed by Willis Lamb and Robert Retherford in 1947 and earned Lamb the 1955 Nobel prize. Having given an alternative method to show how a variation in the density of optical states effects the spontaneous emission lifetime, we will move onto a couple of comments pertaining to the strong coupling regime. These will aim to qualitatively explain the features in the yellow sketch plots in figures 2.6 and 2.7. The oscillations visible in the time domain come from the coherent oscillation of energy between the dipole's excited state and a photonic excitation in the cavity. Considering the Jaynes-Cummings Hamiltonian, these two states are represented by the two terms within the parenthesis. The frequency that these oscillations occur at is known as the Rabi frequency and are generally referred to as Rabi oscillations. In fact, in the full quantum mechanical picture it is not considered two distinct systems with energy oscillating coherently between both, but rather a single system which is simultaneously cavity and atomic in nature with a single quantum of energy. In this picture it is the vacuum-field Rabi splitting which gives the double peak feature, visible in figure 2.7 which is proportional to the coupling strength g_{bmk} . This regime is characterised by three rates included in the generic cavity schematic in

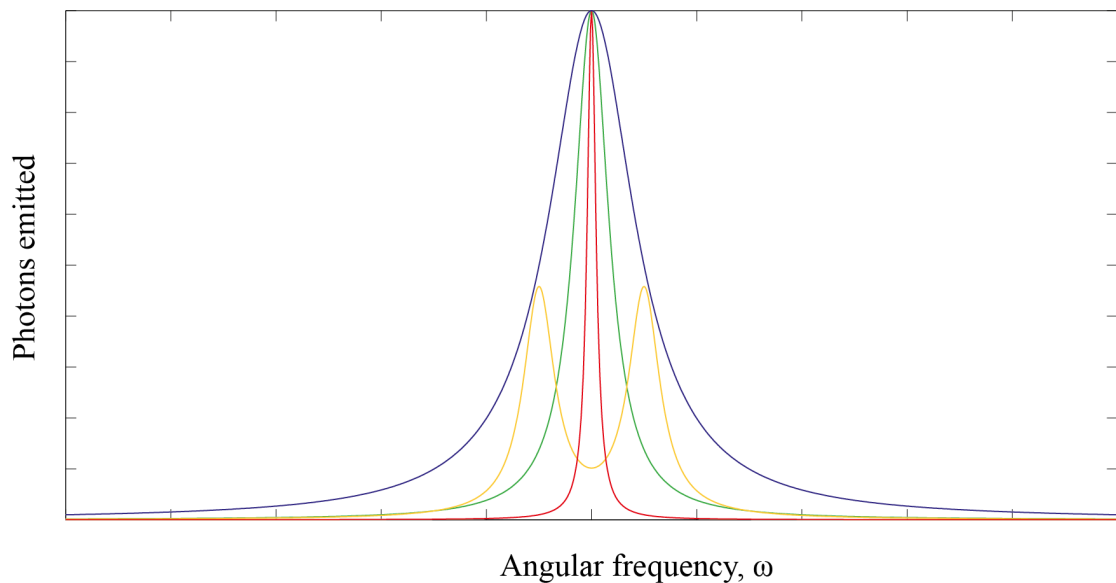


FIGURE 2.7: *The hypothetically observed spectra for each of the emission decay plots shown in figure 2.6.*

figure 2.8. Here κ is the cavity decay rate, $g_{\mathbf{k}}$ is the dipole cavity coupling, which was introduced in the previous section, and γ is the decay rate of the dipole in free space. The weak coupling limit can then be defined as the region where the cavity-dipole interaction is ignored, i.e $g \ll \kappa, \gamma$ and the strong coupling limit is where the coupling rate plays a much larger role or $g \gg \kappa, \gamma$. The strong coupling regime offers a wealth of rich physics, but unfortunately the cavities constructed do not reach this regime, and so this is where the discussion on the interactions between the cavity and emitter will stop. Our attention will now be turned to some considerations more specific to the cavities to be constructed, namely the design considerations of distributed Bragg reflectors and the role of Gaussian modes.

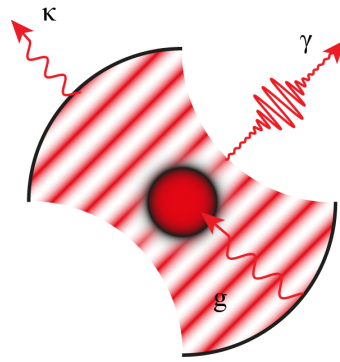


FIGURE 2.8: Pictorial representation of the three rates important to consider in CQED.

2.3 Distributed Bragg Reflectors and Cavity Metrics

2.3.1 DBRs and the 1D Transfer Matrix

The motivation for using distributed Bragg reflectors (abbreviated to DBRs and also referred to as dielectric mirrors) rather than their metallic counterparts lies solely in their ability to reach much much higher reflectivities. This is because they make use of a very different physical effect to reflect light, based on interference rather than accelerating the free charges in a metallic substance. More specifically, it requires alternating layers of two contrasting dielectric media. If the thicknesses of these layers is such that a particular wavelength of light will only perform a quarter oscillation the desired interference effect occurs. For visible wavelengths silica (SiO_2) is often chosen for the low refractive index, so the layer thicknesses being dealt with are around the 100 nm mark. This section will primarily be focused around a 1 dimensional transfer matrix model of distributed Bragg reflectors. In contrast to the previous section, here we will be dealing with physics which can be described classically. This method can then be used to highlight several spectral

features of the open access cavities that will later be looked at in more detail, based on three dimensional modeling in the final modeling chapter (see chapter 6) by making use of more advanced FDTD software. The transfer matrix approach implemented here is quite commonly applied to a variety of problems, and as such descriptions abound in various textbooks [85], however the one implemented is slightly different in some details. Maxwell's equations are most often represented as the set of four differential equations shown in equations 2.31 where, as previously \mathcal{E} and \mathcal{B} are the electric and magnetic fields, ρ is the charge density and \mathbf{J} the current density.

$$\nabla \cdot \mathcal{B} = 0 \quad (2.31a)$$

$$\nabla \cdot \mathcal{E} = \rho/\epsilon_0 \quad (2.31b)$$

$$\nabla \times \mathcal{B} = \mu_0 \mathbf{J} + \mu_0 \epsilon_0 \partial \mathcal{E} / \partial t \quad (2.31c)$$

$$\nabla \times \mathcal{E} = -\partial \mathcal{B} / \partial t \quad (2.31d)$$

For the case of no net charge being present these can be re-arranged to yield the common linear second order differential equations referred to as wave equations, examples for the electric and the magnetic field are given in equations 2.32.

$$\nabla^2 \mathcal{E} = \frac{\mu_r \epsilon_r}{c} \frac{\partial^2 \mathcal{E}}{\partial t^2} \quad (2.32a)$$

$$\nabla^2 \mathcal{B} = \frac{\mu_r \epsilon_r}{c} \frac{\partial^2 \mathcal{B}}{\partial t^2} \quad (2.32b)$$

These can be solved with a standard plane wave function identical to the one within the summation of equation 2.5. As mentioned previously these are only solutions if the waves are transverse, moreover that all three vectors, \mathcal{E} , \mathcal{B} and \mathbf{k} are mutually perpendicular. In addition we find that the magnetic field is a factor of the speed of the light smaller than the electric field. At this stage it is worth considering a single boundary between 2 dielectric media, as shown in figure 2.9. In this brief derivation and for the rest of the section we will be working in terms of the electric field only, as ultimately it is the electric field that we are most interested when considering the emission from an electric dipole. From equation 2.31c, and assuming \mathbf{k} is in the z direction we can write

$$\mathcal{E}_I(z, t) = \mathcal{E}_I e^{ik_1 z - \omega t} \quad (2.33a)$$

$$\mathcal{B}_I(z, t) = \frac{\mathcal{E}_I}{v_1} e^{ik_1 z - \omega t} \quad (2.33b)$$

where v_1 and k_1 are the speed of light and wavenumber in the dielectric with refractive index n_1 . In this sense the refractive index that is considered to effect the speed of light through decreasing the wavelength, leaving the frequency (and therefore ω) unaltered.

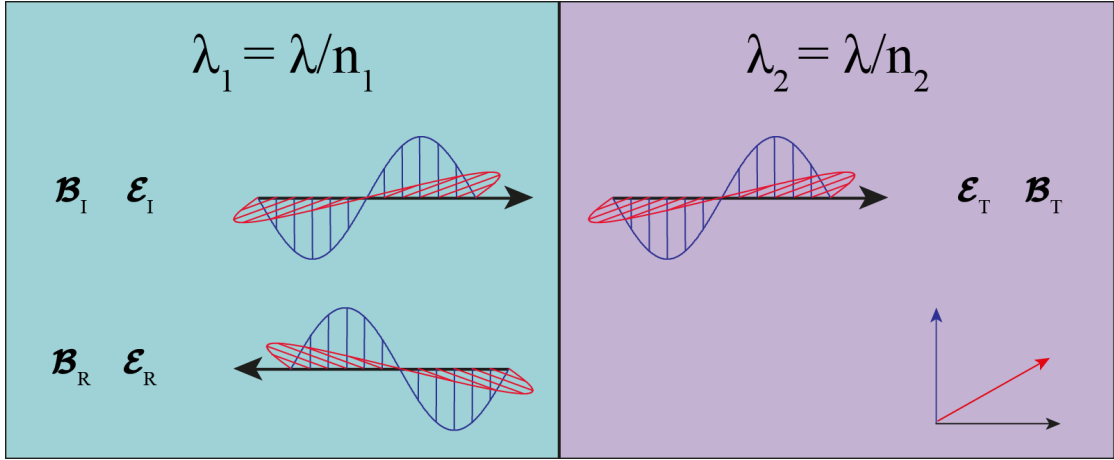


FIGURE 2.9: A single dielectric boundary under consideration. In this scheme material with refractive index n_1 precedes the material with n_2 for light propagating in the positive z direction.

Similarly for the reflected and transmitted waves we can write

$$\mathcal{E}_R(z, t) = \mathcal{E}_R e^{-ik_1 z - \omega t} \quad (2.34a)$$

$$\mathcal{B}_R(z, t) = -\frac{\mathcal{E}_R}{v_1} e^{-ik_1 z - \omega t} \quad (2.34b)$$

$$\mathcal{E}_T(z, t) = \mathcal{E}_T e^{ik_2 z - \omega t} \quad (2.34c)$$

$$\mathcal{B}_T(z, t) = \frac{\mathcal{E}_T}{v_2} e^{ik_2 z - \omega t} \quad (2.34d)$$

noting the reflected wave now traveling in the opposite direction. Since we are only dealing with waves incident normally on the boundary (this is a one dimensional approximation) both of these fields are parallel to the interface between the two dielectric materials and have to equal one another at the interface (the general boundary conditions actually apply to the magnetic field strength, \mathcal{H} , defined in relation to the magnetic field by $\mathcal{B} = \mu_0 \mathcal{H}$ assuming $\mu_r \approx 1$). Equating the electric fields on either side of the interface gives us the boundary condition in equation 2.35a, and equating the magnetic fields yields the condition in 2.35b.

$$\mathcal{E}_I + \mathcal{E}_R = \mathcal{E}_T \quad (2.35a)$$

$$\mathcal{E}_I - \mathcal{E}_R = \frac{n_2}{n_1} \mathcal{E}_T \quad (2.35b)$$

To get to this final form of 2.35b the substitution $v_1/v_2 = n_2/n_1$ has to be used. Applying these two boundary conditions we can then write down both the incident and reflected

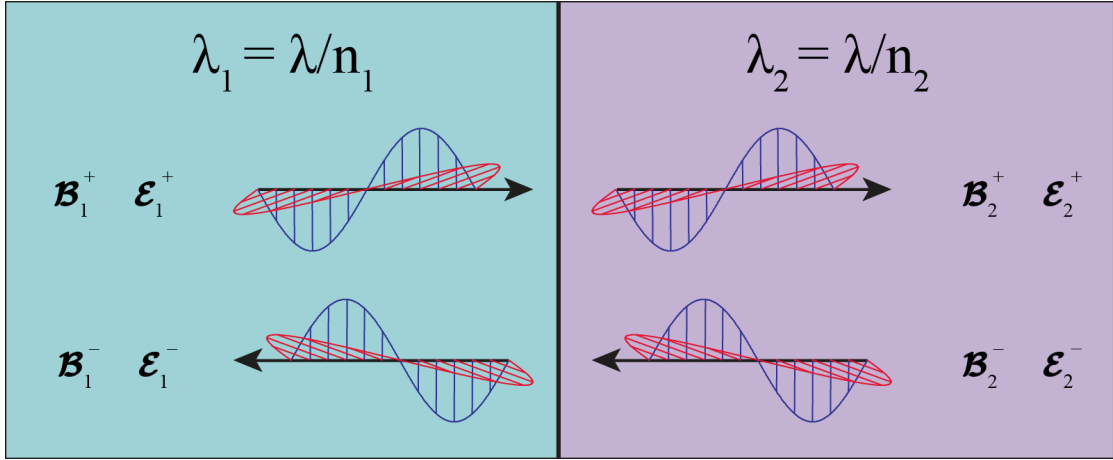


FIGURE 2.10: Notation scheme adaptation for the same situation as that shown in figure 2.9, where the superscript denotes direct (+/- z) and the subscript denotes the refractive index of the medium (1/2).

fields in terms of the transmitted one, these are written in equations 2.36.

$$\mathcal{E}_I = \frac{n_2 + n_1}{2n_2} \mathcal{E}_T \quad (2.36a)$$

$$\mathcal{E}_R = \frac{n_2 - n_1}{2n_2} \mathcal{E}_T \quad (2.36b)$$

This line of reasoning can be brought to bear as if the incident wave was propagating in the negative z direction. Thus, with a suitable alteration in the nomenclature as shown in figure 2.10 we can sum the resultant expressions and are able to write the field propagating in both positive and negative z directions in dielectric n_1 in terms of the fields in dielectric n_2 . These completely general solutions are now written out in equations 2.37.

$$\mathcal{E}_1^+ = \frac{n_2 + n_1}{2n_2} \mathcal{E}_2^+ + \frac{n_2 - n_1}{2n_2} \mathcal{E}_2^- \quad (2.37a)$$

$$\mathcal{E}_1^- = \frac{n_2 - n_1}{2n_2} \mathcal{E}_2^+ + \frac{n_2 + n_1}{2n_2} \mathcal{E}_2^- \quad (2.37b)$$

In this form we can then easily adopt a matrix style approach, with the transfer matrix here acting on a field ‘vector’ constructed by arranging the forward and backward propagating fields in a column. This is written out in equation 2.38.

$$\begin{pmatrix} \mathcal{E}_2^+ \\ \mathcal{E}_2^- \end{pmatrix} = \begin{pmatrix} \frac{n_2 + n_1}{2n_2} & \frac{n_2 - n_1}{2n_2} \\ \frac{n_2 - n_1}{2n_2} & \frac{n_2 + n_1}{2n_2} \end{pmatrix} \begin{pmatrix} \mathcal{E}_1^+ \\ \mathcal{E}_1^- \end{pmatrix} \quad (2.38)$$

A fairly versatile Matlab code was then developed around this transfer matrix which allowed for it to be implemented in a couple of different ways. One of the first developments was to obtain a field plot for the case of normally incident light on a DBR stack.

This was achieved by using a plane wave expression for the electric field. The way this model is run it is necessary to specify the field exiting the structure to the right. Appropriate transfer matrices are then applied to this field depending on whether it is simply propagating through a uniform material (i.e. $n_1 = n_2$) or if it is calculating the fields on the other side of a dielectric boundary. For the case of 10 alternating pairs of two different refractive indices, the field profile shown in figure 2.11 is obtained. This value

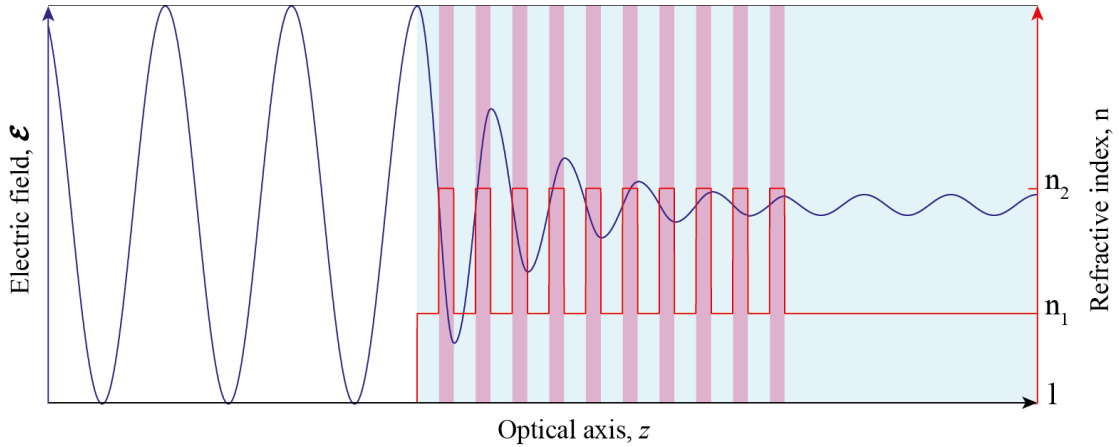


FIGURE 2.11: Field distribution of light of wavelength $\lambda \sim 650$ nm incident on a mirror consisting of 10 pairs of silica ($n_1 = 1.46$) and zirconia ($n_2 = 2.1$) with thicknesses of $\lambda/(4 \times n_i)$ where $i = 1, 2$, where $\lambda_0 = 650$ nm.

of the incident wavelength is close to 650 nm, where the peak reflectivity of the mirrors is. The dielectric mirrors have layer thicknesses of $\lambda_{res}/(4n_1)$ and $\lambda_{res}/(4n_2)$ where $\lambda_{res} = 650$ nm. The reflectivity, R , of the mirror at this wavelength can then be found from the ratio of the incident intensity compared to that which is transmitted (which is incidentally the starting point for the transfer matrix code and normally set at unity). Obviously seeing the field distribution for every wavelength is unnecessary, so an altered code was developed to perform the minimum number of calculations and produce only the reflectivity for the wavelength used. In this way a whole range of wavelengths can be considered. This reflectivity spectrum for the mirror shown in figure 2.11 is plotted in figure 2.12. This method actually also works for finding spectra and field distributions within a one dimensional cavity. To accomplish this one simply needs to incorporate a gap and then another DBR stack facing in the opposite direction. The transmissivity for two mirrors identical to that considered previously arranged opposite one another with a $2 \mu\text{m}$ gap is plotted in figure 2.13 which is simply $1 - R$. This will be used more than the reflectivity plots as they are closer to the experimental data that was acquired. The plot shows clear resonances occurring at 602 nm, 658 nm and 723 nm, where the transmission of the cavity approaches unity. For the rest of this section cavity mode locations will be referred to as λ_n where $n \in \mathbb{N}$, with the peak wavelength of the cavity's reflectivity denoted λ_{res} . A good way to visualise the effect of changing the distance

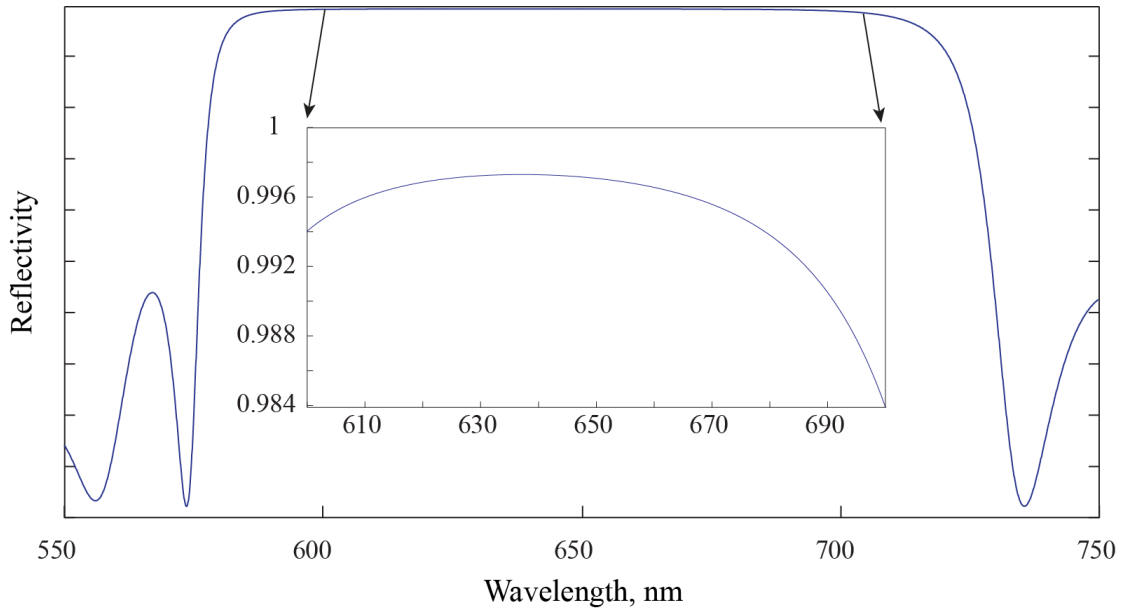


FIGURE 2.12: Reflectivity spectrum obtained for the mirror depicted in figure 2.11 showing a reflection band around 150 nm wide.

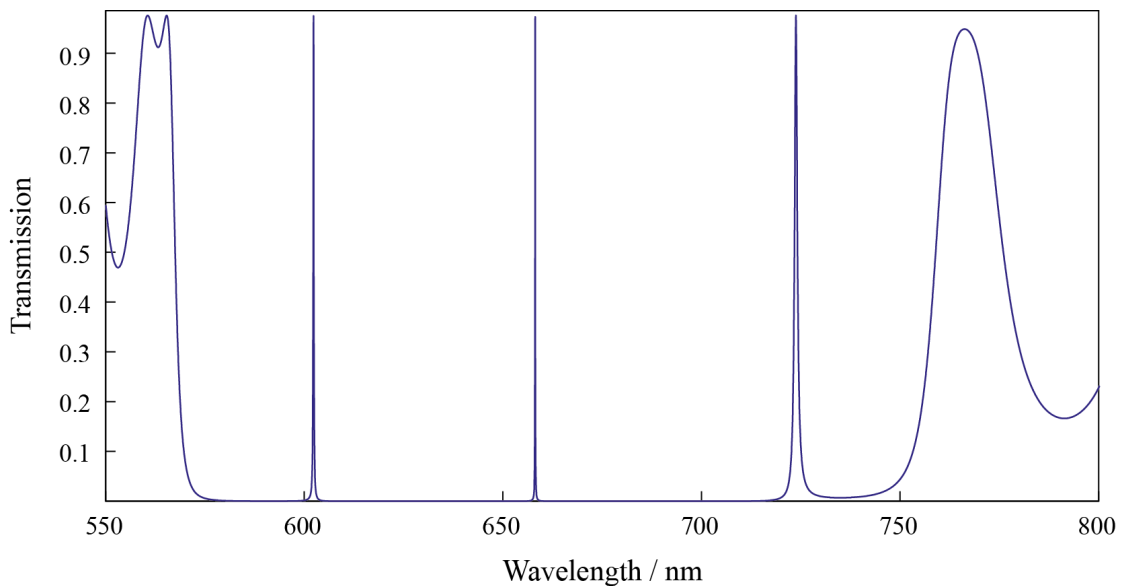


FIGURE 2.13: Plot of transmissivity against wavelength for a 1 dimensional 2 micron long microcavity formed from 2 DBR stacks identical to the mirror characterised in figures 2.12 and 2.11.

between the mirrors (L) is to remember that once the boundary conditions are set by the length of the cavity, an entire geometric series of possible resonances are formed, starting with the fundamental mode, $\lambda_1 = L/2$ then the first overtone, $\lambda_2 = L$ and generalising to $\lambda_n = n(L/2)$. Two such series are shown in figure 2.14 as red and blue arrows for cavities of length $2 \mu\text{m}$ and $0.65 \mu\text{m}$ (which is the peak reflectivity of these mirrors). The shaded region of this image indicates the spectral region that is actually

confined by the cavity. In this way it is clear that dropping the cavity length will shift the modes progressively to shorter wavelengths, and also increase the gaps between the modes, a quantity referred to from here on in as the ‘free spectral range’ (FSR). These

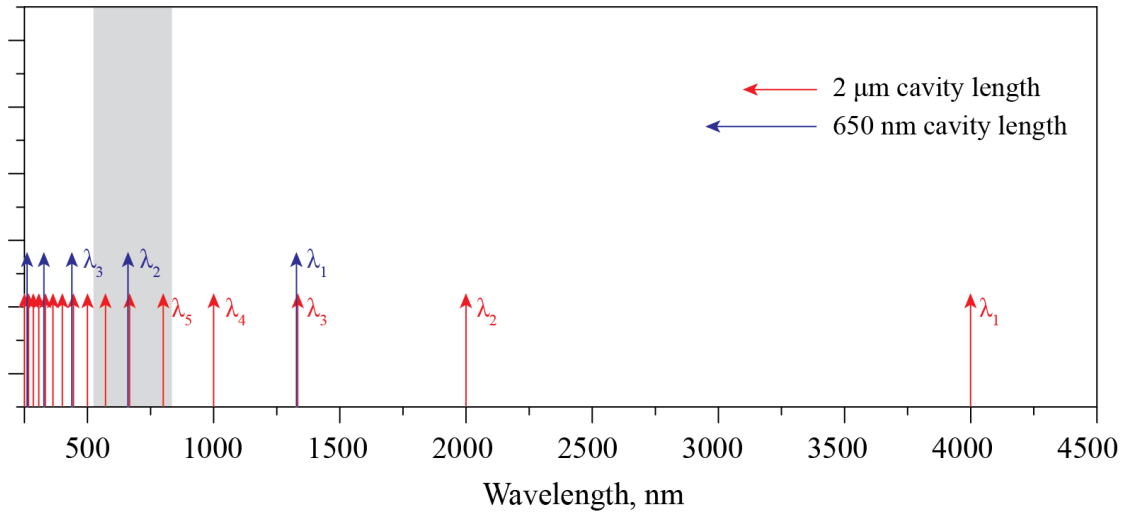


FIGURE 2.14: A graphical plot showing the distribution of modes for a one dimensional cavity with lengths $2\ \mu\text{m}$ (red) and $650\ \text{nm}$ (blue). The grey region is the portion of the spectrum over which the dielectric mirrors are usefully reflective.

considerations show that the shortest cavity achievable (which still has a gap in between the mirrors to fit an emitter) is one with a separation of $325\ \text{nm}$. The spectrum for a cavity with this separation is plotted in figure 2.15, and the field distribution is given in figure 2.16. The field here especially highlights a few important considerations when deciding on the specifics of the DBR coating. One point worth drawing attention to is that assuming perfectly conducting mirrors would lead us to expect the resonance to fall at exactly $650\ \text{nm}$ for this situation, as it is the fundamental mode formed from a cavity of length $325\ \text{nm}$. Clearly this is not the case, as the mode is slightly blue shifted. This is down to the field penetration into the mirrors, which will also have an impact on the volume of a mode formed from DBR stacks such as these. From the field distribution we can see that in this case there is an anti-node of the field on the substrate surface. This may be an advantage for some experiments where the emitters are distributed over the surface of the mirror. This gives a strong justification for the inclusion of the final term added in the complete expression of the Purcell factor (2.19). If in this situation an dipole were placed right in the centre of this one dimensional cavity, it would experience a Purcell factor of zero when emitting into the cavity mode, corresponding to complete suppression. This is obviously undesirable if the goal is to enhance the emission by virtue of coupling to a cavity mode. If the dipole were placed on the mirror surface it would be enhanced by the maximum Purcell factor possible. If field nodes are desired

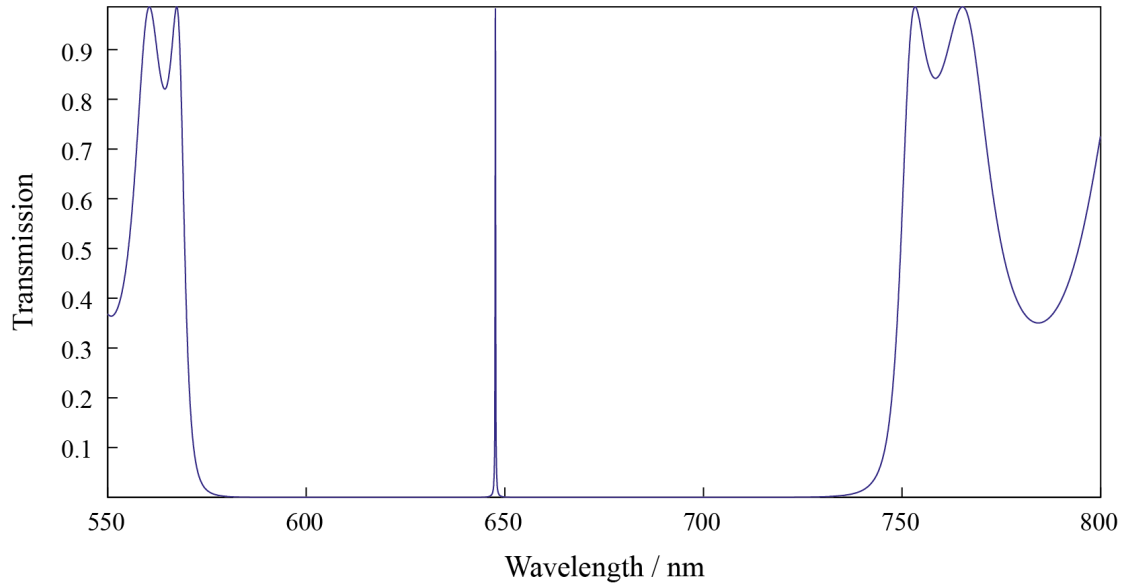


FIGURE 2.15: *Transmission spectrum of a 325 nm long cavity identical in all other respects to that shown in figure 2.13.*

on the surface simply adding an extra layer of higher indexed material on the surface will accomplish this.

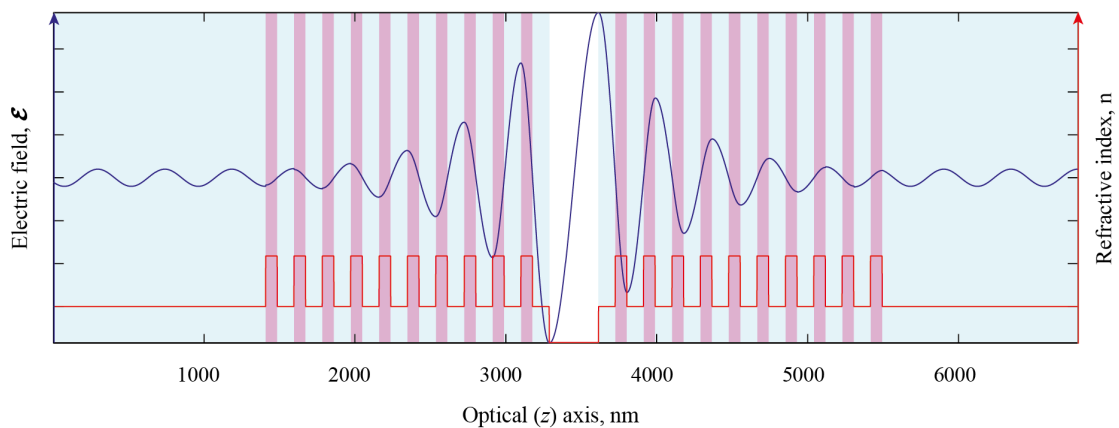


FIGURE 2.16: *Field distribution for the cavity resonance visible close to 650 nm in figure 2.15.*

As is clear from figures 2.12, 2.13, 2.14 and 2.15, the region of the spectrum which is altered is determined by the reflection band of the mirror, so one can imagine that the density of states available to an emitter within the cavity for a \mathbf{k} vector falling within the cavity mode would look something along the lines of that shown in figure 2.17. This shows a clear suppression of emission should the cavity mode and dipole transition energy be detuned from one another by a small amount, with an enhancement when tuned into resonance. A couple of cavity metrics can be investigated with this simple

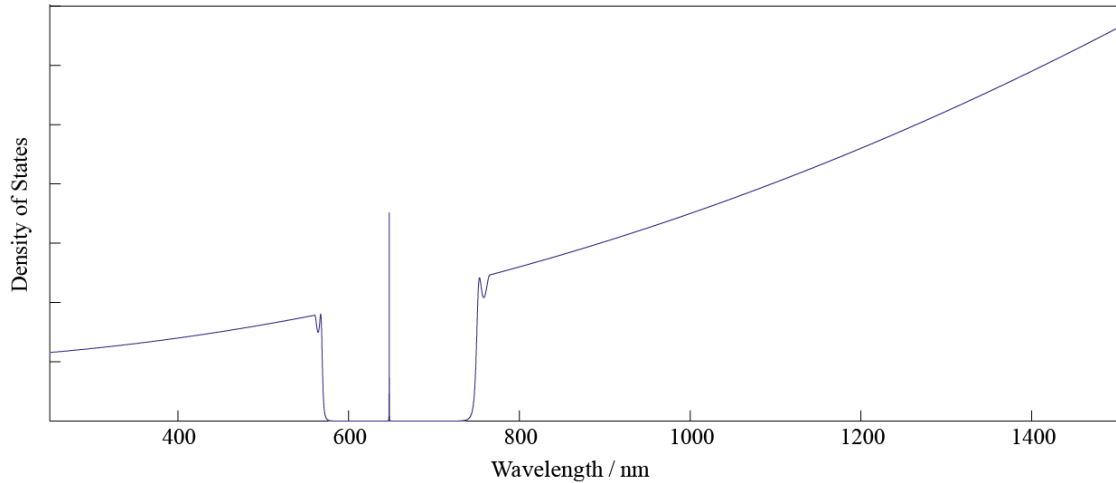


FIGURE 2.17: A sketched plot to indicate the modification of the optical density of states which occurs due to the presence of an optical microcavity. The important point is that strong suppression and enhancement only occur within the reflectivity band of the mirrors. Outside of this region the density of states may be unaltered (as shown) or impacted by other mechanisms.

model.

2.3.2 A Few Cavity Metrics

The first is the Q factor, defined as peak value of resonance divided by the FWHM ($\delta\lambda$) of the peak. An important feature of the Q factor for this sort of cavity is shown in figure 2.18, which is that the Q factor has a cavity length dependence. Here four modes, the fundamental and the tenth, twentieth and fortieth overtones are plotted. They clearly show a red shift, possibly resulting from the fact that the penetration of the field into the mirror becomes less significant as the cavity length is increased. The other obvious feature is the narrowing of the resonant peak. The Q factor of a resonance as mentioned previously is given in expression 2.39 and from the plot in figure 2.18 shows a clear increase as the cavity length is increased.

$$Q = \lambda/\delta\lambda \quad (2.39)$$

This is because another definition of the Q factor, related to the energy stored in the cavity and the power dissipated is given in equation 2.40.

$$Q = \frac{2\pi cE}{\lambda_0 P} \quad (2.40)$$

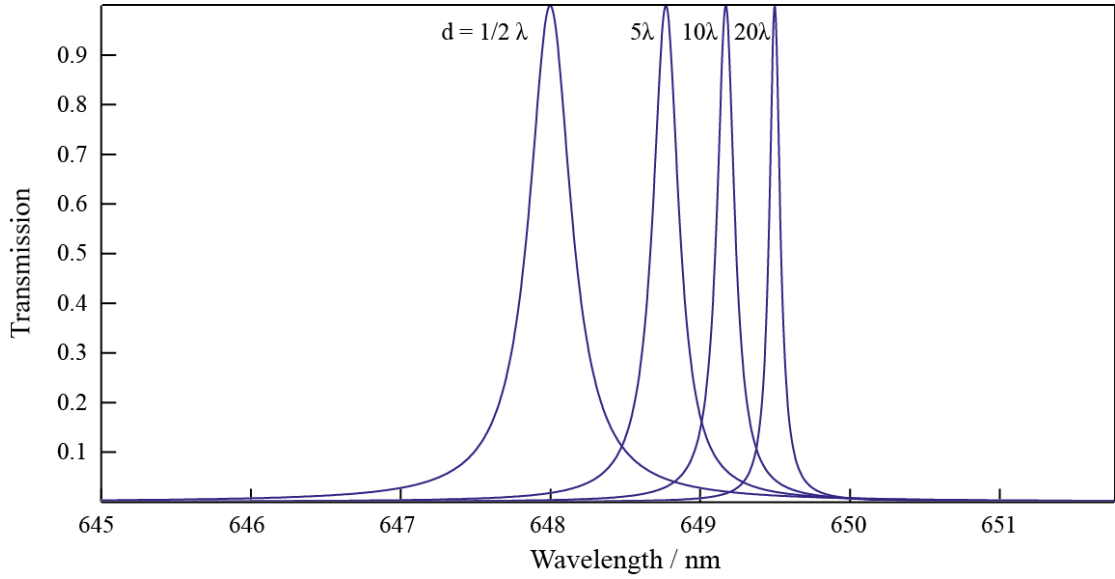


FIGURE 2.18: Cavity modes for cavities of lengths $1/2, 5, 10, 20 \lambda_{res}$. The modes clearly show a redshift, as field penetration into the mirrors becomes less significant, and narrowing width corresponding to increasing Q factors.

Incidentally, for completeness it can be seen that since the power dissipated, $P = -dE/dt$ this can be rearranged with Q as a constant and solved to give

$$E(t) = e^{-t \frac{2\pi c}{\lambda_0 Q}} \quad (2.41)$$

which when Fourier transformed yields the Lorentzian line shape encountered so far for the resonances. Returning to the length dependence of the Q factor, we can see that the only physical method for power to leak from the cavity (included in this model) is through the field leaking out through the mirrors. By increasing the cavity length in this expression we are effectively increasing the energy being stored in the field, E whilst the power dissipation remains constant. An alternative visualisation is to consider photons. In this picture the photons spent more time in flight between collisions with the mirrors, allowing each photon to spend more time inside the cavity before being scattered out. The other metric to be considered is the cavity finesse, \mathcal{F} . This can be found experimentally by dividing the FSR, $\Delta\lambda$ by the resonance line width $\delta\lambda$.

$$\mathcal{F} = \Delta\lambda / \delta\lambda \quad (2.42)$$

An alternative definition in terms of the attenuation per round trip of the cavity is given in equation 2.43.

$$\mathcal{F} = \pi\sqrt{\Gamma}/(1 - \Gamma) \quad (2.43)$$

Here Γ is the attenuation per round trip, and includes the losses resulting from both the mirrors and any medium filling the gap between them. For the experiments conducted within this thesis the absorption of the material within the cavity is considered to be negligible and so Γ is only dependent on the mirror reflectivities. In some senses this a more useful metric for these cavities than the Q factor as it has no dependence on length, and will allow for a straight comparison between the different cavities produced in this thesis.

A third useful expression which will be derived here is one that related the FSR to the cavity length, L . This will prove to be very useful in finding out how long any particular cavity is, from its transmission spectrum. Beginning from the condition that a cavity must contain a natural number of half oscillations, we can write down expression 2.44.

$$L = \frac{\lambda_n n}{2} \quad (2.44)$$

Rearranging and differentiating we can get the expression given in 2.45.

$$\frac{dn}{d\lambda} = -\frac{2L}{\lambda^2} \quad (2.45)$$

Recalling that the FSR is simply the spectral difference between adjacent modes (i.e. $\Delta n = 1$), we can write

$$L = \frac{\lambda^2}{2\Delta\lambda} \quad (2.46)$$

where $\Delta\lambda$ is the FSR, which is especially relevant for calculating the volume of this type of cavity. This concludes the section on the transfer matrix and some of the considerations which are important to bear in mind when making use of distributed mirror coatings.

2.4 Gaussian Beams

This section will be comprised of a very brief discussion on the origins of the Gaussian beam, which will play a large role in describing the distribution of the field in the modes that these open access cavities form. Some of the more useful expressions attached to these modes will be quoted, and a few details of the possible higher order Gaussian modes will be mentioned.

Recalling equation 2.32a, and the fact that we can isolate a single frequency (ω_0) we can find solutions of the form

$$\mathcal{E}(\mathbf{r}, t) = \mathcal{E}e^{-i\omega_0 t} \quad (2.47)$$

to the wave equation, where the lack of bold font implies the quantity is a scalar, which will suffice for this rather cursory discussion. This reduces the full time dependent wave equation to the time independent Helmholtz equation for the spatial distribution of the field (in a vacuum),

$$\nabla^2 \mathcal{E}(\mathbf{r}) + k^2 \mathcal{E}(\mathbf{r}) = \mathcal{E}(\mathbf{r}) e^{-i\omega_0 t} \quad (2.48)$$

where we make use of the established relation $c = \omega k$. This can be solved with equations taking a variety of forms, for example as mentioned in prior sections $\mathcal{E}(\mathbf{r}) = \mathcal{E}_0 e^{i\mathbf{k}\cdot\mathbf{r}}$ for uni-directional waves with infinite extent in the two dimensions perpendicular to the \mathbf{k} vector (i.e. a plane wave) or alternatively $\mathcal{E}(\mathbf{r}) = \frac{A}{r} e^{i\mathbf{k}\cdot\mathbf{r}}$ where A is an arbitrary number and $r = \sqrt{x^2 + y^2 + z^2}$ which is not uni-directional, but has a finite lateral extent (i.e a spherical wave). Instead of these, the trial solution of $\mathcal{E}(\mathbf{r}) = \mathcal{E}_0(\mathbf{r}) e^{ikz}$ and the imposition of the requirement that the angle of divergence of the light is small allows Helmholtz's equation to be simplified to the paraxial wave equation 2.49.

$$\nabla_{\perp}^2 \mathcal{E}(\mathbf{r}) + 2ik \frac{\partial \mathcal{E}(\mathbf{r})}{\partial z} = 0 \quad (2.49)$$

In this equation the ∇_{\perp}^2 is the transverse Laplacian which is the sum of the second derivative of the field in only the directions transverse to the wave's motion. The details of a more complete derivation of the following formulas can be found in many textbooks, for example [86]. The solution for the field distribution that is considered in this approach is given in equation 2.50, and is referred to as a Gaussian beam.

$$\mathcal{E}(\mathbf{r}) = \mathcal{E}_0 \frac{w_0}{w(z)} e^{\left(\frac{-r^2}{w^2(z)}\right)} e^{(-ikz - ik \frac{r^2}{2R(z)} + i\zeta(z))} \quad (2.50)$$

Here $r = \sqrt{x^2 + y^2}$, w_0 is the radius of the beam at its narrowest (when $z = 0$) referred to as the beam waist. There are also three functions of z , namely $w(z)$ the beam width, $R(z)$ the radius of curvature of the phase profile, and $\zeta(z)$ the Guoy phase shift. In order to concisely define these three functions it is useful to define the Rayleigh range, z_R which is the distance along the z axis when the waist, $w(z) = \sqrt{2}w_0$. This is shown in figure 2.19. The value of z_R can be shown to be given by the expression in equation 2.51.

$$z_R = \frac{\pi w_0^2}{\lambda} \quad (2.51)$$

As mentioned above this allows us to write expressions for the beam width, $w(z)$ (or more precisely the radius of the beam at which the intensity falls to 1/e times its value on the optical axis), the z dependent radius of curvature of the beam $R(z)$ and the Guoy

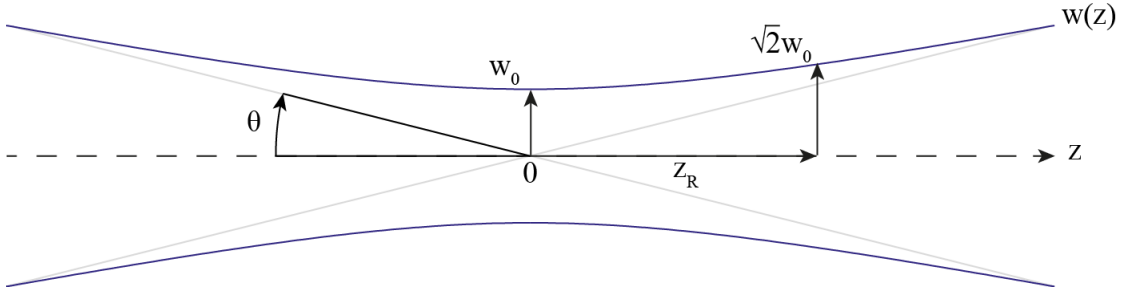


FIGURE 2.19: The beam waist w_0 and the Rayleigh length z_R shown schematically on an arbitrary Gaussian beam profile.

phase shift $\zeta(z)$ as shown in equations 2.52.

$$w(z) = w_0 \sqrt{1 + \frac{z^2}{z_R^2}} \quad (2.52a)$$

$$R(z) = z + \frac{z_R^2}{z} \quad (2.52b)$$

$$\zeta(z) = \tan^{-1} \left(\frac{z}{z_R} \right) \quad (2.52c)$$

One last useful quantity to extract from these beam structures is the divergence angle, θ which is marking on figure 2.19. This can be expressed in terms of w_0 (2.53), and will be particularly useful in calculating the numerical aperture over which a cavity mode is emitted, which is relevant when considering how optical microcavities of this type may be coupled to external optics.

$$\theta = \frac{\lambda}{\pi w_0} \quad (2.53)$$

These beams are ubiquitous in modern optics and it is this beam profile which is formed by the open access microcavities. The effect of decreasing the beam waist has visually dramatic implications on the spacial distribution of the field, in particular the divergence angles it achieves. Figure 2.20 shows the field that is formed with different beam widths to indicate this.

2.4.1 Gaussian Modes

Equation 2.50 describes freely propagating beams, with no form of confinement or cavitation taken into account. It is however still very useful. For example in the cavity set-up used throughout this thesis a planar mirror and a hemispherically featured mirror form the cavity modes. The geometrical arrangement of the two mirrors must then specify a unique set of Gaussian modes. For the planar-hemispherical case the location of the planar mirror specifies the location of the beam waist. The radius of curvature of the hemispherical mirror and its location on the z axis complete the required boundary

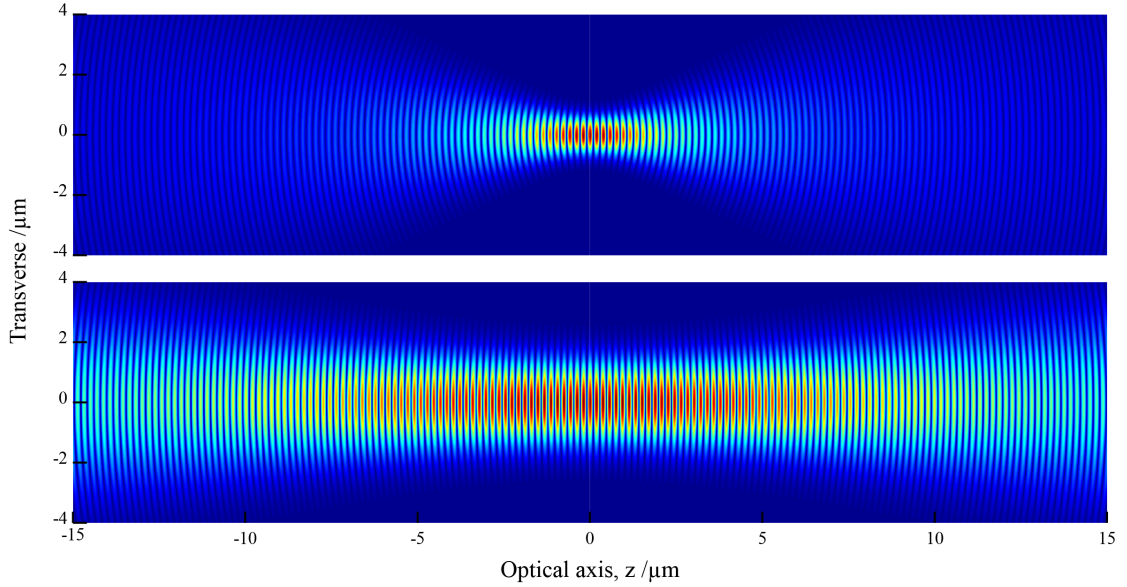


FIGURE 2.20: Field distributions for 2 different beam waists plotted using 2.50, highlighting the impact a reduction in the beam waist has on the divergence of the stable cavity mode.

conditions for a particular Gaussian mode. There are however a few conditions that must be fulfilled. These are more easily explored by defining resonator g parameters for each mirror as

$$g_i = 1 - \frac{L}{R_i} \quad (2.54)$$

where L is the cavity length, and R_i is the radius of curvature each mirror ($i = [1, 2]$). These parameters allow us to write expressions for the beam width on each of the mirrors and at the waist in terms of the radii of curvature and cavity length, shown in equations 2.55.

$$w_1 = \left(\frac{\lambda L}{\pi} \right)^{1/2} \left(\frac{g_2}{g_1(1 - g_1 g_2)} \right)^{1/4} \quad (2.55a)$$

$$w_2 = \left(\frac{\lambda L}{\pi} \right)^{1/2} \left(\frac{g_1}{g_2(1 - g_2 g_1)} \right)^{1/4} \quad (2.55b)$$

$$w_0 = \left(\frac{\lambda L}{\pi} \right)^{1/2} \left(\frac{g_1 g_2 (1 - g_1 g_2)}{(g_1 + g_2 - 2g_1 g_2)^2} \right)^{1/4} \quad (2.55c)$$

As mentioned, within this scheme the second mirror is flat and so g_2 reduces to 1 and 2.55b equates to 2.55c, supporting the assertion made above that the beam waist sits on the surface of the flat mirror, or $w_2 = w_0$. This also helps quantify appropriate sizes for the hemispherical feature. Figure 2.21 indicates the importance of this calculation, as in order for the cavity to effectively confine a Gaussian mode it is necessary for the feature diameter, a to be substantially larger than the beam waist that will appear on its surface. Closer inspection of equation 2.55c also reveals a negative value of w_0 is

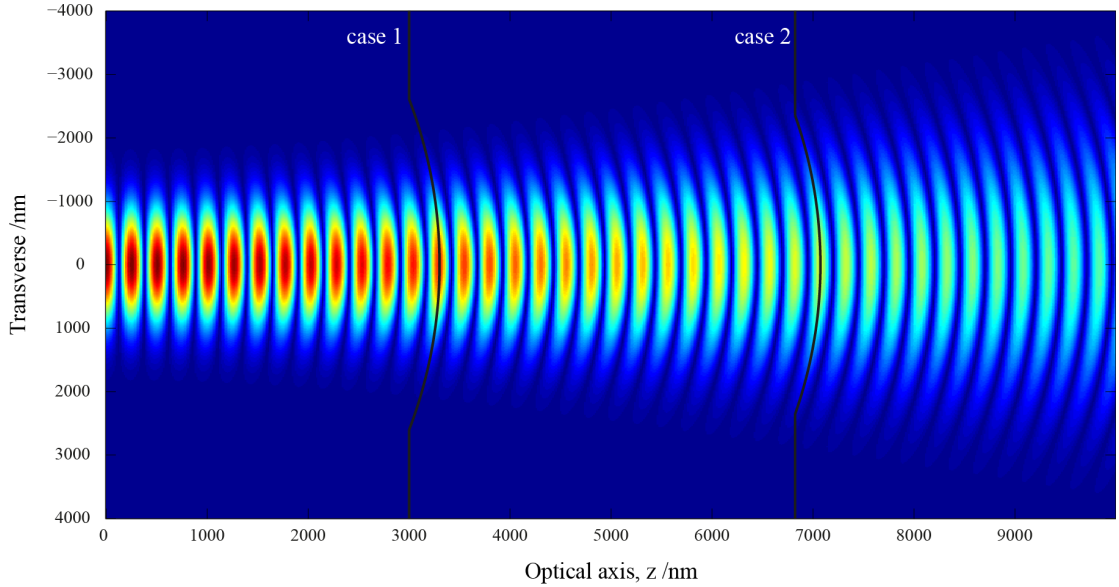


FIGURE 2.21: A visual accompaniment to the condition that the hemispherical feature width needs to be considerably larger than the beam waist incident on in (case 1) rather than smaller, where no optical confinement would take place (case 2).

obtained should $g_1 g_2 (1 - g_1 g_2) \leq 0$. This exposes another condition, that $0 \geq g_1 g_2 \leq 1$ which is the criteria for resonator stability. In the case of one mirror being planar this amounts to the requirement that the cavity length, $L \leq R$ where R is the radius of curvature of the hemispherical feature.

An important point to note about this confinement regime is that the distribution of resonant frequencies for the one dimensional case mentioned in 2.14 is altered by the curvature of the mirrors from the rather simple condition mentioned in the preceding text, that $\lambda_n = n(L/2)$. The plot in figure 2.22 shows Lorentzian peaks plotted at the locations of the resonances for a 1 μm long cavity where both mirrors are planar and there is no lateral confinement. The red peaks are the resonances for a cavity with the same length as the planar-planar case except here one of the mirrors has a radius of curvature of 5 μm . The inset of the figure shows how this blue shift due to the radius of curvature becomes less important for higher order longitudinal modes. The analytic expression for the mode spacing, ν_n is given in equation 2.56.

$$\nu_n = \frac{c}{2L} \left(n + \frac{1}{\pi} \cos^{-1} \sqrt{g_1 g_2} \right) \quad (2.56)$$

A final, very relevant quantity which can be calculated for these modes is the volume. For expediency the equation will be quoted here but can be derived from integrating the Gaussian mode equation derived earlier in this section. Alternatively this can be done numerically making use of the FDTD software utilised later in this thesis. The quoted

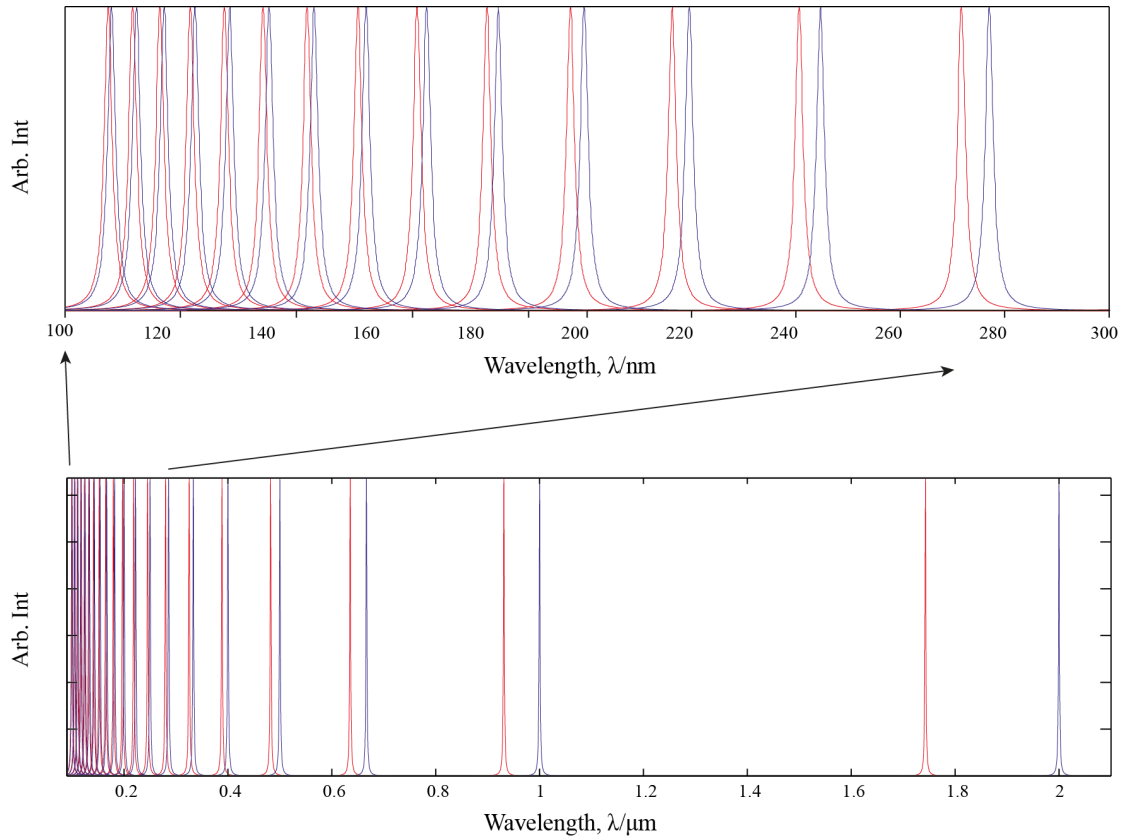


FIGURE 2.22: Lower plot shows the mode locations for a 1 μ m long planar-planar cavity (blue) and a planar-hemispherical cavity with radius of curvature 5 μ m (red), showing a marked divergence for the lower order longitudinal modes. The upper plot shows that for higher order longitudinal modes this divergence becomes less prominent.

formula for the volume is given in equation 2.57.

$$V = \frac{\pi w_0^2 L}{4} \quad (2.57)$$

To summarise the discussion up to this point three main conditions have been isolated for the construction of stable Gaussian modes. Firstly there was the paraxial approximation, as the Gaussian beam is only a solution to the paraxial wave equation which is an approximation to Helmholtz's equation for small angular divergences. The second is that (for the scheme proposed) the cavity length, L cannot exceed the radius of curvature of the hemispherical feature. Finally that the lateral extent of the featured mirror must exceed the beam width at that point.

2.4.2 Hermite-Gaussian and Laguerre-Gaussian Beams

Having discussed the mathematical description of the Gaussian beam, and presented a few of the considerations which lead to the conditions for the formation of stable Gaussian cavity modes the final topic in this theory section will be a discussion of ‘transverse modes’. These kinds of modes will also be referred to as higher order, or lateral modes. Similarly to previous sections this will consist of a fleeting presentation of a few of the key results. The solution to the paraxial equation presented in the preceding section (equation 2.50) has several more general versions, accommodating additional structure in the transverse $x - y$ plane. One more general version of this solution form is shown in equation 2.58, which does allow for this richer structure.

$$\mathcal{E}(\mathbf{r}) = AF_x \left[\frac{x}{w_0} \right] F_y \left[\frac{y}{w_0} \right] e^{iG(z)} e^{ik \left(\frac{r^2}{2R(z)} \right)} \quad (2.58)$$

Here we have introduced two new functions F_x and F_y which are functions of $\frac{x}{w_0}$ and $\frac{y}{w_0}$ denoted through the use of square brackets rather than parentheses, and a constant A . This can be used as a trial solution, and after some considerable manipulation including a separation of variables (see [86]) this eventually allows us to write an ordinary differential equation for each F_x, F_y and G_z . The two ‘ F ’ functions have the form

$$\frac{d^2 F}{du^2} - 2u \frac{dF}{du} + \frac{c}{2} F = 0 \quad (2.59)$$

where the variable u is a function of x or y and $w(z)$, and c is a constant. Equations of this form are solved by the Hermite polynomials, the first four of which are given in equation 2.60.

$$H_0 = 1 \quad (2.60a)$$

$$H_1 = 2u \quad (2.60b)$$

$$H_2 = 4u^2 - 2 \quad (2.60c)$$

$$H_3 = 8u^3 - 12u \quad (2.60d)$$

The function G_z can be integrated by normal means to yield an overall expression for the field in all spacial coordinates of

$$\mathcal{E}_{m,n}(\mathbf{r}) = \frac{Aw_0}{w(z)} H_m \left[\frac{\sqrt{2}x}{w_z} \right] H_n \left[\frac{\sqrt{2}y}{w_z} \right] e^{i(kz - (m+n-1)\tan^{-1}(\frac{z}{z_0}))} e^{ik \left(\frac{r^2}{2R(z)} \right) - \frac{r^2}{w^2}} \quad (2.61)$$

where m and n denote the order of the Hermite polynomial. This provides a labelling system for these, ‘TEM_{mn}’ where the TEM stands for Transverse Electric Magnetic field. This nomenclature also emphasises the importance of the small angular divergence, as

for modes with a very high numerical aperture a portion of the electric and magnetic fields lies in the z direction. These distributions in the $x - y$ plane have been plotted for the first ten modes in figure 2.23 when the beam waist is $1 \mu\text{m}$. It should be noted that the TEM_{00} reduces equation 2.61 to the Gaussian mode considered in the previous section. The higher order transverse modes are also blue shifted and the expression

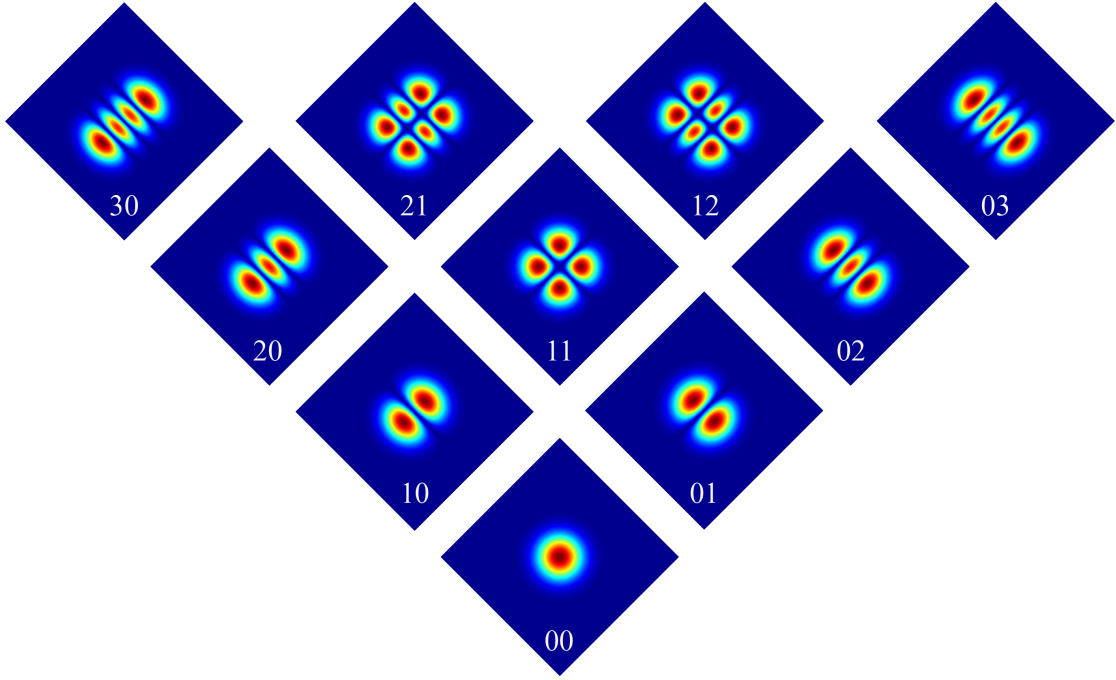


FIGURE 2.23: The electric field lying on the $1 \mu\text{m}$ wide beam waist for the first ten Hermite-Gauss modes. The white text indicates the labelling subscripts and each image is $4 \mu\text{m} \times 4 \mu\text{m}$.

shown in equation 2.56 can be developed to incorporate these transverse modes. This is shown in equation 2.62 where we now label the longitudinal number q (labelled n in equation 2.56), with m and n describing the transverse mode number.

$$\nu_{qnm} = \frac{c}{2L} \left(q + \frac{1}{\pi} (m + n + 1) \cos^{-1} \sqrt{g_1 g_2} \right) \quad (2.62)$$

Figure 2.24 shows how these modes fall for an $L = 1 \mu\text{m}$ long cavity with radius of curvature $5 \mu\text{m}$, identical to the one plotted in figure 2.22 in red. Here it is possible to see the richer mode structure resulting from incorporating the transverse Hermite-Gauss modes. In the plot energetically degenerate modes have been separated slightly and the peak height reduced in proportion to the degeneracy. In addition each longitudinal mode, $q = 1, 2, 3$ has been plotted in a different colour. From equation 2.62 clearly the transverse modes make up a two dimensional infinite set, however to improve figure clarity this series was curtailed at $m + n = 6$. The origin of these particular transverse

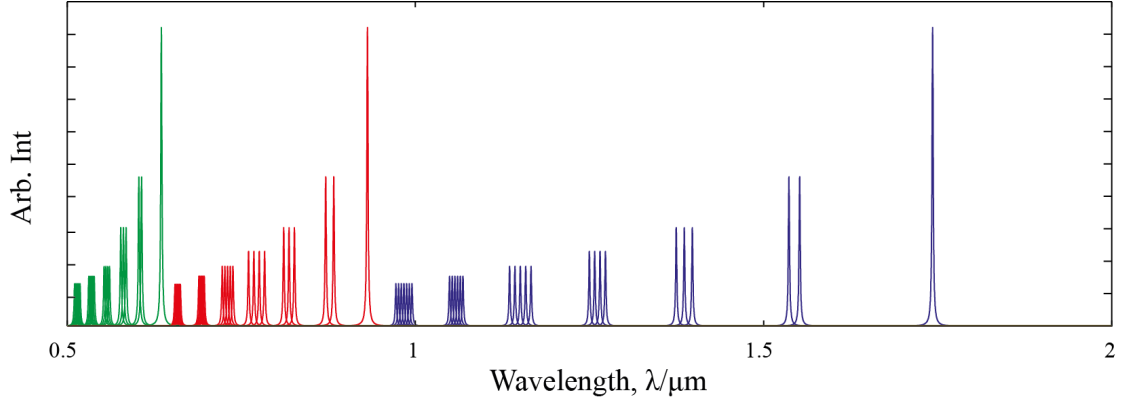


FIGURE 2.24: Resonant modes plotted for $q = 1, 2, 3$ and $m+n = 6$ from equation 2.62. Degenerate modes have been separated slightly and reduced in height in proportion to the degeneracy for ease of viewing.

modes lies in the coordinate system chosen, and that in an effort to find a more general solution with equation 2.61 we cast the unknown functions F_x and F_y in terms of Cartesian x - y coordinates. If we instead write the the paraxial equation in terms of cylindrical coordinates we get equation 2.63 and we can follow a similar approach to finding a solution as before.

$$\left(\frac{\partial^2}{\partial r^2} + \frac{1}{r} \frac{\partial}{\partial r} + \frac{1}{r^2} \frac{\partial^2}{\partial \phi^2} + 2ik \frac{\partial}{\partial z} \right) \mathcal{E}(r, \phi, z) = 0 \quad (2.63)$$

In this case we can arrive at equation 2.64 where L_p^l are the associated Laguerre polynomials and are a function of the expression in the square brackets (as before).

$$\mathcal{E}_{pl}(r, \phi, z) = A \frac{w_0}{w(z)} e^{il\phi} \left(\frac{r\sqrt{2}}{w(z)} \right)^{|l|} L_p^{|l|} \left[\frac{2r^2}{w^2(z)} \right] e^{\frac{-r^2}{w(z)^2}} e^{\frac{ikr^2}{2R(z)}} e^{-i(2p+l+1)\tan^{-1}\left(\frac{z}{z_0}\right)} \quad (2.64)$$

The first ten of these Leguerre-Gauss mode distributions can also be plotted in the same way that the Hermite-Gauss modes were, and are shown in figure 2.25. We now have two perfectly consistent ways of solving the same differential equation. In fact both of these series of solutions form complete sets, and any mode from the Laguerre-Gauss set can be formed from a linear combination of modes in the Hermite-Gauss set. As an aside the Laguerre-Gauss set have the additional property that they can have non-zero orbital angular momentum values, a result of this functional form also being an eigenvalue of the angular momentum operator. It is the physics of the situation that determines which of these two spatial distributions is resultant, in some sense Laguerre-Gauss is the highest symmetry solution as in a perfectly aligned cavity with no polarisation dependent elements it is these that are found. However if the cylindrical symmetry of this situation is broken imparting a Cartesian symmetry, it is the Hermite-Gauss modes which are found.

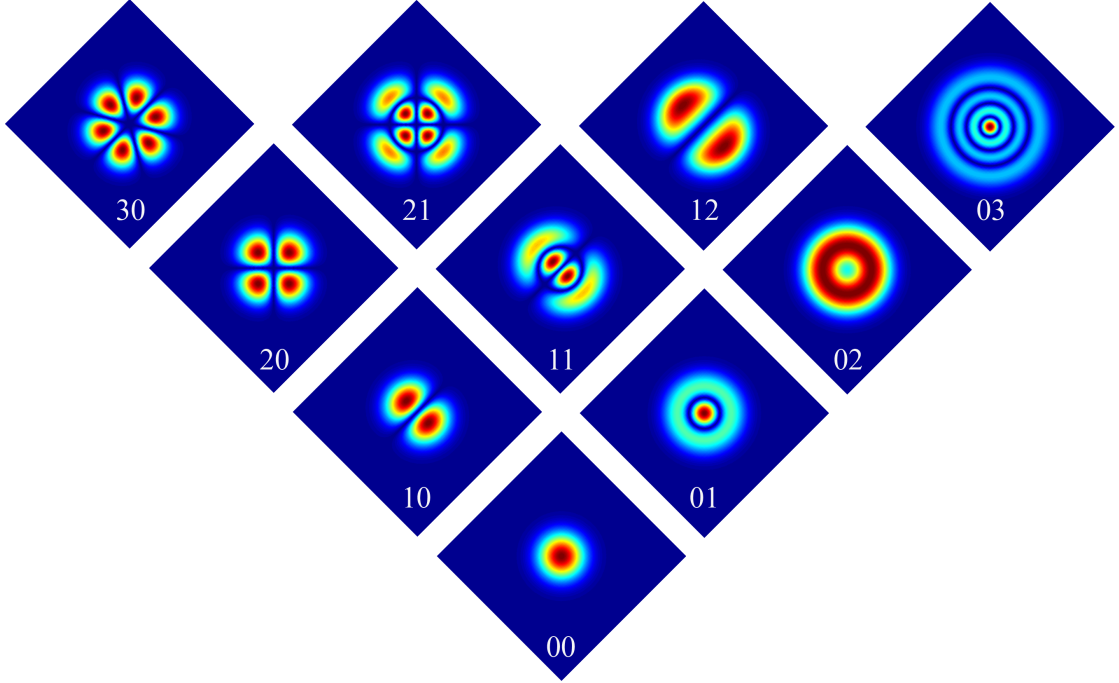


FIGURE 2.25: Lower plot shows the mode locations for a $1 \mu\text{m}$ long planar-planar cavity (blue) and a planar-hemispherical cavity with radius of curvature $5 \mu\text{m}$ (red), showing a marked divergence for the lower order longitudinal modes. The upper plot shows that for higher order longitudinal modes this divergence becomes less prominent.

2.5 Finite Difference Time Domain Simulations

2.5.1 Physical Background of Simulations

In this section some of the theoretical details of the computer modeling carried out during the course of this thesis will be discussed. The software package used throughout the project is called Lumerical, and is commercially available. Finite difference time domain, or FDTD software works by solving Maxwell's curl equations, also known as Ampère and Faraday's laws. These can be expressed for isotropic materials as:

$$\nabla \times \boldsymbol{\mathcal{E}} + \frac{\partial \boldsymbol{\mathcal{B}}}{\partial t} = 0 \quad (2.65a)$$

$$\frac{\partial \boldsymbol{\mathcal{D}}}{\partial t} - \nabla \times \boldsymbol{\mathcal{H}} = \boldsymbol{J} \quad (2.65b)$$

which makes use of the electric displacement and magnetic field strength, $\boldsymbol{\mathcal{D}}$ and $\boldsymbol{\mathcal{H}}$. Doing so simplifies the form of the equations when describing the media response to the presence of an electromagnetic field. They are defined in equations 2.66a and 2.66b.

$$\boldsymbol{\mathcal{D}} = \epsilon_0 \epsilon_r(\omega) \boldsymbol{\mathcal{E}} \quad (2.66a)$$

$$\boldsymbol{\mathcal{B}} = \mu_0 \mu_r(\omega) \boldsymbol{\mathcal{H}} \quad (2.66b)$$

Here the dependence of the relative permittivity and permeability on the frequency of the excitation field is explicitly shown. In general this can be a complex quantity to allow the consideration of a lossy material's response. For completeness the relative permeability of the material is included, although these computations assumes no magnetic response and so its value can be assumed to be unity. In a Cartesian coordinate system Ampère and Faraday's laws are equivalent to a set of six scalar partial differential equations. These in turn can be discretised into a set of finite difference equations, where rather than differentials ($\partial\mathcal{G}/\partial x$), small numerical differences ($[\mathcal{G}(x+\Delta x)-\mathcal{G}(x)]/\Delta x$) are considered. This effectively casts a 4 dimensional mesh over the region under consideration and the time span within which the time-domain incident wave will be propagated. The time is usually divided into constant discrete time steps. Each of the volume cells making up the geometrical extent of the mesh is called a Yee Cell. A general cuboid Yee Cell is shown in figure 2.26. This is named for the author of the seminal paper which first outlined the finite-difference computational method for electromagnetics which is implemented during these simulations [87]. By constructing cells in the way shown in figure 2.26, with

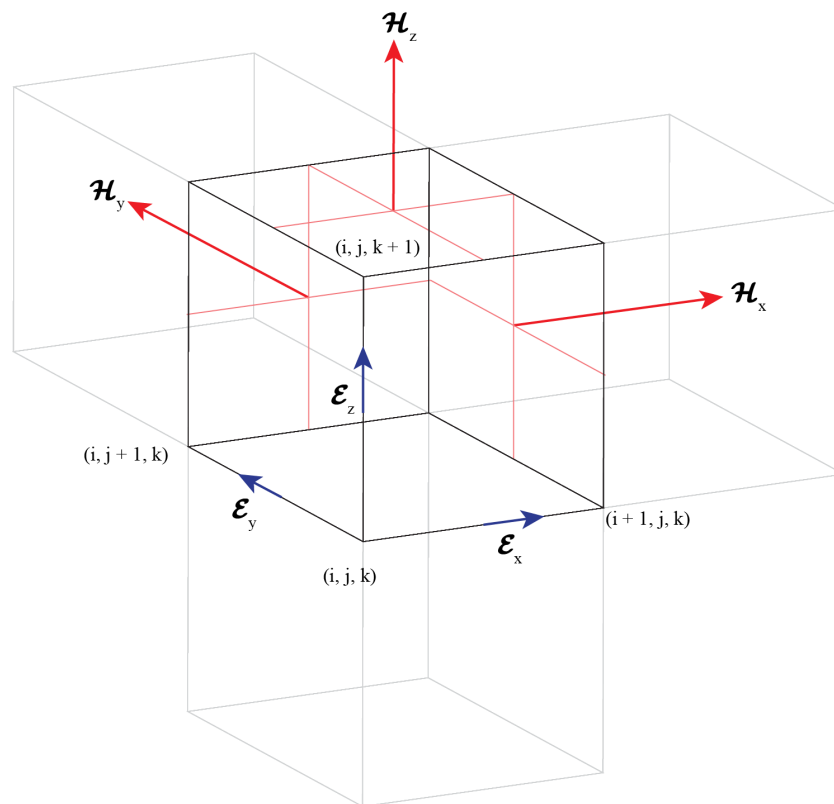


FIGURE 2.26: A diagram of a single cuboid Yee Cell in a 3D mesh comprised of several such cells. Components of the electric field (\mathcal{E}_{xyz}) are calculated along the edges and the magnetic field strength (\mathcal{H}_{xyz}) in the faces midpoints.

the electric field vectors midway along each edge and the magnetic field strength vectors in the centre of the each cell face, a leap-frog iterative computation can be implemented for the time evolution of the system. This is done as the electric field at a particular

location at the next time step depends on the current value and the curl of the magnetic field strength. Conversely the value of the magnetic field strength at the next time step depends only on its current value and the curl of the electric field. In order for this iterative method to converge and yield a meaningful solution Courant's criterion described in equation 2.67 must be satisfied.

$$\sqrt{(\Delta x)^2 + (\Delta y)^2 + (\Delta z)^2} > c\Delta t \quad (2.67)$$

Simultaneously the physical size of the Yee cell must be considerably smaller than the wavelength of the radiation being considered. For the visible region and for the structures that have been described previously in this thesis, this means cell sizes smaller than a nanometre, and therefore step sizes in the femtosecond timescale. In addition these simulations should run for sufficient time to reach a steady state, most often for these cavities once the majority of the field has leaked away through the simulation boundaries. The determination of the meshing approach to use and the appropriate time steps, along with the details of how to extract the relevant information is all coded by the software developers. The user defines some physical structure and sets the simulation region. The user also specifies the source of illumination (e.g. dipole emission, incident plane wave etc.) the monitors, which dictate what information is retained as the simulation proceeds, the boundary conditions to use at the simulation region boundary, and any aspects of the simulation symmetry which may reduce the computational overhead. This method is suitable for the cavities constructed in this thesis, as it allows for their performance to be assessed, and the limits of the technique to be established.

2.5.2 General Model Details

In this section the general model that was constructed will be described, along with the sources and monitors that were inserted. The substrate was modeled as a perfect hemispherical depression surrounded by a large flat region (which extends beyond the simulation region) as shown in the leftmost depiction in figure 2.27. Layers of this surface geometry were then stacked in the z -direction, and arranged opposite planar layers forming the opposing mirror. This construction approach was written into a script file which allowed the user to specify the details of the cavities desired, including the number of layers on each mirror, the width and radius of curvature of the features and the cavity length. Once the substrate is constructed and the dimensions of the simulation region are determined the sources and monitors can be placed. The source used throughout this chapter is an electric dipole. The location of the source generally depends on the details of the Bragg stacks used. For example in the case where the DBRs end with the lower refractive index material, the source is located centrally with

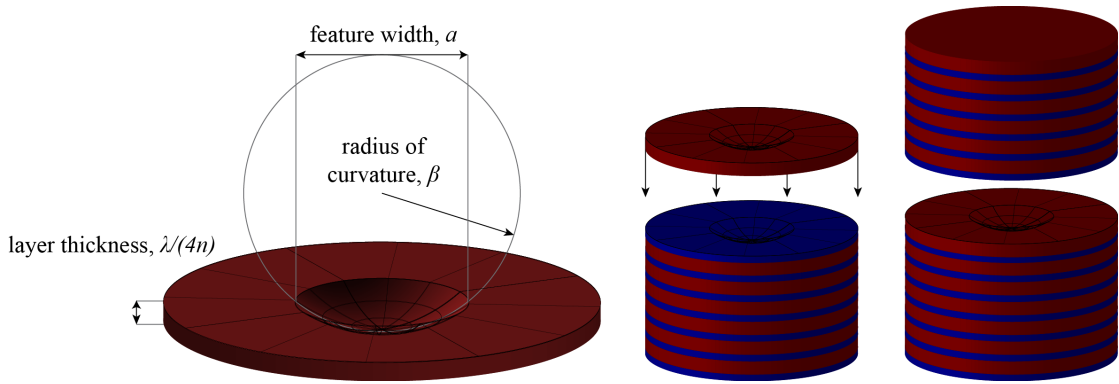
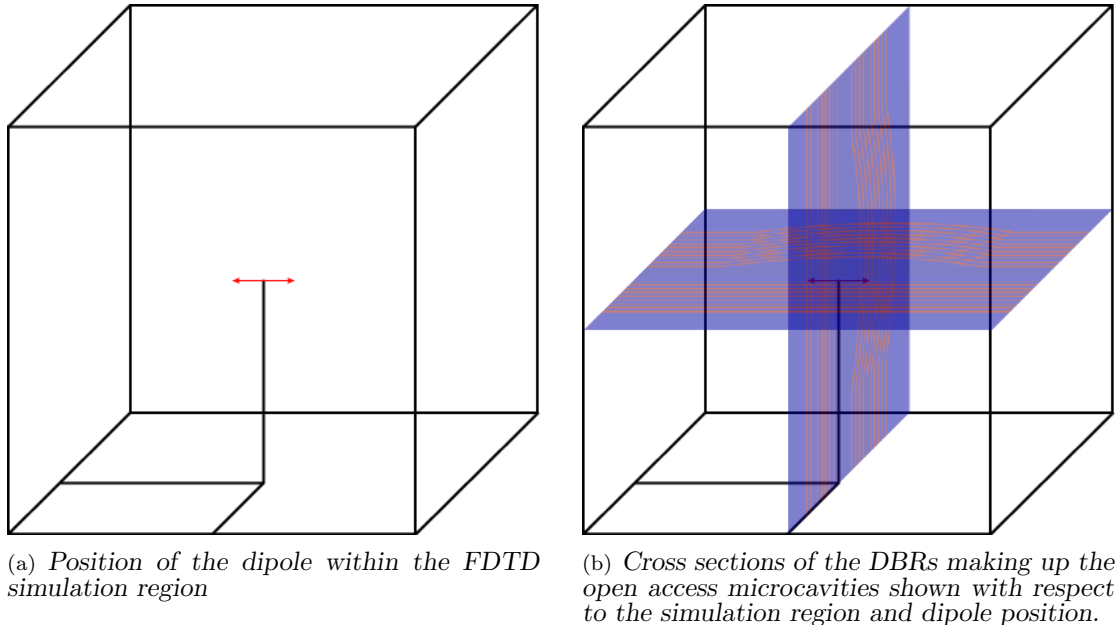


FIGURE 2.27: The leftmost diagram indicates the most relevant cavity properties. The DBRs are then constructed layer-by-layer in both the planar and featured case by the automated design script.

respect to the feature, and a small ($\sim 1 - 10$ nm) distance inside the cavity away from the planar surface. In the case where the DBR is terminated with the higher refractive index the source is located approximately $\lambda_0/4$ away from the planar surface, in both cases this accomplishes close to optimal spatial coupling and so allows the modes to be well populated and easily measured. Figure 2.28(a) shows the dipole position within the FDTD simulation region, and figure 2.28(b) indicated its position within the open access microcavity. The emission characteristics of the source are also determined by



(a) Position of the dipole within the FDTD simulation region

(b) Cross sections of the DBRs making up the open access microcavities shown with respect to the simulation region and dipole position.

FIGURE 2.28: The modeled dipole location and refractive index cross sections shown within the cuboid simulation region (the outer wireframe box).

the user to some extent, although they are constrained to have a spectral Gaussian distribution. Even as a Gaussian the full-width half-maximum of the function can be

chosen to accomplish broadband mode excitation, single mode excitation or to simulate a particular emitter's spectral properties. This choice has implications on the time domain as the narrower the pulse spectrally the longer it takes the dipole to produce the pulse. Three different types of monitor are used to retrieve the data that is required over the course of the simulation. These are all preprogrammed but are essentially just an instruction to save the $\mathcal{E}_{x,y,z}$ and or the $\mathcal{H}_{x,y,z}$ values associated with individual or user defined planes of Yee cells. The first monitor is the spectral monitor, and only addresses a single Yee cell. For all of these simulations it was placed on the optical, z -axis which is normal to the planar mirror and passes through the centre of the hemispherical feature. This records a time series of values of the electric field in all three Cartesian directions and performs a Fourier transform to yield the spectral information. The second type of monitor outputs the electric field intensity (or any of its Cartesian components) over a plane. It was found most useful to have the plane of monitored Yee cells run through the centre of the feature and be parallel to the normal of the planar DBR. Finally the power monitors were arranged to form a cuboid on the boundary of the simulation region. These were vital in calculating Purcell factors during the modeling of the colloidal nanocrystals within the cavities, and calculate the Poynting vector of the electromagnetic waves propagating out of the simulation region from the cross product of the electric field and the magnetic field strength. The analysis of the data recorded by this model set-up will now be described, and fall roughly into three sections. The first is a consideration of the cavity mode volumes making use of the spectral and spatial field monitors. The second is how the Purcell factor can be determined for an emitter by using the power monitors situated along the boundary of the simulation region. The final section will pursue a maximisation of both volume and Q factor to yield an optimum coupling strength.

2.5.3 Mode Volume Calculations

It is clear from its appearance in the crucial equations determining the Purcell factor that an accurate value for the volume of a mode of a microcavity has to be obtained. When running the FDTD simulations there are several 2D and 3D monitors available which are precoded to analyse resonances and calculate the mode volumes directly. Unfortunately this means collecting data to fill a 4D matrix, as it has to monitor the values of the field for every spectral value at each spatial location. This places a demand on computational memory requirements that surpasses those available by over an order of magnitude, if the data obtained is to have an acceptable level of accuracy. The TEM_{00} modes we are considering as candidates to couple emitters to are quite symmetrical and so a less memory intensive method for calculating the volume is available. This begins

with the expression shown in 2.68, which shows that the effective mode volume can be found by performing a triple integral over the entire spatial mode distribution and then normalising it by dividing by the intensity maximum (for simplicity, in this case located at the origin) multiplied by the refractive index at that point.

$$V_{eff}I(0)n(0) = \iiint I(\mathbf{r})n(\mathbf{r})dV \quad (2.68)$$

Due to the cylindrical symmetry of the Gaussian modes being considered, the computational overhead can be removed by analytically performing the integration around the azimuthal angle in cylindrical coordinates. Equation 2.69 shows the effect of reducing the dimensionality of the integration and discretising it to a summation, for the context of the numerical arrays yielded by the FDTD simulations.

$$V = \sum_{r=0}^{r_{max}} \sum_{z=z_{min}}^{z_{max}} I_{r,z}n_{r,z}2\pi rdzdr \quad (2.69)$$

Here dz and dr are each mesh cell area in the plane monitored. These are not necessarily constant, as Lumerical automatically decreases the mesh size in regions containing refractive index interfaces, and so each must be calculated from the data supplied. $I_{r,z}$ and $n_{r,z}$ are the normalised intensity and refractive index measure at each monitored mesh cell. Figure 2.29 shows some of the values appearing in the equation more visually. In terms of memory capacity, this means that the entire mode volume can be calculated

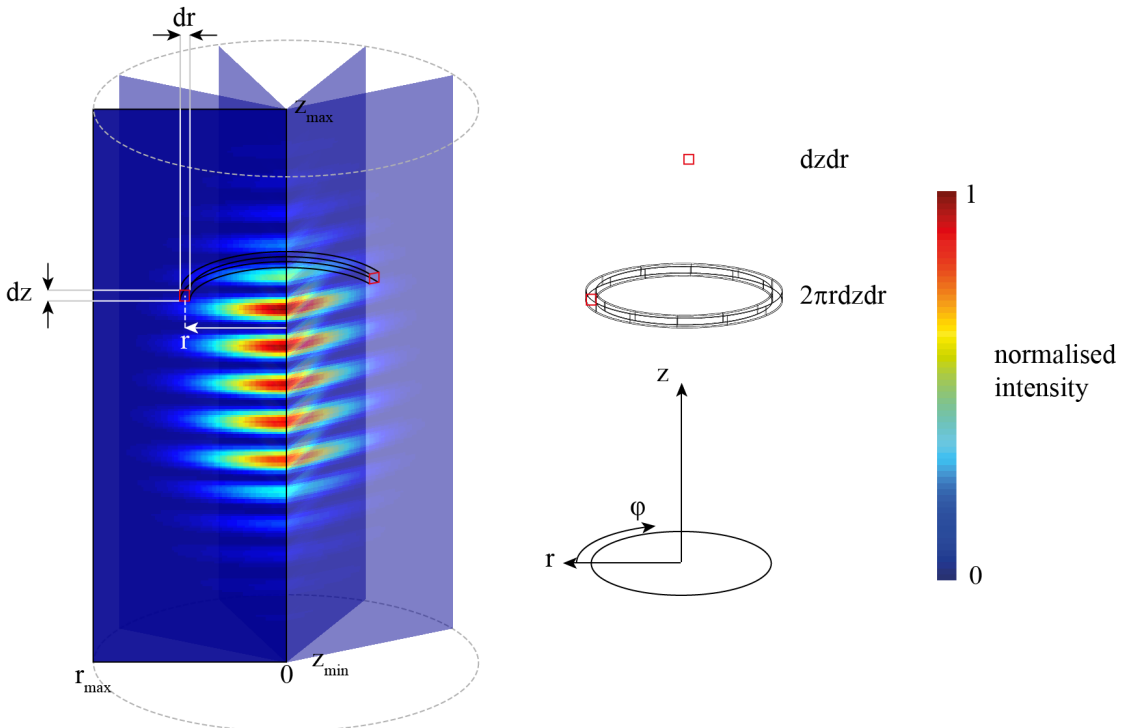


FIGURE 2.29: Depiction of the volume calculation by partial analytic integration (over ϕ) and numerical integration (over r and z).

by recording a 2 dimensional plane going through the centre of the cavity. Granted it is still a 3 dimensional array that is recorded, due to the range of spectral values, but this reduction is sufficient to make these simulations straightforward with a modest application of computational power. If additional accuracy is required one further step would be to run an initial simulation which monitors no spatial information about the field distribution, but obtains the spectral location of the resonances. Once this information is acquired all of the spectral monitors can be inserted and the simulation could be re-run with the spatial monitors recording only the resonant frequency, further reducing the dimensionality of the memory requirements. Balancing the memory required against the convenience of only running a single simulation meant that this further step was not required.

2.6 Summary and Conclusions

It is hoped that this chapter served as a brief reminder on some of the origins of the phenomena arising in the forthcoming text. A fuller expression for the Purcell factor was derived, which emphasises the importance of spectral and positional tune-ability of microcavities. A few of the most relevant cavity figures of merit were highlighted via the development of a simple one dimensional transfer matrix model to describe modern distributed dielectric mirrors. Some details of the Gaussian cavity modes were presented which play a central role in almost all of the chapters to come. Finally a discussion of the FDTD simulations implemented towards the end of this project were discussed.

Chapter 3

Cavity Construction

3.1 Introduction

In this chapter the precise details of how the hemispherical cavity features were constructed will be discussed. It will begin with a brief description of how the focused ion beam (FIB) system works, and then will outline some of the details of producing arbitrary patterns for milling. The majority of the chapter will then outline in detail the topographical analysis of the features which has been developed throughout the period of this project. Central to this is the atomic force microscope (AFM), which can assess the surface topography of the features with sub-nanometre accuracy. Included in this section are details of the numerical analysis of the AFM's results which was conducted in the MATLAB programming environment.

3.2 The Focused Ion Beam Milling

3.2.1 The Focused Ion Beam System

Although the focused ion beam is by now a well established tool in the semiconductor industry, an overview of the workings of the device will be presented here. This overview serves to give some context to the parameters that must be optimised in order to achieve a consistently high fidelity of feature to the desired pattern. I will also mention a few features of more advanced FIB systems than the one used, to emphasize that the details of the microcavity construction technique presented here do not represent the limit to which this approach can be developed.

Focused ion beam systems function very similarly to a scanning electron microscope (SEM) the main difference being the FIB uses a source of relatively large atomic mass ions rather than electrons. Once accelerated, these (normally gallium) ions pass through a series of lenses and apertures, finally focusing them to a spot which can ablate the target substrate. This technique requires the sample to be kept under a high vacuum throughout the milling procedure. A few of the key elements in a generic ion column are shown in figure 3.1, alongside a diagram of the focal region.

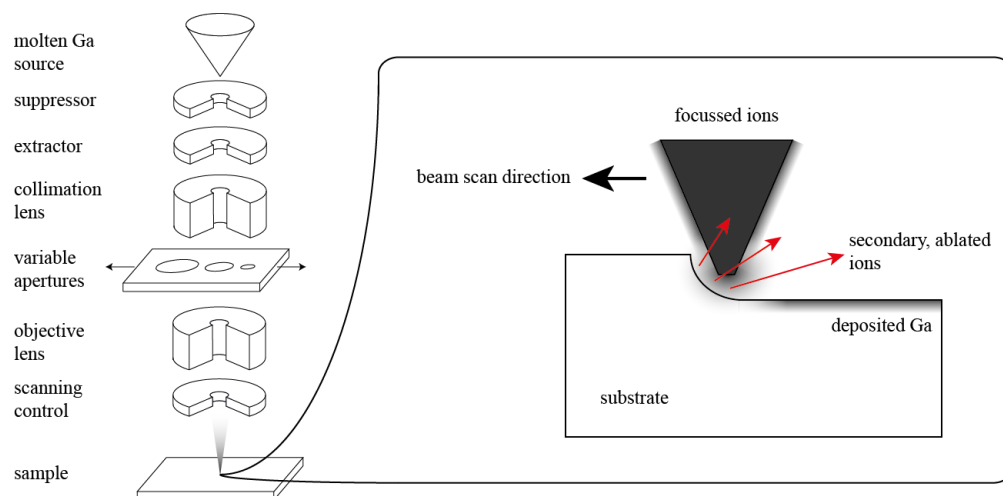


FIGURE 3.1: Exploded diagram of single FIB column, with diagram of focal region.

The FIB system used throughout this thesis was a single beam FEI FIB 200. The ‘single beam’ distinction is made as many FIBs have a separate acceleration column with an electron source (as in a conventional SEM). This allows non-destructive imaging to be carried out whilst simultaneously milling with the Ga ions. In some circumstances the electrons can also be used to neutralise positive charge build up, although this can also be achieved by including an ion flood gun in the chamber. The implication of using a single beam is that any region imaged will incur some damage from the incident ions. For the purposes of this project these shortcomings were inconsequential or at least surmountable, and so the single beam system sufficed. In addition to adding a second acceleration column FIBs often have gas injection systems. The premise of these systems is that the etching or milling rate can often be enhanced by altering the chemical environment at the location of the focal spot. This is done by mechanically positioning an injection needle close to the target area and pumping in a gas. The choice of gas is entirely dependent on the substrate being milled, for example when milling diamond, water is often injected to enhance the etch rates. For milling silicon dioxide a special enhanced etch has been developed, however this was unavailable on the system used, but would have probably benefited the rate of production of features.

The extractor voltage is permanently set to 30 kV on the FIB 200 system, with the source in this case being molten gallium (Ga). Once accelerated by this potential difference, the ions can then be shifted laterally, focused and passed through a variable aperture, taking the beam current down from the order of μA to a current determined by the radius of the aperture chosen, any of several values in the range of 20 nA down to 10 pA. This variable beam current is then further focused with an electromagnetic objective lens, and can be scanned across a stationary sample.

When obtaining an image the FIB (and SEM) work in a very similar way to a scanning confocal microscope, at least as far as the ‘excitation beam’ is concerned. The upper limit of the FIB’s resolution is largely determined by the ion beam’s spot size. At lower beam currents this can be as small as 10 nm, but as the variable aperture is increased in size to increase the beam current, so the spot size increases. At its highest current throughput of 20 nA the FIB’s spot size (and therefore resolution) is of the order of a 100 nm. An example image of a few milled features is shown in figure 3.2a). Image b) shows a zoomed out version of image a). This clearly shows the damage that is incurred when imaging with a single ion beam.

As an aside image c) shows the imaged region with a small enough magnification to include areas close to the periphery which suffer strongly from aberrations incurred by the electromagnetic lens’s octopole structure. High quality images can only be taken from the central region, at higher magnifications ($> 250\times$).

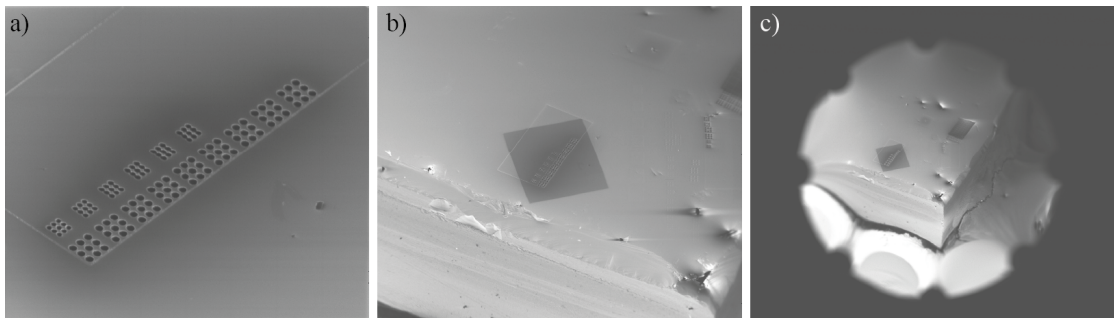


FIGURE 3.2: a) An example image taken with a mid-range beam current, b) zoomed out image including the region imaged in a), showing mild damage incurred, c) further drops in magnification revealing octopole objective lens silhouette and severe aberrations around the edges.

3.2.2 Sample Patterning

Here the approach used to pattern the sample with arbitrary features will be discussed. The field of view is digitised into a region of 4096 by 4096 pixels by passing the voltages applied to the scanning controls through a 12-bit digital to analogue converter. Its numbering system labels the top left pixel (0, 0) and the bottom right one (4096, 4096).

The key to the feature milling is the ability to control the dwell time of the beam at each of these pixels. This is done by uploading a ‘stream’ file with a straightforward, but

	s			
	# of loops			
	# of pixels			
particular structure:	t_1	x_1	y_1	Here the ‘s’ is
	t_2	x_2	y_2	
	\vdots	\vdots	\vdots	
	t_n	x_n	y_n	

largely redundant except for allowing file recognition by the native FIB column control software. Then comes the number of times the entire mill sequence is implemented, followed by the total number of pixels in the pattern. The bulk of the file is then taken up with the list of coordinate pairs and dwell times. These files can be written directly by a MATLAB script, but the manufacturer of the system also provide a piece of software that generates these scripts from a bitmap image.

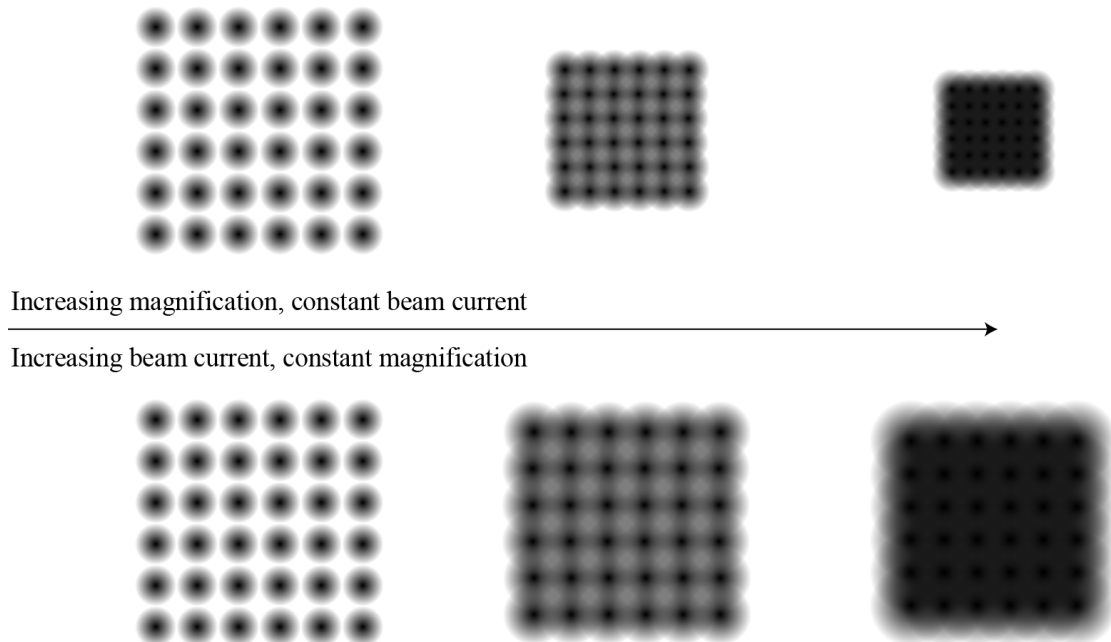


FIGURE 3.3: A visualisation of the effect of increasing the magnification (above) and the beam current (below) on the overlap of adjacent pixels during stream file milling.

Throughout most of this project the latter of the two, the FEI software was used to generate the stream files. Several points about the structure of the stream file should be appreciated at this stage. Nowhere within the structure does it specify what magnification, or what beam current is being used. These parameters have to be decided

upon by the user. These decisions however are not trivial to make. As the FIB system discretises the available field of view into the same number (4096^2) of pixels no matter what magnification is chosen, the effective physical size of each pixel varies with the magnification. There is a balance then, between what magnification is chosen and how much the focal spot will overlap between adjacent pixels (this is also dependent on the beam current chosen, as this changes the spot size). This is described more visually in figure 3.3. Here one can see that by either increasing the magnification or increasing the beam current will result in an increased beam overlap.

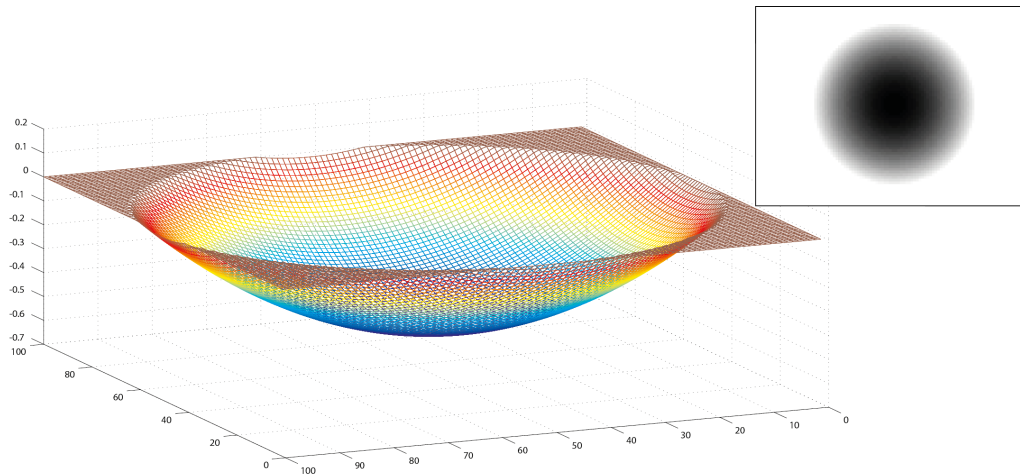


FIGURE 3.4: *An example surface generated by a simple MATLAB code, (inset) shows the greyscale bitmap to be read by the FIB system.*

The other important factor to consider when designing the stream file is the order of the points. The beam is not blanked between pixels, which means that the full milling current is dragged from A to B, milling out a track in between the two points. In order to mitigate this affect one might be tempted to only ever run a single loop of the pattern, multiplying the dwell times in the first column up by whatever number loops was desired initially. There are other things to be considered however, such as redeposition of ablated material and charging effects (leading to sample drift) both vary non-linearly with dwell time. Balancing all of these factors to achieve a good fidelity to the desired pattern was largely accomplished by a method of trial and error. The coordinates of an arbitrary hemispherical surface, such as one shown in figure 3.4 can be generated by a straightforward MATLAB code. This code was written to output a feature with a user defined radius of curvature, feature diameter, and image resolution. It then outputs both a greyscale bitmap version of the surface plotted, shown in the inset of figure 3.4, and was later developed to generate a ‘.str’ stream file which is directly compatible with the FIB200. As mentioned previously the stream file most often used was then generated by a piece of software provided by the FIB manufacturer from the bitmap image and used in place of the MATLAB generated one. The stream

file generated was organised such that a standard x-y raster across the image was used during milling, which was found to yield the best results. The MATLAB code could quite easily have been altered to remove this step. It was found early on that arrays of these features could be milled into the substrate by constructing stream files made from stenciling several (~ 100) individual features together.

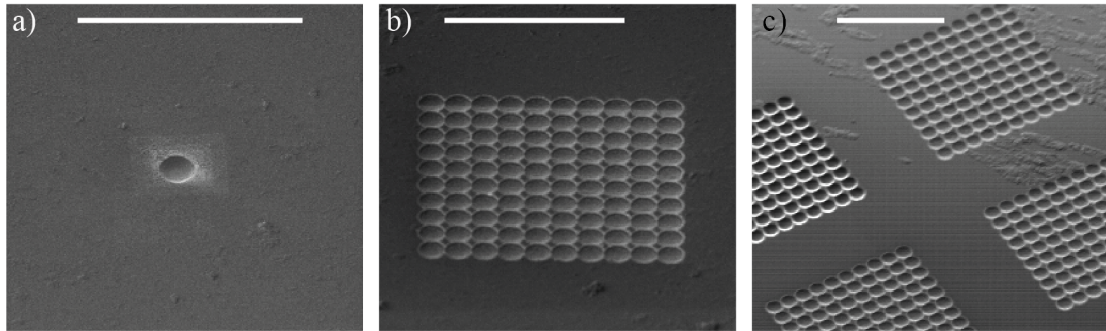


FIGURE 3.5: a) A single feature milled into silicon, b) An array of 100 features milled from an arrayed stream file, c) Several arrays of features stenciled together by moving the sample stage between mills. Scale bar $20\ \mu\text{m}$.

This process was found to be rather quick, and it was decided that prior to coating in order to maximize the possible optical experiments we could conduct, we should aim to mill as many of these features into the substrates as possible. In addition to milling in up to 100 individual cavities in a single milling step, the focussed ion beam system used has in place a slightly higher level scripting language. This language can be used to control (and therefore automate) many of the other parameters of the system, including the sample stage location, the milling current, the magnification and also what stream file is being milled. In this way we can effectively control the precise milling location and the dwell time with the stream file system, and all of the other relevant parameters with the script file. Figure 3.5 shows the progression from single features to arrays and on to stenciled arrays of features. For a slightly more visceral sense of scale a human hair is included in the field of view of figure 3.6.

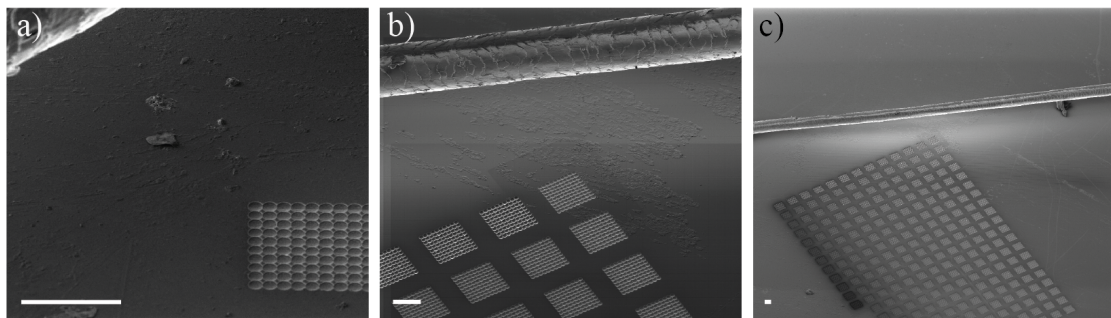


FIGURE 3.6: Arrays of cavities milled into silicon next to a single hair. Scale bar $20\ \mu\text{m}$.

This set of mills was performed in around six hours yielding of the order of 10^4 microcavities (once coated). As mentioned, the combination of both the scripting language and computationally generated stream files allows for a great deal of versatility. Parameter sweeps of dwell times, magnifications and beam currents were straight forward to implement and allowed for high levels of optimisations to be achieved.

The structure of the stream files that can be read by the FIB system leaves both the magnification and the beam current to be optimised. In order to effectively perform this optimisation a method of quantitatively analysing the quality of the features had to be developed. Ideally this would involve many iterations of milling features, coating with dielectric stacks and comparing the highest achieved finesses and Q factors. The iteration of this full process would have been impractical to say the least, and so a method of quantitatively assessing the topography of the features prior to coating was developed. As mentioned in the introduction this involves the use of an AFM and some digital image processing and will be discussed in the next section.

It is worth mentioning that since this entire process is computer controlled, hemispherical shapes are only one possible structure. Figure 3.7a) shows an early attempt at milling in a simple sinusoidal plane wave, with b) and c) showing arrays of elliptical cavities and solid immersion lenses. None of these avenues were developed, but help to show the versatility of this processing technique.

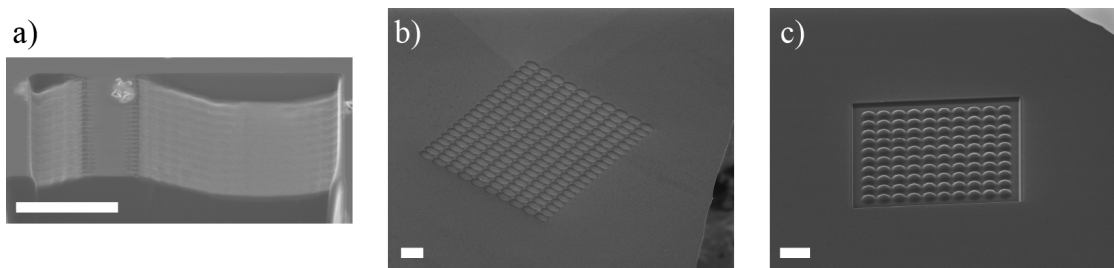


FIGURE 3.7: A variety of other features milled into substrates. a) A sinusoidal curve, b) elliptical microcavities, c) arrayed SILs. Scale bar $2 \mu\text{m}$.

3.2.3 Substrate Preparation and Imaging Details

As discussed in the section 3.2.1 the focused ion beam functions by accelerating positive ions onto a small region of a substrate. This means that it is very important for the sample to be sufficiently conductive so that the charge that builds up during the course of a mill can dissipate. In order to get around silica's inherent lack of conductivity it is therefore necessary to coat the sample with a very thin layer of gold. In addition silver conductive paint also needs to be used to ensure that there is a clear conductive path leading from the top of the sample to the metallic sample holder. It was found

that about 60 seconds of sputtering would deposit between 30 - 80 nm of gold, which provided ample charge dissipation. Although clear conductive paths allows the milling to effectively implemented, the imaging system works by correlating the charge collected by a detector placed within the chamber with the location of the focus of the ion beam. The brightness of any particular region on the sample depends on both the region's composition, and its orientation with respect to the detector. Since the gold is such a good conductor and the silica so poor, the contrast in signal between these regions is very hard to image with either a FIB or an SEM, although it is straightforward to view them optically, shown in figure 3.8. This imaging would still require the high vacuum of

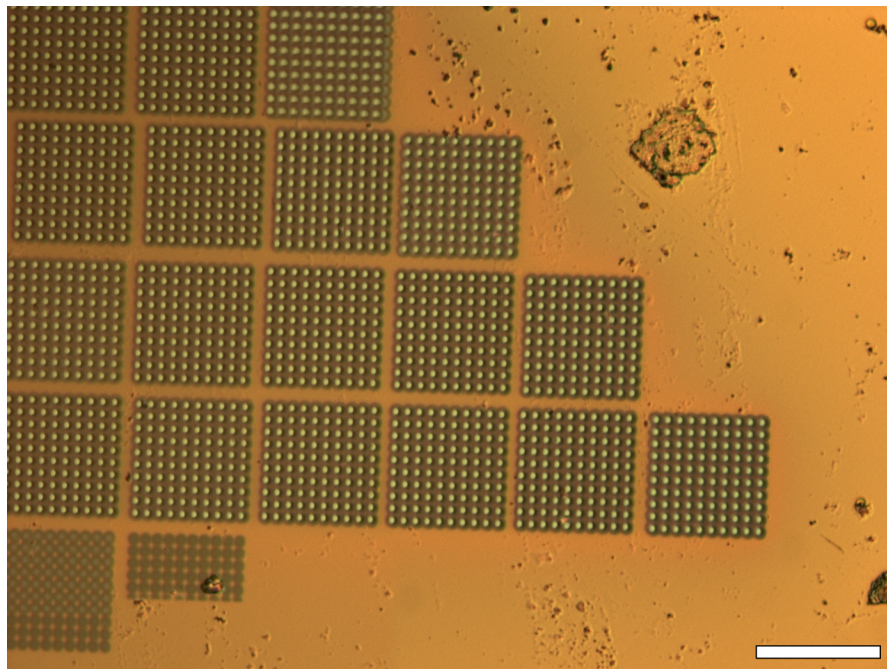


FIGURE 3.8: *Arrays of features imaged optically. Scale bar 80 μm .*

the FIB to be broken and the sample extracted to gauge success. In order to have a more immediate method to assess the performance of any particular milling operation silicon was used as a test substrate, which is much more amenable to imaging. An example of two identical routines milled into both silicon and silica is shown in image 3.9. It should be understood that all of the SEM style images of the features shown here (with the exception of figure 3.9 b)) are patterns milled into silicon. Identical patterns were then milled into silica which provided a better substrate for optical interrogation. Figure 3.10 shows AFM data of two identical patterns milled into silicon a), and silica, b). They have been plotted with the same colour scale and justify the assertion that silica and silicon mill in very similar ways.

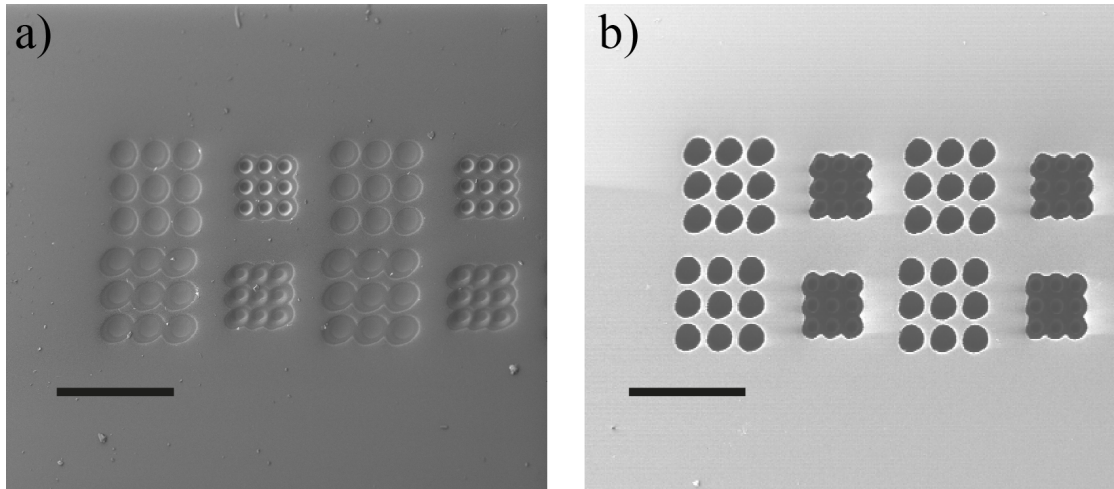


FIGURE 3.9: Identical features milled into silicon a), and silica b). Scale bar 50 μm .

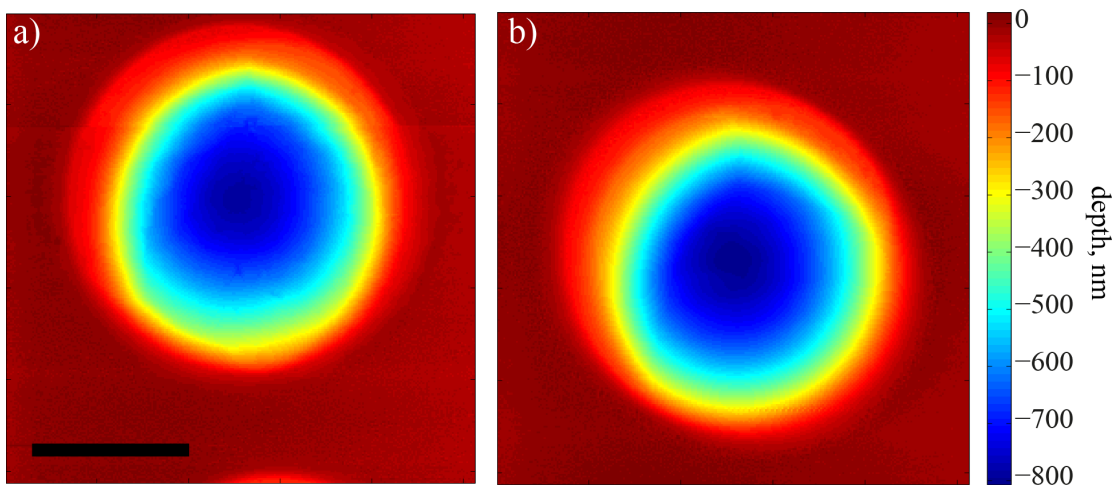


FIGURE 3.10: AFM topography of identical features milled into silicon a), and silica b). Scale bar 5 μm .

3.3 Atomic Force Microscopy

3.3.1 AFM Introduction

In order to most accurately analyse the topography of the features milled into the silica substrate, it was decided make use of the excellent vertical resolution of the atomic force microscope (AFM). An ‘AUTOPROBEcp’ AFM ran in contact mode was used for all of the measurements to be discussed in this section.

The most relevant information to be gained from this analysis is the root mean square (RMS) roughness of a surface, denoted (σ). This roughness relates to the maximum possible reflectivity of a dielectric stack through, equation 3.1.

$$R = e^{-(4\pi\sigma/\lambda)^2} \quad (3.1)$$

The AFM collects data by rastering a very sharp tip over a small region of the sample whilst measuring changes in height of the tip. It achieves its phenomenal vertical resolution by using a feedback loop between a vertical positioner and the deflection of a laser spot off the back of the tip. Figure 3.11 a) shows an optical image of the AFM tip in use, with the laser aligned to the back of the tip, with figure 3.11 b) showing an SEM image of the tips themselves. After each scan in the x direction the microscope proceeds

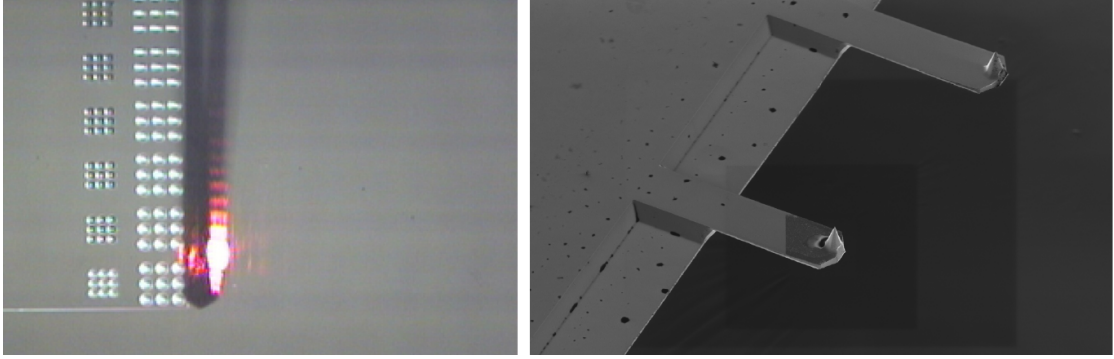


FIGURE 3.11: *Optical and SEM images of the AFM tips used in this project.*

to shift the tip in the y direction. This yields an array of data with the value of the element of the array giving the z height, and its position within the array containing the lateral (x, y) position:

$$Z_{m,n} = \begin{matrix} a_{1,1} & a_{1,2} & \cdots & a_{1,n} \\ a_{2,1} & a_{2,2} & \cdots & a_{2,n} \\ \vdots & \vdots & \ddots & \vdots \\ a_{m,1} & a_{m,2} & \cdots & a_{m,n} \end{matrix}$$

It was found that a degree of image reconstruction has to be performed on the raw data obtained from the AFM. This is due to the AFM data acquisition software redefining the location of the vertical (z) origin after every row scan. This means that a region similar to the one shown in figure 3.12 a) is read by the AFM to look like the mesh plotted in 3.12 b).

3.3.2 One dimensional curve fitting

Initially fits were performed in only one dimension, using a single line profile of the central micron of the feature. The results of this are shown in figure 3.13. According to these measurements values for sigma were consistently shown to be less than 1 nm, sometimes getting as low as 0.5 nm. This can be compared with the roughness of a similar scan on a single crystal of silicon, known to be approaching atomic flatness, which had measured values of $\sigma = 0.51$ nm. Anecdotally this particular AFM will never

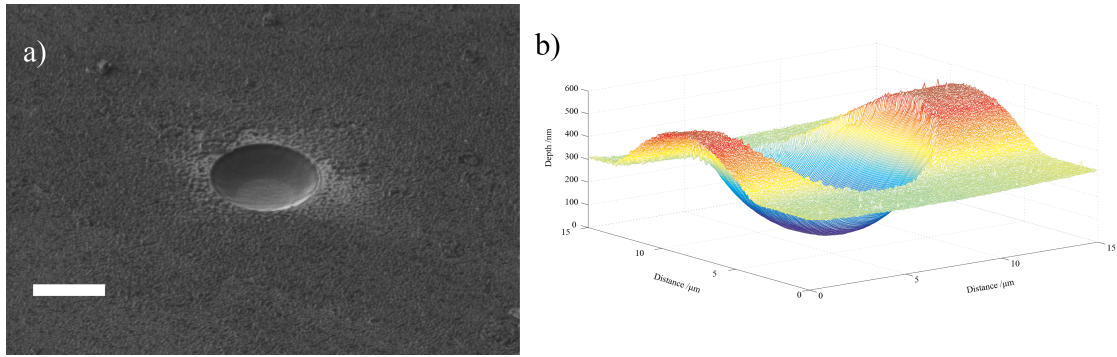


FIGURE 3.12: a) SEM image of a feature milled into silicon, scale bar $3\mu\text{m}$ and b) An AFM scan of a comparable area.

measure a surface to have less than 0.2 nm of roughness. This is likely to be due to a variety of factors including undamped vibrations and to a certain extent, lack of clean room environment.

To be accurate the values obtained for the hemispherical features are not so much actual roughness, but more the deviation away from the circular fit. This is worth appreciating, as it may be that the surface is extremely smooth, and so can accommodate very highly reflective mirror coatings, but is not of the right shape to set up the Hermite-Gauss modes commonly observed in macroscopic hemispherical cavities. This value must be minimised either way, in order to set up the high Q modes that are required to achieve reasonable Purcell Factors.

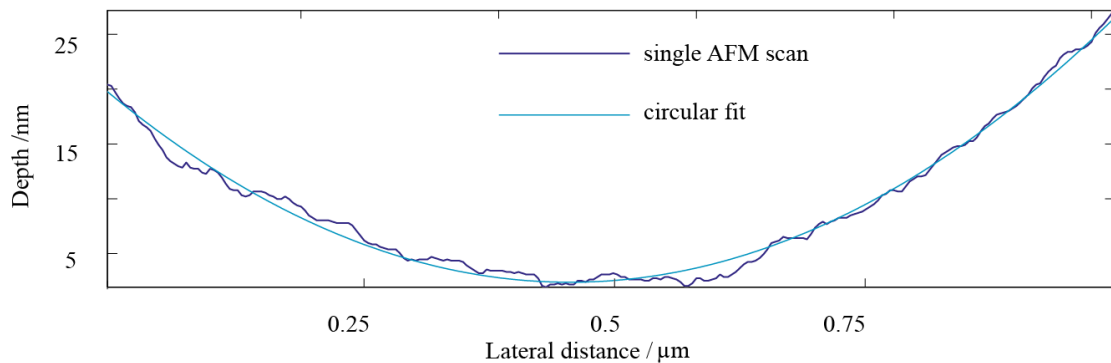


FIGURE 3.13: Single line profile of the central micrometer of a hemispherical cavity.

3.3.3 AFM Image reconstruction

Although the one dimensional curve fitting yields useful results, work has been carried out to develop this line of analysis in order to more effectively monitor the quality of the milling. This begins by digitally altering the AFM data that is acquired from the device software. It is assumed that the region around the feature is flat. This means

that the AFM is imparting an instrumental artifact in the y direction. With this in mind the profile of one of these ‘flat’ regions is isolated. It is presumed that this artifact is consistent across the entire extent of the row. Provided this is true, if this value can be determined or at least approximated by analysing part of the image, it can then be subtracted from the entire row, yielding a more representative set of values. For a single column this data can be thought of as being the sum of the unwanted

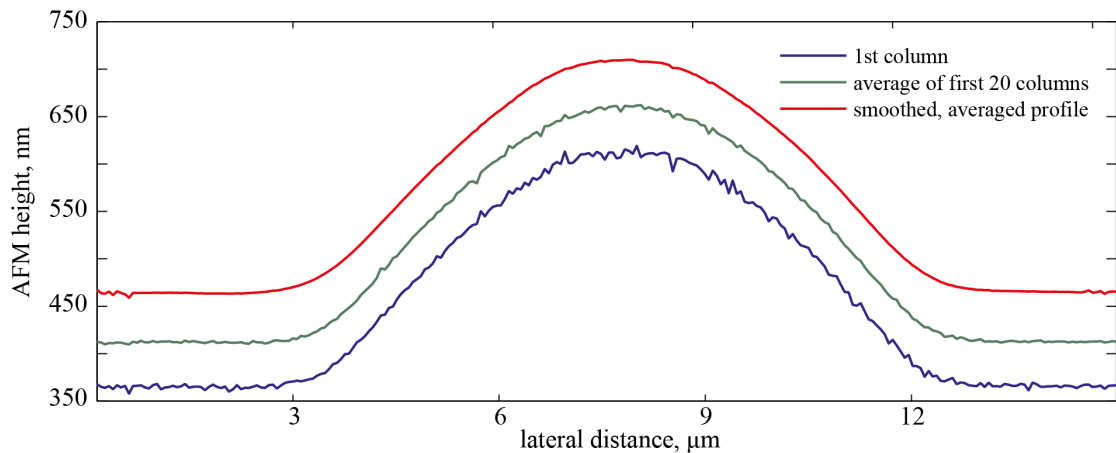


FIGURE 3.14: Blue - Single column of data depicted in figure 3.12b), Green - Average of first twenty columns from figure 3.12b), Red - Gaussian blur applied to an average of the first twenty columns.

artifact and the actual surface variation. It is expected that since according to SEM and optical evidence the region being considered appears flat, the actual surface variation will be smaller than the artifact. By averaging the measured surface in some way, it is hoped that this will wash out any local (i.e. actual) features and leave us with a set of values we can subtract from the entire image, without losing the high resolution surface topography. Figure 3.14 shows the effect of implementing two averaging methods. The first is to sum several columns and divide through by the number of columns summed. The effect of this averaging is plotted as the green line in figure 3.14 as a slight smoothing of the first plot, which is the raw data. The second step is to apply a Gaussian blur in the y direction by summing a central pixel with two or three above and below, and replacing that pixel’s value with that of the mean, and shows an additional smoothing affect on the third red plot in 3.14. Implementing both of these averaging schemes is straightforward within MATLAB. This new column vector, the third plot in figure 3.14 can then be subtracted horizontally from the entire image, to yield the much more realistic mesh plot shown in figure 3.15. This process of image analysis also removes any tilt in the y direction. The code written was also altered to remove any aberrations along the x direction. This complete process is shown in figure 3.16, on a larger 40 μm area scan demonstrating its apparent efficacy. Once this method of image reconstruction was developed, it allowed for several qualitative improvements to the milling sequence

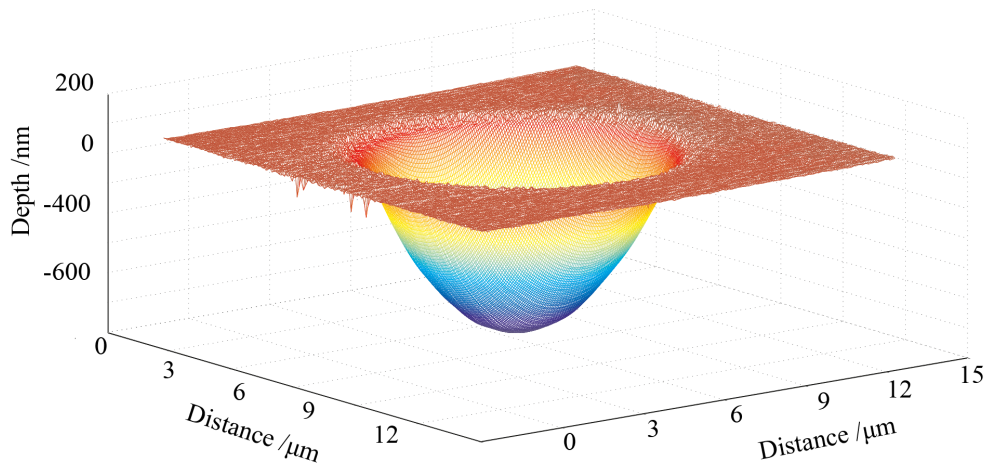


FIGURE 3.15: Mesh plot of AFM data shown in figure 3.12b) with artifact digitally removed.

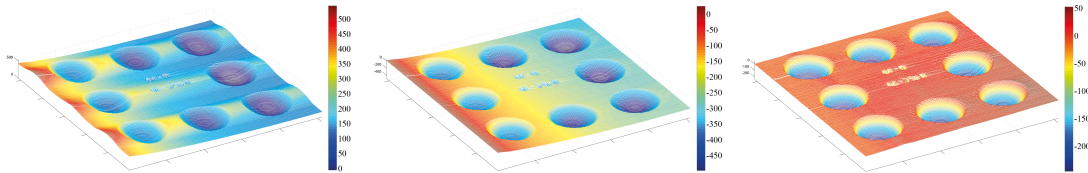


FIGURE 3.16: Complete removal of non-linear AFM tip response in x and ‘re-zeroing’ artifact in y .

to be made. For example image b) in figure 3.10 shows a good degree of asymmetry. This is likely to be due to a degree of redeposition occurring as the beam sweeps through the mill sequence. It was found that this could be minimised by lowering the number of loops the stream file performs. Any drop in this number has to be offset by increasing either the maximum dwell time or the beam current, in order to achieve features of the same radius of curvature. By optimising these parameters it was eventually possible to mill far more symmetric features. Figure 3.17 shows the result of this improvement, and was implemented on the second batch of microcavities that was sent to be coated.

3.3.4 Two dimensional surface fitting

Once this process was established it was possible to make use of the MATLAB coding environment’s surface fitting toolbox. The post-processed data can be fitted with a hemispherical function given in equation 3.2, for a hemisphere of radius r centred at x_0 , y_0 , z_0 .

$$z = z_0 + \sqrt{(r^2 - (x - x_0)^2 - (y - y_0)^2)} \quad (3.2)$$

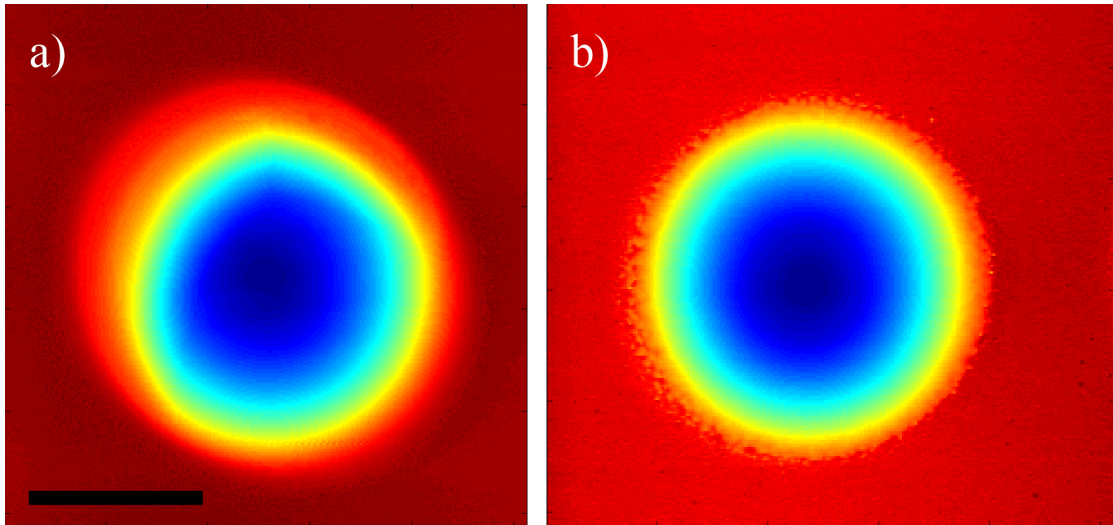


FIGURE 3.17: AFM topography of features before, a), and after, b), optimising mill parameters. Scale bar $5 \mu\text{m}$.

This surface fitting algorithm can be customised to extract a few of the most pertinent figures of merit for these surfaces, namely the radius of curvature of the sphere, and the RMS deviation from the fit. An example plot of the data with the best surface is shown in figure 3.18. It is straight forward to then plot the residuals of the fitted function,

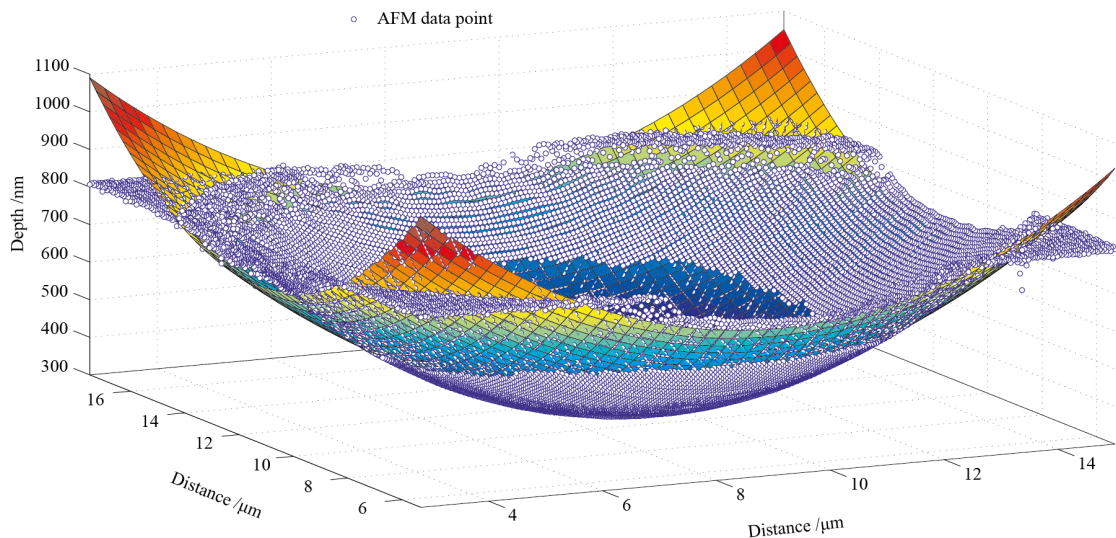


FIGURE 3.18: A surface fit of equation 3.2 to a complete set of AFM data.

shown in figure 3.19, which highlights the inadequacy of the surface fitting function at accommodating the planar substrate. By looking at the residuals it was possible to ascertain the effects of altering the milling current used. Figure 3.20 shows the residuals from milling identical stream files, but varying the beam current and number of pattern loops to maintain an overall constant ion dose. For example the first plot (furthest to the left) the pattern was milled in over 84 loops with a beam current of 500 pA . Overall this delivered 42 nC of charge but left undesirable ring like residuals close to the

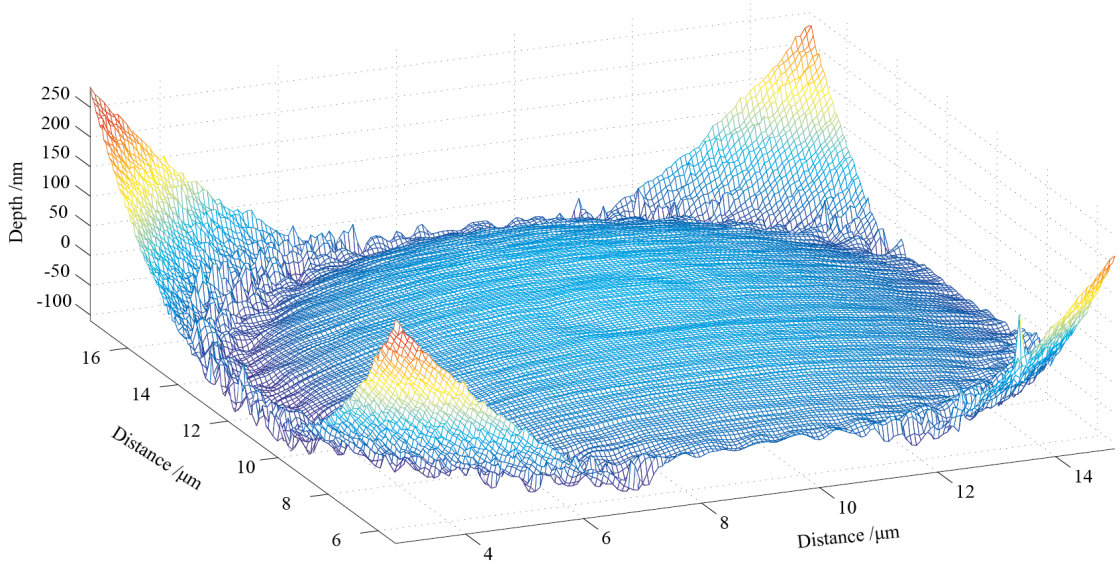


FIGURE 3.19: *The residuals from the fit performed in figure 3.18.*

centre of the feature. By increasing the beam current, and proportionally decreasing the number of loops (3000 pA with 14 loops, 7000 pA with 7 loops and 20,000 pA with 3 loops) the residuals can be directly compared, leading to the conclusion that higher beam currents and lower numbers of loops gives best looking residuals. At this stage it is

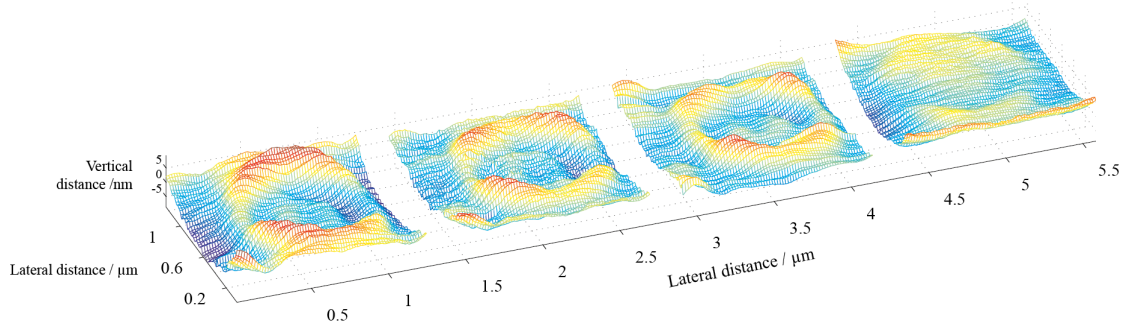


FIGURE 3.20: *Here increasing beam currents of 500, 3000, 7000 and 20000 pA (L to R) were used to mill in identical patterns.*

worth considering what portion of the feature is most important. As discussed in chapter 2, section 2.4.1, the mathematical description of a mode formed from solving Maxwell's equations for planar waves passing through a dielectric with spherical symmetry is reiterated here, in equation 3.3.

$$\mathcal{E}(r, z) = \mathcal{E}_0 \frac{w_0}{w(z)} \exp\left(\frac{-r^2}{w^2(z)}\right) \exp(-ikz - ik\frac{r^2}{2R(z)} + i\zeta(z)) \quad (3.3)$$

Gaussian modes have the property of cylindrical symmetry, and so (z, r) are the cylindrical coordinate axis. In addition w_0 is the minimum width of the beam, the 'beam waist' and $w(z)$ and $R(z)$ are the (z dependent) beam width and radius of curvature of

the beam respectively. The field maximum, at $(0, 0)$ is \mathcal{E}_0 , k is the wavenumber and $\zeta(z)$ is the Guoy phase shift. In this description the ‘beam width’ is defined as the width at which the field drops to a value of $1/e$ times its maximum (at that z coordinate), or when the intensity drops to $1/e^2$ of its maximum, and can be calculated in from the expression in equation 3.4.

$$w(z) = w_0 \sqrt{1 + \left(\frac{z}{z_R}\right)^2} \quad (3.4)$$

The features we are aiming to mill have an upper radius of curvature of around $25 \mu\text{m}$ with some getting as low as $5 \mu\text{m}$. Experimentally we would be keeping the cavity length short, in the range of $1 - 10 \mu\text{m}$. Plotted in figure 3.21 are the Gaussian modes formed from a $25 \mu\text{m}$ feature placed at $1 \mu\text{m}$ intervals from $1 - 10 \mu\text{m}$ (blue) and $5 \mu\text{m}$ radius of curvature feature placed at $0.5 \mu\text{m}$ intervals (red). These plots indicate that the majority of the field is only going to be distributed over the central $1 - 3 \mu\text{m}$. From these considerations it seems useful to sample the central region of the feature

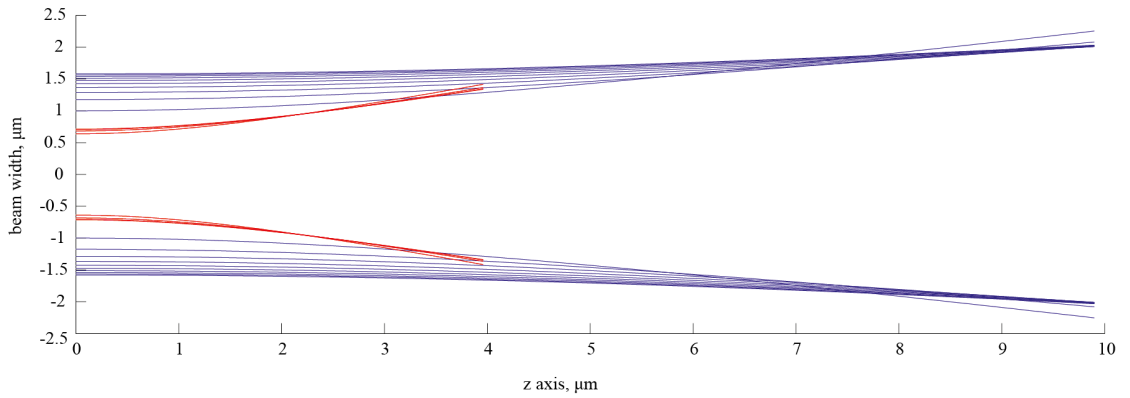


FIGURE 3.21: The beam widths of Gaussian modes with radii of curvature 25 (blue) and 5 (red) μm for a variety of cavity lengths.

and perform the fits to these data points. In this way we can also develop an idea of how good the features are as one increases the mode’s extent on the surface, so we can more accurately attribute the decrease in finesse at longer cavity lengths observed experimentally in the first batch of cavities.

To retrieve this information from the processed AFM data, one samples a small central region of the data and performs a surface fitting routine, extracting the radius of curvature of the surface, and also the RMS of the residuals. The sampled region is then expanded and a new fitting routine performed. Figure 3.22 shows how several square regions may be isolated within an image. Fits to these regions can then be calculated yielding values for the radius of curvature and the RMS deviation from the fit. Figure 3.23 shows two different radii of curvature measured using this method for two sets of nine cavities. This plot shows the amount of variation one can expect from identical mill routines, for each designated radius of curvature. Figure 3.24 shows the residual values

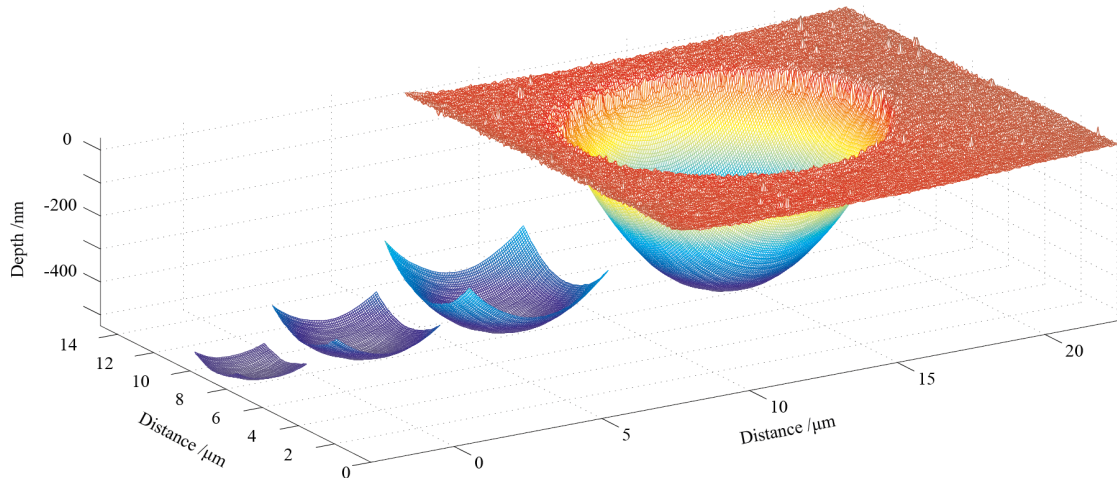
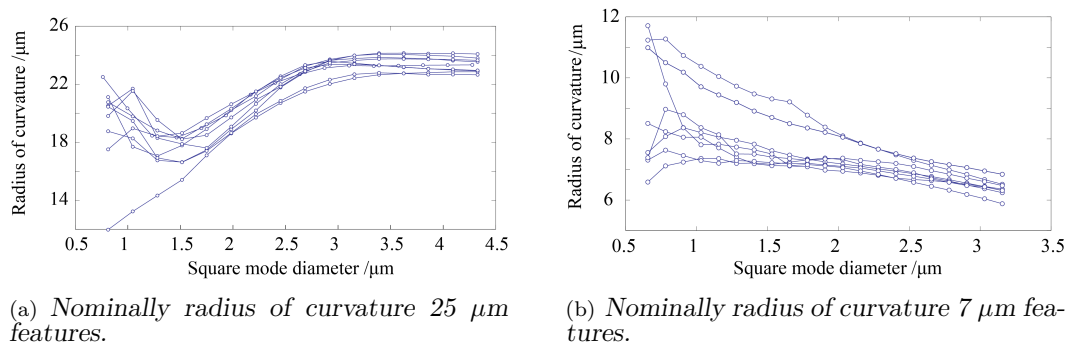


FIGURE 3.22: Mesh plot of a complete data set alongside three smaller samples of the same data.



(a) Nominally radius of curvature $25 \mu\text{m}$ features.

(b) Nominally radius of curvature $7 \mu\text{m}$ features.

FIGURE 3.23: Plots of the ‘square’ mode diameter (from sampling square regions of AFM data) against fitted surface radii of curvature for 9 identical cavities.

for a set of nine identical cavities. In all but one case these values are comfortably below 1 nm for the central region of the features. This is encouraging, setting a limit on the maximum reflectivities (according to equation 3.1) of ~ 0.9998 . Finally the impact of this full two dimensional surface analysis method can be seen in a comparison of the first and second iterations of the cavities. Data sets from the first iteration of features were subjected to the full 2D topographical analysis. Figure 3.25(a) shows data from the first and second iterations of features RMS residuals plotted as black outlines and filled red shapes respectively. This shows a greatly improved fidelity to the hemispherical shape as the sampled area is increased. In addition figure 3.25(b) shows that the consistency of the radius of curvature is also much improved by the further optimisation facilitated by the two dimensional analysis.

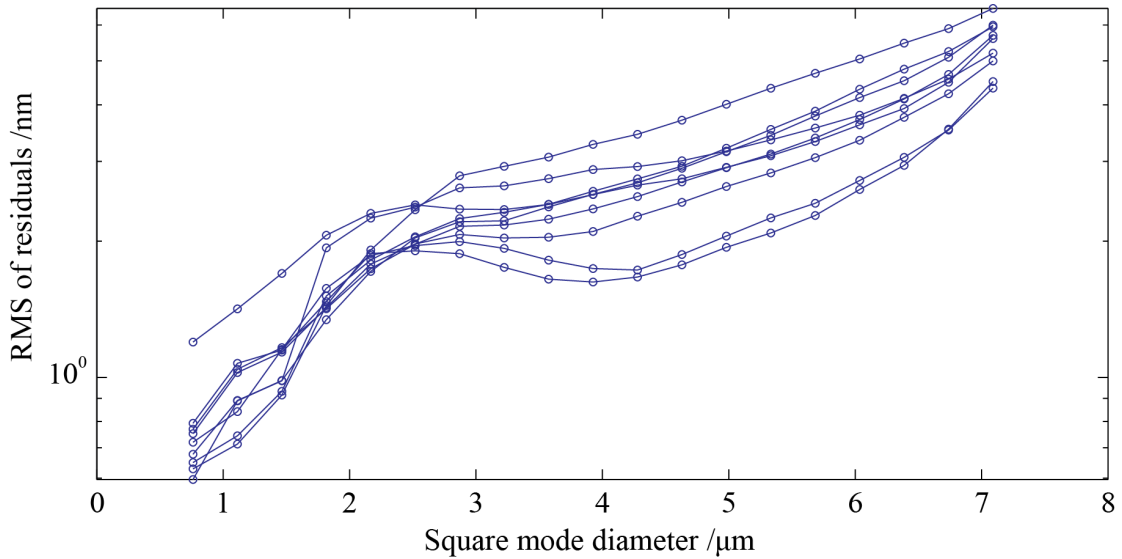
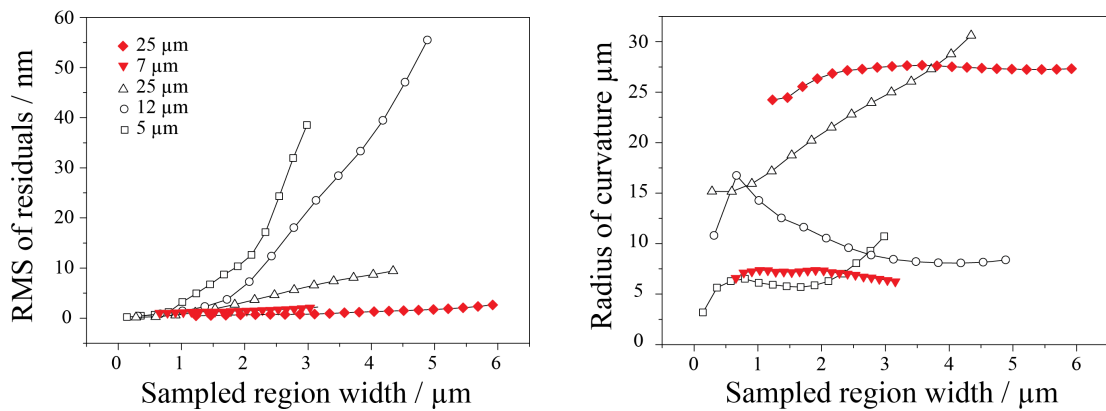


FIGURE 3.24: *Nine identical cavities showing almost all residuals < 1 nm for the central 1 μm of the feature.*



(a) *Comparison of the RMS residuals from the first and second iterations of the cavity features.*

(b) *Comparison of the radius of curvature from the first and second iterations of the cavity features.*

FIGURE 3.25: *Comparison of the most relevant metrics for the first (black outlined circles squares and triangles) and second (filled red diamonds and triangles) iteration of cavity features.*

3.4 Substrate Development

During characterisation of the first batch of cavities to be coated (see chapter 4), it became obvious that simply pressing the substrates together was insufficient to ensure that the very smallest cavity lengths be achieved. The substrates chosen for the first iteration were $5 \times 5 \times 1$ mm planar fused silica slabs, with arrays of features milled into the centre of one of the largest surfaces. It is thought that during optical characterisation, this relatively large redundant (features only covered $< 1 \text{ mm}^2$ of the 25 mm^2 substrate

surface) portion of the substrate prevented the substrates getting all the way down to the fundamental longitudinal mode. There are two candidate mechanisms for this, first that the edges of the substrate come into contact and the mounts and substrates can only be stressed a certain amount before motion ceases. The other was that relatively large pieces of dust settle on the planar regions of the substrate slightly away from the features, preventing the very shortest cavity lengths from being reached. The solution applied to mitigate these negative effects involved making use of a silicon dicer, which is essentially a circular saw with a fully automated, and very precise sample mounting system. This allowed us to reduce the thickness of large areas of substrate leaving the cavity features projecting up from the surface on a small plinth, whilst still allowing manual manipulation with tweezers. This development allowed for reduced cavity lengths to be achieved, as discussed in chapter 5. For the second iteration of microcavities this feature was engineered in from the outset, preparing substrates with arrays of plinths to be coated simultaneously. Figures 3.26 and 3.27 show these plinth structures with features of diameter $a = 10$ and $5 \mu\text{m}$, with radii of curvature $\beta = 25$ and $7 \mu\text{m}$ milled into the surface.

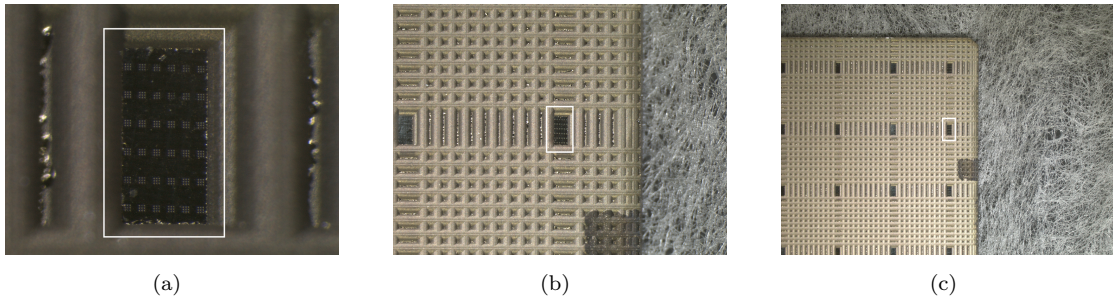


FIGURE 3.26: *Optical microscope images at various magnifications of cavity arrays milled into plinth like structures arrayed onto a single fused silica substrate. Each plinth is approximately $200 \mu\text{m} \times 600 \mu\text{m}$.*

3.5 Summary and Conclusions

This chapter set out to describe in detail the fabrication procedure used to construct the novel microcavities which are the topic of this thesis. This relied exclusively on the precise control of the focused ion beam to ablate the substrate in a highly controlled manner, whilst maintaining sub-nanometer RMS residuals. Programming routines were developed to digitally analyse the three dimensional data collected by an atomic force microscope which allowed for the optimisation of the FIB milling routines. In addition a system was developed to allow reduced cavity lengths to be achieved. Table 3.1 shows a summary of the cavities produced by the methods described above. In the subsequent

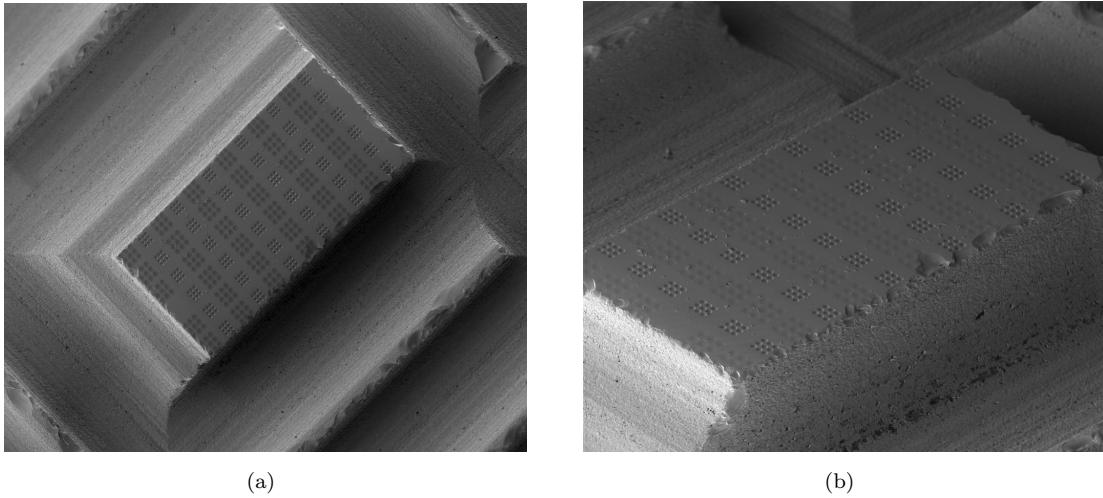


FIGURE 3.27: SEM images of the second iteration of features milled onto plinth like projections from a fused silica substrate which has been gold coated a second time to facilitate FIB imaging. As in figure 3.26 the plinths are approximately $200 \mu\text{m} \times 600 \mu\text{m}$ in size.

TABLE 3.1: Summary of the main characteristics of the cavities produced using FIB milling. Figures 3.25(b) and 3.25(a) depict their measured radii of curvature and RMS residuals.

Nominal RoC, β (μm)	Feature width, a (μm)	Reflective coating	Surface analysis	Sample surface area (mm^2)
25	8	10 pairs	1D	25
12	5	10 pairs	1D	25
5	3	10 pairs	1D	25
25	10	20 pairs	2D	0.24
7	5	20 pairs	2D	0.24

chapters the optical characterisation of the first iteration will be described, making use of white light transmission measurements. These cavities will also be used to couple to semiconductor nanocrystals at room temperature. Nanocrystal photoluminescence will also be used to perform a preliminary analysis of the second iteration of microcavities.

Chapter 4

Cavity Characterisation

4.1 Introduction

This chapter is the first of several presenting results obtained of an optical nature. In this chapter the optical characterisation of the first iteration of optical cavities will be discussed. These results formed the basis of a paper published in the journal *Optics Letters* [12]. This characterisation consists exclusively of white light transmission measurements, and there is no coupling to emitters at this stage.

4.2 Room Temperature Transmission Set-Up

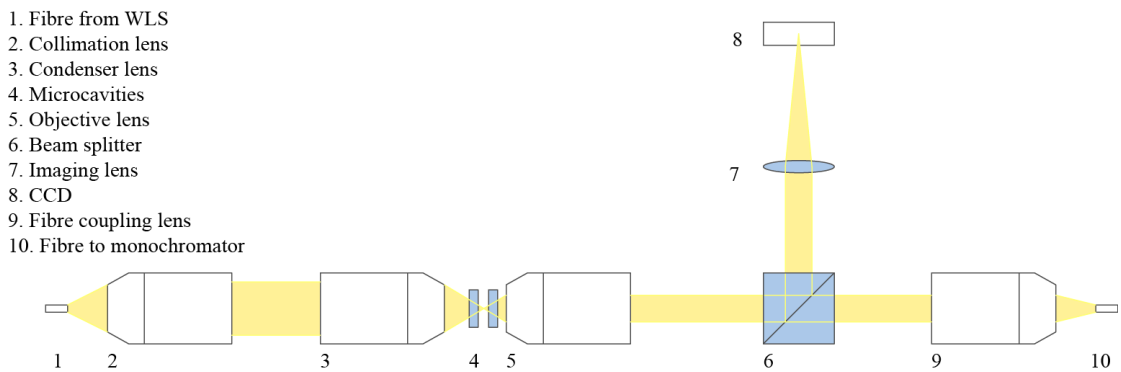


FIGURE 4.1: *Schematic of the bench top confocal microscope designed and constructed for interrogation of individual cavity modes.*

Initially a bench top confocal optical set-up, a schematic of which is shown in figure 4.1 was constructed. This set-up was designed allow a condenser lens to focus white light from a fibre coupled ‘Bentham WLS100’ white light source. The fibre core is effectively

imaged by the second microscope objective, labeled 3 in the figure. The size that is being illuminated is determined by the physical size of the input fibre core, and the ratio of the magnifications of lenses 2 and 3. Prior to coating the initial batch of cavities the transmission spectrum of a set of planar dielectric mirrors, with the wavelength of the maximum reflectivity chosen to be 637 nm was measured. These mirrors were made up of ten pairs of silica ($n_1 = 1.4$) and titania ($n_2 = 2.1$), with a final layer of $\lambda/2$ silica so that an anti-node of the cavity field is located on the mirror surface. Although this has implications on the minimum cavity length achievable it is a desirable feature since it was anticipated that surface contamination would be the main source of scattering losses and background luminescence. By ensuring that there is an anti-node on the surface these can be minimised. It should be noted that this also means we would expect very little Purcell enhancement from an emitter placed on this surface, effectively the final term incorporated in the complete Purcell equation in 2.19 would be close to zero. The peak reflectivity was designed to be at 637 nm as this is the location of the zero phonon line (ZPL) of the negatively charged nitrogen vacancy emission in diamond. The transmission spectrum, as recorded by an ‘Acton Instruments sp2500i’ imaged onto a liquid nitrogen cooled ‘Princeton Instruments Spec10:100B’ CCD is plotted in figure 4.2 in blue. Also plotted on the axis in red is the transmissivity as calculated by the transfer matrix discussed in chapter 2, section 2.3. This effectively shows what one would expect in an idealised situation. The explanation for this discrepancy could include the fact that the model assumes only normally incident light so any deviation from this, if the mirror is slightly out of the focal plane for example would result in a divergence from the theory. In addition any imperfections in the coating procedure would also contribute.

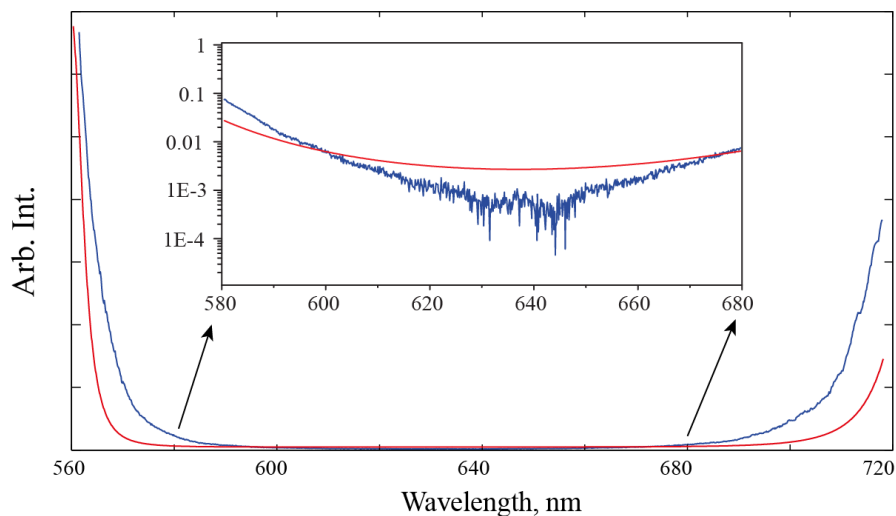


FIGURE 4.2: Transmission spectrum for a dielectric mirror consisting of 10 pairs of $\text{SiO}_2/\text{ZrO}_2$ capped with a final layer of $\lambda/2$ SiO_2 (blue). A one dimensional model of these mirrors based on the transfer matrix approach is also plotted (red). Inset shows central region plotted logarithmically.

4.3 Fabry-Pérot etalons

A pair of these (planar) mirrors were also arranged opposite one another to form a Fabry-Pérot etalon. This arrangement was afforded a cursory investigation whilst the featured substrates were in production. Transmission spectra for a selection of cavity lengths are plotted in 4.3. The lengths can be calculated by making use of equation

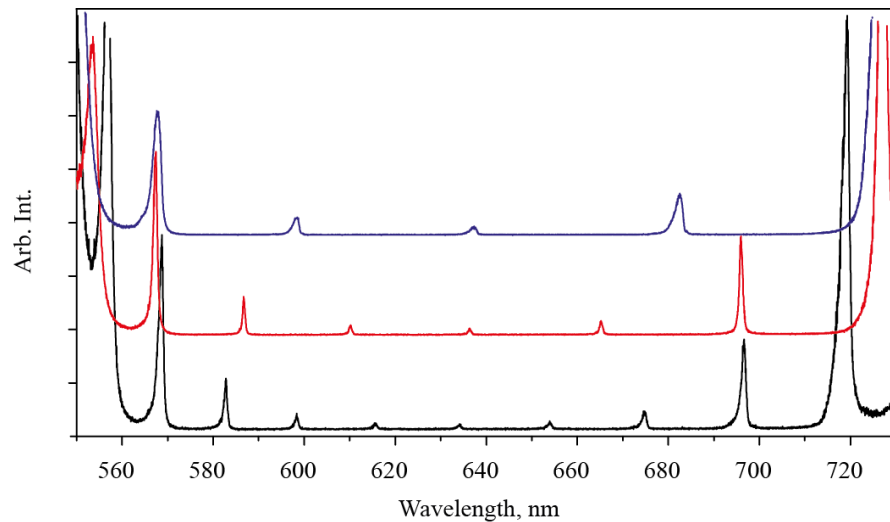


FIGURE 4.3: *Transmission spectra from a Fabry-Pérot etalon formed of two of the mirrors characterised above, for cavity lengths decreasing from black to red to blue. In each case a mode was settled close to 637 nm*

2.45. This method however has a shortcoming in that the FSR is different depending on whether it is measured to the next highest or lowest peak, yielding different lengths. For the shortest cavity which is the blue plot in figure 4.3, the average of these two values is $4.8 \mu\text{m}$. Figure 4.4 shows the shortest cavity length plotted with some results extracted from the transfer matrix method. The modeled plot here shows how the shortcoming mentioned above is rendered insignificant, as the cavity length used to generate the modeled data in figure 4.3, taking into account the extra layers of SiO_2 , is around a micrometer less than the value given by the equation. The root cause of the analytic expression's inaccuracy lies in the assumption that no field permeates within the mirror structure. Initially this discrepancy made the transfer matrix model vital to calculate the physical cavity length. At this point experiments moved on to look at the featured mirrors, which were coated in with DBR stacks almost identical to those used for these planar mirrors.

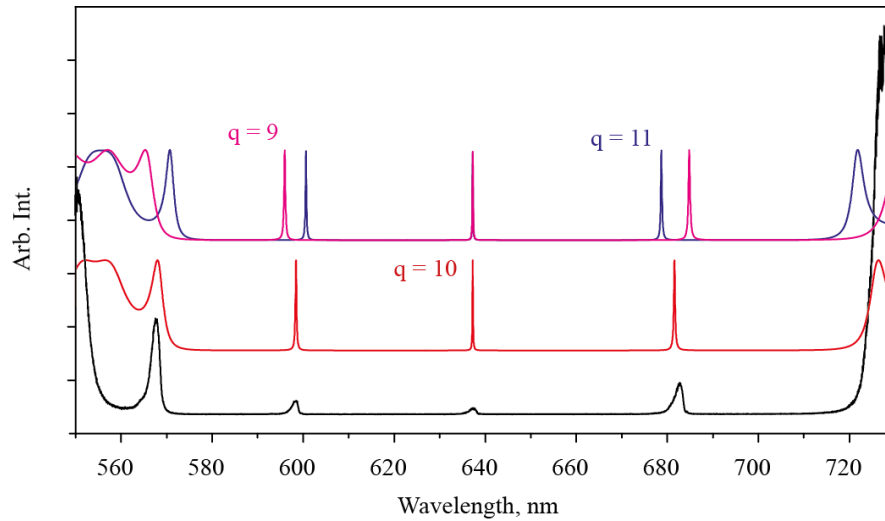


FIGURE 4.4: Transmission spectrum from the shortest cavity shown in figure 4.3 plotted with the results from a one dimensional transfer matrix model. The modeled data in red is for a cavity length of $10 \times \lambda/2$, or $q = 10$ using the labeling system of section 2.4, with the pink and blue plots above showing the cases where $q = 11, 9$ for $\lambda_q = 637 \text{ nm}$ for comparison.

4.4 Preliminary Microcavity Analysis

The preliminary investigation into the Fabry-Pérot etalons highlighted some of the details involved in mounting the cavities, with special consideration being given to sufficient degrees of freedom of motion whilst maintaining mechanical stability. In order to be tunable one mirror had to be decoupled from the other, but to maintain cavity stability the mechanical distance between the two mirrors had to be minimised. To achieve this end both mirrors were set up on a short cage rod system, one on a kinematic positioner, the other on a manual ‘z’ positioner. This is shown in more detail in figure 4.5, in an exploded diagram. This system allows for the mirrors to be made as parallel as possible to one another which is vital in order to achieve the shortest cavity lengths. This cage system is then attached to an $x - y - z$ manual positioner that allows the cavities to be moved around in all three dimensions with respect to the focused illumination. Manual actuators were used to provide a large range of motion, and micrometer positioning accuracy. Some backlash and drift was observed, but the detrimental effects this had on acquiring spectra was mitigated by allowing a short time for the cavity length to stabilise. Alignment was also aided by initially using a large core, multimode fibre optic to couple light in. These large core fibres put in sufficient light to be visible to the naked eye and allowed initial ‘rough’ alignment to take place. The multimode fibres were then swapped out for single mode fibres, to allow single cavities to be illuminated. Images of the focused spots from multimode and single mode fibres are shown in figure 4.6, clearly showing that multimode fibres would illuminate multiple cavities simultaneously. Once

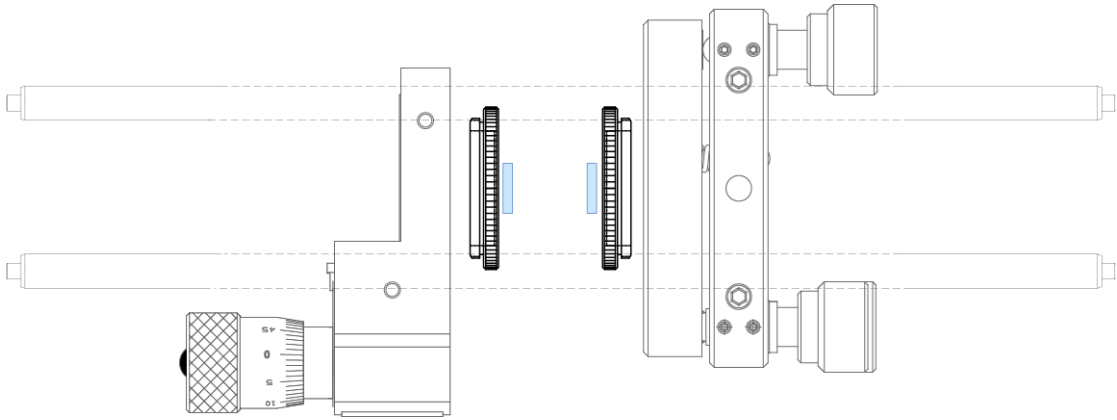


FIGURE 4.5: Exploded view showing the arrangement of the substrates and manual actuators on a cage rod set-up.

the light is focused into the cavity, transmitted light is collected by a second microscope objective. The collimated beam of transmitted light is then split, with the larger portion (70%) being coupled back into a fibre, and the smaller portion imaged onto a webcam CCD. Having the imaging was vital for alignment purposes. As previously, the light that is focused back into a fibre goes on to be coupled into the monochromator which has three modes, an imaging mode, a low resolution large range diffraction grating (500 blazes per millimetre) and a high resolution small spectral range grating (1200 blazes per millimetre). The monochromator/CCD combined device is used throughout the rest of this thesis to obtain all the included spectral information and will be referred to as the ‘spectrometer’ from here on in. The first batch of microcavities were designed to have

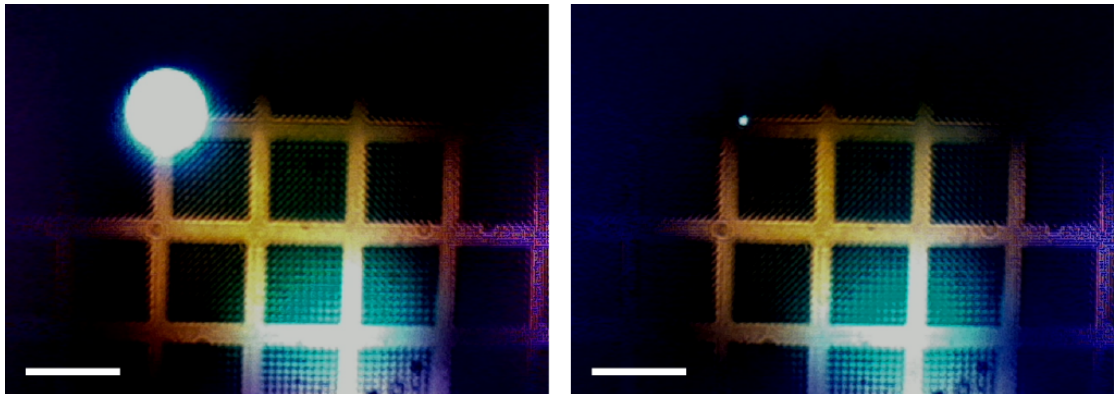


FIGURE 4.6: Images of illumination spots generated by multimode and single mode fibres. In order to see the cavity arrays diffuse white light was coupled into the setup between lens 9 and fibre coupler 10 on the optical schematic shown in figure 4.1. Scale bar 50 μm .

three nominal radii of curvature, denoted β . These were milled into the central region (approximately 1 mm²) of a 5 × 5 × 0.5 mm slab of fused silica. Fused silica was the material of choice to minimise unwanted fluorescence when the time came to perform PL studies. The first set experimentally investigated were the largest in both feature width

($a = 8 \mu\text{m}$) and nominal radius of curvature ($\beta = 25 \mu\text{m}$). These cavities were therefore predicted to be the easiest to achieve stable cavity modes in recalling the discussion in chapter 2 section 2.4.1 about the criteria for a stable Gaussian mode being that the feature diameter a must be large compared to the beam width, and the cavity length L must be less than the radius of curvature. Immediately the cavity modes from these features stood out much better than the modes obtained from the Fabry-Pérot etalons with an example for a long cavity transmission spectrum given in figure 4.7. The one

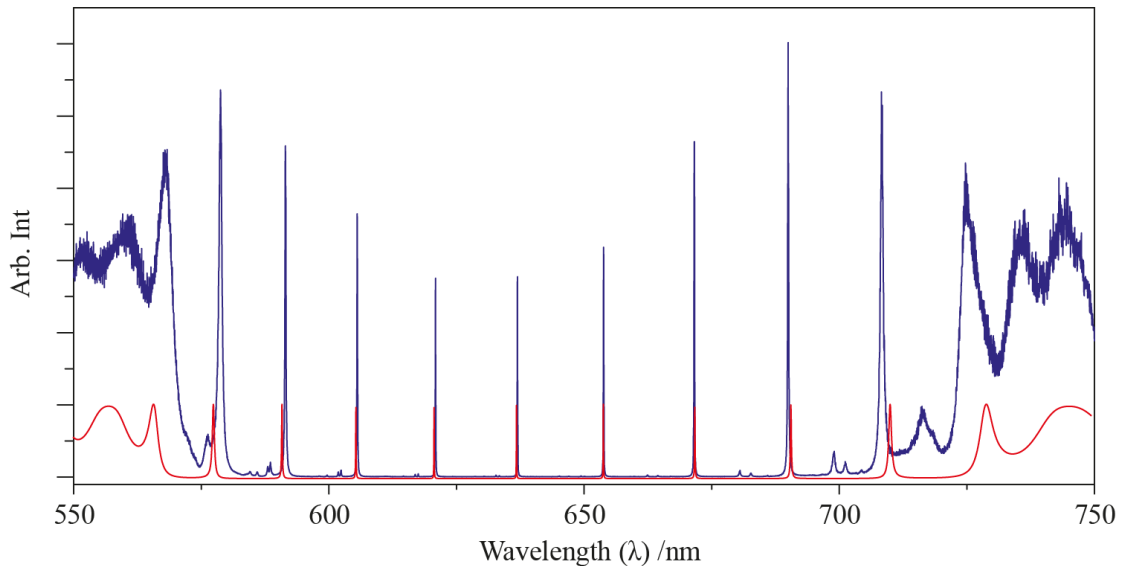


FIGURE 4.7: *Transmission spectrum from a relatively long cavity with RoC nominally $25 \mu\text{m}$ in blue. The red plot is given by an appropriate transfer matrix model with cavity length of $10.05 \mu\text{m}$, or a longitudinal mode of $q = 33$.*

dimensional transfer model still shows reasonably good agreement which is probably due to the corrective term included in equation 2.56, which accounts for the blue shift of the resonances due to the confinement coming from the radius of curvature of the mirror, being quite small compared to the longitudinal mode number. One thing that is missing from the experimental data in figure 4.7 is a strong sign of the transverse modes discussed in section 2.4.2 (see figure 2.24). During the alignment procedure care was taken with the CCD to ensure that the single mode white light spot was illuminating the centre of the feature, as shown in figure 4.8. If the cavities are slightly shifted so that the illumination is now off centre, we see that it is indeed possible to explore these lateral modes with this transmission set up (figure 4.9). Analysis of these lateral modes will prove to be a fruitful characterisation approach for the cavities, however before these are explored in more detail, a thorough investigation into the length dependence of the primary longitudinal TEM_{00} modes will be carried out.

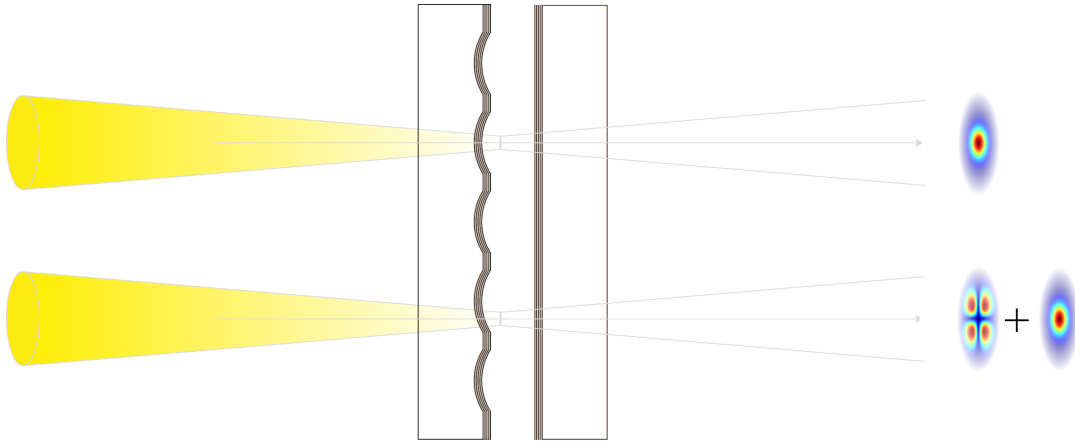


FIGURE 4.8: Diagram showing that when aligned to the centre of the cavity, white light illumination excites only the TEM_{00} mode (upper). Upon mis-alignment towards the edge of the feature, higher order lateral modes are excited by the illumination (lower).

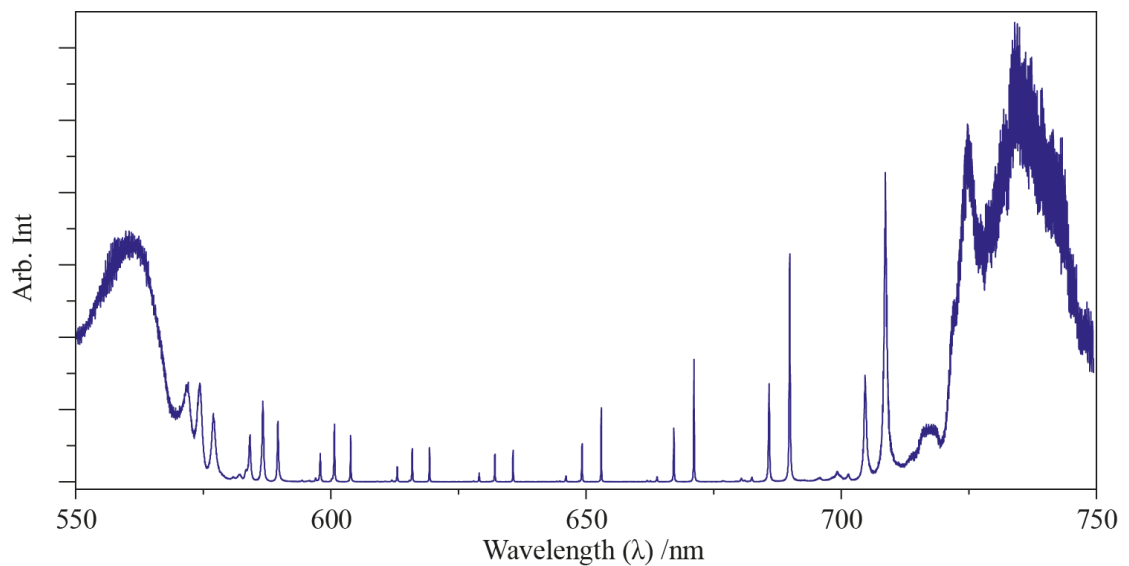


FIGURE 4.9: Spectrum obtained for a cavity with length almost identical to that of figure 4.7, however now the spot has been misaligned towards the edge of the feature, allowing increased coupling of light into the transverse modes.

4.5 Length Dependent Measurements

The first complete data sets obtained whilst characterising the first iteration of these microcavities were the length dependencies of several of the figures of merit. These were obtained by changing the length of the cavity so that sequential modes occurred at (or as close to as possible) 637 nm. This required cavity length decreases in steps of around 318 nm with a manual actuator, with nanometer precision. Realistically the only way that this was possible is hypothesised to be because the substrates were already in contact at their edges, and so the actuators were delivering small changes of pressure, bending or straining the substrates in some way. This had several positive

effects, the first (as suggested above) being a level of accuracy that surpasses the manual actuator manufacturer's claims by several orders of magnitude. It also minimised drift to a large extent, although it did not remove it entirely. In fact it was this contact between the substrates which largely determined what the maximum achievable cavity length was for the largest cavities, as once the substrates were backed off sufficiently so that they were no longer in contact the spectral resonances would drift at rates which made settling a mode at 637 nm rather difficult. Figure 4.10 shows the spectra taken from some of the longer stable cavities with the top spectrum being the longest. Here the mirrors were clearly in contact and it was possible to consistently tune each consecutive mode to resonance at 637 nm. The data set can then be labeled accurately

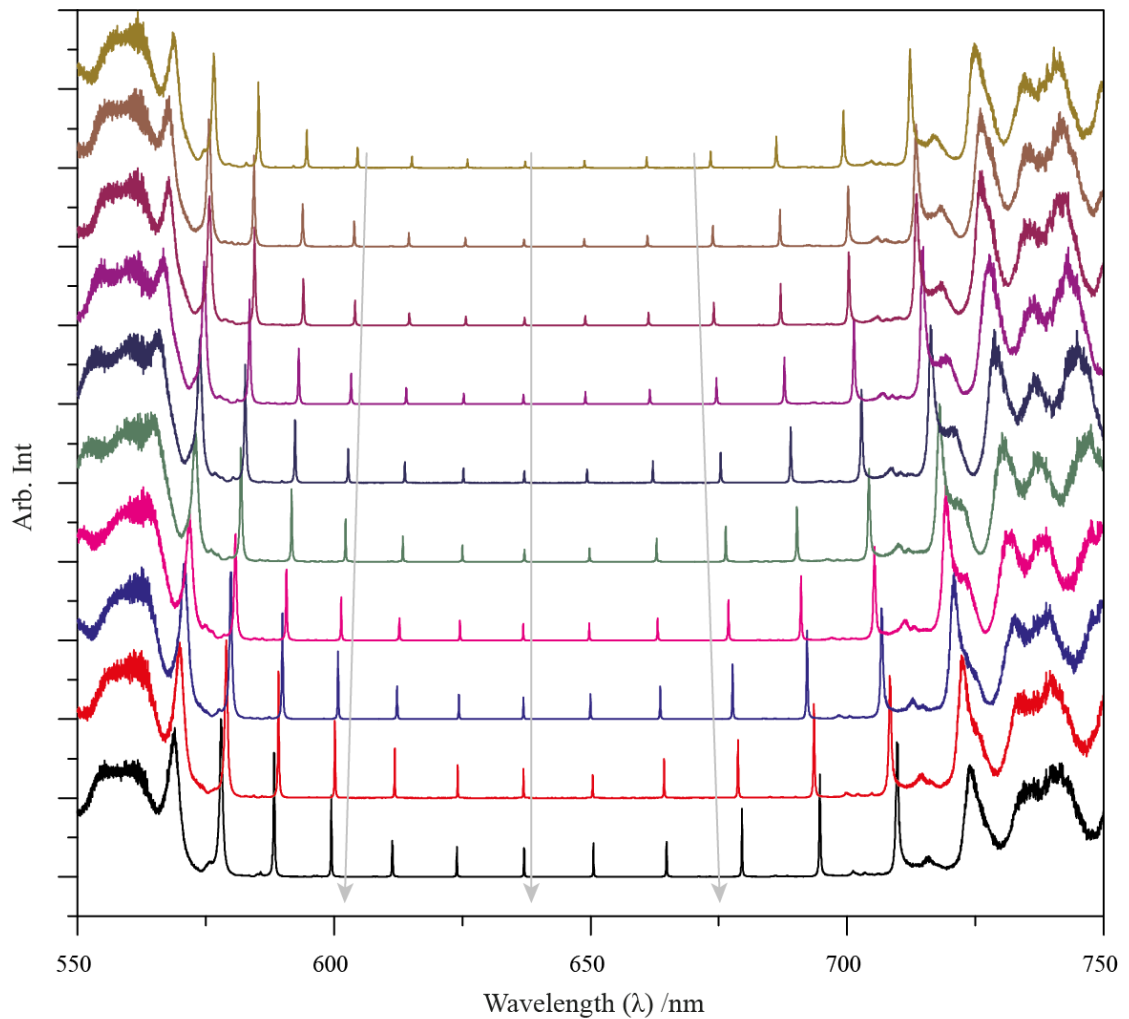


FIGURE 4.10: A series of 10 spectra stacked with the longest cavity length at the top. In the uppermost spectrum the mode at approximately 637 nm (closest to the central grey arrow) corresponds to the 43rd longitudinal mode and a cavity length of $13.378 \mu\text{m}$. Each spectrum below was acquired after $\approx 318 \text{ nm}$ decrease in cavity length, so that the longitudinal modes situated at 637 nm correspond to the 42nd, 41st, 40th, ... 34th longitudinal mode.

by the longitudinal mode number, q where the first mode in the sequence is $q = N$,

the second being $q = N - 1$ and so on. As the transfer matrix modeling approach is most accurate for the longest cavity the value of N can be obtained by matching the transmission spectrum outputted by the model to the longest cavity shown in figure 4.10. This is rather indulgently plotted in figure 4.11 despite its similarity to figure 4.7 due to the striking agreement between this simple model and experiment supporting the assertion that the transfer matrix is more accurate for the higher q cavities. The model gives us the information that this is the forty second mode, with the separation of the mirrors being within a nanometer or two of $13.378 \mu\text{m}$. These sequences of

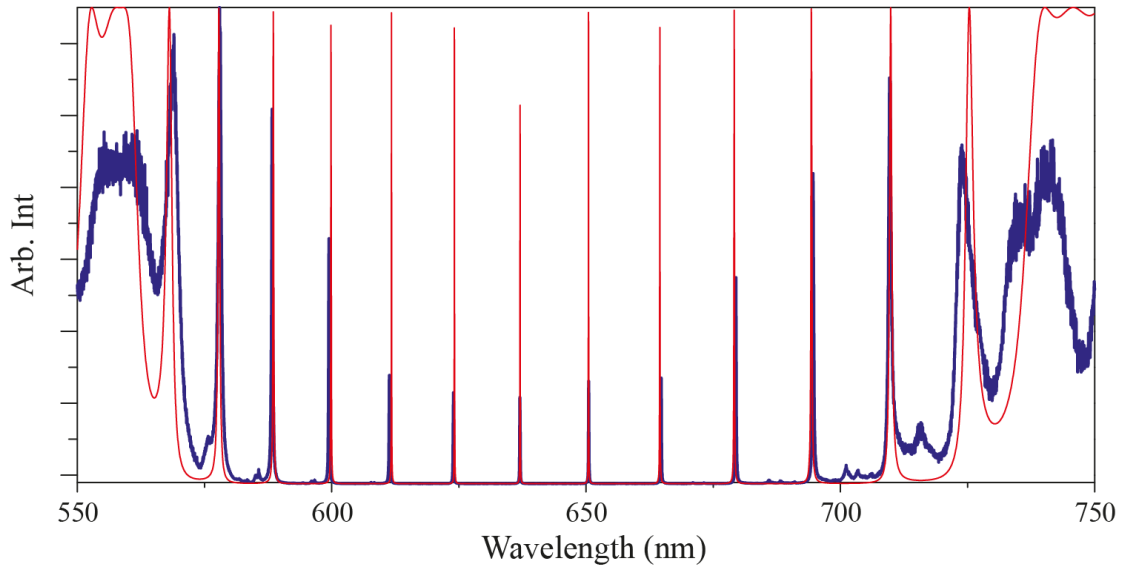


FIGURE 4.11: *Transfer matrix model of transmission spectrum for the 42nd mode, plotted with the experimental data showing good agreement.*

mode steps were carried on until spectrally the modes were no longer moving to shorter wavelengths despite action on the actuator. Specifically the modes would momentarily shift to slightly shorter wavelengths, but promptly relax to the same point. It seemed unwise to exert too much pressure on the silica substrates, and so the sequence was terminated at this point. Figure 4.12 shows the final thirteen spectra taken. Since the entire sequence was taken without break, the longitudinal mode could be assigned simply by keeping track of how many modes were stepped through. The transfer matrix adds credence to the conclusion that it is the fifth longitudinal mode that is reached, which corresponds to a physical gap of $1.593 \mu\text{m}$. Similar sequences were obtained for cavities with (nominal) values for $\beta = 12$ & $5 \mu\text{m}$ and $a = 5$ & $3 \mu\text{m}$ respectively although the sequences were necessarily shorter as the condition that the cavity length be shorter than the radius of curvature curtails the formation of stable cavity modes earlier for smaller RoCs. The final spectra for all three of the shortest cavities are plotted in figure 4.13. In order to obtain the mode volume from this information we will require analysis of the transverse modes, to establish the radii of curvature of the mirrors with more

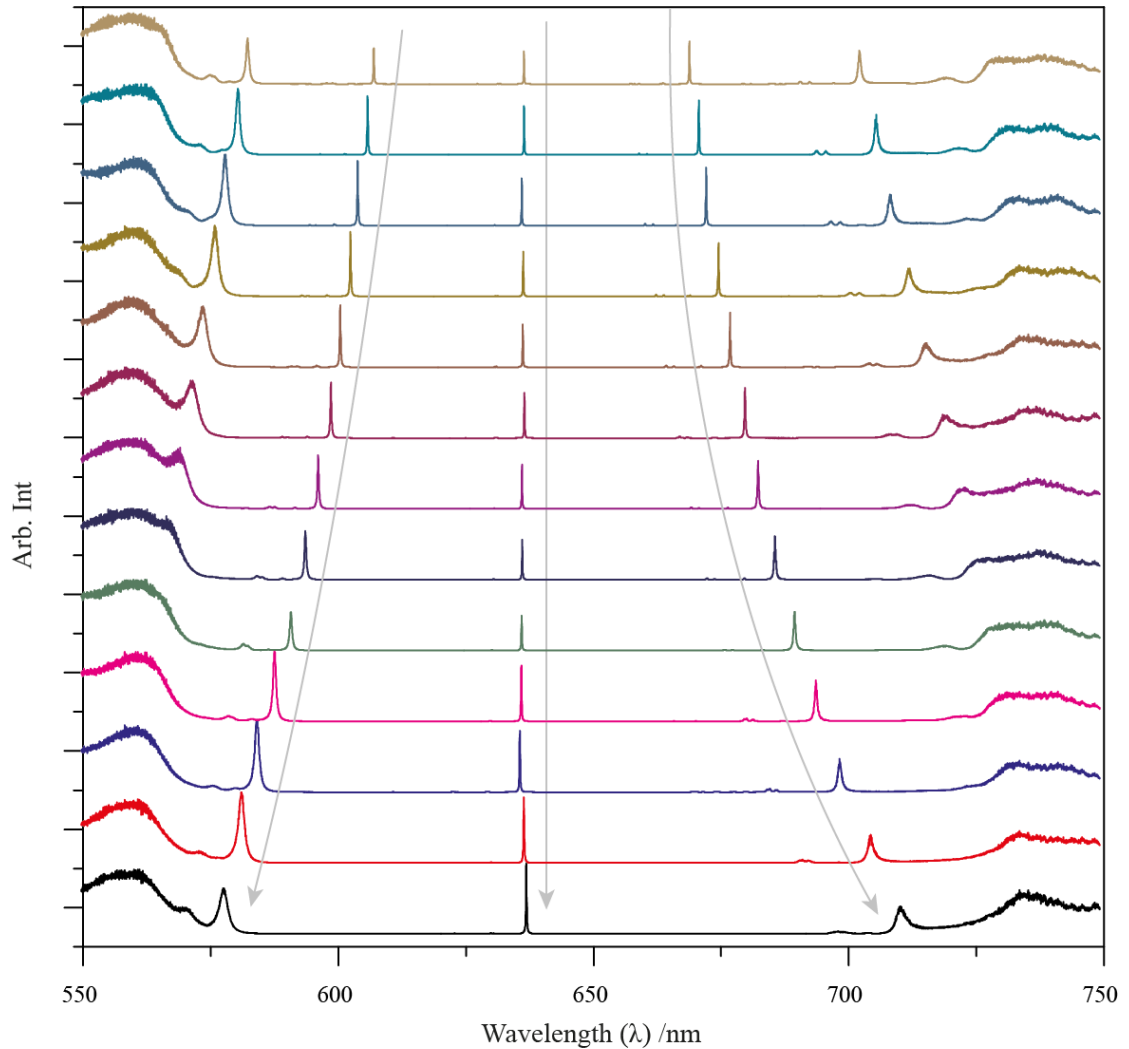


FIGURE 4.12: A similar set of spectra as those shown in figure 4.10. In the uppermost spectrum the mode closest to 637 nm is the 17th longitudinal mode of the cavity. Each spectrum below is taken after a reduction in cavity length of ≈ 318 nm so that the 16th, 15th, ... 5th longitudinal mode is situated at 637 nm. The very shortest of these cavities (the lowermost spectrum) corresponds to a gap between the mirrors of around $1.593 \mu\text{m}$ or with single distinct mode with longitudinal number $q = 5$.

certainty. Before we proceed with this some more useful information may be gathered from analysis of the cavity metrics, specifically the cavity Q factor and the finesse, \mathcal{F} . As discussed in section 2.3, both Q and \mathcal{F} can be easily obtained from the spectra. For absolute transparency, when using the free spectral range to calculate the finesse the average of the spectral distance to the next highest, and the next lowest was used. The Q factor was found by fitting the data points with Lorentzian line shapes and using the FWHM of the fitted curve. It was noticed that this was in fact getting close to the spectrometer's resolution limit of 0.05 nm, obtained by coupling an attenuated laser directly into the spectrometer. This meant that a deconvolution with the spectral response (a *sinc* function) of the spectrograph was performed on the very narrowest line

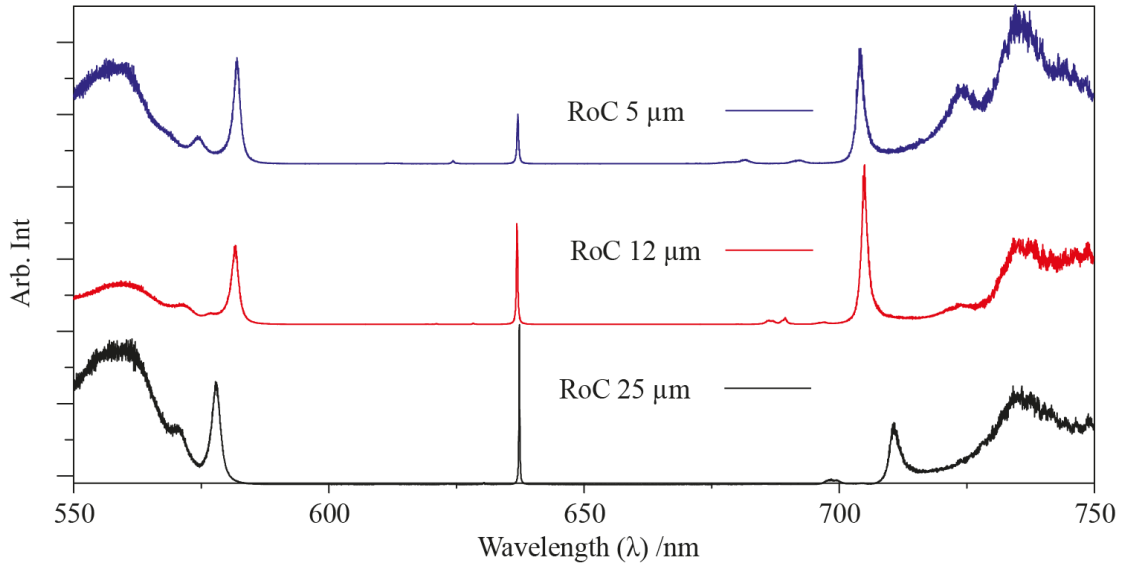


FIGURE 4.13: *The spectra of the shortest cavities for all three cavity types investigated. The uppermost plot (blue) shows the transmission spectrum for the smallest (nominal) $\beta = 5 \mu\text{m}$ cavities, the red is the intermediate $\beta = 12 \mu\text{m}$ with the black is a re-plot of the lowermost curve in figure 4.12, with $\beta = 25 \mu\text{m}$.*

widths, to yield the final results. As mentioned, the Q factors are obtained by fitting a Lorentzian curve to the obtained data. Figure 4.14 shows the data and the fit for the highest Q factor cavity. This corresponds to a Q factor of ~ 14000 . In addition the

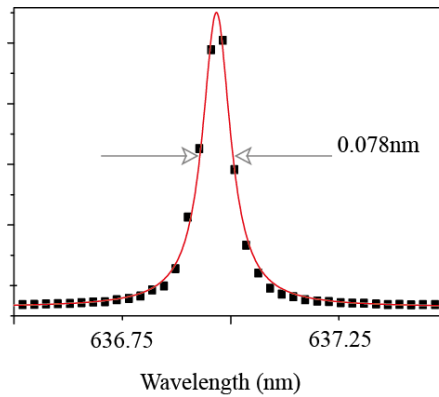


FIGURE 4.14: *A high resolution spectrum of the narrowest cavity mode measured (black squares) with a Lorentzian function fitted yielding a Q factor of 14000.*

length, (L) of the cavities used to calculate the mode volume has been increased by an addition of amount equal to λ , to include the field inside the mirror's contribution to the mode volume. This value is very much an estimate at this stage, but we will see how it can be determined with more accuracy in subsequent chapters. Figure 4.15 shows plots of finesse and Q against cavity length. Here the black circles are the largest cavities ($a = 8 \mu\text{m}$, nominally $\beta = 25 \mu\text{m}$), the red squares are an intermediate size ($a = 5 \mu\text{m}$, nominally $\beta = 12 \mu\text{m}$) and the blue triangles are the smallest ($a = 3 \mu\text{m}$, nominally

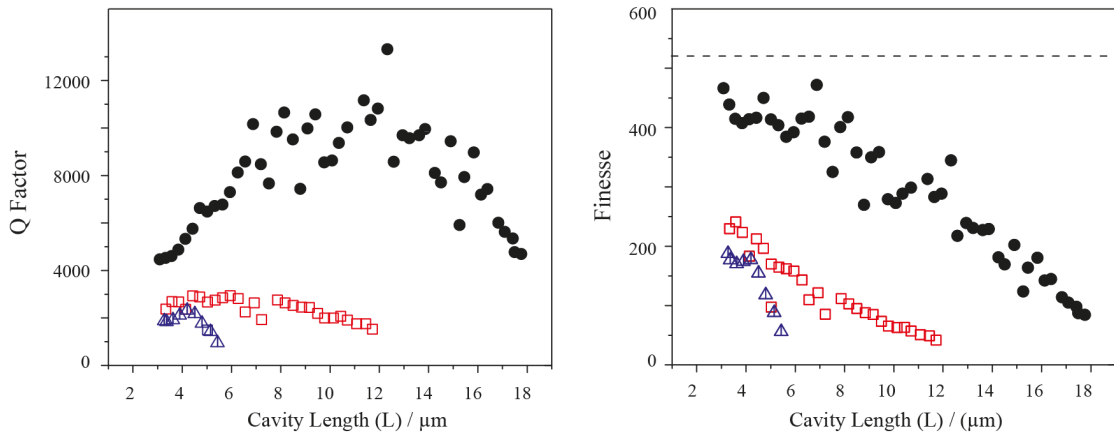


FIGURE 4.15: *The finesse and Q factors for every mode at 637 nm in sequences running from the shortest possible cavity to the point at which the cavity becomes too long to support stable modes (for the $\beta = 5 \mu\text{m}$ blue triangles, and $\beta = 12 \mu\text{m}$ red squares) or when drift prohibited alignment (for $\beta = 25 \mu\text{m}$ black disks).*

$\beta = 5 \mu\text{m}$). At first glance the apparent instability of each of these cavities is fairly close to their nominal radii of curvature, at least for the smaller two. As an experimental detail whilst for the smallest two cavity sizes the modes simply faded out (the resonant peaks lost all contrast), for the largest radius of curvature design it was the occurrence of excessive drift which prohibited further spectra being taken. From the discussion in section 2.3 one would expect the Q factor to have a linear increase right up to the instability limit of the cavity length, and the finesse for all three of the mirrors should be constantly just about 520 shown by the dotted line. Clearly this is not the case. All three cavity types do show at least some linear increase with cavity length initially, but this seems to be overridden by other factors as the length increases. One explanation for this can be seen from considering the size of the beam width for Gaussian beams with similar properties specifically the beam width on the second, featured mirror. This dependence is plotted for beam waists normalised to the same initial size in figure 4.16, and since one would expect the Q to drop with increased width, it is the numerical inverse ($1/w$) which is actually plotted on the y axis. The point to draw attention to is that the size of the beam width at the curved interface increases more rapidly for Gaussian modes with smaller radii of curvature. This supports the association of the decreasing finesse, and also Q, with an increase in the beam waist on the featured mirror. This suggests then that whilst the beam waist is small on the featured mirror it is spherical enough to accommodate high Q factors, but it deviates away from sphericity as the beam size increases. This conclusion was supported by AFM data once the more thorough two dimensional analysis was brought to bear upon the data, recalling figure 3.24 and the increase in rms roughness as the size of the sampled region is increased. We will now consider the transverse modes that, as mentioned above and is shown in figure 4.8 can be excited by mis-aligning the white light illumination with respect to

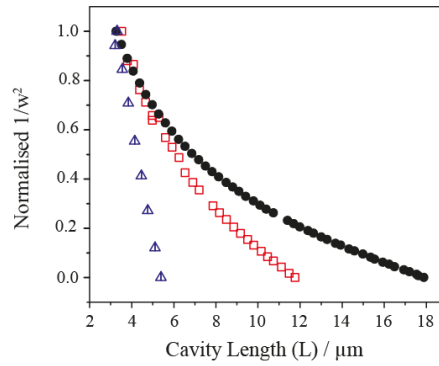


FIGURE 4.16: *The normalised numerical inverse of the mode width on the featured mirror, plotted against cavity length. The feature of note is the relative decreases in value for the three radii of curvature, suggestive of the role this plays in the drop in finesse shown in figure 4.15.*

the emitter. By making use of the cavity lengths which are obtained by matching the cavity spectrum with that of the transfer matrix model, we can extract values for the radius of curvature for any particular spectrum, where the transverse modes are visible. Figure 4.17 shows Lorentzian curves plotted at the locations given by equation 2.62 for a cavity with a radius of curvature of around $45 \mu\text{m}$. From this figure we can see that the

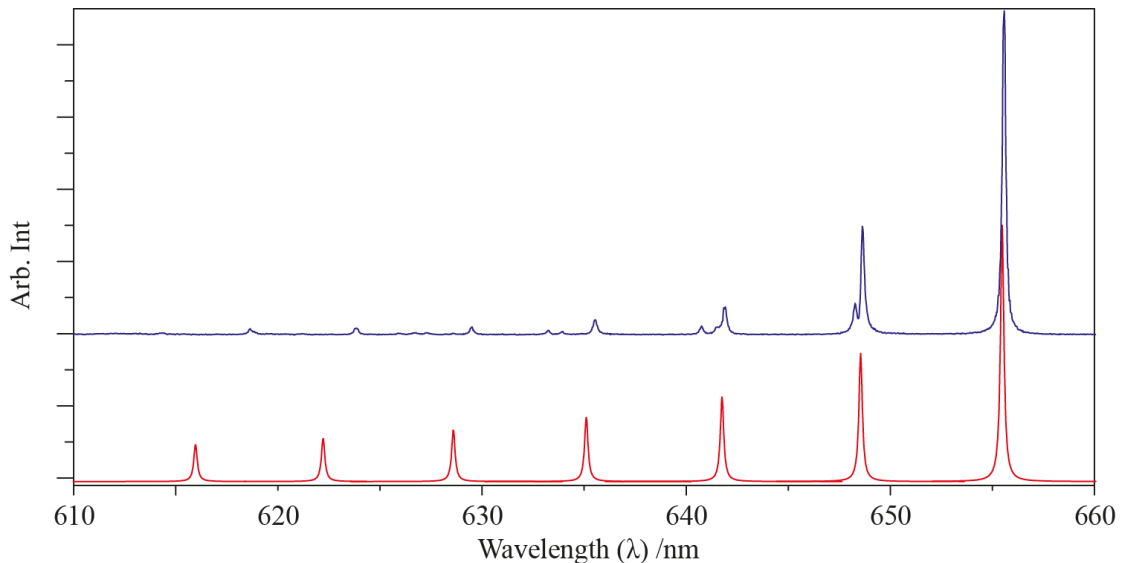


FIGURE 4.17: *Plots of several higher order transverse modes once the cavities have been mis-aligned with respect to the illumination (blue), and the locations of the modes predicted by equation 2.62.*

highest order modes do not line up with the modelled positions, whilst the lower order transverse modes agree quite well. This is likely to be because, since the higher order the mode the larger its lateral extent (see figures 2.23 and 2.23), the radius of curvature of the feature is not constant and that as the beam waist extends further across the feature it experiences a different amount of lateral confinement. Also several features examined

showed visible splitting of the first order ($n + m = 1$) transverse modes, as shown in figure 4.18. Although it was mentioned in section 2.4.2 that there are a couple of ways that these higher order modes can be formed, this degeneracy is most likely to be due to slightly elliptical cavities. This would suggest that we are in fact dealing with the Hermite-Gauss flavour of transverse modes, as the major and minor axis of the ellipse cast the problem into Cartesian coordinates quite naturally, breaking the radial and azimuthal symmetry of the Laguerre-Gauss modes. Although not the most complete justification experiments conducted in subsequent chapters will investigate this splitting in more detail. As it stands, by fitting two different radii of curvature to the mode positions it was found that in some cases there was up to 20% difference in the radii of curvature for the two orthogonal directions. The radii of curvature for data series

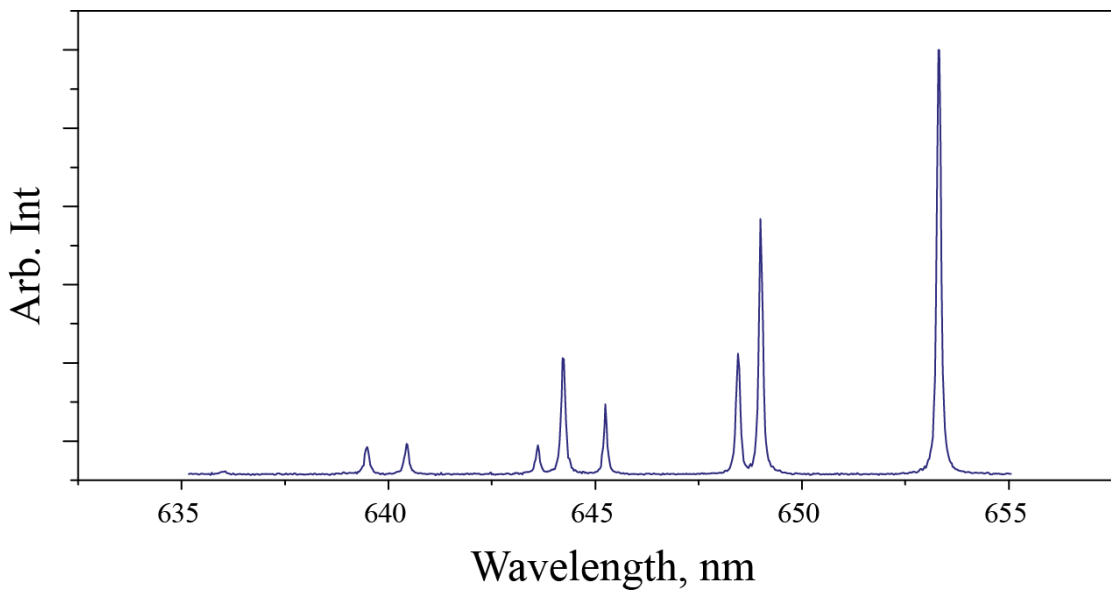


FIGURE 4.18: *Spectrum obtained from cavity displaying pronounced splitting of the TEM_{01} and TEM_{10} transverse modes.*

containing lateral mode positions for all three cavity types is shown in figure 4.19. This shows that for longer cavities the nominal ‘mill’ parameters used, at least for the 25 and 12 μm cases are reasonably accurate, the values for the radius of curvature of the smallest cavities only get as low as 7 μm . These values allows us to volunteer an explanation for another phenomenon observed in the series of TEM_{00} , which is the increase in relative height of the central mode to the leaky light at the edge of the reflectivity band of the mirrors. By finding the divergence angle (using the calculated radii of curvature from figure 4.19) of the mirror of the modes formed we can plot the mode divergence as a numerical aperture, (N.A.). This is plotted against cavity length for the radius of curvature 25 μm cavities, and shows a marked increase as the cavity length is decreased (figure 4.20. This offers a possible explanation for the increased signal in the resonant

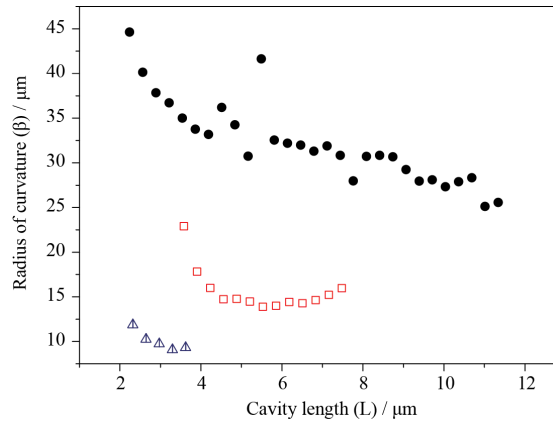


FIGURE 4.19: Radii of curvature determined from the relative positions of the first order transverse modes ($TEM_{01\&10}$) plotted against cavity length.

frequencies at shorter lengths in that improved coupling to the N.A.= 2.5 condensing lens which is focusing the light into the cavities. These radii of curvature also allowed

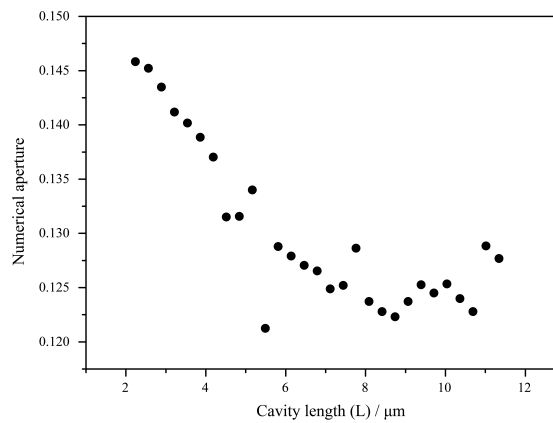


FIGURE 4.20: Plots of the numerical aperture of each of the modes formed calculated from figure 4.19, against cavity length.

the other most vital cavity property to be calculated, that of the cavity volume. This gave the smallest result measured for this type of cavity to date, of just over $2 \mu\text{m}^3$ for the smallest radius of curvature feature. There appears to be a trade off at this stage however between the radius of curvature of the feature and the Q factor that is achieved. The achievable Purcell factors for all three of these cavity specifications are plotted in figure 4.21. The challenge for this cavitation approach is to improve and better understand the milling procedure, and any limitations with the commercial DBR deposition to see if the sort of Q factor seem for the larger features can be maintained down to the very smallest of radii of curvature. As a slight aside, and the final point in this chapter the consistency of the cavities milling was examined by measuring the spectra of an entire array of one hundred cavities, when brought to their very shortest cavity length. The Q factors of the entire data set are shown in figure 4.22. With the

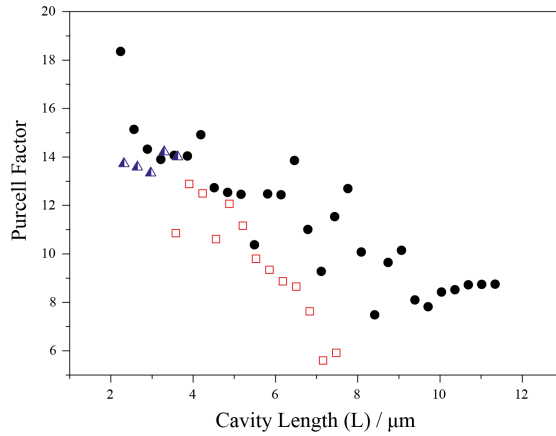


FIGURE 4.21: *The hypothetical maximum Purcell factors achievable for the cavities characterised.*

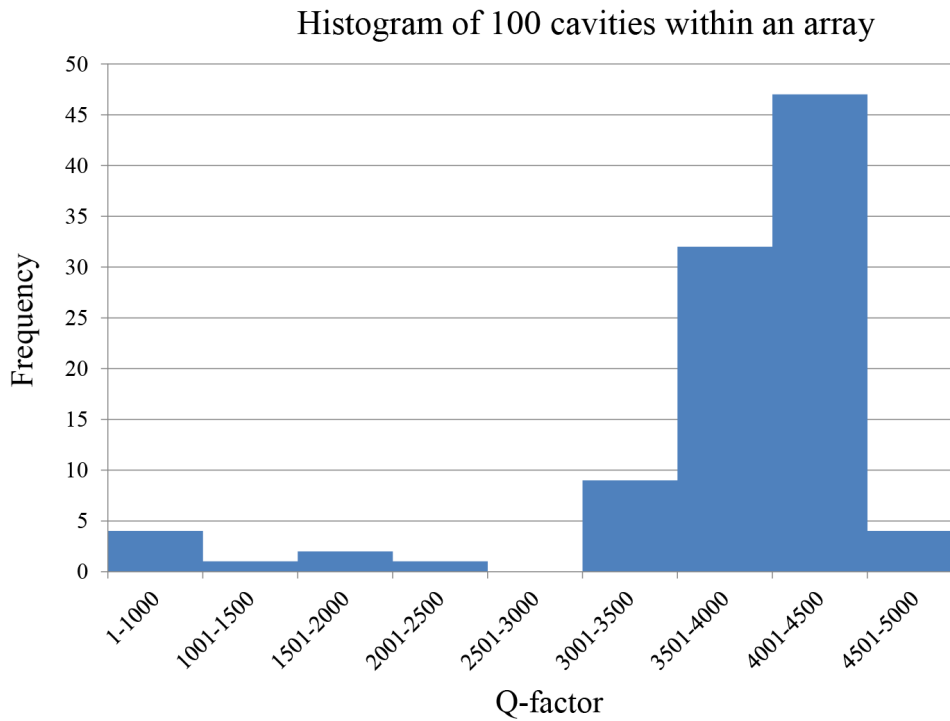


FIGURE 4.22: *Histogram of the frequency of occurrence of various Q factors from 1000 up to 5000 for an entire array of 100 features.*

use of clean room environments this level of consistency could easily be improved.

4.6 Summary and Conclusions

Here we have shown the characterisation of a novel construction method of open access cavities. This method has been shown to be capable of achieving Q factors consistently in excess of 10^4 with the smallest mode volumes ever shown for this type of cavity,

$< 3 \mu\text{m}^3$. These cavities are remarkably robust to their chemical environment, and are versatile enough to be applied to a variety of problems. Experiments involving coupling these cavities to optically active emitters will be the subject of the next two chapters.

Chapter 5

Nanocrystals in Cavities

5.1 Introduction

In this chapter results obtained from coupling colloidal semiconductor nanocrystals, NCs (for these purposes, synonymous with quantum dots, QDs) will be presented. The work undertaken in this chapter was of a more collaborative nature with results being taken by Dr ZiYun Di and Helene Jones as well as myself. Any results which I played a minor role in taking will be clearly marked and attributed appropriately to the primary experimentalist. The chapter will begin with a description of the experimental arrangements, followed by a section where the results will be presented. The results displayed here formed the basis of a publication (submitted, NJP [18]). The penultimate section of this chapter will present a series of results from the second iteration of features constructed. This data constitutes a very cursory investigation into this second batch of microcavities, and is the very latest data involving nanocrystal photoluminescence and this type of open access microcavity.

From the characterisation of the cavities, although the predicted Purcell factors were not insignificant, one of the key results was the extremely small mode volumes achieved. This becomes especially important in the case where the emitter spectral width is considerably larger than the cavity's. This case was not covered in the discussion on cavitation effects in chapter 2, and is only recently becoming more completely understood. This situation, referred to as the 'bad emitter' (as opposed to the more common 'bad cavity') regime is beginning to garner some attention due to theoretically predicted cavity feeding effects [88, 89]. This could have strong implications on the characteristics of emitters most desirable for single dipole lasing and potential room temperature single photon sources [90].

5.2 Experimental Setup

In order to collect photoluminescence (PL) from nanocrystals an epi-florescent microscope was used. A schematic of the optical elements comprising this system is shown in figure 5.1. Here the 473 nm laser light is coupled into the system via a single mode fibre, from a PicoQuant LDH470 laser diode. Once collimated by an objective lens a second, long focal distance singlet lens was mounted such that it could be switched in and out of the optical path without requiring realignment. This allowed for easy switching between focused illumination without the lens in place, usually only during alignment and focusing procedures, and a broader illumination with the lens in place for general use and data collection. This is vital due to the relatively fragile nature of semiconductor quantum dot photoluminescence, which is quickly bleached by strong (i.e. focused) laser light. As previously, a CCD was incorporated to aid alignment by splitting the beam before the dichroic mirror. Throughout these experiments, a relatively low N.A. lens of 0.45 was used as the objective. This lens had a sufficiently long working distance to see through the upper substrate, and since it is cavity modes that are being investigated rather than single emitters even this N.A. was sufficient to collect ample PL. Finally the light was propagated directly into the spectrometer without any further fibre coupling, allowing the CCD within the spectrometer to image the focal plane of the objective. The physical set up of the cavity holder went through several stages of development.

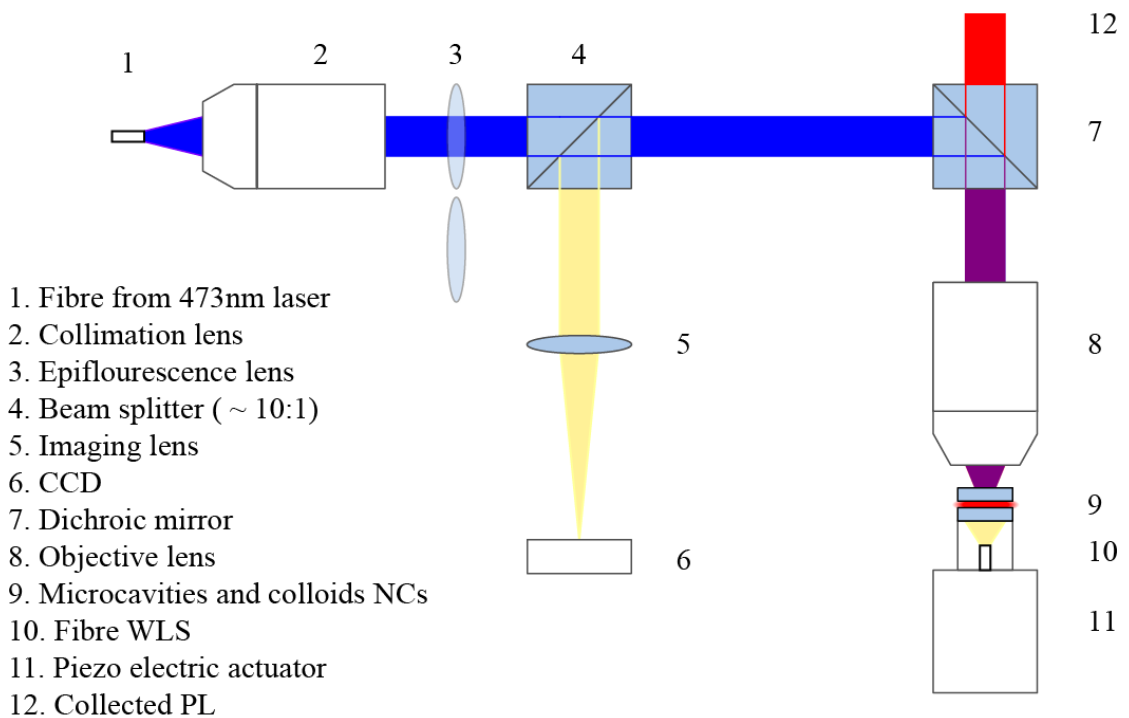


FIGURE 5.1: Schematic of the optical set-up used to obtain the photoluminescence from colloidal nanocrystals coupled to the open access optical microcavities.

It was realised during the characterisation of the cavities, that manual actuators had severe limitations in that although modes could be positioned quite precisely, any physical contact with the system would momentarily shift the alignment considerably, making any precise spectral optimisation impossible. To circumvent this drawback a piezo-electric actuator was used as the mount for the lower, featured mirror to allow fine tuning of the cavity length. As mentioned in 3.4, the requirement of getting the mirrors perfectly parallel was somewhat mitigated by using only a small plinth of features. This advance allowed the upper mirror to be mounted on a manual z actuator for coarse tuning of the cavity length. As in the cavity holding schematic of figure 4.5 these were connected by a cage rod assembly to minimise the mechanical distance between the two surfaces, although as mentioned previously they are only usefully stable when in physical contact. The final construction of this set up included a spacer being placed on top of the piezo actuator, but below the lower, featured mirror (labeled 10 in figure 5.1). The purpose of this development was to allow white light to back-illuminate the cavities, which could be imaged by the CCD marked 6 in the schematic, and make alignment somewhat easier. The colloidal quantum dots used for this work were commercially available cadmium-selenide/zinc-sulphide core-shell structures kindly provided to us by eBioscience. In order to ameliorate evaporation imposing an experimental time constraint octadecene was used as the solvent for its rather low volatility. This solution was simply drop cast onto the lower, featured substrate prior to assembling the upper mirror of the cavity. The viscosity of the liquid was such that it completely filled the gap between the substrates. This is drawn pictographically in figure 5.2 where the large excess of nanocrystal solution is actually quite beneficial, as it provides a reservoir of unbleached nanocrystals allowing experiments to be run with relatively high laser intensities and which generate plenty of PL signal. This schematic also shows the white light delivery from below the microcavities, and the two alternative laser illuminations which will be referred to as ‘focused’ (when the marked lens 3 in figure 5.1 is out) and ‘broad’ (when the lens is in). Having discussed the details of setting up the experiment, the chapter will now move on to a presentation of the results obtained with this optical set up.

5.3 Modified Emission Spectra

Prior to aligning the optics to the plinth region cavities, it was possible to take PL spectra from the nanocrystal solution away from the mirrored region. This PL will have had a fairly diminished intensity, as away from the plinth structure there was only the upper planar mirror between the solution and the collection optics. Nevertheless it was possible to collect PL and also perform photon counting statistical analysis. Since these regions were assumed to be equivalent to nanocrystals which are emitting into free

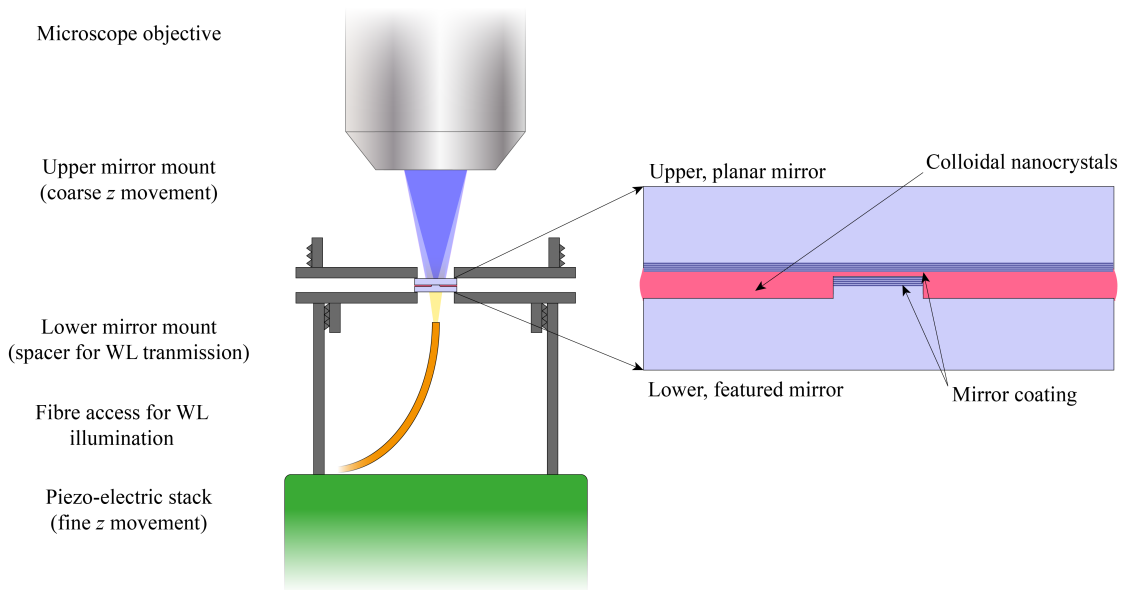


FIGURE 5.2: *Diagram of the sample mounting approach to allow coarse and fine adjustment of the cavity length. In addition a lower spacer was added to allow for white light illumination to aid in alignment.*

space, they can be used as a comparison for any emission collected from cavity coupled nanocrystals. The upper plot in figure 5.3 shows an example, ensemble PL measurement taken from this region, showing a strongly Gaussian spectral profile as expected for inhomogeneously broadened emitters. In addition their peak emission occurs close to the centre of the reflective region of the dielectric stacks in use, at around 640 nm with a width of around 20 nm. Plotted below is an example of a spectrum once the cavities (with $\beta = 25 \mu\text{m}$) have been moved into the field of view. Analysis of transverse and longitudinal mode spacings allows to note that the cavity length is approximately $5.5 \mu\text{m}$. From an experimentalist's point of view, one clear difference with this method of cavity mode population is the abundance of the higher order modes. With the white light transmission measurements considerable care was required to misalign the beam and excite the lateral modes, whereas with the nanocrystals they are easily populated. This is to be expected as with the white light the excitation illumination was injected only over a relatively small angle, corresponding to an N.A. = 0.25 objective. With the colloidal nanocrystals the illumination is over the full 4π str and so excites many more transverse modes.

As mentioned previously, the spectrometer has the capacity to image the focal plane of the objective lens onto its liquid nitrogen cooled CCD. Once the system is properly aligned, and the cavity length reduced it is possible to obtain images of the kind shown in figure 5.4(a). One of the striking features is the clear visibility of the cavities' positions. This is due to the cavities directing a higher proportion of the light towards

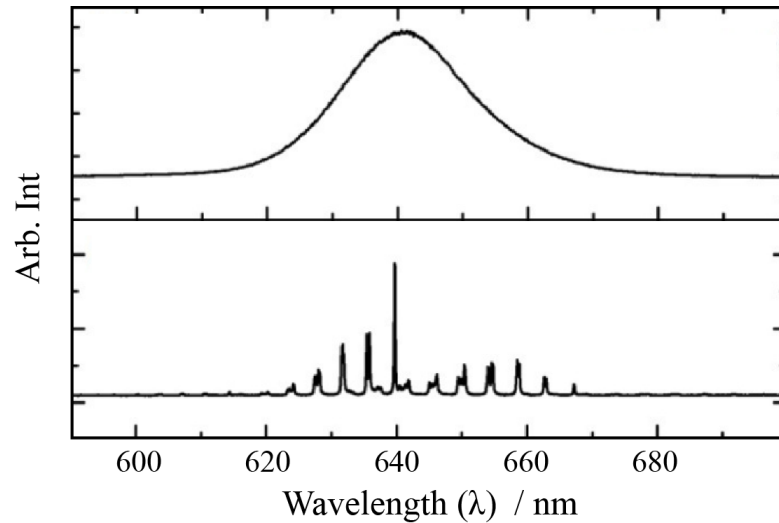
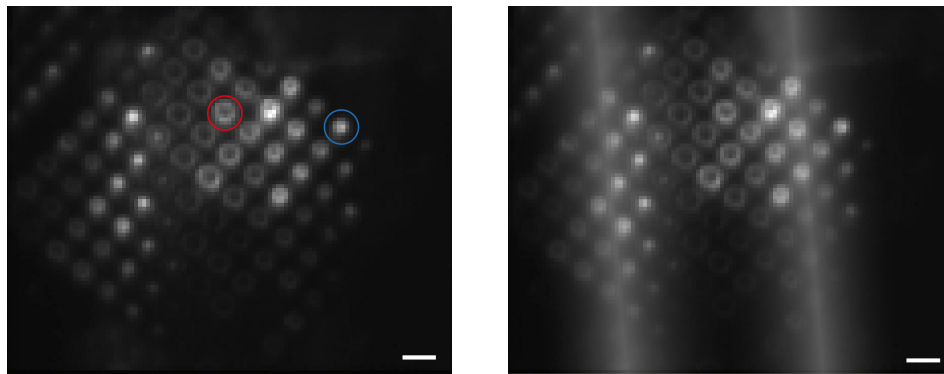


FIGURE 5.3: Upper plot - Emission spectra from reservoir of colloidal nanocrystals away from cavity plinth, showing ~ 20 nm width Gaussian profile centred on 640 nm as expected for the free space emission of these nanocrystals. Lower plot - Emission spectra from colloidal nanocrystals for a cavity of $L = 5.5 \mu\text{m}$, $\beta = 25 \mu\text{m}$. Data obtained by Dr. ZiYun Di.



(a) Image taken by spectrograph whilst in imaging mode, showing cavity coupled emission of colloidal nanocrystals.

(b) The image shown in figure a) with a graded overlay to highlight the Fabry-Pérot modes

FIGURE 5.4: An image taken by the spectrograph without next to the same figure with a graded overlay to highlight the Fabry-Pérot etaloning visible. Data obtained by Dr. ZiYun Di, scale bar $10 \mu\text{m}$.

the collection optics than in regions outside the cavities, and efforts to quantify this collection enhancement will be discussed with the aid of FDTD modeling in section 5.5. Clearly not all coupling is the same however, as there are some cavities emitting from a central region (e.g blue circled feature) whilst others seem to be emitting from an annulus around a dark central region (e.g. red circle). Emission profiles seem to be correlated with Fabry-Pérot modes which are also visible in planar regions between the mirrors, as emphasized by the graded overlay on the image shown in figure 5.4(b). The presence of this interference indicates that the mirrors are not totally parallel. The

fact that a complete interference fringe can be observed within the field of view shows that the mirrors are considerably less parallel than is possible for these substrates, with flatnesses quoted by the manufacturers measured in fractions of a wavelength across the whole substrate. This highlights one of the implications that choosing the ‘plinth’ has on the experimental set-up. The reasoning for incorporating this feature lay in reducing the surface area for large pieces of dust to settle, and also to reduce the distance between the cavity arrays and any edge where contact will inevitably occur first. It seems that one drawback is that it is now much easier to get the substrates very close, whilst still not being particularly parallel. The reduced size is ultimately preferable however, as using a commercial piezo-goniometer or any kind of kinematic control would then render the problem trivial to surmount. With this set-up, where no such degree of freedom is available, simply checking cavities close to each edge of the plinth and using cavities at the edge with the largest free spectral range suffices in order to achieve the shortest cavity lengths. One thing which is rather encouraging is that stable modes are still formed within the cavities despite the angle between the mirrors being of the around $\tan^{-1}(0.3/50) = 6$ mrad. One possible explanation for the correlation of the Fabry-Pérot etaloning and the visibility of ‘doughnut’ shaped cavity photoluminescence is that for these cavity lengths the primary, TEM_{00} modes are positioned away from the nanocrystal emission region and of the available higher order modes only the very largest radii modes appear, with the lower order transverse modes destructively interfering with the more central portions of the higher order ones. This conclusion is born

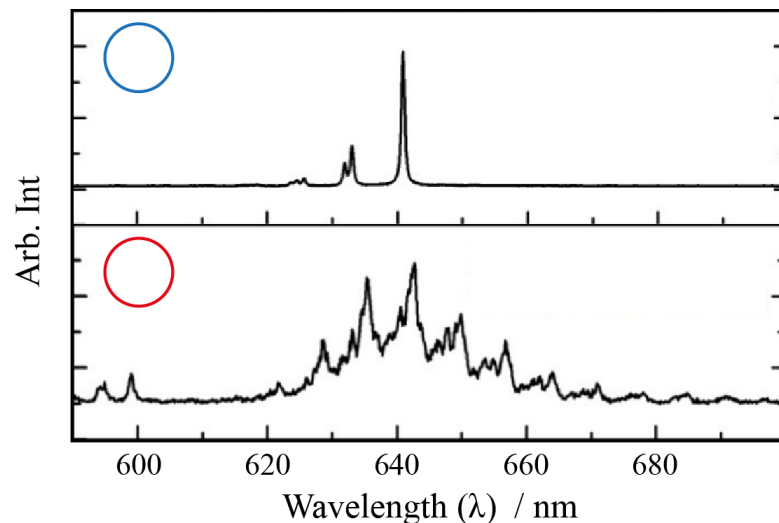


FIGURE 5.5: Spectra taken from the two cavities marked in figure 5.4(a), the upper plot from a central bright region within the cavity, and the lower plot taken from the doughnut shaped mode visible in the red circle on figure 5.4(a). Data obtained by Dr. ZiYun Di.

out when spectra for each of the two cases are considered. Figure 5.5 shows the spectra from the cavities marked in blue and red in the upper and lower panes respectively. The

upper plot shows clear cavitation effects, with only a single primary longitudinal mode falling within the emissive region of the nanocrystals, whilst the plot from the doughnut shaped mode had much more background PL contributing to the signal, with much less mode structure. In any case, it is obvious that when one is interested in collecting single mode coupling from a microcavity the central bright feature is the mode structure to look out for. By keeping track of the number of longitudinal modes transited through it is possible to assign this spectrum to a cavity with a length of $1.6 \mu\text{m}$, including the penetration depth of the field into the mirror. This shows a marked improvement on the shortest cavity achieved during the empty cavity characterisation discussed in chapter 4, and is attributed to the reduction in the featured mirror size allowing cavities to be considered which are in close proximity to the edge where the two surfaces are in contact. These results were repeated with the smaller cavities with a radius of curvature iden-

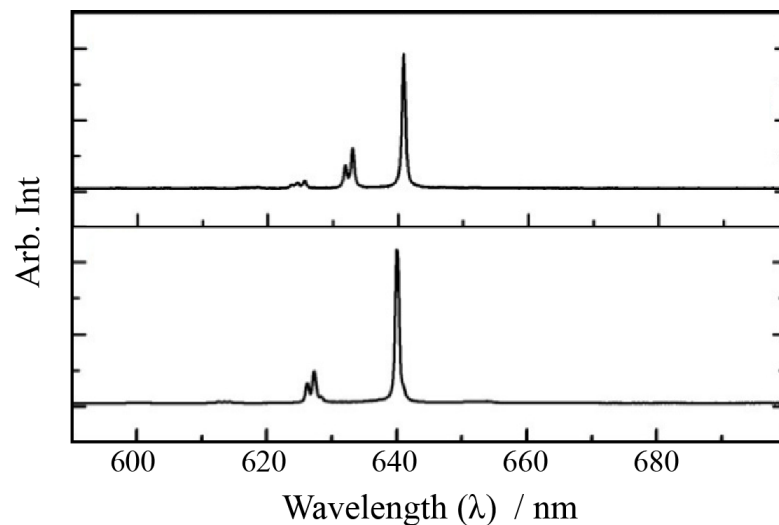


FIGURE 5.6: Spectra taken from cavities of $L = 1.6 \mu\text{m}$ and $\beta = 25$ and $7 \mu\text{m}$ for the upper and lower plots respectively. Data obtained by Dr. ZiYun Di.

tified as $\beta = 7 \mu\text{m}$ in the characterisation chapter (chapter 4). Once again, by closing the cavity length as much as possible and then checking the edges of the plinth to find the shortest possible cavity, a cavity length equaling that found for the larger features was achieved. The spectra obtained from these two cavity types, of equal length but different radius of curvature are plotted in figure 5.6. This clearly shows the affect of raising the transverse energy levels effected by applying tighter lateral confinement from the higher radius of curvature. With a complete description of the cavity modes from the spectral information, it is now possible to investigate what impact the presence of the microcavity has on the excited lifetime of the nanocrystals generating the PL shown in the plots of figure 5.6.

5.4 Modified Lifetimes

In order to collect temporal information on the excited state of the nanocrystals it is necessary to pass the collected photons onto a different detection device, and use a pulsed laser source. This is necessary as the read out of this CCD system is not rapid or sensitive enough to record arrival times of individual photons. Devices that can achieve this include avalanche photo-diodes (APDs), photomultiplier tubes (PMTs) and a single photon avalanche diode (SPADs) which was the detector used. This device functions by holding the depletion region of a reverse biased p-n junction at a voltage just above the breakdown voltage. This means that a single photon can cause a current pulse on the order of mA with a timing resolution of the order of 100s of ps. These current pulses can then be correlated with the current pulses used to generate the light pulses in the laser diode. In order to maintain sufficient timing resolution this correlation must happen very rapidly, and so a high frequency electronic device called a time-correlated single-photon counter or TCSPC is used. This records the duration between the arrival of the trigger pulse from the laser, and the arrival of the next pulse from the SPAD, indicating the arrival of a photon. The controlling software then plots this data in the form of histograms, which are shown as the output and are referred to as time-resolved-photoluminescence or TRPL. Although this method obtains excitation/emission results taken from many different emitters at many different times, it can be used to extract detailed information about the nature of the decay for single emitters. This entire set-up is shown in an approximate schematic in figure 5.7, and data was obtained using 100 ps long excitation pulses with an overall timing resolution of 900 ps. This set-up makes use of the exit port of the monochromator part of the spectrograph. This is particularly convenient, as it allows the precise alignment of the optical set-up, making use of the low noise spectral read-out of the LN cooled CCD with easy switching to the SPAD using the internal flip mirror. This arrangement allowed for the option of projecting either the image of the cavity mode onto the fibre coupled SPAD port, by selecting the mirror on the rotating turret mount, or alternatively the signal can be diffracted by the choice of a grating in place of the mirror and the light coupled into the fibre can be spectrally filtered. This will have no effect on the results obtained after correlation with the laser pulses, and it was found that by spectrally filtering the luminescence coupled into the fibre, a higher signal to noise ratio could be achieved. These correlation studies could be carried out on all of the spectral signals shown so far. As shown by [91] amongst others, the excited state decay rate should follow a single exponential decay curve provided that the excitation laser is of a low enough intensity that the creation of bi-excitons does not occur. On a log-linear plot, as in 5.8, this should appear as a straight line, the gradient of which contains the decay rate. It is changes in this rate which will be used to determine what (if any) Purcell enhancement has occurred. The

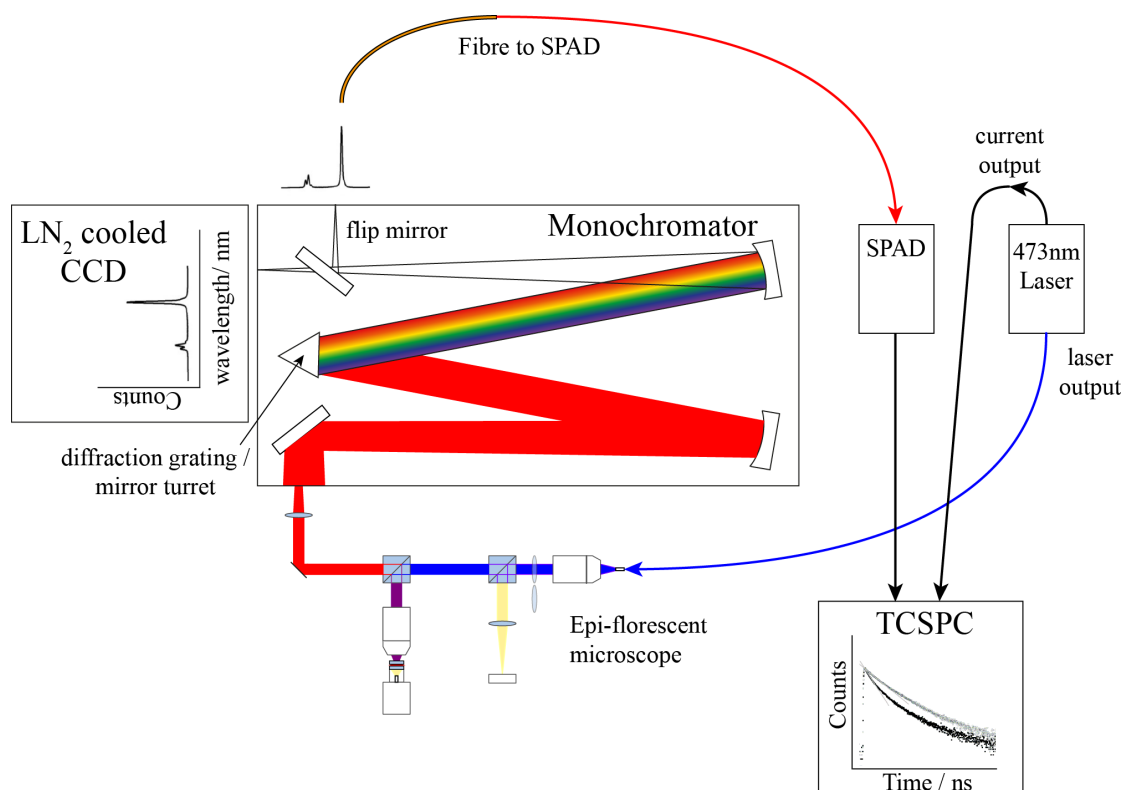


FIGURE 5.7: Schematic of the experimental set-up designed to facilitate easy switching of spectral, spacial and temporal interrogation of sample photoluminescence. The light path within the monochromator is expanded slightly and several of the optical elements inconsequential to the overall picture have been removed to simplify the diagram.

recorded TRPL data for nanocrystals in the smallest cavities achieved (filled squares) and the TRPL from the free space emission (open squares) are plotted in figure 5.8. The smallest cavity volumes achieved correspond to those of the spectrum shown in the lower plot of figure 5.6 ($L = 1.6 \mu\text{m}$ and $7 \mu\text{m}$). The free space emission is approximately linear on the log-linear axis, and has a noticeably longer time constant than the initial time constant of the cavity coupled case. This altered exponential decay for the cavity is clearly no longer even approximately a single exponential, and has several distinct regions with a range of quite different decay constants. Since the measurement was taken on a timescale much longer than the motion of nanocrystals in solution along with the relatively high concentration of solution used the distribution of nanocrystals is assumed to be uniform within the cavity. From equation 2.19 this implies that we will be recording PL from nanocrystals coupled to cavity field anti-nodes, nodes, and every field strength in between. By only using the first 20 ns when extracting the decay rates from the TRPL data we can effectively restrict the PL contributing to the time constant to that of nanocrystals located close to the field anti-nodes. The red lines shown on both data sets are the gradients of lines of best fit for first 20 ns. The ratio of these two gradients yields the overall decay rate enhancement achieved by these cavities. As before, the volumes were calculated by rearranging the expressions for the beam waist

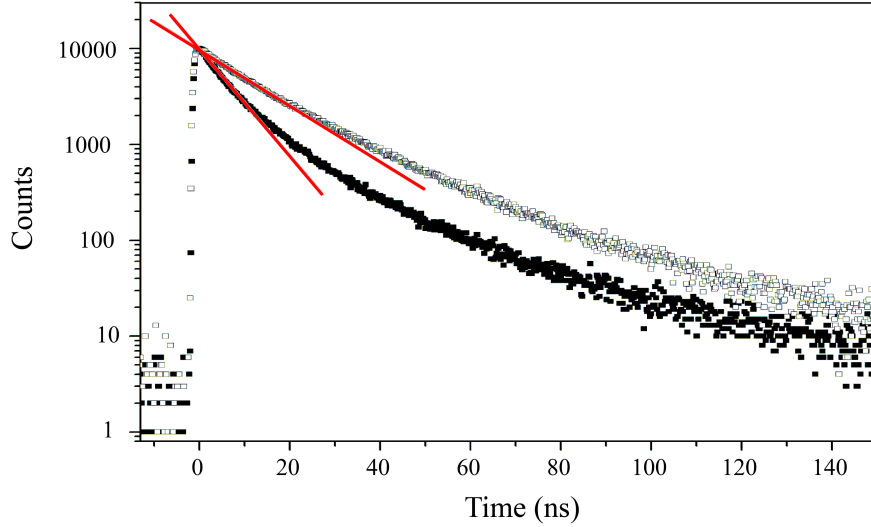
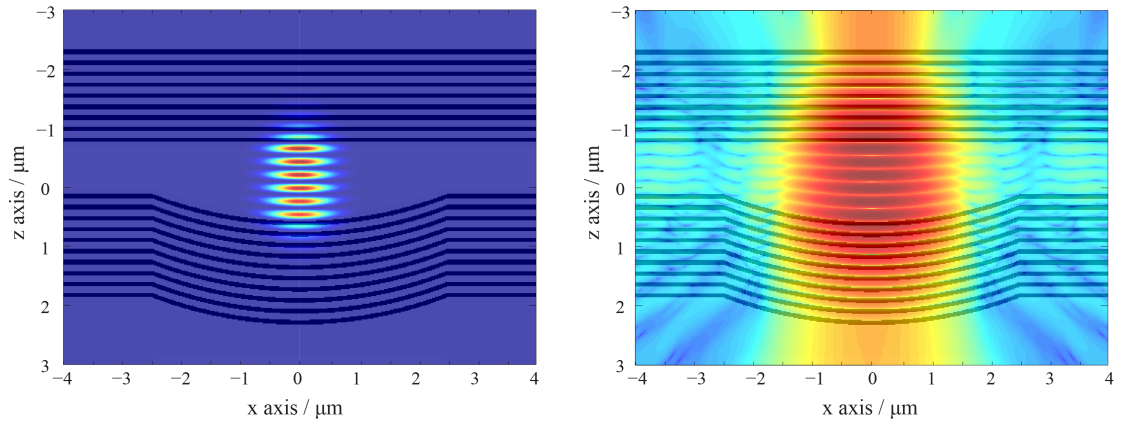


FIGURE 5.8: Time resolved photoluminescence histograms for free space emission (open squares) and cavity coupled emission (filled squares), with counts plotted logarithmically. Red lines of best fit are for the first 20 ns only to exclude poorly coupled PL. Data obtained by Dr. ZiYun Di.

on the featured mirror, given in equation 2.55a and the volume of a TEM_{00} Gaussian mode in equation 2.57 to get the expression shown in equation 5.1.

$$V = \frac{\lambda L^2}{4n} \sqrt{\frac{\beta}{L} - 1} \quad (5.1)$$

As before, this equation must be altered slightly so that the cavity length includes some field penetration into the mirror. To arrive at a more accurate value for this penetration depth FDTD simulations were performed, and volume calculations as discussed in chapter 2 section 2.5 were carried out. The field distribution is plotted in figure 5.9(a). The plot in figure 5.9(b) is the same field distribution except plotted on a logarithmic color axis. This is illustrative as it shows quite vividly the main loss mechanism of this cavity mode having a very clear directionality, which facilitates efficient collection. In both images translucent refractive index cross sections have been overlain and indicate the positions of the mirror layers. In this color scheme the final layer of the lower refractive index (the physical front surface of each mirror) is not visible as, fitting with the experimental circumstances the medium filling the cavity has the same refractive index as lower refractive index material (silica). The volumes calculated for the very smallest cavities achieved experimentally were determined to be $0.53 \mu\text{m}^3$, according to the FDTD method. In order to agree with this value, a field penetration of 1.09λ into each mirror must be included in the cavity length, L of equation 5.1. This value can then be used to calculate accurate volumes for all of the experimental data. Figure 5.10 shows the calculated volumes of each cavity plotted against the measured decay rate enhancement. Here the open squares are cavities with $\beta = 25 \mu\text{m}$ and the open



(a) An example resonant field distribution with a linear color scale.

(b) An example resonant field distribution with a logarithmic color scale.

FIGURE 5.9: Intensity plots for the normalised electric field distribution of a resonant TEM_{00} mode.

circles are for cavities with $\beta = 7 \mu\text{m}$. The four stars are results arrived at after further

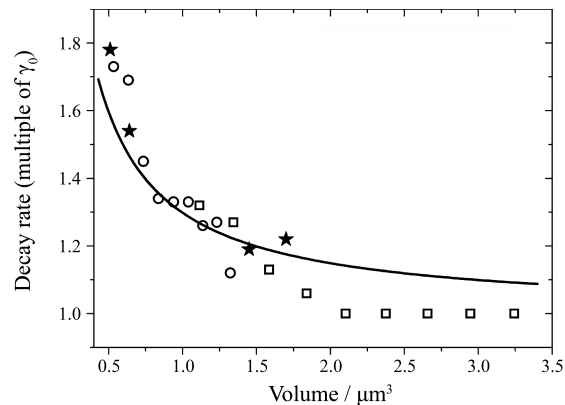


FIGURE 5.10: Plot of measured decay rate enhancement (as a multiple of the free space rate) plotted against cavity volume. The open squares are for $\beta = 25 \mu\text{m}$ cavities, and the open circles for $\beta = 7 \mu\text{m}$ cavities. The stars represent results obtained by FDTD analysis. Experimental data obtained by Dr. ZiYun Di.

simulations to find the effective decay enhancements for a dipole situated within the modeled cavities. The solid line is the result of some preliminary decay rate analysis which will be discussed in the next section.

5.5 Decay Rate Analysis

Figure 5.10 shows that the microcavities are only beginning to have an effect on the exciton recombination time once the mode volume drops below $\sim 2 \mu\text{m}^3$, regardless of the geometry of the cavity emphasising the crucial role that cavity volume plays in

this regime. According to our current understanding is that this is the first time that a tunable Purcell effect has been observed through cavity volume control. Clearly however these measured Purcell factors are only a fraction of what is predicted by the Purcell expression derived earlier, and plotted in figure 4.21. As mentioned at the start of the chapter, the spectral line width of the cavity is much less than the spectral line width of the nanocrystals at room temperature ($\delta\lambda_{cav} < \delta\lambda_{NC}$). This directly contradicts a key assumption in the derivation of the Purcell expression, that the transition line width is much narrower than the cavities'. The expression can be modified to take this, and some of the other effects seen in this room temperature experiment, into account. First off the Q factor which is used in expression 2.19 can be modified to take into account dominance of the nanocrystal's much larger Q factor by defining an overall cavity plus emitter Q factor given as

$$Q_{tot} = \frac{\lambda_{peak}}{\delta\lambda_{cav} + \delta\lambda_{NC}} \quad (5.2)$$

where λ_{peak} is the centre wavelength of the resonant mode [92, 93]. For the experiments detailed above this reduces the effective Q factor from ~ 1000 (from figure 4.15) to 45 with very little change for the range of Q factors achieved for the empty cavities. Since the Q factor is effectively rendered constant by the large line width of the emitters at room temperature, the Purcell factor now only scales as $1/V$. If one assumes that the overwhelming majority of emission by the nanocrystal is still into the free space density of states, then the expected modification to the free space emission is equal to $F_P + 1$. The solid line plotted in figure 5.10 shows this decay rate's volume dependence. This model can be developed further with the inclusion of three further physical factors pertinent to this particular situation. Firstly the cavity may support several modes within the emissive region of the nanocrystal. In addition there are portions of the nanocrystal's emission which are effectively detuned from the cavity modes, and therefore suppressed. Finally there is the non-radiative recombination routes which are usually available to the excitons in the nanocrystals. The first two of these are considered more pictorially in figure 5.11. These factors can be accommodated algebraically in the equation 5.3.

$$\gamma' = \gamma_{nr} + \left(\sum_i F_{p,i} + \alpha \right) \gamma_r = \gamma_0 \left(1 + \eta \left(\sum_i F_{p,i} + \alpha - 1 \right) \right) \quad (5.3)$$

Here γ_{nr} and γ_r are the non-radiative and radiative recombination rates of the excitons for nanocrystals emitting into free space. The total free space recombination rate γ_0 is the sum of these to possible recombination routes, $\gamma_0 = \gamma_r + \gamma_{nr}$ and finally $\eta = \gamma_r / \gamma_0$ and is the fluorescence quantum yield in free space. Here we introduce α as the suppression of emission into continuum modes (i.e non-resonant modes) and so will take values less than 1, (i.e. $0 \leq \alpha \leq 1$). It was possible to make use of the finite difference time domain software to calculate the modified spontaneous emission rates. The method to

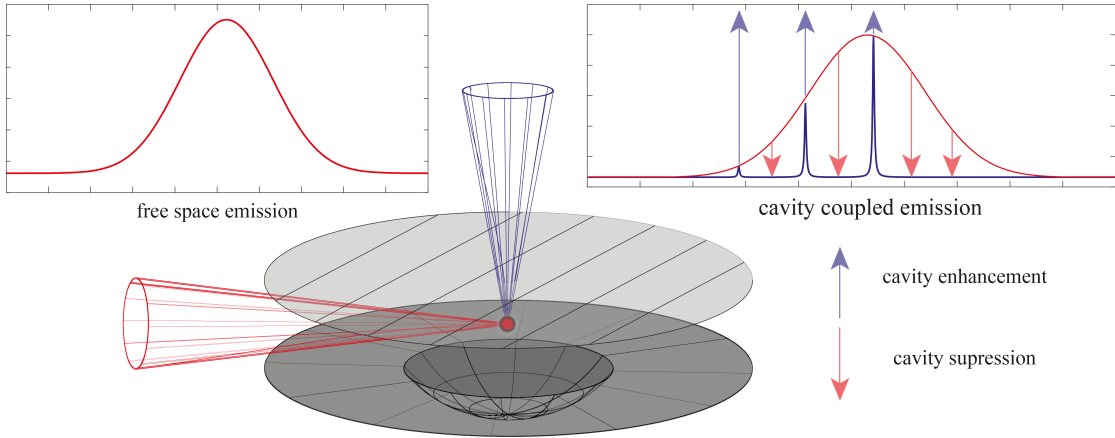


FIGURE 5.11: *Graphical representation of the multi-mode coupling and off-resonant suppression of emitter coupled to cavities in the bad cavity regime.*

determine the spontaneous enhancement achieved in the bad emitter regime using FDTD methods involves calculating the total power radiated from a dipole into free space, and then comparing that to the total power radiated from the same dipole when placed within a cavity [94, 95]. Power monitors were arranged in a cuboid around the dipole, and the total power transmitted through each region is calculated from the Poynting vector automatically. As well as calculating the total power emitted through the entire planar region, the power distribution can be extracted. For a 14 nm Gaussian dipole emitting into free space (approximately equal to the nanocrystal's emission profile), the power plots are shown arranged as the monitors were during the simulation, in figure 5.12(a). The cavity can then be inserted and the simulation repeated, the results of which are shown in figure 5.12(b). In this plot the geometry of the cavity has been excluded to facilitate viewing, whilst the dipole and its orientation is included in both plots. The cavity is arranged such that the planar mirror is closest to, and parallel with the back surface of the cuboid (with the highest field intensity). In both plots the colour scale is normalised to the maximum value. The symmetry of the situation allows one monitor to be used for each pair of x and y normal planes, the presence of the cavity however requires the two z normal planes to be monitored. Clearly the cavity has a profound effect on the directionality of the field emitted, but the total power transmitted through each surface is also altered, and the ratio of the two integrated powers gives the Purcell factor experienced for this dipole. The enhancement factor for this particular arrangement is approximately 1.7, which is in good agreement with the experimental results. Because this method involved numerically integrating over all possible emission \mathbf{k} vectors, it is comprised of both the resonant mode contribution to the decay rate enhancement, F_p and also the suppression of off resonant continuum (or 'leaky') modes. In order for this value to be accurate it is necessary to ensure that the source has the appropriate emission characteristics, and so a peak wavelength

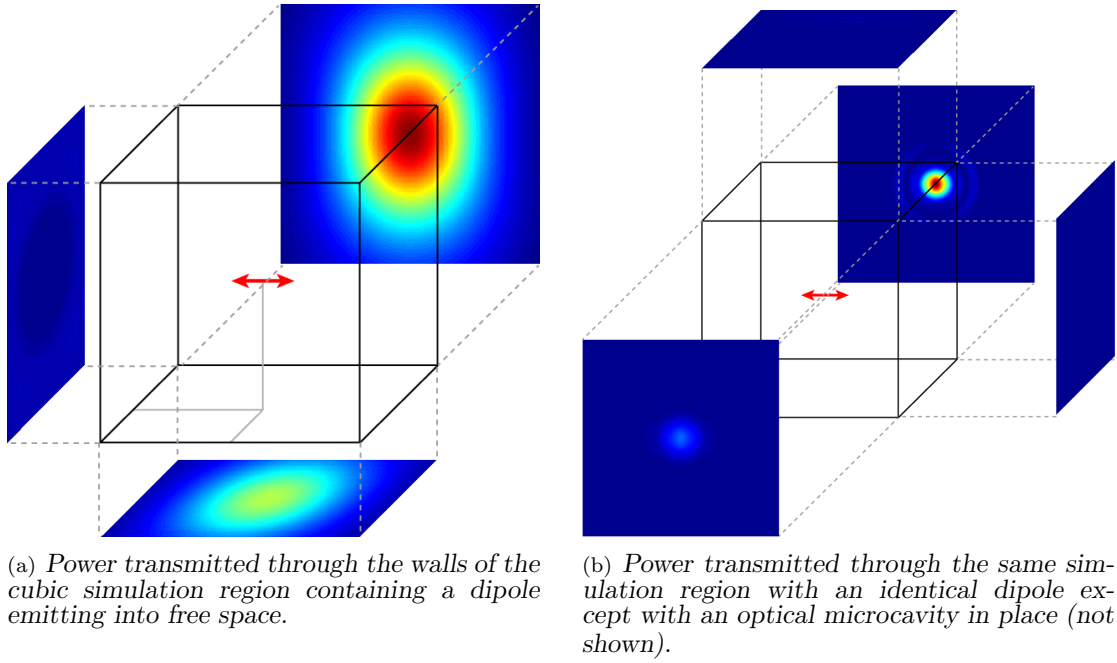


FIGURE 5.12: The distribution of power transmitted out of the simulation region for the case of without (a) and with a cavity (b). With no cavity in place the symmetry of the simulation means opposite faces of the cube are identical. With the cavity in place the symmetry is broken along the optical (z) axis (out of the page). The cavity parameters used match the smallest cavity achieved experimentally ($\beta = 7 \mu\text{m}$, $L = 1.6 \mu\text{m}$).

of $\lambda = 640 \text{ nm}$ with a homogeneous line width of 14 nm . For these simulations the cavity was arranged such that the primary mode occurred at the peak wavelength of the dipole's emission. Simulations were ran for several cavity lengths for a feature design with $\beta = 7 \mu\text{m}$ and a width of $5 \mu\text{m}$. The results yielded are the four points marked as black stars in figure 5.10 which agree remarkably well with the experimental data. The modeled rate for the smallest mode volume is equal to $1.78\gamma_0$. In addition to giving good agreement with the experimentally measured rate enhancements, the data from the simulations allow us to isolate the contributions to the total emission rate as described in equation 5.3. By spectrally selecting only the emission into the primary mode we find that for the smallest cavity emission occurs at a rate close to that of the entire free space emission, with $F_P = 0.77$. It was also shown that emission into the continuum modes is suppressed by 32% giving $\alpha = 0.68$. The rest of the enhancement was found to arise from emission into other resonant modes fall within the nanocrystals emission line width, which appear in equation 5.3 as additional terms counted within the summation. The coupling efficiency between the nanocrystal and the microcavity can also be ascertained, for which an accurate value of the quantum efficiency (η) of the nanocrystal is required. The close agreement between the modeled emission rates and those obtained experimentally suggest that the value provided by the manufacturer is

accurate putting η close to unity. It is still included here for completeness as for many other colloidal quantum dots and emitters in general this may not be the case. It can easily be seen from equation 5.3 that the quantum efficiency for coupling into the i th cavity mode is given by equation 5.4.

$$\eta_i = \frac{\eta F_{P,i}}{1 + \eta (\sum_i F_{P,i} + \alpha - 1)} \quad (5.4)$$

Using the values determined above and $\eta = 0.9$ we find that emission into the primary cavity mode occurs with an efficiency of 40.7%.

5.6 Single Particle Sensing

In a final set of experiments we present evidence that demonstrates the measurement of emission from a single nanocrystal into the cavity mode. For this no additional modification to the experimental apparatus was required, only a serial dilution of the colloidal nanocrystal solution to the point where on average a single nanocrystal would occupy a volume comparable to that of the microcavity. There are two pieces of evidence which suggest single dot photoluminescence is visible. The first result to be presented indicating single nanocrystal emission is shown in figure 5.13 and shows a time trace of the cavity coupled emission spectrum. This reveals substantial fluctuation in the mode intensity which is attributable to single dot fluorescence intermittency. The second corroborating evidence is taken from a comparison of spectra, examples of which are shown in figure 5.14. The upper plot (blue) shows the spectrum for a single nanocrystal at room temperature in free space and the lower, plotted in black is the emission seen from dots within the cavity. The range of excited modes is comparable with the homogeneous line width of the nanocrystal which is around 14 nm. This can be contrasted against with the upper spectra in figure 5.3 where the nanocrystal emission is seen with width of around 20 nm due to the origin being an inhomogeneously broadened ensemble. This result brings to a close the data which was contributed to the submitted publication. The penultimate section presents some of the most recent nanocrystal PL obtained from this type of microcavity.

5.7 Characterisation of the Second Cavity Iteration

Towards the end of the thesis, whilst efforts were primarily being directed towards the construction of an apparatus to facilitate coupling NV centres to the optical microcavities at low temperature the second iteration of featured silica substrates were coated

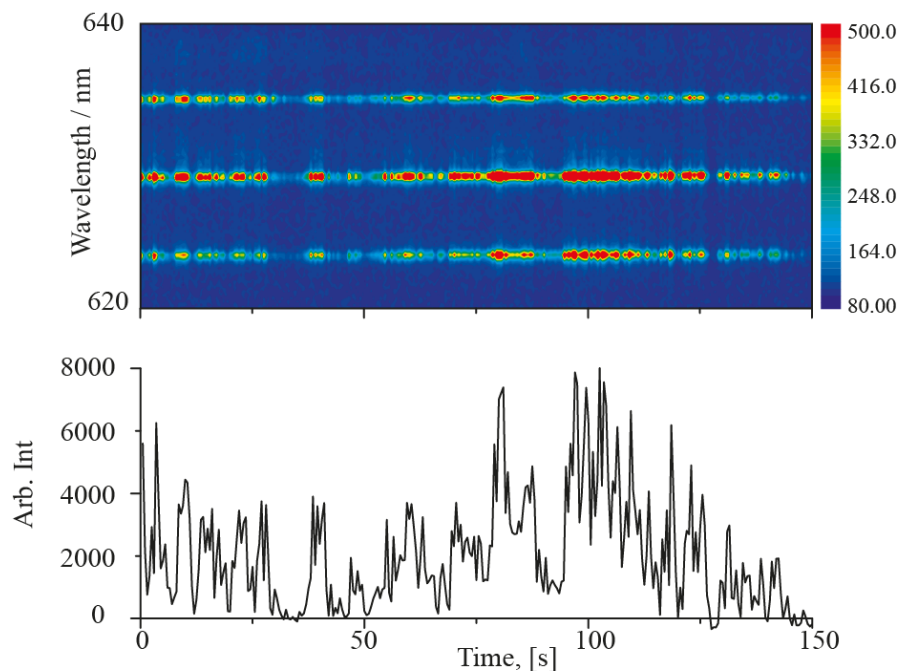


FIGURE 5.13: *Time series of spectra showing the intermittency of the nanocrystal photoluminescence suggestive of single dot detection (above). The lower plot shows the total PL over the same time period, with background subtraction. Data taken by Helene Jones.*

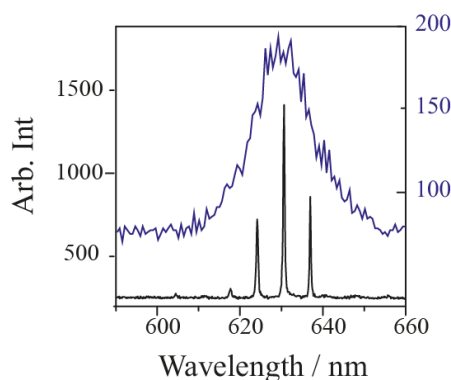


FIGURE 5.14: *Emission spectrum of a Lorentzian shaped, narrower emission profile suggestive of single dot emission (blue) plotted about the mode distribution for a highly diluted colloidal nanocrystal solution exhibiting comparable spectral extent. Data taken by Dr ZiYun Di.*

with twenty pairs of dielectric stacks. This process was performed commercially and so the precise details of the deposition method are unavailable, but it allows particularly pure dielectrics to be deposited using ion beam sputtering. These coatings can achieve ultra low absorptive losses, and so should be able to achieve reflectivities of 99.999%. It was found that when cavities were formed by these mirrors and white light transmission was attempted insufficient light was transmitted through the mirror pair, and so characterisation similar to that conducted in chapter 5 was impossible. It was realised

however that making use of nanocrystals to populate cavity modes would remove the requirement of the light to pass through a mirror prior to mode population. A limited series of data was obtained, and represents the very latest in what is achievable by this microcavitation approach. Figure 5.15 shows the PL obtained from a series of cavity

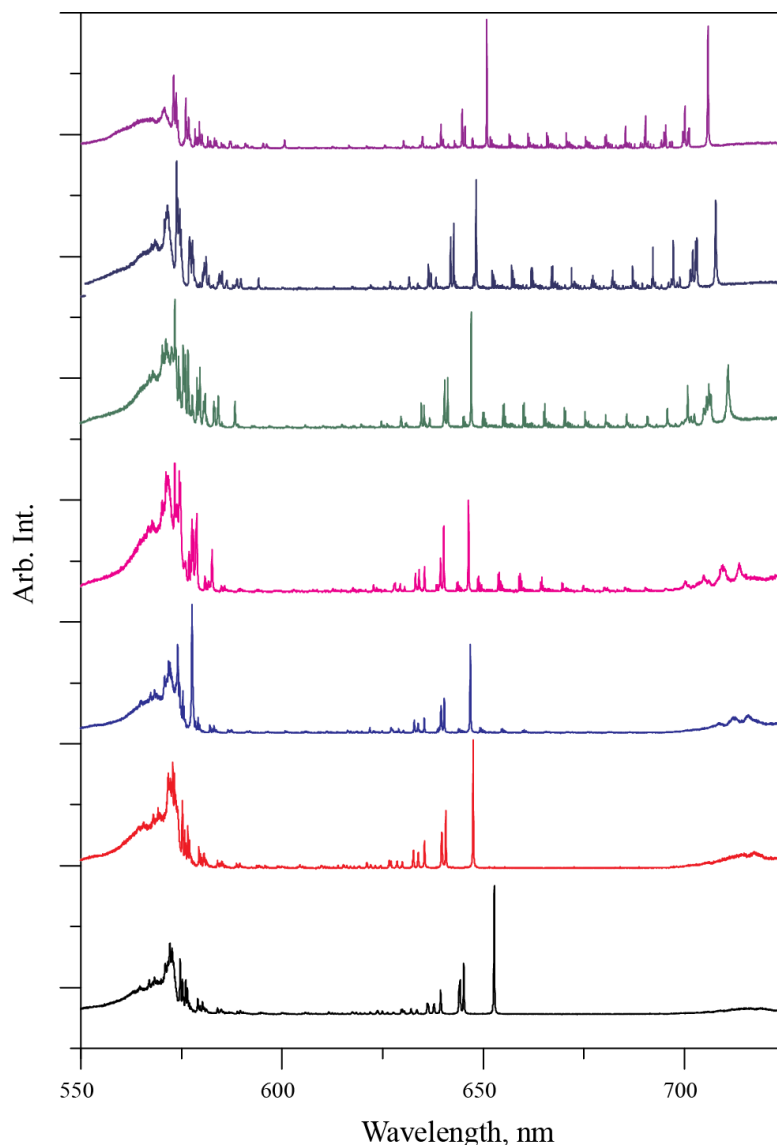


FIGURE 5.15: A stack of NC emission spectra coupled to the second iteration of microcavities produced. The uppermost plot is taken with a cavity length of $3.25 \mu\text{m}$. Each spectra below is taken after reducing the cavity length by a further 325 nm , so that a primary (TEM_{00}) mode is located at 650 nm . The lowermost spectrum corresponds to a cavity length of $\approx 1.25 \mu\text{m}$.

lengths, stepped through in an identical manner to the results shown in figures 4.10 and 4.12. The same batch of CdSe/ZnS nanocrystals previously mentioned in this chapter was used, however it seems that these nanocrystals have experienced a red shift of their photoluminescence, and it is now centred around 650 nm . In addition the inhomogeneous broadening has increased to be closer to 30 nm . Both of these features are

commonly observed phenomena for the degradation of such nanocrystals when exposed to air, and ultimately results in total loss of PL. The cavity lengths and Q-factors for these cavities are plotted for these cavities in figure 5.16 as black disks. The red disks are results obtained using the first iteration of cavities with the same nominal radius of curvature. The minimal lengths achieved for this set of cavities was comparable to those achieved with the first iteration once the plinth architecture was incorporated. The similarity of achieved Q-factor is rather surprising, as the second iteration (black points) had mirrors consisting of 20 pairs of very low loss coatings, and are expected to achieve much higher reflectivities, compared to the first iteration of cavities with mirror surfaces of only 9 pairs and $R = 99.4\%$. Shortly after this data set was obtained additional

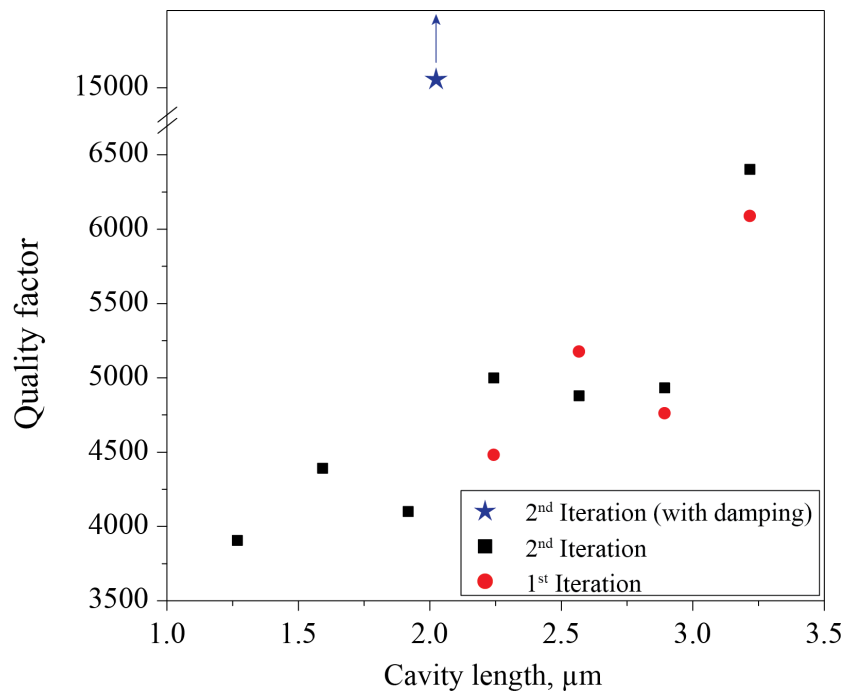


FIGURE 5.16: Comparison of the data series shown in figure 5.15 (black disks) with several of the results obtained from the first iteration of cavities (red disks). Also plotted is the result of a single spectrum obtained once additional care was taken to remove vibration and drift (blue star). The arrow emphasises this Q-value is a lower limit.

acoustic dampening was placed around the microcavity set-up, and the optomechanics were allowed relax over longer periods of time to mitigate drift. With these measures in place the spectrum shown in figure 5.17(a) was obtained showing a free spectral range of 75 nm, corresponding to a cavity length of 2.09 μm . This cavity displayed a mode width at the limit of the spectrograph's resolution, which places lower limit on the Q-factor's value of ~ 15000 . This is also included in figure 5.16 as a blue star. This mode is plotted on an expanded axis next to the highest Q-factor achieved by the first iteration (although for this mode the cavity length was considerably longer at around 12 μm) in figure 5.17(b), with the upper x axis showing the spectral region of the second iterations

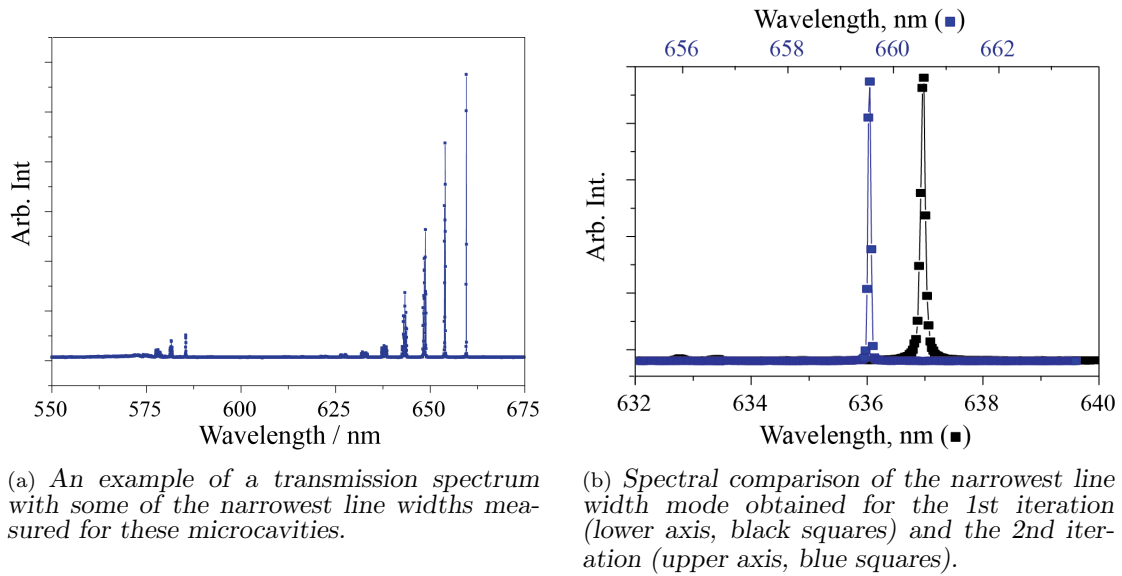


FIGURE 5.17: Spectral plots of nanocrystal PL populating cavity modes in the second iteration of cavities constructed (blue plots).

location. The plots are given with individual data points to indicate proximity to the resolution limit of the spectrograph. In this case the mode is sitting close to 660 nm, and so is spectrally some distance away from the very highest reflectivity (and therefore highest Q) region of the mirrors, and so even though the line width is too narrow to be ascertained accurately, it could be further narrowed by tuning the cavity length closer to 637 nm. Using the penetration depth of the field into the mirrors found earlier on in this chapter, the volume can be shown to be approximately $2.5 \mu\text{m}^3$. This volume can clearly be reduced, as smaller lengths were achieved for these cavities without the vibration dampening. The smallest volume, corresponding to the shortest cavity length plotted in figure 5.16 was around $1 \mu\text{m}^3$. Having found that direct interrogation with the spectrograph will not satisfactorily characterise this second batch of microcavities and an alternative experimental set-up would be required, further efforts to drop the cavity length whilst maintaining unquantifiably high Q-factors were halted. The high Q-factor observed in the spectrum shown in figure 5.17(b) and 5.17(a) was not the sole evidence that these mirrors are capable of exceeding the resolution of spectrometer. Another spectrum obtained whilst drift and vibrations were minimised is shown in figure 5.18, showing considerable coupling into the higher order modes. Crucial to the visibility of these modes is the narrowness of the peaks. Figure 5.19 shows a smaller region of these modes fitted with Lorentzian line fits. Even at these spectral locations, which are reasonably close to the edge of the reflectivity band of these mirrors the line widths are close to the resolution limit of the spectrograph for the longest wavelengths and quickly reach the resolution limit as the modes location gets closer to the highest reflectivity of the

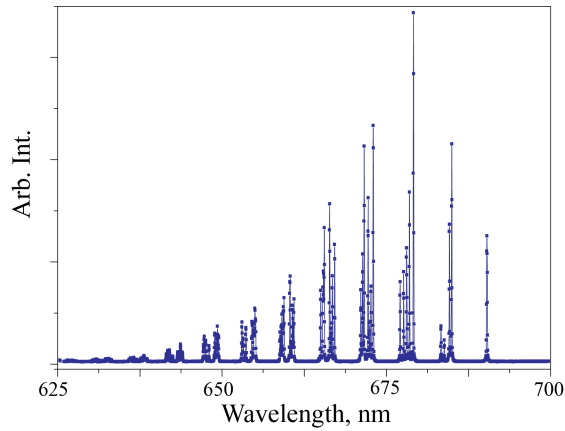


FIGURE 5.18: *Emission spectrum obtained showing coupling of PL to transverse modes right up to the $m + n = 10$ case. This spectrum also clearly shows the degradation of the nanocrystal solution, redshifting past 675 nm.*

mirrors. For these features the full two dimensional surface fitting technique discussed in chapter 3 was implemented, and so a factor in the improved coupling to these modes could also be the improved sphericity of the features. Another obvious difference on top

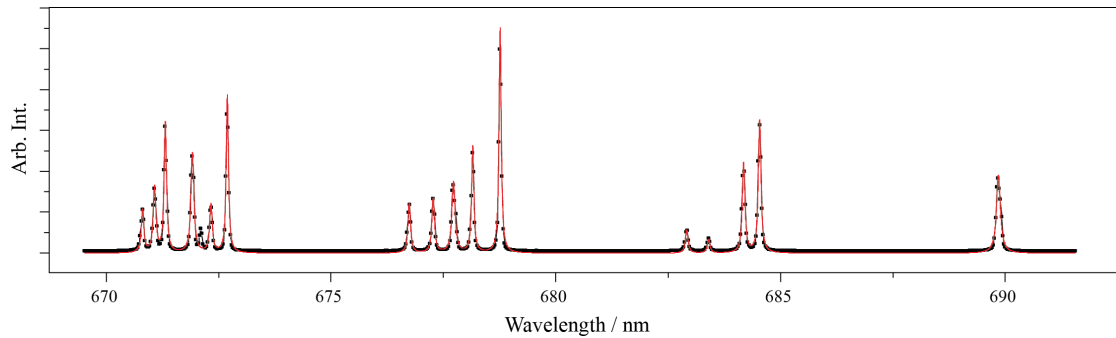


FIGURE 5.19: *Expanded view of the $m + n = [0, 1, 2, 3]$ TEM_{mn} shown in figure 5.18. Note the additional degeneracy which has been lifted for the TEM_{01} and TEM_{10} modes.*

of the additional visibility of the transverse modes is the appearance of additional mode structure. In previous chapters the TEM_{01} and TEM_{10} degeneracy which is lifted has only been two fold, where as in these spectra it has doubled to being four fold. This was investigated by passing the collected photoluminescence through a linear polariser. The polariser was then rotated through π radians in several approximately equal intervals. This highlighted the polarisation dependence of the mode structure. Figure 5.20 shows this dependence, with the central arrows showing the approximate angle of the polariser during the collection of the PL. The overall displacement comes from the ever present drift (although in this case it was as low as the set-up has achieved to date). The figures shown along the edges of the spectra are a suggested arrangement of polarisations with respect to the major and minor axis of the elliptical feature.

in excess of 15000 can be achieved with volumes at least as low as $1 \mu\text{m}^3$. This suggests a considerable increase in the optical cavitation effects, and a marked improvement over the first iteration. Results from other groups making use of high reflectivity mirrors very similar to the ones used here have quoted values for the finesse of the cavities of the order of 10^5 [24–26]. Should these values be confirmed for the features described here, these microcavities stand an excellent chance of achieving considerable Purcell enhancements and even approaching the strong coupling regime. Improved population of the transverse modes also indicates more hemispherical features achieved, compared to the first iteration. A final data set showed the emergence of non-degenerate polarisation specific mode distributions.

Chapter 6

Nanodiamonds in Cavities

6.1 Introduction

As well as nanocrystals, efforts were also made to couple nitrogen vacancy defects in diamond to microcavity arrays. The goal of this series of experiments was to measure Purcell enhancements of these emitters at low temperature, which experimentally is a significant complication. After a brief introduction and review of the historical background of the NV centre and some recent publications relevant to optical coupling, the home built scanning confocal microscope will be introduced. This will include a few further characterisation details of the microcavities, as well as some results obtained during the characterisation of the nanodiamonds used as the source of NV centres. Finally the chapter will end with a description of the low temperature cavity coupling optical set-up which was designed and constructed at the end of this thesis.

6.2 The Diamond and the Nitrogen Vacancy Defect

Diamond is renowned for its optical and mechanical properties, with its high refractive index (2.418 for 500 nm) and hardness (the ancient Greek for unbreakable being the root of its modern name) contributing to its aesthetic appeal. Other useful properties extraneous to its gemstone attractiveness are its impressive thermal conductivity (900 - 2400 W/mK, cf. that of Cu at 400 W/mk) and large band gap (5.5 eV). Boron, a common impurity in diamond which is responsible for a blue hue, is a good 'p' type dopant, and should a suitable 'n' type dopant emerge, its thermal conductivity could make it preferable to silicon as a semiconductor in certain circumstances. Advances in synthetic diamond production have proceeded along two main avenues, that of the high pressure high temperature (HPHT) in which carbon is crushed into its diamond

allotrope, and chemical vapour deposition (CVD) in which the crystal is grown by allowing atoms of carbon to deposit on a pre-existing substrate, normally another diamond. It is now possible to grow high purity diamond of a standard that does not exist in nature. Nanocrystals of diamond, as opposed to bulk crystals have also been used in many experimental investigations, as they often provide a way of isolating single defect centres. Diamond has more than 500 defects catalogued [96], with over 100 luminescent defects naturally occurring [97], and partly owing to each stone's intrinsic value, a large proportion of these have been analysed in sufficient detail to reveal several remarkable properties. The most notable in recent times of these is the negatively charged nitrogen vacancy (NV) centre [98], although new centres are continually being identified and investigated [99–107]. The first spectrum of the NV centre was published in 1971 [108] and five years later it was attributed to a nitrogen based defect [109]. Theoretical descriptions of the centre did not emerge until much later, and a noteworthy initial study by Lenef *et al* contained both experimental and theoretical progress [110, 111]. The theoretical paper considered the general case of two, four or six electrons (the triplet state had been identified by electron paramagnetic resonance (EPR), [112, 113] and hole burning [114, 115] experiments) in the NV. In 2006 Manson *et al* [116] made a large contribution to a complete description of the electronic states by showing that it is in fact six electrons, although *ab initio* work is still progressing [117, 118]. In an important study in 2004, the group led by Wrachtrup *et al* [119] demonstrated single centre read-out, spin polarisation and coherent oscillations all at room temperature. In this case it was nanocrystals that were used, but there have been demonstrations making use of single crystal diamond for single photon generation [120–122] and coherent population trapping [123]. In fact NV centres are promising candidates for a whole range of possible QIP (quantum information processing [124–128]) applications, and have been shown to couple to nuclear spins [119, 129, 130]. In terms of QIP, the double heralding scheme proposed by Barrett and Kok in 2005 [131] offers a measurement-based approach to realise a scalable diamond based quantum computer [132, 133]. This scheme makes much less rigorous demands on the Q factor of the cavity being used, (also see [134, 135]) which many other approaches require [136, 137].

A lot of effort has been invested by the scientific community in recent years to find suitable methods of extracting these photons in a more efficient way by coupling to optical microcavities. Silica and polystyrene microspheres were used in [138] and [139] respectively and were coupled through the evanescent field to NV centres in nanodiamonds. In the former case strong coupling was observed, but in neither case were particularly large collection efficiencies recorded. Efforts were also made to couple a 200 nm nanodiamond to a high Q microdisk involving nanoscale manipulation of the nanodiamond with a tapered optical fibre [70], which recorded values of < 1 for the Purcell enhancement of

the ZPL. The small degree of enhancement is at least partly due to the NV centre's unfavourable Debye-Waller factor, which is related to the ratio of phonon assisted emission to phonon free emission. An alternative approach was used in [140, 141] in which the entire microdisk was constructed out of a polycrystalline diamond, however the disks constructed were unable to achieve usefully large Q factors. In 2006 Tomljenovic-Hanic *et al* published a couple of papers outlining developments recently made with the application of photonic crystal cavities [142, 143] to optically couple light out of the emitters. Of particular interest to this review is the latter, [143], in which diamond is taken as the substrate. In this paper two optimisation approaches are applied to the periodic structure in the photonic crystal, and the optimum Q factor found was 6000 for the diamond substrate. To conclude it seems that efforts to couple native NV centres in bulk diamond to optical microcavities constructed directly in the diamond itself will require advancements in nanofabrication techniques. When nanodiamonds are used in place of bulk diamonds coupling is more straightforward although it is generally accepted that the extraordinary spin coherence of the NV centre is absent. This spin coherence has still allowed for many many publications which demonstrate various quantum effects including repetitive read out, single shot measurements and dynamic decoupling from the background spin bath [144–150]. An alternative photon extraction method to microcavitation is to make use of a solid immersion lens (SIL) [13, 151–153]. This step forward only helps with the collection of photons emitted by the NV centre and so will never achieve the suppression of undesirable phonon assisted decay routes or enhancement of ZPL photons. Nevertheless this advance has allowed for the entanglement of two remote NV centres through their emitted photons, which is a major milestone towards a fully distributed quantum information processor [151].

6.3 Experimental Set-up

In order to optically interrogate NV centres a home built scanning confocal microscope was constructed [154]. The optical elements comprising this system are shown schematically in figure 6.1. In this diagram, and in the experiments in general a frequency doubled neodymium - yttrium aluminium garnet (NdYAG) laser was used as the excitation laser. When set to its maximum power output this system could achieve delivery of around 10 mW of laser power to the sample. In doing so the light is directed through a dichroic mirror and off a fast steering mirror, marked as 3 and 7 in figure 6.1 respectively. The fast steering mirror uses a mechanism very similar to a domestic speaker system and can rapidly and reproducibly alter the angle of incidence the static excitation beam makes with the mirror surface. When combined with two tele-centric lenses forming a '4-f' (standing for four focal lengths) system, this results in the ability to shift the angle

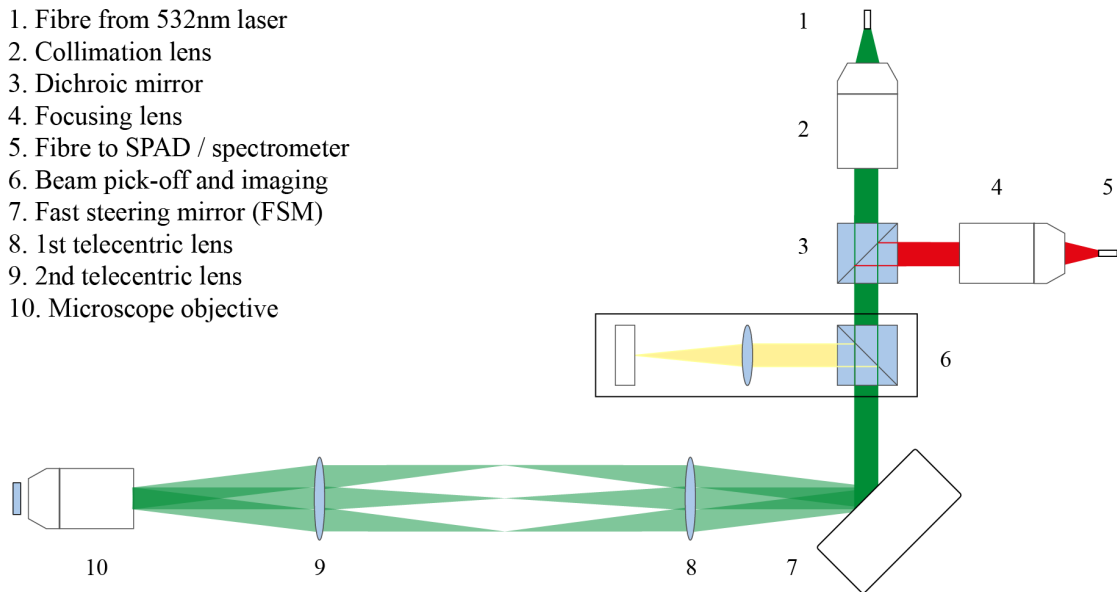


FIGURE 6.1: Schematic of the scanning head used to control the location of the focus of the collection optics (marked 4 and 5) and the excitation beam (marked 1 and 2). The dichroic mirror is selected so that it reflects red photoluminescence and transmits green excitation light. This light is then directed through a 4- f system via a fast steering mirror, allowing the confocal spot at the sample to be scanned by the distal scanning optics.

of incidence of the excitation beam into the microscope objective located at the sample (marked 10 on the diagram), which corresponds to a shift in the location of the beam's focal spot in the microscope objective's focal plane. With the development of appropriate control software, this allowed the focal spot to be scanned across the sample and the position of the spot (calculated from the angular shift of the FSM) to be matched with the count rate recorded by the collection fibre (marked as 5) to construct an image of the photoluminescence. In this case it is the fibre optic cores at locations 1 and 5 in the set up which are providing the pin-holes to get the benefit of confocally exciting and collecting only from the same region. The presence of the tele-centric lenses becomes vital when it is desirable for the sample to be cooled, as they allow the optical components of the scanning head to be distal to the sample and microscope objective. The resolution of this microscope is limited by the confocal spot size, which is ultimately limited by the numerical aperture of the microscope objective. Figure 6.2 shows the smallest resolvable feature from an N.A. = 0.7 microscope objective, in this case an NV centre in bulk diamond. This essentially is an image of the excitation beam profile at the focus, and represents the limit of standard diffraction limited microscopy.

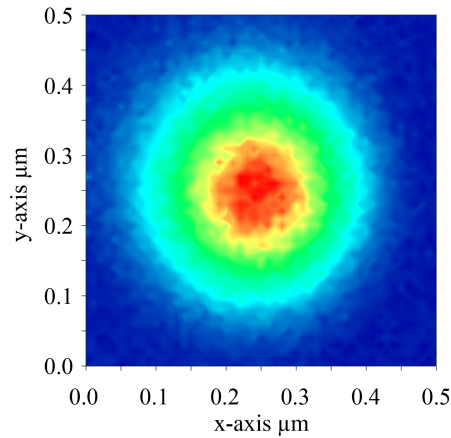
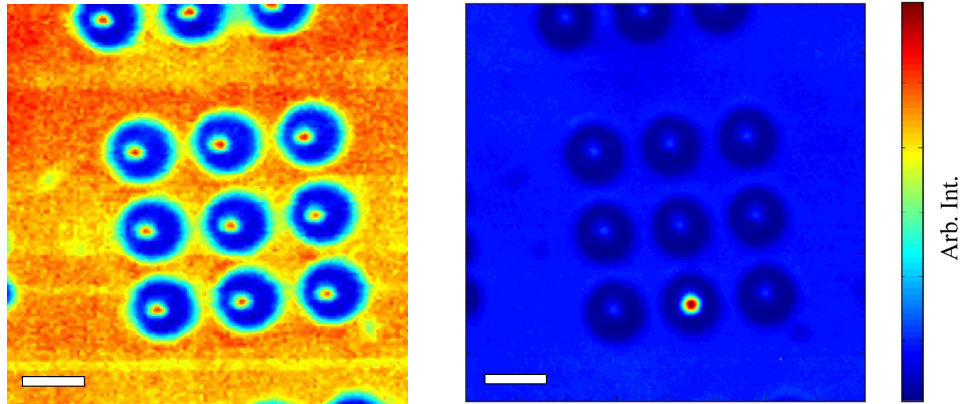


FIGURE 6.2: *Diffraction limited spot obtained by the home built scanning confocal microscope by imaging the PL of an isolated NV centre in bulk diamond. Image taken by Dr Brian Patton.*

6.4 Scanning Confocal Imaging of Microcavities

It was possible to combine the scanning confocal head described above with the transmission set-up illustrated in chapter 4, figure 4.1. This allowed for an additional imaging capacity for the characterisation of the empty cavities. By using either broad or focused illumination, scanning confocal images of the cavities can be obtained provided the signal is sufficiently attenuated to avoid damaging the single photon detector. These two illumination schemes are shown for the second iteration of cavities with the image on the left showing de-focused white light illumination and the right showing the light being focused into a single cavity. In this arrangement it is only the collection spot which is being scanned, with the cavities being back illuminated by a static light source. Clearly in both cases the illumination is populating cavity modes. During the collection of the focused illumination image a weak source of diffuse white light was left on, which allows the positions of the cavities to be identified. One realisation from consideration of these images is that there does not appear to be the same variety of spatial distributions of cavity modes as in figure 5.4(a) taken during nanocrystal investigations with the spectrometer. This can be explained since incorporated in this optical set-up is a kinematic degree of freedom, so the cavities can be made much more parallel. Once the imaging is complete, the collection fibre can then be coupled into the spectrometer and the steering mirror control software can direct the collection spot back to any particular features of interest to obtain spectral information. Collection from the focal spot in figure 6.3(b) yields identical results to those obtained for the white light transmission measurement performed during characterisation in chapter 4. Once the optical set-up was arranged in this way it was possible to use 637 nm laser illumination to provide the focal spot rather than white light. In this way it was possible to excite individual modes, due to the narrow spectral width of the laser illumination. By carefully varying the cavity length it



(a) Image obtained by scanning confocal head of cavity arrays in transmission optical set-up shown in figure 4.1 with de-focused illumination.

(b) The same region as shown in figure 6.3(a) with diffuse illumination to indicate cavity position and a fibre coupled WLS focused into a single cavity.

FIGURE 6.3: Scanning imaging of the white light illuminated cavities. This can be performed with diffuse (a) or focused (b) illumination, scale bar $10\ \mu\text{m}$.

was possible to tune different cavity modes into resonance with this illumination. This is illustrated, along with the anticipated Hermite-Gauss mode outputs in figure 6.4. A selection of the spatial mode distributions obtained in this manner are shown in figure 6.5. The first series of images, a_1), a_2) and a_3) clearly show the expected spatial distributions for Hermite-Gauss mode structure discussed in chapter 2, and correspond to TEM_{00} , TEM_{10} and TEM_{01} respectively. The second sequence has missed out the primary TEM_{00} mode and shows a more complicated mode structure, likely to be due to combinations of various stable higher modes due to a slightly irregular surface shape. Although a more thorough investigation into the mode structure of the cavities could have ensued, it would have required the introduction of a piezo-electric actuator to allow more precise control. As the aim of this thesis is to couple emission to the primary modes, since they possess the smallest mode volumes, the discussion will now move onto results taken from the optical interrogation of NV centres emitting into free-space.

6.5 Preliminary NV Centre Studies

The ability to perform scanning confocal microscopy at low temperatures is advantageous for the NV centre as it reduces the thermal broadening of the zero-phonon line, and allows it to be spectrally selected. The temperature dependence of the NV centre's spectral emission properties is clearly visible for native NVs in bulk diamond, and is shown in figure 6.6. Ultimately the goal of this chapter is to be able to couple the ZPL of the NV centre at low temperatures to a cavity mode, as substantial Purcell enhancement of

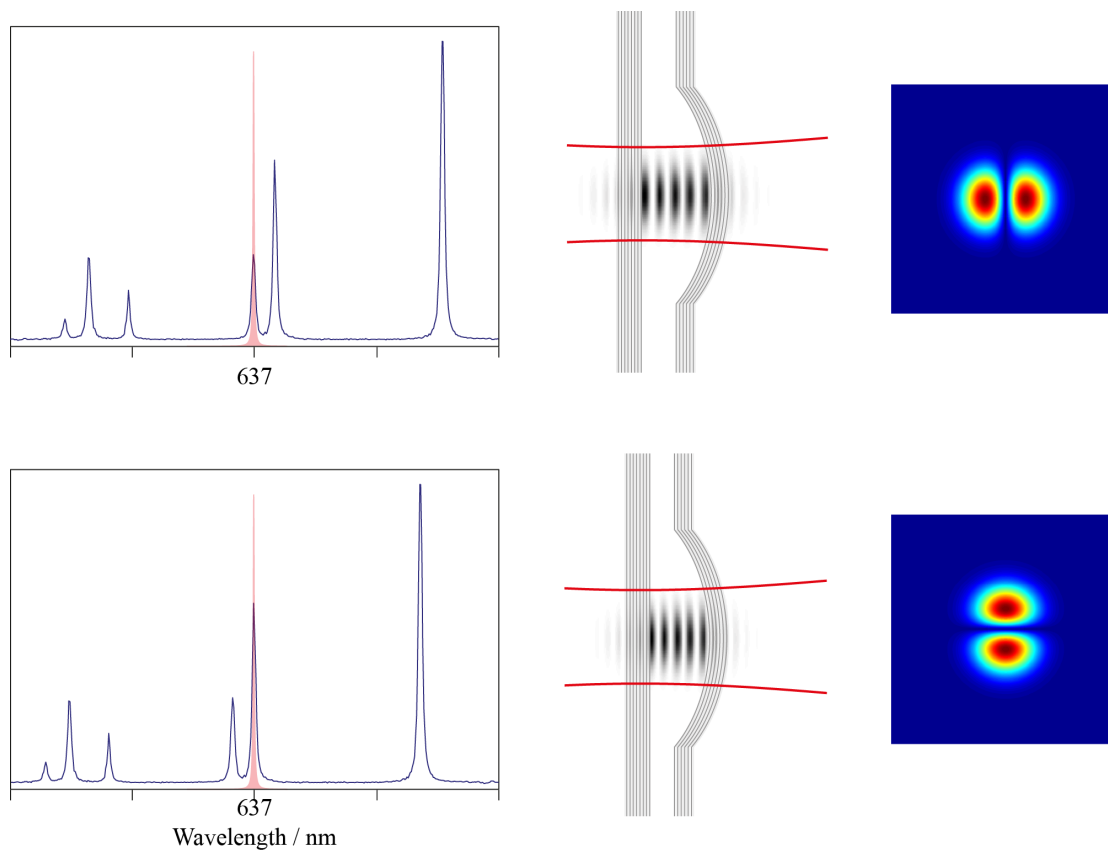


FIGURE 6.4: Schematic indicating the method for imaging the higher order modes. The spectra show the alignment of the higher order mode with the 637 nm illumination. The cavity schematics show the required length tuning, and the images the anticipated mode structure.

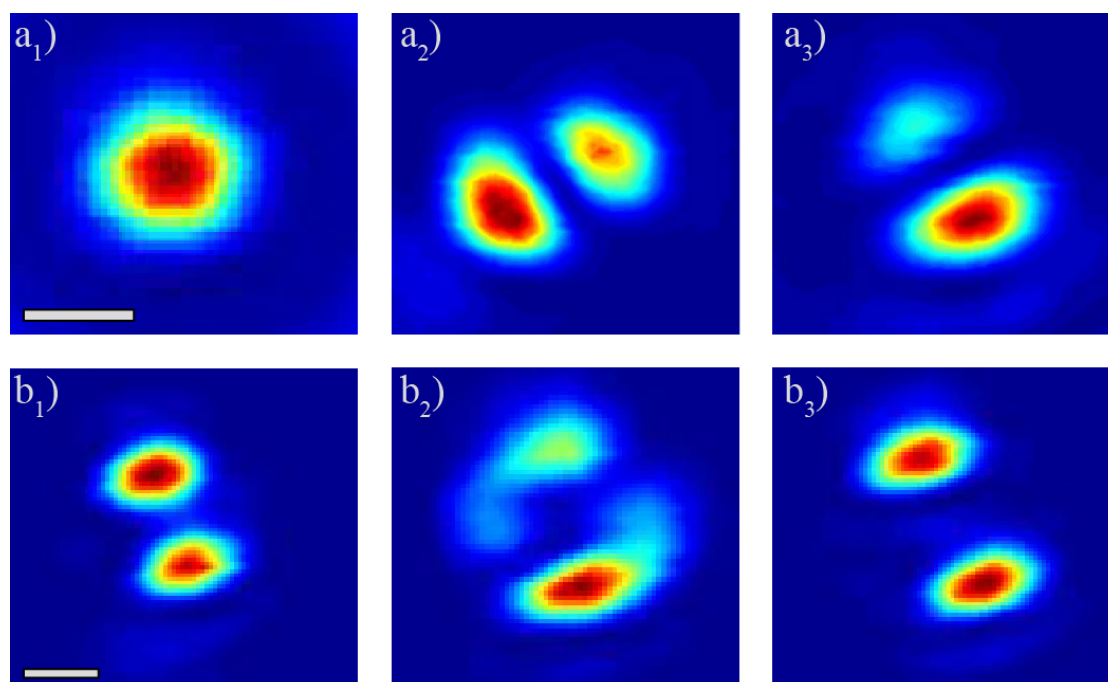


FIGURE 6.5: Two sequences of higher order modes obtained by tuning the length to allow successive cavity modes to become resonant with the 637 nm laser illumination. Scale bar 2 μm .

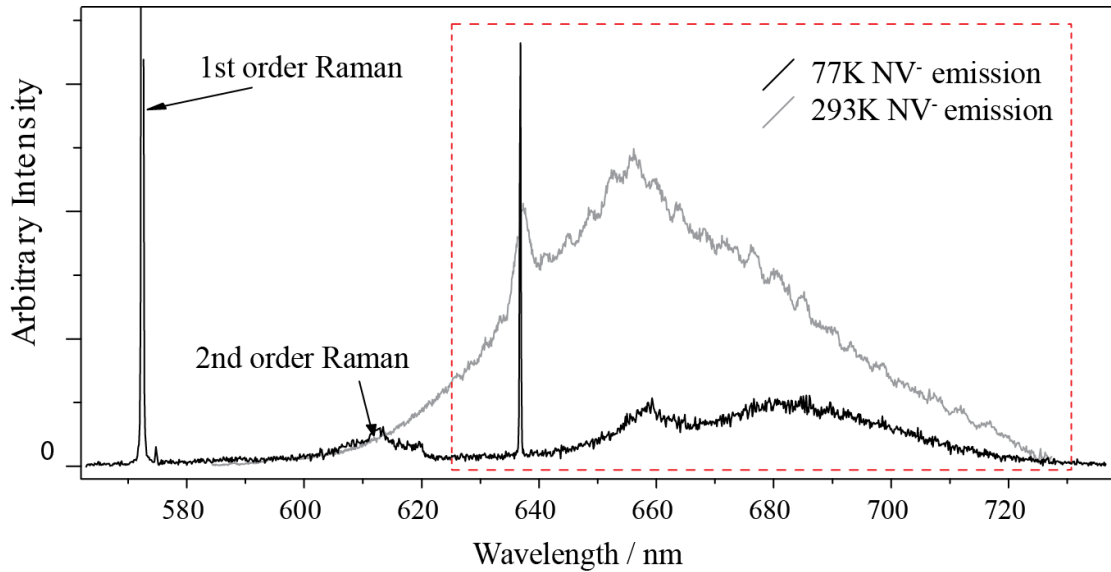


FIGURE 6.6: Spectra for the NV^- colour centre obtained at room (grey) and liquid nitrogen (black) temperatures. Also marked on the spectrum are the first and second order Raman peaks generated by the non-linear response of the diamond crystal.

this transition would be profoundly useful in the development of a distributed quantum computer. This chapter will go on to show the development towards this goal although in the end it was regrettably not achieved. The results shown in figure 6.6 make use of bulk diamond as the source of NV centres. Native NVs in single crystal isotopically pure diamond have shown the longest spin coherence times [155], and so any effort to couple NV emission to a cavity mode should be ultimately compatible with bulk diamond. For the approach, which is the topic of this thesis, it is definitely conceivable that some of the thin ($\sim 1 \mu\text{m}$) film single crystal diamond substrates which are beginning to be produced could be placed on the planar mirror. Initially however nanodiamonds will be used as the source of NV centres, and the samples used for the rest of this chapter were kindly provided by collaborators in the University of Melbourne.

The nanodiamonds were prepared in a solution of methanol and drop cast onto the planar mirror surfaces prior to being placed into the scanning confocal microscope. Several mirror surfaces were marked with registration features making use of the patterning engine of the focused ion beam, in order to facilitate the ability to revisit the same nanodiamonds. Figure 6.7(a) shows the optical image of the marked planar mirror, with the approximate area scanned by the 532 nm excitation source marked in red. This photoluminescence image is shown in 6.7(b). In order to proceed towards cavity coupling of single NV centres to optical cavity modes it has to be established whether any particular luminescent point shown in figure 6.7(b) is generated by a single NV centre. Coupling the collection fibre into the spectrometer will reveal whether it is some form of NV emission, but in order to tell conclusively that it is a single centre

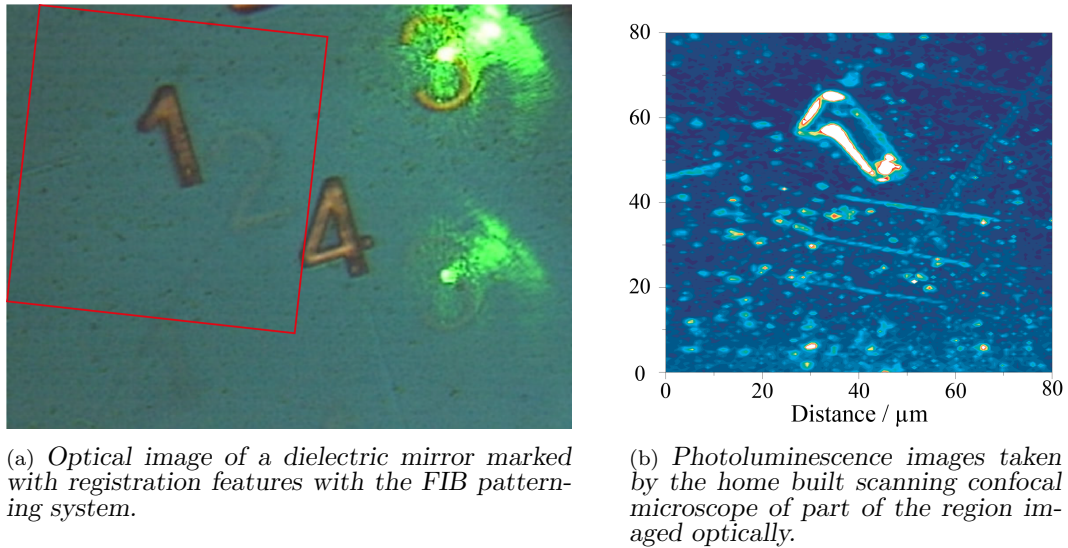
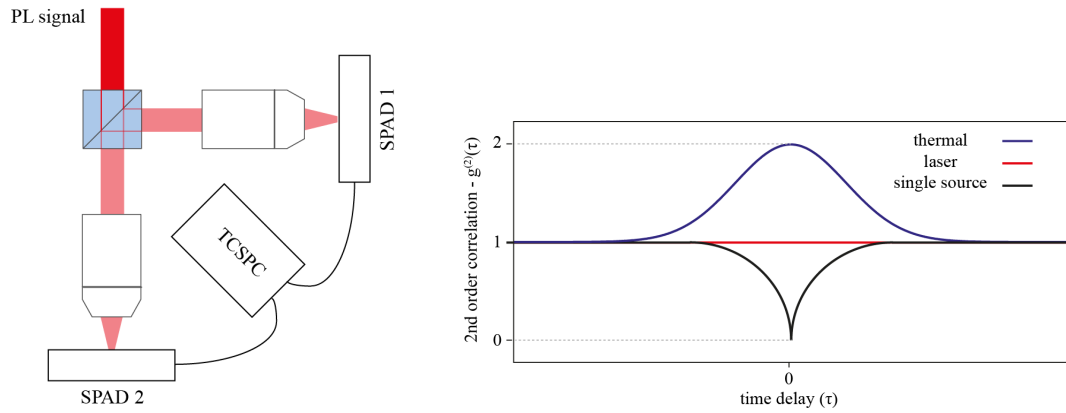


FIGURE 6.7: Optical and PL images of the FIB marked dielectric mirrors.

a Hanbury-Brown Twiss measurement needs to be taken. This makes use of the same fast counting device used to correlate the arrival times of the photons with the trigger times of a pulsed laser. In this case however the photoluminescent signal is split by a 50:50 beam splitter, and the end of each path is directed to the SPAD, as shown in figure 6.8(a). In practice it was more convenient to use a fibre beam splitter which splits light via the evanescent field in the fibre cladding. It is now the arrival times of photons at each of the two detectors which are tracked. This experimental apparatus effectively monitors the intensity correlation properties of the light being split, and figure 6.8(b) shows sketches of ideal second order correlation plots for three forms of radiation - thermal, laser and single emitter as described in [86]. Experimentally, histograms of the arrival times can be straightforwardly achieved from the time difference in the arrival time of the photons. Either electronically or physically one of the paths between beam splitter and the detectors in figure 6.8(a) can be increased. This has the effect of shifting the location of the expected anti-bunching feature in figure 6.8(b) up and down the time axis. In order to categorically say that it is in fact a single quantum emitter it is necessary for the anti-bunching dip to reach below half of the average count rate at long delay times, and in ideal situations this dip should reach right down to zero.

This approach, combining the FIB milled registration marks on the mirror and the HBT analysis would eventually allow for a complete characterisation of the decay rates fitting curves to the anti-bunching dips observed. Figure 6.9 shows one such region, with three stable, diffraction limited sources of photoluminescence circled and labeled. Their corresponding HBT data is shown in figure 6.10. Experimentally speaking obtaining this data was considerably time consuming, as clear from figure 6.9 within a very small



(a) Schematic of the signal splitting and correlation arrangement in order to record second order correlation measurements (HBTs).

(b) Theoretical second order correlation functions for thermal, laser and single emitter radiation.

FIGURE 6.8: Schematic of the optical set-up for obtaining the experimental HBT results and the theoretical results for results obeying Bose-Einstein (blue) and Poissonian (red) statistics, and a single emitter (black).

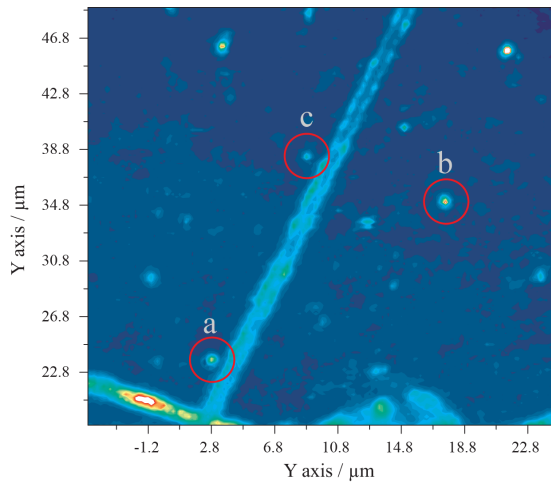


FIGURE 6.9: PL map of marked substrate with the locations of three emitters highlighted for photon statistical analysis.

region there are many possible candidate sources. In this case each one was checked and the very best three were selected. In fact a considerable portion of the substrate was examined in this way yielding very few positive identifications of single emitters. The likely explanations for why the chances of getting high quality anti-bunching data is so low lies in the sensitivity of the measurement to background radiation and noise. For example in bulk diamond the only contribution to background count rates in the vicinity of the NV centre comes from Raman generated photons. This can be easily filtered and positive HBT dips are straightforward to find. With nanodiamond the surface of the crystal lies well within the diffraction limited spot size and so any contaminants on or

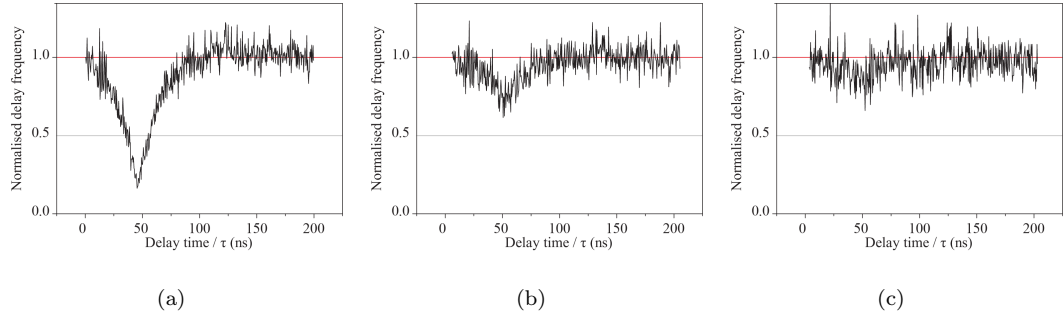


FIGURE 6.10: *HBT data for the three marked emitters in figure 6.9. The first shows clear single emitter statistics, whilst the second show a partial anti-bunching. The third has only the slightest of anti-bunching dips visible.*

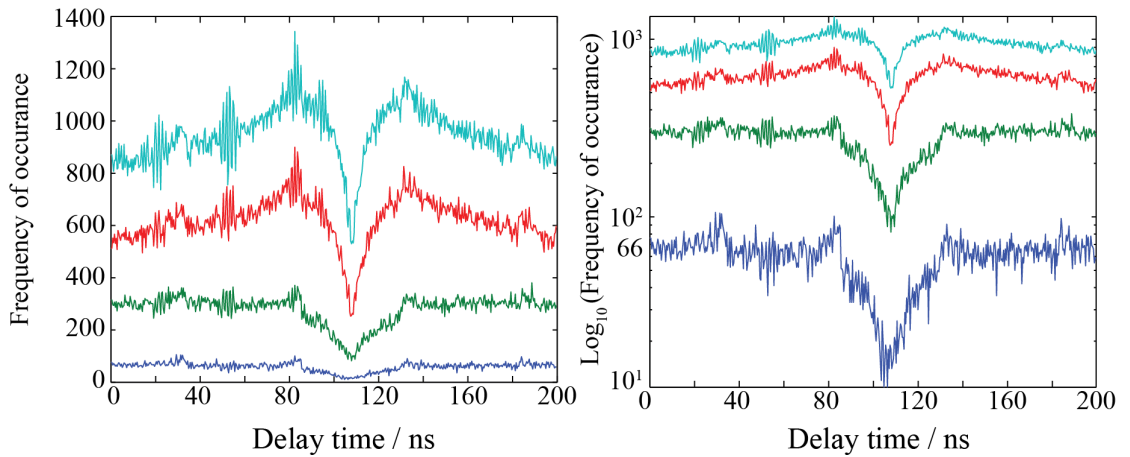


FIGURE 6.11: *Linear and logarithmic y-axis plots for various illumination intensities of the same emitter. There is clear bunching around the central anti-bunching dip, indicating the presence of a third, metastable ‘dark’ state.*

around the nanodiamond can contribute to a background count rate. Cleaning processes are vital in order to increase the prohibitively low rate of success. The fact that these nanodiamonds were distributed on distributed Bragg reflectors removes high temperature oxidation as a cleaning method since large sustained increases in temperature can cause catastrophic de-lamination of the mirror surface. It was discovered towards the end of the thesis that short time spans of plasma cleaning will not alter the reflectivity of the mirror surface. The final point of discussion relevant to the NV centre’s second order correlation function is the intensity dependence. Due to the fact that the NV centre is comprised of an optically active transition between ground and excited states with a long lived dark metastable state situated between them, the NV centre displays pronounced bunching of the HBT plots as the incident intensity is increased. These are shown on both log and linear scales in figure 6.11. It is this metastable dark state which is responsible for the room temperature optically detected magnetic resonance and is

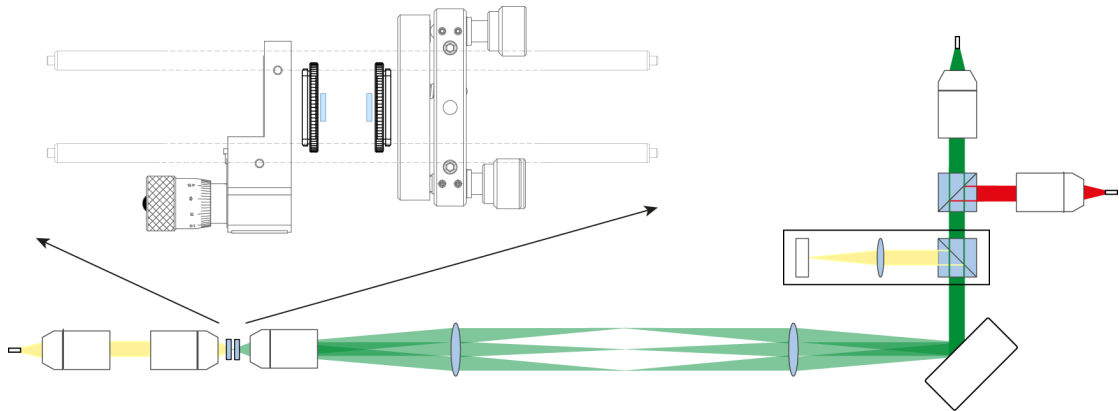


FIGURE 6.12: *Schematic of the optical set-up used to obtain room temperature coupling of NV centres to optical microcavities.*

also crucial for the distributed QIP approaches mentioned previously. This study sufficed as a proof of principle series of experiments, and it was decided that once a suitable optical set-up was constructed and shown to work an appropriate sample could then be marked and characterised in free space, and then re-characterised whilst coupled to an optical microcavity at low temperature to ascertain the cavity's effects. At this point it was decided that some effort would be directed towards room temperature coupling of NV centres in nanodiamonds to the microcavities, with a view to quickly moving onto the design and construction of the low temperature set-up.

6.6 Room Temperature NV Centre Coupling

Proceeding with the combined set-up utilising the room temperature transmission and the scanning confocal head it was possible to arrange arrays of the microcavities opposite a planar mirror as shown in the schematic in figure 6.12. An important note on the optical set-up is that it was found that incorporating any relative $x - y$ motion between the two mirrored substrates had intolerable adverse effects on the stability. In any case, the manual positioners available had insufficient accuracy to achieve the goal precisely tuning an NV centre to the field maximum of a TEM_{00} mode. Furthermore, any necessarily convoluted adaptation of the room temperature set-up would be mis-directed effort, as low temperatures are required to isolate the ZPL as at room temperatures the line-width of the NV centre is far too large to measure any enhancement. The goal of this series of experiments is therefore simply to find evidence of coupling. With the $x - y$ degree of freedom unavailable the arrayed nature of the microcavities reveals its usefulness. Figure 6.13 is an illustration of the illumination scheme for this series of experiments. In order to perform the PL scans a relatively high numerical aperture lens was used, with variable cover slip correction. This is especially important for the experiments described here,

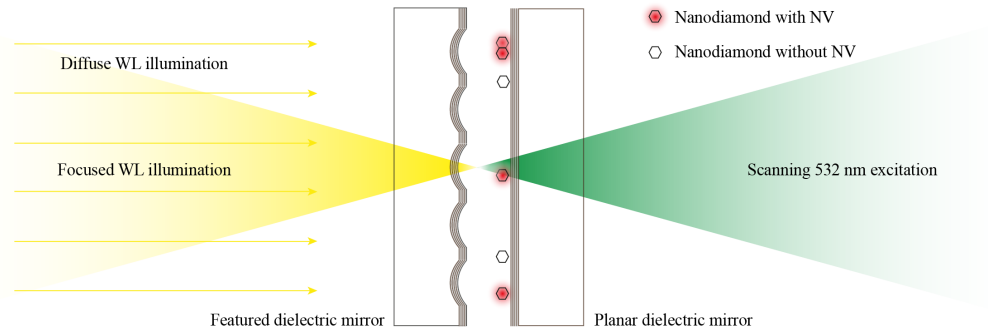
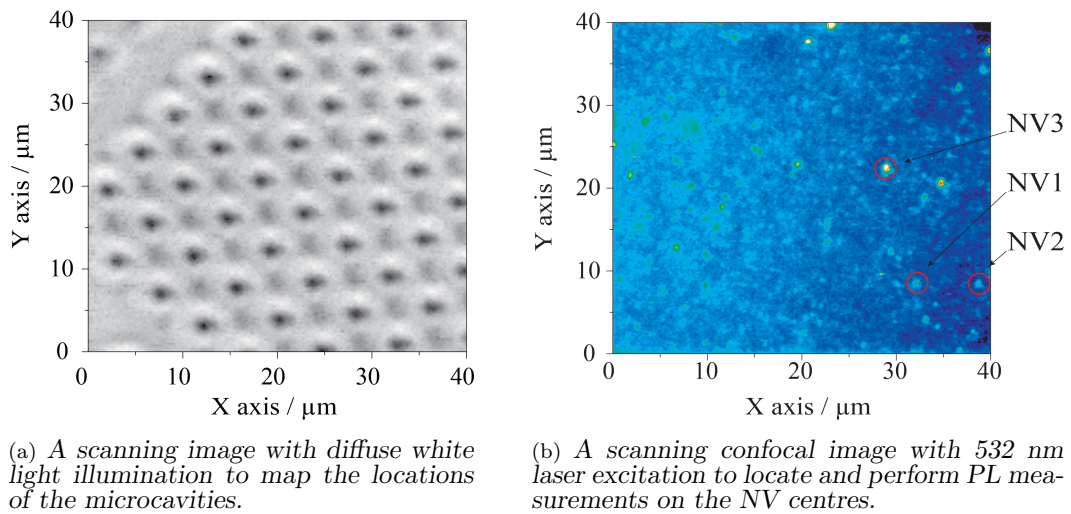


FIGURE 6.13: An illustration to clarify the emitter and microcavity arrangement.



(a) A scanning image with diffuse white light illumination to map the locations of the microcavities.

(b) A scanning confocal image with 532 nm laser excitation to locate and perform PL measurements on the NV centres.

FIGURE 6.14: Consecutive images taken to ascertain the relative positions of the NV centres on the front planar mirror and microcavities on the back featured mirror.

as a large portion of the possible \mathbf{k} vectors will be reflected away from the collection optics due to the presence of the dielectric mirror, and so efficient PL collection was of paramount importance. That said, once an NV centre is well coupled to a microcavity an increased portion of its emission will be directed into easily collected modes, as discussed in chapter 5. Figures 6.14(a) and 6.14(b) are scanning confocal images of the same area, with the former being back illuminated by a diffuse white light source and the latter a more routine PL scan with 532 nm excitation. The white light image is plotted with a grey colour scale, and clearly shows the position of the cavity array. At this stage the cavity length was reduced so that the mirrors were in contact so the mode drift would be reduced. In addition this measurement was performed on substrates without the featured plinth arrangement discussed in chapter 3 section 3.4 and used throughout 5. Labeled on the PL image are three stable, point like emitters that were spectrally interrogated. The motivation for the selection of these three emitters in particular can be seen most clearly in figure 6.15, which shows the superimposing of these two figures.

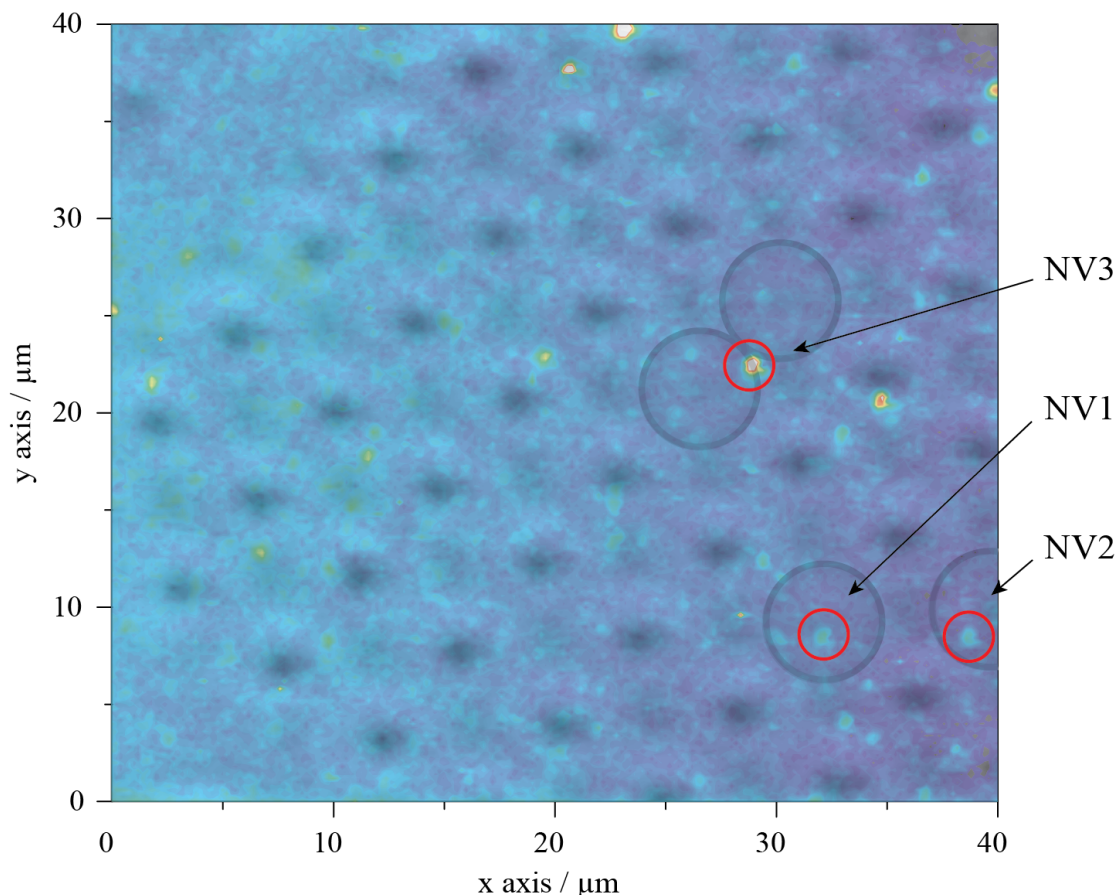


FIGURE 6.15: *The images in figure 6.14 superimposed on one another to clearly show the relative locations of the NV centres and the optical microcavities*

In addition to superimposing one image on the other, the locations of several relevant cavities have also been highlighted. From this image it may be predicted that centres 1, 2 and 3 will experience a variety of spatial coupling efficiencies to the cavity modes, as clearly emitter 3 is located opposite the boundary between two microcavities, emitter 2 towards the edge of a cavity, and emitter 1 closer to the centre. The spectra obtained from these points are plotted in figure 6.16, and support this line of reasoning. For emitters 1 and 2, the ranges over which cavity coupling occurs is closely comparable to the room temperature emission range of the NV centre into free space (grey plot in figure 6.6). This, combined with the small spatial extent and high stability even under intense illumination support the assertion that this is in fact NV centre coupling to cavity modes. A final set of data was recorded by focusing white light into the cavity that the NV centre marked as 1 is situated opposite. The transmission spectrum obtained this way, along with the photoluminescence of NV centre 1 are plotted in figure 6.17. As expected there is a strong agreement between the mode locations and as with the colloidal nanocrystals, a stronger coupling to transverse modes is apparent. Attempts to vary the cavity length results in considerable lateral shifts between the mirror, making it impossible to track the increase in coupling efficiency and collection efficiency one

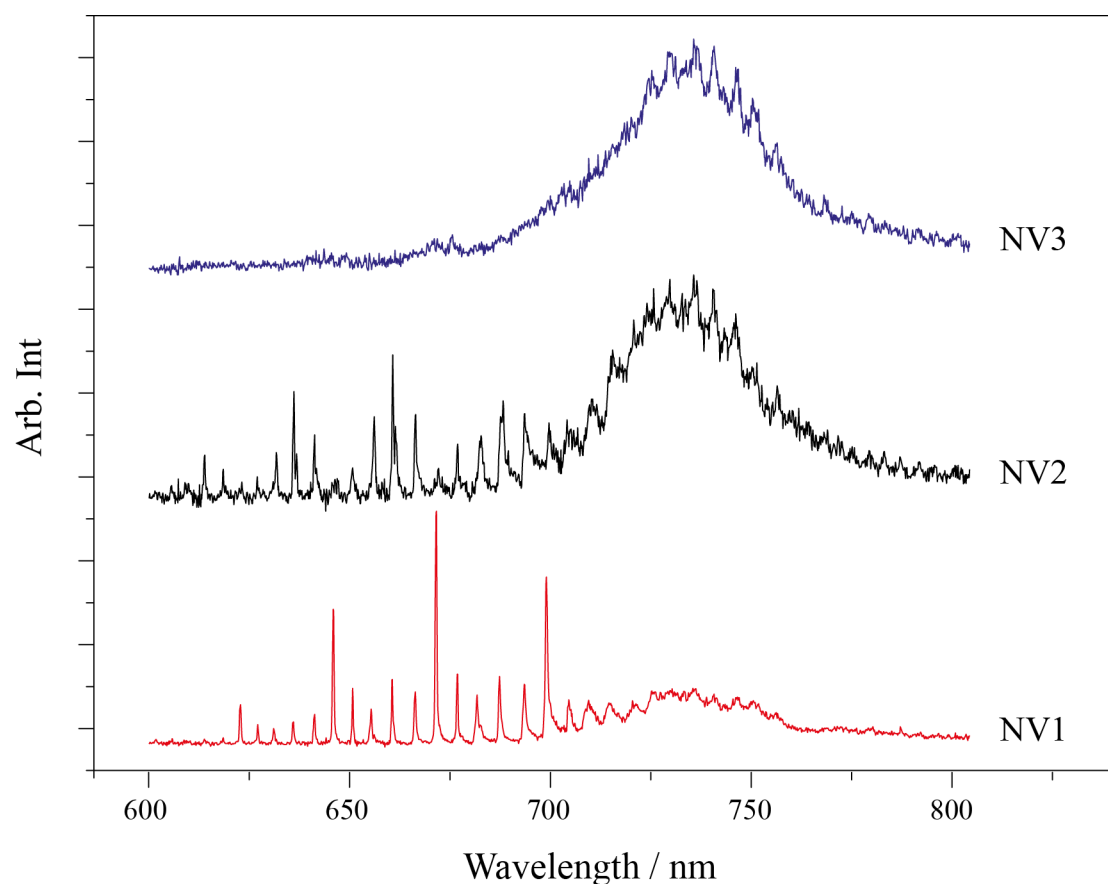


FIGURE 6.16: Spectra obtained from the 3 microcavities labeled in figure 6.15.

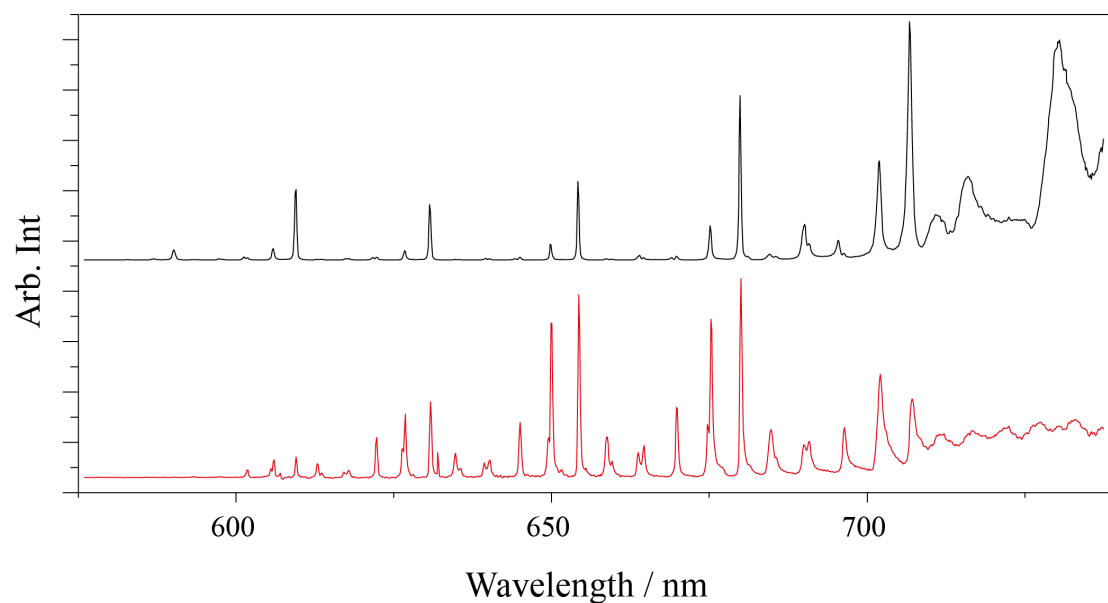


FIGURE 6.17: Comparison of the white light transmission spectrum obtained from the cavity close to the NV1. This shows identical mode locations, with the NV centre showing increased coupling to the transverse modes.

might hope occurs as the cavity length decreases. Also, presumably because of some large agglomerations of nanodiamonds elsewhere on the sample the shortest achievable cavity lengths were considerably longer than those obtained previously for empty cavities, and also for coupling to colloidal quantum dots, although on that occasion the plinth substrate architecture was implemented. As emphasised earlier the scope of the room temperature coupling investigation was judicially narrow, and since clear signs of coupling were achieved efforts were directed towards cryogenic temperatures.

6.7 Design and Construction of Low Temperature Set-up

In order to effectively couple the NV centres to the cavities at low temperature, the key to success will be in the design of a suitable sample holding stage. There are several degrees of freedom which are absolute requisites. For example ability to tune the cavity length, and also position the NV centre accurately in the focal plane of the microscope objective whilst at low temperature. Once again the fact that the cavities are milled in arrays will be useful as it slightly relaxes the requirement to be able to translate the lower, featured substrate in x and y with respect to the objective lens. This is not quite ideal as in order to get the very shortest cavity lengths obtained so far it was necessary to obtain cavity emission spectra at each corner of the substrate and use cavities close to the edge or corner found to be in contact with the upper mirror. This can be mitigated slightly with the incorporation of a crude kinematic degree of freedom which could be set at room temperature prior to cooling. The layout of the microscope when arranged to function at low temperatures is shown in the figure 6.18 a), the original conception and design of which is outlined in [154]. This takes advantage of the telecentric lenses to organise the scanning head distally with respect to the sample which, along with the microscope objective can be cooled to cryogenic temperatures. Here the sample stage, the sample and the microscope objective are all sealed in a vacated tube which has a small amount of helium released into it to provide better thermal contact with the cryogen bath. In order to maneuver the sample at low temperatures over relatively large ranges we make use of 4 ‘attocube’ piezo-electric nanopositioners. These positioners extend the normally limited range of piezo-electric actuators (for example the one used throughout chapter 5) by employing a novel ‘slip-slide’ mechanism. This incorporates a bolt which holds the piezo-electric crystal with a very precise force, such that when the piezo crystal expands slowly, the bolt holds it in place and the sample is moved a small amount. A sharp contraction of the crystal then follows, overcoming the frictional force of the bolt, returning the crystal to its original length but translated (along with the sample) some small distance in the direction of the crystal’s axis of expansion. This process can be repeated many times (ultimately determined by the

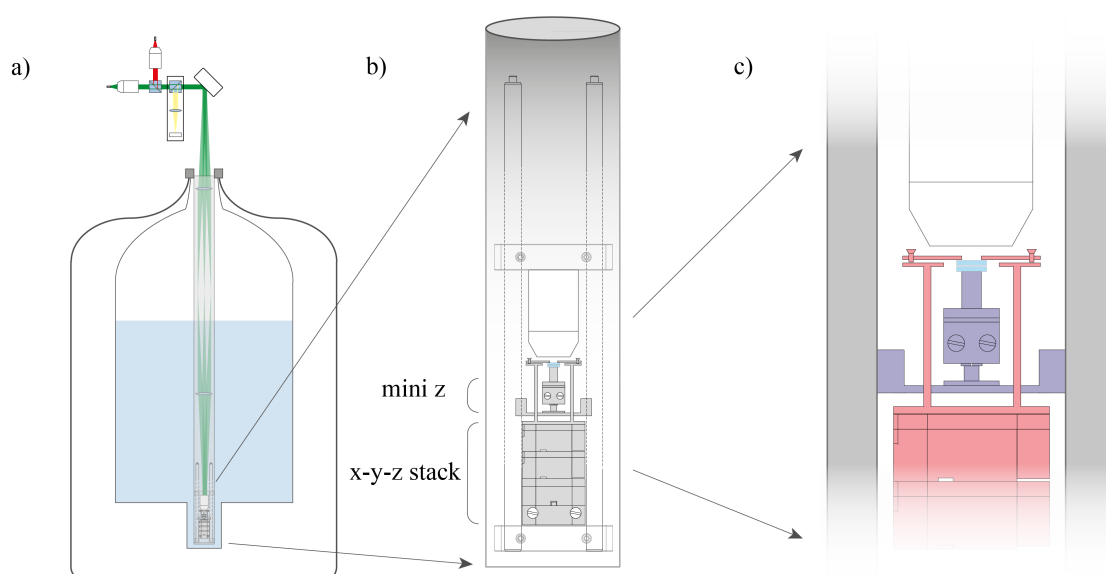


FIGURE 6.18: a) - Schematic of the scanning confocal head arranged above a large cryogenic dewar to allow for low temperature measurements to be taken b) An expanded view of the sample region, b) Expanded view of the piezo positioners.

length of the crystal) and thus increases the piezo's intrinsic range of $\sim 5 \mu\text{m}$ to $\sim 2 \text{mm}$. In addition this functionality can be maintained at low temperatures. Four such devices were available to be incorporated into the low temperature cavity positioning set-up, and their arrangement is shown in figure 6.18 b). This consists of three larger positioners stacking together to provide full $x - y - z$ motion, and also one smaller z positioner. With regards to the placement of the planar and featured mirror, as with the previous measurements it makes most sense to collect PL and image through the planar mirror rather than the featured mirror, to avoid unnecessary aberrations detracting from the microscope objective's performance. It was also decided that once a fully registered and characterised nanodiamond distribution is inserted it will be more important to locate the identified single emitters rather than a particular cavity, and so the planar mirror should have all three degrees of motion. As mentioned previously, this means that the very shortest cavity lengths may not be achieved. The third of the images contained in figure 6.18 shows how the substrates were arranged on a custom built sample holder to achieve this. The red highlighted metal work forms a table like structure. On the upper surface coarse kinematic action is achieved by altering the relative depths of the bolts. This structure can then be moved in all three directions with respect to the static microscope objective, and also the featured substrate which is static in the $x - y$ plane. The purple highlighted metalwork shows how the lower mirror is suspended beneath the table structure with bolts pressing against the inner surfaces of the cage rods. The mini

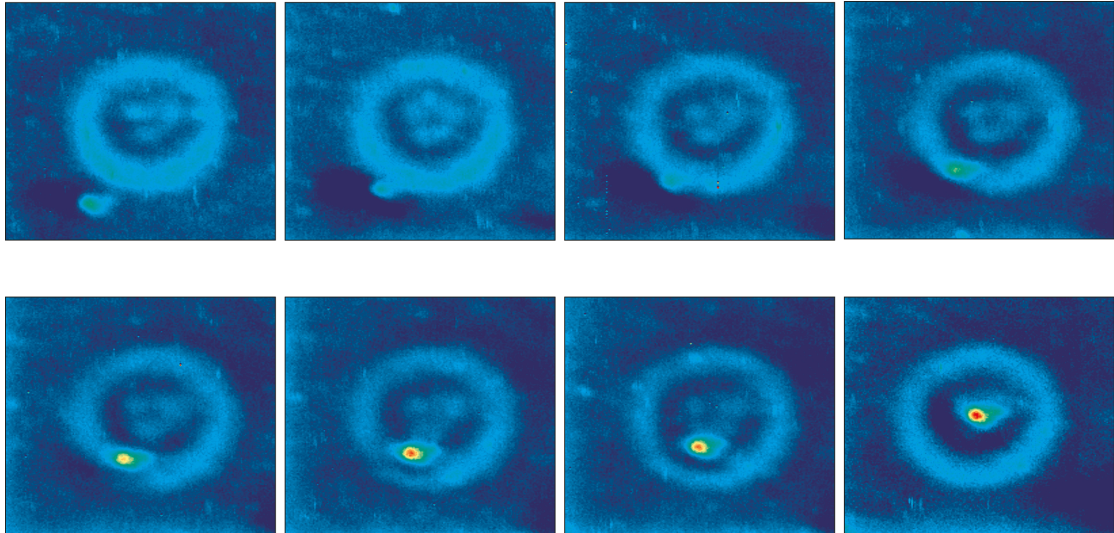


FIGURE 6.19: Room temperature PL measurements taken showing the ability to traverse an emitting object into spatial resonance with an optical microcavity.

z nanositioner then allows the cavities to be lowered and raised independently of the upper mirror. Once the construction of this cavity holder and positioning system was completed and ready to use it was tested at room temperatures. Figure 6.19 shows the results of this testing. A stable emitter was located and positioned close to a cavity, one of the second iteration with diameter $10\ \mu\text{m}$ and yet to be fully characterised. The emitter was then stepped through, using the nanositioning system, to be well coupled to the centre. All eight images are plotted with the same colour scale. The apparent increase in brightness can be better quantified by taking the ratio between the average background and the peak intensity for the emitter. This is plotted in 6.20 and shows between a 25% to 40% increase in PL intensity, depending on what is taken as the original uncoupled value. This increase in count rate could be due to a combination of any number of the following explanations. The most optimistic is that it is down to an enhanced coupling efficiency, although the area was photobleaching during the imaging process which could potentially have contributed to the enhanced contrast. With the laser power staying constant for all eight images, the peak count rate saw a 30% increase in intensity but it could have been the case that the excitation power was better coupled to the emitter once well situated in the cavity, thus although the power delivered to the microscope objective remained constant, the excitation power experienced by the emitter could have increased. Spectral interrogation was inconclusive, as it appeared that most of the increase in intensity was from leakage around the reflectivity edges of the mirror coatings. This can occur if this emitter was particularly large in spatial extent (for example it was a large agglomeration of NV centres), then its presence in the cavity may very well have stopped high Q stable modes forming. Another feature worth remarking on which appears in all the images in figure 6.19 is the background

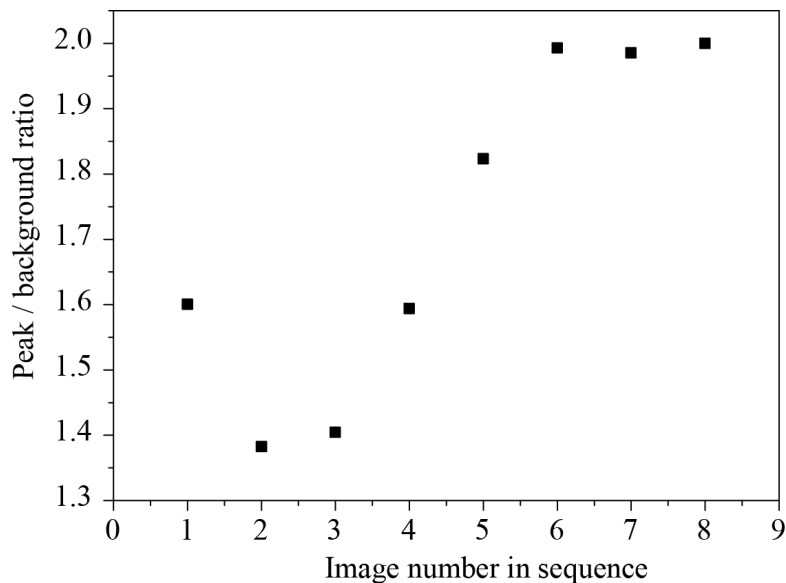


FIGURE 6.20: Room temperature PL measurements taken showing the ability to traverse an emitting object into spatial resonance with an optical microcavity.

illumination forming a spatial profile reminiscent more of the poorly coupled ‘doughnut’ shaped modes imaged by the spectrograph in chapter 5. It may well have been the case that this location on the mirror was situated in between resonant modes, similarly to that of the red circled cavity, spectrally shown in figure 5.5, and so was unlikely to spectrally yield clear cavity modes. A sentiment that will be echoed in the final chapter is that some potentially useful low temperature coupling of NVs to these optical microcavities can be achieved with this set-up in the very near future.

6.8 Summary and Conclusions

This chapter summarises some of the work carried out in the study of NV centres in diamond during the course of this DPhil. Crucial to much of this work was the reliability of the unique scanning confocal microscope which was designed and constructed by colleagues. This allowed for the development of a systematic approach to identify, characterise and register individual NV centres prior to cavity coupling. It was then shown that coupling of these centres to the ultra small open access microcavities was indeed possible at room temperatures. Attention was then turned towards the development of a low temperature mounting system which incorporates all of the necessary degrees of freedom. This was achieved and provided results suggesting improved PL collection efficiencies were obtained at room temperature. Should these approaches and equipment developments be brought together assuming the mirrors perform as well at low

temperatures as they do at room temperature (as the manufacturers claim) measurable enhancements of the NV's ZPL should be possible.

Chapter 7

Conclusions and Outlook

7.1 Introduction

The final chapter in this thesis will be comprised of two sections. The first will be a summary of the work presented in the preceding chapters, reiterating several of the more salient details. The thesis will then finish by making some estimates on what the very smallest achievable mode volumes are, by making use of FDTD simulations, followed by a look to the future.

7.2 Conclusions

The results in this thesis describe the production, characterisation and application of a novel fabrication method for microcavitation. The FIB construction method presented in chapter 3 outlines the steps taken to mill and topographically analyse the features. The joint application of atomic force microscopy and focused ion beam milling led to a method of optimising the construction procedure yielding surface topographies smooth enough to support the very highest mirror reflectivities whilst simultaneously achieving some of the smallest mode volumes for this type of cavity. The fourth chapter of this thesis was based around the optical characterisation of the first iteration of cavities to be produced by this milling procedure. The results obtained included finesses in excess of 400, Q factors in excess of 10^4 and mode volumes less than $3 \mu\text{m}^3$.

In a collaborative effort, these cavities were then modified to improve the achievable mode volumes, and used to investigate the room temperature enhancements possible by coupling emitters to optical microcavities in the bad emitter regime. With mode volumes of approximately $0.5 \mu\text{m}^3$, a 75% enhancement of the spontaneous emission rate of

colloidal nanocrystals was demonstrated. These results were supported by FDTD modeling which allowed for the estimate of a photoluminescence coupling efficiency of over 40%. This facilitated the observation of luminescence from individual colloidal nanocrystals with a relatively low N.A. lens. Also included in this chapter were preliminary results from the characterisation of the second iteration of the cavities. This yielded spectral line widths beyond the resolution of the spectrometer, above 15,000 or a finesse of at least 1800. Similar coatings have been shown to yield finesses as high as 10^5 , which may be taken as an estimate as comparable surface roughnesses. Chapter 6 outlined the development of apparatus to conduct cryogenic scanning confocal microscopy incorporating the ability to spatially and spectrally optimise the coupling of emitters to the cavity modes. The target emitter for this apparatus was the nitrogen vacancy centre in diamond. During the construction of this equipment initial results indicated room temperature coupling of NV centres in nanodiamond, and also an enhanced collection efficiency due to the presence of the microcavities.

7.3 Outlook

In addition to providing supporting evidence for experimental data, the FDTD modeling software was also used to estimate the limitations of this approach to microcavitation. This is included in the very final section of this thesis, as it is suggestive of what might be possible in the future, for this fabrication technique.

7.3.1 Ultra Small Volumes

Once the method of simulating the cavity modes and calculating the volumes was established (see chapter 2, section 2.5 and chapter 5, sections 5.4 and 5.5), it was straightforward to reduce the size of the features in an attempt to explore the very smallest cavities achievable. In order to allow straight comparison with these experimentally achieved ‘large’ cavities the smaller cavities modeled in the previous section have several features in common, including 10 pairs of coating layers and the refractive index of the medium filling the cavity the same as that of silica. The first step in reducing the volume is to construct the cavities so that a single anti-node of the field exists between the surfaces of the mirror, effectively minimising its extent in the z direction. To achieve this, the final layer of the DBR must be constructed out of the higher refractive index material. A further reduction in mode size is achieved by minimising the lateral extent of the mode by decreasing the radius of curvature. In order to maintain only a single anti-node within the cavity the depth of the feature cannot exceed more than half a wavelength. This means that as the feature radius of curvature is decreased so is the feature width.

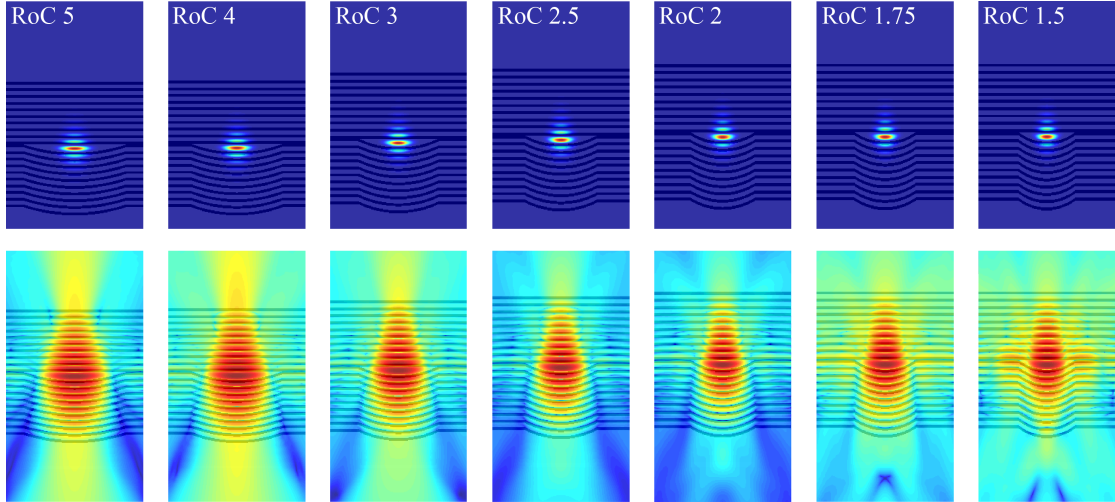


FIGURE 7.1: Series of resonant field cross sections plotted with linear and logarithmic color scales. The series forms a subset of the results presented in figure 7.2, showing the numerical values for the calculated volumes.

Figure 7.1 shows a series cavity modes for sequentially smaller radii of curvature. As discussed in section 2.4 and described precisely in equation 2.56 the location of the resonant modes of these cavities is dependent on the radius of curvature. Therefore, in order to prevent the resonant mode shifting out of the reflectivity band of the mirror the widths were chosen so that the fundamental TEM_{00} mode remained close to the centre of the reflection band of the mirrors. Once again, the logarithmic color plots prove useful as they show that initially the majority of the loss is highly directional (leftmost, largest RoC). This switches to most of the loss being much more isotropic with substantial proportions of the field spilling out over the feature edge. The cavity volumes calculated from the MATLAB analysis are plotted against cavity radius of curvature in figure 7.2 and are shown as black squares. This data shows the effect of the field leakage as a larger portion of the field extends beyond the confined region within the feature, ultimately giving larger volumes for reduced curvature and feature width. Also included in this plot are the two sets of values based on the analytic formula, given in equation 2.57 in chapter 2 and shown again as:

$$V = \frac{\pi w_0^2 L}{4} \quad (7.1)$$

This equation does not incorporate any field penetration into the mirrors, and so the volumes calculated show a poor agreement with the simulation values (red disks). As discussed in chapter 5 the field penetration can be incorporated into this equation by increasing the effective cavity length by some amount. When choosing this value the structure of the mirrors used must be considered, for example the depth chosen in chapter 5, 1.09λ provided best agreement. For the results plotted in figure 7.2 the mirror structure was altered to end with the higher refractive index material, and so the penetration depth would be immediately reduced. Good agreement was found by

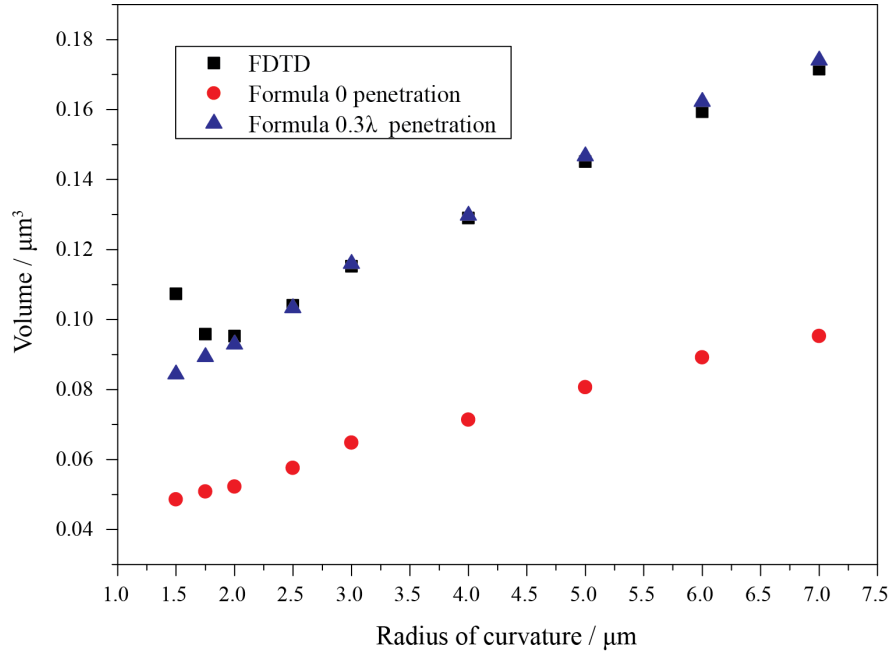


FIGURE 7.2: Plot showing the decrease in mode volume as the radius of curvature of the feature is lowered, such that a TEM_{00} is situated close to the maximum reflectivity. Black squares show the modeled volumes, with blue triangles showing the unaltered formula (7.1), and red disks with a penetration depth of 0.3λ included in the formulas length parameter.

using a depth of 0.3λ , and is plotted in figure 7.2 with blue triangles. This formula is obtained from integrating the field of a Gaussian mode. As the feature width decreases to allow more of the field to escape from this Gaussian mode, this formula fails to describe the volume increase observed at the very lowest curvatures and widths. This modeling showed volumes as low as $0.1 \mu\text{m}^3$ could be achieved, corresponding to less than $0.5\lambda^3$.

7.3.2 The Future

It is hoped that this method of optical microcavitation goes on to yield more results. In the short term, the subject matter of chapters 6 and the results immediately preceding this section offer more immediate routes for possible series of experiments and simulations respectively. In the case of the former, the optical set-up has been constructed and the second iteration of microcavities have shown the capacity to achieve suitably high Q factors. Experiments on the NV centres at low temperature could yield measurable Purcell enhancements in the near future. As far as the simulation side of things goes, comprehensive data was only taken using up to ten pairs of dielectrics on the substrates. A similar series for an even more reflective set of mirrors, similar to the second iteration of cavity feature would be of interest, to gain an idea of what may be achievable by this latest batch. In addition, exploring the formation of unbalanced cavities modes, where

additional layers on the featured mirror compared to the planar mirror, might mean light is even more efficiently coupled into the primary TEM_{00} mode and collected by external optics.

In the more distant future there are many, many ways this technology may be applied. In fluid sensing for example, particular optical transitions could be enhanced and detected at much lower levels by exploiting the Purcell enhancement. This could also be useful in flow cytometry, allowing more light to be collected and so the cells can be pumped much faster through the system allowing assaying times to be dramatically reduced. The arrayed nature of the cavities could also be exploited. One could imagine using cutting edge inkjet techniques to print functionalised regions on the planar mirror. The reduction in the Q factor of cavities formed opposite these particular regions could then indicate the presence of particular chemical species. Another technology that may benefit in the distant future is that of single photon generation. With sufficiently high coupling efficiencies it might be that pulsed excitation of stable emitters (e.g. the NV centre) would result in the consistent production and collection of single photons, which could be very useful for modern cryptography.

Bibliography

- [1] G. V. Prakash, L. Besombes, T. Kelf, Jeremy J. Baumberg, P. N. Bartlett, and M. E. Abdelsalam. Tunable resonant optical microcavities by self-assembled templating. *Optics letters*, 29(13):1500–2, July 2004. ISSN 0146-9592. URL <http://www.ncbi.nlm.nih.gov/pubmed/15259726>.
- [2] G. Cui, J. M. Hannigan, R. Loeckenhoff, F. M. Matinaga, M. G. Raymer, S. Bhongale, M. Holland, S. Moser, S. Chattergee, H. M. Gibbs, and G. Khitrova. A hemispherical, high-solid-angle optical micro-cavity for cavity-QED studies. *Optics Express*, 14(6):2289–2299, June 2006. doi: 10.1063/1.2132066. URL <http://www.opticsinfobase.org/oe/abstract.cfm?URI=oe-14-6-2289>.
- [3] H. Mabuchi and A. C. Doherty. Cavity quantum electrodynamics: coherence in context. *Science (New York, N.Y.)*, 298(5597):1372–7, November 2002. ISSN 1095-9203. doi: 10.1126/science.1078446. URL <http://www.sciencemag.org/content/298/5597/1372.full.pdf>.
- [4] J. M. Gerard, D. Barrier, J. Y. Marzin, R. Kuszelewicz, L. Manin, E. Costard, V. Thierry-Mieg, and T. Rivera. Quantum boxes as active probes for photonic microstructures: The pillar microcavity case. *Applied Physics Letters*, 69(4):449, 1996. ISSN 00036951. doi: 10.1063/1.118135. URL <http://link.aip.org/link/APPLAB/v69/i4/p449/s1&Agg=doi>.
- [5] J. Gérard, B. Sermage, B. Gayral, B. Legrand, E. Costard, and V. Thierry-Mieg. Enhanced Spontaneous Emission by Quantum Boxes in a Monolithic Optical Microcavity. *Physical Review Letters*, 81(5):1110–1113, August 1998. ISSN 0031-9007. doi: 10.1103/PhysRevLett.81.1110. URL <http://link.aps.org/doi/10.1103/PhysRevLett.81.1110>.
- [6] N. C. Frateschi, a. P. Kanjamala, a. F. J. Levi, and T. Tanbun-Ek. Polarization of lasing emission in microdisk laser diodes. *Applied Physics Letters*, 66(15):1859, 1995. ISSN 00036951. doi: 10.1063/1.113301. URL <http://link.aip.org/link/APPLAB/v66/i15/p1859/s1&Agg=doi>.

- [7] B. Gayral, J.-M. Gerard, B. Sermage, a. Lematre, and C. Dupuis. Time-resolved probing of the Purcell effect for InAs quantum boxes in GaAs microdisks. *Applied Physics Letters*, 78(19):2828, 2001. ISSN 00036951. doi: 10.1063/1.1370123. URL <http://link.aip.org/link/APPLAB/v78/i19/p2828/s1&Agg=doi>.
- [8] K. J. Vahala. Optical microcavities. *Nature*, 424(6950):839–46, August 2003. ISSN 1476-4687. doi: 10.1038/nature01939. URL <http://www.nature.com/nature/journal/v424/n6950/pdf/nature01939.pdf>.
- [9] J. C. Knight, G. Cheung, F. Jacques, and T. A. Birks. Phase-matched excitation of whispering-gallery-mode resonances by a fiber taper. *Optics letters*, 22(15):1129–31, August 1997. ISSN 0146-9592. URL <http://www.ncbi.nlm.nih.gov/pubmed/18185771>.
- [10] Mani Hossein-Zadeh and Kerry J Vahala. Free ultra-high-Q microtoroid: a tool for designing photonic devices. *Optics express*, 15(1):166–75, January 2007. ISSN 1094-4087. URL <http://www.ncbi.nlm.nih.gov/pubmed/19532232>.
- [11] Dirk Englund, David Fattal, Edo Waks, Glenn Solomon, Bingyang Zhang, Toshihiro Nakaoka, Yasuhiko Arakawa, Yoshihisa Yamamoto, and Jelena Vučković. Controlling the Spontaneous Emission Rate of Single Quantum Dots in a Two-Dimensional Photonic Crystal. *Physical Review Letters*, 95(1):2–5, July 2005. ISSN 0031-9007. doi: 10.1103/PhysRevLett.95.013904. URL <http://link.aps.org/doi/10.1103/PhysRevLett.95.013904>.
- [12] Philip R Dolan, Gareth M Hughes, Fabio Grazioso, Brian R Patton, and Jason M Smith. Femtoliter tunable optical cavity arrays. *Optics letters*, 35(21):3556–8, November 2010. ISSN 1539-4794. URL <http://www.ncbi.nlm.nih.gov/pubmed/21042348>.
- [13] L. Marseglia, J. P. Hadden, a. C. Stanley-Clarke, J. P. Harrison, B. Patton, Y.-L. D. Ho, B. Naydenov, F. Jelezko, J. Meijer, P. R. Dolan, J. M. Smith, J. G. Rarity, and J. L. OBrien. Nanofabricated solid immersion lenses registered to single emitters in diamond. *Applied Physics Letters*, 98(13):133107, 2011. ISSN 00036951. doi: 10.1063/1.3573870. URL <http://link.aip.org/link/APPLAB/v98/i13/p133107/s1&Agg=doi>.
- [14] P Siyushev, F Kaiser, V Jacques, I Gerhardt, S Bischof, H Fedder, J Dodson, M Markham, D Twitchen, F Jelezko, and J Wrachtrup. Monolithic diamond optics for single photon detection. *Applied physics letters*, 97(24):241902, December 2010. ISSN 0003-6951. doi: 10.1063/1.3519849. URL <http://www.pubmedcentral.nih.gov/articlerender.fcgi?artid=3017569&tool=pmcentrez&rendertype=abstract>.

- [15] Tim Schröder, Andreas W Schell, Günter Kewes, Thomas Aichele, and Oliver Benson. Fiber-integrated diamond-based single photon source. *Nano letters*, 11(1):198–202, January 2011. ISSN 1530-6992. doi: 10.1021/nl103434r. URL <http://www.ncbi.nlm.nih.gov/pubmed/21138271>.
- [16] J. R. Rabeau, S. T. Huntington, a. D. Greentree, and S. Praver. Diamond chemical-vapor deposition on optical fibers for fluorescence waveguiding. *Applied Physics Letters*, 86(13):134104, 2005. ISSN 00036951. doi: 10.1063/1.1890484. URL <http://link.aip.org/link/APPLAB/v86/i13/p134104/s1&Agg=doi>.
- [17] E. M. Purcell. Spontaneous Emission Probabilities at Radio Frequencies. *Physical Review*, 69:681, 1946.
- [18] Ziyun Di, HV Jones, and PR Dolan. Controlling the emission from semiconductor quantum dots using ultra-small tunable optical microcavities. *arXiv preprint arXiv: . . .*, 2012. URL <http://arxiv.org/abs/1206.6046>.
- [19] Yannick Dumeige, Romain Alléaume, Philippe Grangier, François Treussart, and Jean-François Roch. Controlling the single-diamond nitrogen-vacancy color center photoluminescence spectrum with a FabryPerot microcavity. *New Journal of Physics*, 13(2):025015, February 2011. ISSN 1367-2630. doi: 10.1088/1367-2630/13/2/025015. URL <http://stacks.iop.org/1367-2630/13/i=2/a=025015?key=crossref.ff85aca39b6b7f2b925e869abee5b9b3>.
- [20] Timothy Andrew Kelf. *Light-Matter Interactions on Nano-Structured Metallic Films*. PhD thesis, Univeristy of Southampton, 2006.
- [21] M. Trupke, E. a. Hinds, S. Eriksson, E. a. Curtis, Z. Moktadir, E. Kukharenska, and M. Kraft. Microfabricated high-finesse optical cavity with open access and small volume. *Optics Express*, 14(6):3, June 2005. doi: 10.1063/1.2132066. URL <http://arxiv.org/abs/quant-ph/0506234>.
- [22] T. Steinmetz, Y. Colombe, D. Hunger, T. W. Hansch, a. Balocchi, R. J. Warburton, and J. Reichel. Stable fiber-based Fabry-Perot cavity. *Applied Physics Letters*, 89(11):111110, 2006. ISSN 00036951. doi: 10.1063/1.2347892. URL <http://link.aip.org/link/APPLAB/v89/i11/p111110/s1&Agg=doi>.
- [23] Andreas Muller, Edward B. Flagg, Michael Metcalfe, John Lawall, and Glenn S. Solomon. Coupling an epitaxial quantum dot to a fiber-based external-mirror microcavity. *Applied Physics Letters*, 95(17):173101, 2009. ISSN 00036951. doi: 10.1063/1.3245311. URL <http://link.aip.org/link/APPLAB/v95/i17/p173101/s1&Agg=doi>.

- [24] D Hunger, T Steinmetz, Y Colombe, C Deutsch, T W Hänsch, and J Reichel. A fiber FabryPerot cavity with high finesse. *New Journal of Physics*, 12(6):065038, June 2010. ISSN 1367-2630. doi: 10.1088/1367-2630/12/6/065038. URL <http://stacks.iop.org/1367-2630/12/i=6/a=065038?key=crossref.e6ea72b3da2564be9138384f611286d0>.
- [25] Andreas Muller, Edward B Flagg, John R Lawall, and Glenn S Solomon. Ultrahigh-finesse, low-mode-volume FabryPerot microcavity. *Optics Letters*, 35(13):2293–2295, 2010. URL <http://www.opticsinfobase.org/ol/abstract.cfm?URI=ol-35-13-2293>.
- [26] Russell J. Barbour, Paul a. Dalgarno, Arran Curran, Kris M. Nowak, Howard J. Baker, Denis R. Hall, Nick G. Stoltz, Pierre M. Petroff, and Richard J. Warburton. A tunable microcavity. *Journal of Applied Physics*, 110(5):053107, 2011. ISSN 00218979. doi: 10.1063/1.3632057. URL <http://link.aip.org/link/JAPIAU/v110/i5/p053107/s1&Agg=doi>.
- [27] Ju Nockel, G Bourdon, Le Ru E, R Adams, I Robert, Jm Moison, and I Abram. Mode structure and ray dynamics of a parabolic dome microcavity. *Physical review. E, Statistical physics, plasmas, fluids, and related interdisciplinary topics*, 62(6 Pt B):8677–99, December 2000. ISSN 1063-651X. URL <http://www.ncbi.nlm.nih.gov/pubmed/11138170>.
- [28] H Mabuchi, Q a Turchette, M S Chapman, and H J Kimble. Real-time detection of individual atoms falling through a high-finesse optical cavity. *Optics letters*, 21(17):1393–5, September 1996. ISSN 0146-9592. URL <http://www.ncbi.nlm.nih.gov/pubmed/19876363>.
- [29] E.T. Jaynes and F.W. Cummings. Comparison of quantum and semiclassical radiation theories with application to the beam maser. *Proceedings of the IEEE*, 51(1):89–109, 1963. URL http://ieeexplore.ieee.org/xpls/abs_all.jsp?arnumber=1443594.
- [30] B.W. Shore and P.L. Knight. The Jaynes-Cummings Model. *Journal of Modern Optics*, 40(7):1195–1238, 1993. URL <http://scholar.google.com/scholar?hl=en&btnG=Search&q=intitle:The+Jaynes-Cummings+Model#0>.
- [31] P Meystre. Theoretical developments in cavity quantum optics: a brief review. *Physics Reports*, 219(3-6):243–262, October 1992. ISSN 03701573. doi: 10.1016/0370-1573(92)90141-L. URL <http://linkinghub.elsevier.com/retrieve/pii/037015739290141L>.

- [32] C. J. Hood. The Atom-Cavity Microscope: Single Atoms Bound in Orbit by Single Photons. *Science*, 287(5457):1447–1453, February 2000. ISSN 00368075. doi: 10.1126/science.287.5457.1447. URL <http://www.sciencemag.org/cgi/doi/10.1126/science.287.5457.1447>.
- [33] Christina Hood, H. Kimble, and Jun Ye. Characterization of high-finesse mirrors: Loss, phase shifts, and mode structure in an optical cavity. *Physical Review A*, 64(3):1–7, August 2001. ISSN 1050-2947. doi: 10.1103/PhysRevA.64.033804. URL <http://link.aps.org/doi/10.1103/PhysRevA.64.033804>.
- [34] S. Fernandez, F. B. Naranjo, F. Calle, M. a. Sanchez-Garca, E. Calleja, P. Venegues, A. Trampert, and K. H. Ploog. High-quality distributed Bragg reflectors based on Al_xGa_{1-x}N/GaN multilayers grown by molecular-beam epitaxy. *Applied Physics Letters*, 79(14):2136, 2001. ISSN 00036951. doi: 10.1063/1.1401090. URL <http://link.aip.org/link/APPLAB/v79/i14/p2136/s1&Agg=doi>.
- [35] Yinan Zhang and Marko Lončar. Submicrometer diameter micropillar cavities with high quality factor and ultrasmall mode volume. *Optics Letters*, 34(7):902, March 2009. ISSN 0146-9592. doi: 10.1364/OL.34.000902. URL <http://www.opticsinfobase.org/abstract.cfm?URI=ol-34-7-902>.
- [36] Lord Rayleigh. The Problem of the Whispering Gallery. *Scientific Papers (Cambridge University)*, pages 617–620, 1912.
- [37] Q.-Y. Lu, X.-H. Chen, W.-H. Guo, L.-J. Yu, Y.-Z. Huang, J. Wang, and Y. Luo. Mode Characteristics of Semiconductor Equilateral Triangle Microcavities With Side Length of $520\mu\text{m}$. *IEEE Photonics Technology Letters*, 16(2):359–361, February 2004. ISSN 1041-1135. doi: 10.1109/LPT.2003.821063. URL <http://ieeexplore.ieee.org/lpdocs/epic03/wrapper.htm?arnumber=1266423>.
- [38] VB Braginsky and ML Gorodetsky. Quality-factor and nonlinear properties of optical whispering-gallery modes. *Physics Letters A*, 137(7):393–397, 1989. URL <http://linkinghub.elsevier.com/retrieve/pii/0375960189909122>.
- [39] a Serpengüzel, S Arnold, and G Griffel. Excitation of resonances of microspheres on an optical fiber. *Optics letters*, 20(7):654–6, April 1995. ISSN 0146-9592. URL <http://www.ncbi.nlm.nih.gov/pubmed/19859286>.

- [40] N. Dubreuil, J. C. Knight, D. K. Leventhal, V. Sandoghdar, J. Hare, and V. Lefèvre. Eroded monomode optical fiber for whispering-gallery mode excitation in fused-silica microspheres. *Optics letters*, 20(8):813–5, April 1995. ISSN 0146-9592. URL <http://www.ncbi.nlm.nih.gov/pubmed/19859338>.
- [41] D. W. Vernooy, V. S. Ilchenko, H. Mabuchi, E. W. Streed, and H. J. Kimble. High-Q measurements of fused-silica microspheres in the near infrared. *Optics letters*, 23(4):247–9, February 1998. ISSN 0146-9592. URL <http://www.ncbi.nlm.nih.gov/pubmed/18084474>.
- [42] S. M. Spillane, T. J. Kippenberg, and K. J. Vahala. Ultralow-threshold Raman laser using a spherical dielectric microcavity. *Nature*, pages 621–623, 2002.
- [43] T. J. Kippenberg, S. M. Spillane, and K. J. Vahala. Modal coupling in traveling-wave resonators. *Optics letters*, 27(19):1669–71, October 2002. ISSN 0146-9592. URL <http://www.ncbi.nlm.nih.gov/pubmed/18033330>.
- [44] Takao Aoki, Barak Dayan, E Wilcut, W P Bowen, a S Parkins, T J Kippenberg, K J Vahala, and H J Kimble. Observation of strong coupling between one atom and a monolithic microresonator. *Nature*, 443(7112):671–4, October 2006. ISSN 1476-4687. doi: 10.1038/nature05147. URL <http://www.ncbi.nlm.nih.gov/pubmed/17035998>.
- [45] O. Painter. Two-Dimensional Photonic Band-Gap Defect Mode Laser. *Science*, 284(5421):1819–1821, June 1999. ISSN 00368075. doi: 10.1126/science.284.5421.1819. URL <http://www.sciencemag.org/cgi/doi/10.1126/science.284.5421.1819>.
- [46] Yoshihiro Akahane, Takashi Asano, and BS Song. High-Q photonic nanocavity in a two-dimensional photonic crystal. *Nature*, 425(October):4–7, 2003. doi: 10.1038/nature02015.1. URL <http://www.nature.com/nature/journal/v425/n6961/abs/nature02063.html>.
- [47] K. Srinivasan, P. Barclay, M. Borselli, and O. Painter. Optical-fiber-based measurement of an ultras-small volume high-Q photonic crystal microcavity. *Physical Review B*, 70(8):1–4, August 2004. ISSN 1098-0121. doi: 10.1103/PhysRevB.70.081306. URL <http://link.aps.org/doi/10.1103/PhysRevB.70.081306>.
- [48] Bong-Shik Song, Susumu Noda, Takashi Asano, and Yoshihiro Akahane. Ultra-high-Q photonic double-heterostructure nanocavity. *Nature Materials*, 4(3):207–210, February 2005. ISSN 1476-1122. doi: 10.1038/nmat1320. URL <http://www.nature.com/doi/10.1038/nmat1320>.

- [49] Yasushi Takahashi, Hiroyuki Hagino, Yoshinori Tanaka, Bong-Shik Song, Takashi Asano, and Susumu Noda. High-Q nanocavity with a 2-ns photon lifetime. *Optics express*, 15(25):17206–13, December 2007. ISSN 1094-4087. URL <http://www.ncbi.nlm.nih.gov/pubmed/19551013>.
- [50] Jelena Vučković, Marko Lončar, Hideo Mabuchi, and Axel Scherer. Design of photonic crystal microcavities for cavity QED. *Physical Review E*, 65(1):1–11, December 2001. ISSN 1063-651X. doi: 10.1103/PhysRevE.65.016608. URL <http://link.aps.org/doi/10.1103/PhysRevE.65.016608>.
- [51] T Yoshie, A Scherer, J Hendrickson, G Khitrova, H M Gibbs, G Rupper, C Ell, O B Shchekin, and D G Deppe. Vacuum Rabi splitting with a single quantum dot in a photonic crystal nanocavity. *Nature*, 432(November):9–12, 2004. doi: 10.1038/nature02969.1.
- [52] K Hennessey, A Badolato, M Winger, D Gerace, M Atatüre, S Gulde, S Fält, E L Hu, and A Imamolu. Quantum nature of a strongly coupled single quantum dot-cavity system. *Nature*, 445(7130):896–9, February 2007. ISSN 1476-4687. doi: 10.1038/nature05586. URL <http://www.ncbi.nlm.nih.gov/pubmed/17259971>.
- [53] Dirk Englund, Andrei Faraon, Ilya Fushman, Nick Stoltz, Pierre Petroff, and Jelena Vučković. Controlling cavity reflectivity with a single quantum dot. *Nature*, 450(7171):857–61, December 2007. ISSN 1476-4687. doi: 10.1038/nature06234. URL <http://www.ncbi.nlm.nih.gov/pubmed/18064008>.
- [54] Y. K. Wang and I. C. Khoo. On the Wigner-Weisskopf approximation in quantum optics. *Optics Communications*, 11(4):323–326, 1974. URL <http://linkinghub.elsevier.com/retrieve/pii/0030401874902272>.
- [55] Alexander Högele, Stefan Seidl, Martin Kroner, Khaled Karrai, Richard Warburton, Brian Gerardot, and Pierre Petroff. Voltage-Controlled Optics of a Quantum Dot. *Physical Review Letters*, 93(21):19–22, November 2004. ISSN 0031-9007. doi: 10.1103/PhysRevLett.93.217401. URL <http://link.aps.org/doi/10.1103/PhysRevLett.93.217401>.
- [56] Kartik Srinivasan, Matthew Borselli, Thomas J. Johnson, Paul E. Barclay, Oskar Painter, Andreas Stintz, and Sanjay Krishna. Optical loss and lasing characteristics of high-quality-factor AlGaAs microdisk resonators with embedded quantum dots. *Applied Physics Letters*, 86(15):151106, 2005. ISSN 00036951. doi: 10.1063/1.1901810. URL <http://link.aip.org/link/APPLAB/v86/i15/p151106/s1&Agg=doi>.

- [57] Yoshihiro Akahane, Takashi Asano, Bong-Shik Song, and Susumu Noda. Fine-tuned high-Q photonic-crystal nanocavity. *Optics Express*, 13(4):1202–14, February 2005. ISSN 1094-4087. URL <http://www.ncbi.nlm.nih.gov/pubmed/19494990>.
- [58] Ziyang Zhang and Min Qiu. Small-volume waveguide-section high Q microcavities in 2D photonic crystal slabs. *Optics express*, 12(17):3988–95, August 2004. ISSN 1094-4087. URL <http://www.ncbi.nlm.nih.gov/pubmed/19483936>.
- [59] Snjezana Tomljenovic-Hanic, C Martijn de Sterke, and M J Steel. Design of high-Q cavities in photonic crystal slab heterostructures by air-holes infiltration. *Optics express*, 14(25):12451–6, December 2006. ISSN 1094-4087. URL <http://www.ncbi.nlm.nih.gov/pubmed/19529678>.
- [60] Po-tsung Lee, Tsan-wen Lu, and Feng-mao Tsai. Octagonal Quasi-Photonic Crystal Single-Defect Condensed Device Size. *IEEE PHOTONICS TECHNOLOGY LETTER*, 19(9):2007–2009, 2007.
- [61] K. Aoki, D. Guimard, M. Nishioka, M. Nomura, S. Iwamoto, and Y. Arakawa. Coupling of quantum-dot light emission with a three-dimensional photonic-crystal nanocavity. *Nature Photonics*, 2(11):688–692, October 2008. ISSN 1749-4885. doi: 10.1038/nphoton.2008.202. URL <http://www.nature.com/doifinder/10.1038/nphoton.2008.202>.
- [62] Masaya Notomi, Eiichi Kuramochi, and Takasumi Tanabe. Large-scale arrays of ultrahigh-Q coupled nanocavities. *Nature Photonics*, 2(12):741–747, November 2008. ISSN 1749-4885. doi: 10.1038/nphoton.2008.226. URL <http://www.nature.com/doifinder/10.1038/nphoton.2008.226>.
- [63] a. Dousse, J. Suffczynski, O. Krebs, A. Beveratos, A. Lematre, I. Sagnes, J. Bloch, P. Voisin, and P. Senellart. A quantum dot based bright source of entangled photon pairs operating at 53 K. *Applied Physics Letters*, 97(8):081104, 2010. ISSN 00036951. doi: 10.1063/1.3475487. URL <http://link.aip.org/link/APPLAB/v97/i8/p081104/s1&Agg=doi>.
- [64] Adrien Dousse, Jan Suffczynski, Alexios Beveratos, Olivier Krebs, Aristide Lemaître, Isabelle Sagnes, Jacqueline Bloch, Paul Voisin, and Pascale Senellart. Ultrabright source of entangled photon pairs. *Nature*, 466(7303):217–20, July 2010. ISSN 1476-4687. doi: 10.1038/nature09148. URL <http://www.ncbi.nlm.nih.gov/pubmed/20613838>.
- [65] K. Hennessy, a. Badolato, a. Tamboli, P. M. Petroff, E. Hu, M. Atature, J. Dreiser, and a. Imamoglu. Tuning photonic crystal nanocavity modes by

- wet chemical digital etching. *Applied Physics Letters*, 87(2):021108, 2005. ISSN 00036951. doi: 10.1063/1.1992656. URL <http://link.aip.org/link/APPLAB/v87/i2/p021108/s1&Agg=doi>.
- [66] Andrei Faraon, P.E. Barclay, Charles Santori, K.M.C. Fu, and R.G. Beausoleil. Resonant enhancement of the zero-phonon emission from a colour centre in a diamond cavity. *Nature Photonics*, (1):3–7, 2011. URL <http://www.nature.com/nphoton/journal/vaop/ncurrent/full/nphoton.2011.52.html>.
- [67] S. Mosor, J. Hendrickson, B. C. Richards, J. Sweet, G. Khitrova, H. M. Gibbs, T. Yoshie, a. Scherer, O. B. Shchekin, and D. G. Deppe. Scanning a photonic crystal slab nanocavity by condensation of xenon. *Applied Physics Letters*, 87(14):141105, 2005. ISSN 00036951. doi: 10.1063/1.2076435. URL <http://link.aip.org/link/APPLAB/v87/i14/p141105/s1&Agg=doi>.
- [68] M Calic, P Gallo, M Felici, KA Atlasov, and B Dwir. Phonon-Mediated Coupling of InGaAs/GaAs Quantum-Dot Excitons to Photonic Crystal Cavities. *Physical Review Letters*, 227402(June):1–4, 2011. doi: 10.1103/PhysRevLett.106.227402. URL <http://link.aps.org/doi/10.1103/PhysRevLett.106.227402>.
- [69] F. S. F. Brossard, X. L. Xu, D. a. Williams, M. Hadjipanayi, M. Hugues, M. Hopkinson, X. Wang, and R. a. Taylor. Strongly coupled single quantum dot in a photonic crystal waveguide cavity. *Applied Physics Letters*, 97(11):111101, 2010. ISSN 00036951. doi: 10.1063/1.3487937. URL <http://link.aip.org/link/APPLAB/v97/i11/p111101/s1&Agg=doi>.
- [70] P. E. Barclay, C. Santori, K. Fu, R. G. Beausoleil, and O. Painter. Coherent interference effects in a nano-assembled diamond NV center cavity-QED system. *Optics Express*, 17(10):8081, April 2009. ISSN 1094-4087. doi: 10.1364/OE.17.008081. URL <http://www.opticsinfobase.org/abstract.cfm?URI=oe-17-10-8081>.
- [71] T. van der Sar, J. Hagemeyer, W. Pfaff, E. C. Heeres, S. M. Thon, H. Kim, P. M. Petroff, T. H. Oosterkamp, D. Bouwmeester, and R. Hanson. Deterministic nanoassembly of a coupled quantum emitterphotonic crystal cavity system. *Applied Physics Letters*, 98(19):193103, 2011. ISSN 00036951. doi: 10.1063/1.3571437. URL <http://link.aip.org/link/APPLAB/v98/i19/p193103/s1&Agg=doi>.
- [72] T. van der Sar, E. C. Heeres, G. M. Dmochowski, G. de Lange, L. Robledo, T. H. Oosterkamp, and R. Hanson. Nanopositioning of a diamond nanocrystal containing a single nitrogen-vacancy defect center. *Applied Physics Letters*, 94(17):173104, 2009. ISSN 00036951. doi: 10.1063/1.3120558. URL <http://link.aip.org/link/APPLAB/v94/i17/p173104/s1&Agg=doi>.

- [73] Eiichi Kuramochi, Masaya Notomi, Satoshi Mitsugi, Akihiko Shinya, Takasumi Tanabe, and Toshifumi Watanabe. Ultrahigh-Q photonic crystal nanocavities realized by the local width modulation of a line defect. *Applied Physics Letters*, 88(4):041112, 2006. ISSN 00036951. doi: 10.1063/1.2167801. URL <http://link.aip.org/link/APPLAB/v88/i4/p041112/s1&Agg=doi>.
- [74] A Einstein. Zur Quantentheorie der Strahlung. *Physikalische Zeitschrift*, 18:121+, 1917.
- [75] P. a. M. Dirac. The Quantum Theory of the Emission and Absorption of Radiation. *Proceedings of the Royal Society A: Mathematical, Physical and Engineering Sciences*, 114(767):243–265, March 1927. ISSN 1364-5021. doi: 10.1098/rspa.1927.0039. URL <http://rspa.royalsocietypublishing.org/cgi/doi/10.1098/rspa.1927.0039>.
- [76] P A M Dirac. *The Principles of Quantum Mechanics*. International Series of Monographs on Physics. Clarendon Press, 1981. ISBN 9780198520115. URL <http://books.google.co.uk/books?id=XehUpGiM6FIC>.
- [77] M Planck. Ueber das Gesetz der Energieverteilung im Normalspectrum. *Annalen der Physik*, 309:553–563, 1901. doi: 10.1002/andp.19013090310.
- [78] F W Cummings. Stimulated Emission of Radiation in a Single Mode. *Phys. Rev.*, 140(4A):A1051—A1056, November 1965. doi: 10.1103/PhysRev.140.A1051. URL <http://link.aps.org/doi/10.1103/PhysRev.140.A1051>.
- [79] Mark Fox. *Quantum Optics: An Introduction (Oxford Master Series in Physics, 6)*. Oxford University Press, USA, 2006. ISBN 0198566735. URL <http://www.amazon.com/Quantum-Optics-Introduction-Oxford-Physics/dp/0198566735?SubscriptionId=0JYN1NVW651KCA56C102&tag=techkie-20&linkCode=xm2&camp=2025&creative=165953&creativeASIN=0198566735>.
- [80] Rodney Loudon. *The Quantum Theory of Light (Oxford Science Publications)*. Oxford University Press, USA, 2000. ISBN 0198501765. URL <http://www.amazon.com/Quantum-Theory-Oxford-Science-Publications/dp/0198501765?SubscriptionId=0JYN1NVW651KCA56C102&tag=techkie-20&linkCode=xm2&camp=2025&creative=165953&creativeASIN=0198501765>.
- [81] Alexey Kavokin, Jeremy J Baumberg, Guillaume Malpuech, and Fabrice P Laussy. *Microcavities (Semiconductor Science and Technology)*. Oxford University Press, USA, 2008. ISBN 0199228949. URL <http://www.amazon.com/Microcavities-Semiconductor-Science-Technology-Kavokin/>

- [dp/0199228949?SubscriptionId=0JYN1NVW651KCA56C102&tag=techkie-20&linkCode=xm2&camp=2025&creative=165953&creativeASIN=0199228949](http://www.amazon.com/Modern-Classical-Optics-Optical-Physics/dp/0199228949?SubscriptionId=0JYN1NVW651KCA56C102&tag=techkie-20&linkCode=xm2&camp=2025&creative=165953&creativeASIN=0199228949).
- [82] V Weisskopf and E P Wigner. Calculation of the natural brightness of spectral lines on the basis of Diracs theory. *Z. Phys*, 63:54–73, 1930.
- [83] D Meschede. *Optics, light and lasers*. Wiley-vch, 2008.
- [84] M O Scully and M S Zubairy. *Quantum optics*. Cambridge University Press, 1997.
- [85] Geoffrey Brooker. *Modern Classical Optics (Oxford Master Series in Atomic, Optical and Laser Physics)*. Oxford University Press, USA, 2003. ISBN 019859965X. URL <http://www.amazon.com/Modern-Classical-Optics-Optical-Physics/dp/019859965X?SubscriptionId=0JYN1NVW651KCA56C102&tag=techkie-20&linkCode=xm2&camp=2025&creative=165953&creativeASIN=019859965X>.
- [86] Peter W Milonni and Joseph H Eberly. *Laser Physics*. Wiley, 2010. ISBN 0470387718. URL <http://www.amazon.com/Laser-Physics-Peter-W-Milonni/dp/0470387718?SubscriptionId=0JYN1NVW651KCA56C102&tag=techkie-20&linkCode=xm2&camp=2025&creative=165953&creativeASIN=0470387718>.
- [87] K Yee. Numerical solution of initial boundary value problems involving Maxwell’s equations in isotropic media. *Antennas and Propagation, IEEE Transactions on*, 1966. URL http://ieeexplore.ieee.org/xpls/abs_all.jsp?arnumber=1138693.
- [88] Alexia Auffèves, Jean-Michel Gérard, and Jean-Philippe Poizat. Pure emitter dephasing: A resource for advanced solid-state single-photon sources. *Physical Review A*, 79(5):1–5, May 2009. ISSN 1050-2947. doi: 10.1103/PhysRevA.79.053838. URL <http://link.aps.org/doi/10.1103/PhysRevA.79.053838>.
- [89] A. Auffèves, D. Gerace, J.-M. Gérard, M. Santos, L. Andreani, and J.-P. Poizat. Controlling the dynamics of a coupled atom-cavity system by pure dephasing. *Physical Review B*, 81(24):1–10, June 2010. ISSN 1098-0121. doi: 10.1103/PhysRevB.81.245419. URL <http://link.aps.org/doi/10.1103/PhysRevB.81.245419>.
- [90] Clemens Matthiesen, Anthony Vamivakas, and Mete Atatüre. Subnatural Linewidth Single Photons from a Quantum Dot. *Physical Review Letters*, 108(9):1–4, February 2012. ISSN 0031-9007. doi: 10.1103/PhysRevLett.108.093602. URL <http://link.aps.org/doi/10.1103/PhysRevLett.108.093602>.

- [91] P. H. Sher, J. M. Smith, P. a. Dalgarno, R. J. Warburton, X. Chen, P. J. Dobson, S. M. Daniels, N. L. Pickett, and P. OBrien. Power law carrier dynamics in semiconductor nanocrystals at nanosecond timescales. *Applied Physics Letters*, 92(10):101111, 2008. ISSN 00036951. doi: 10.1063/1.2894193. URL <http://link.aip.org/link/APPLAB/v92/i10/p101111/s1&Agg=doi>.
- [92] a Meldrum, P Bianucci, and F Marsiglio. Modification of ensemble emission rates and luminescence spectra for inhomogeneously broadened distributions of quantum dots coupled to optical microcavities. *Optics express*, 18(10):10230–46, May 2010. ISSN 1094-4087. URL <http://www.ncbi.nlm.nih.gov/pubmed/20588877>.
- [93] C. T. Yuan, Y. C. Wang, Y. C. Yang, M. C. Wu, Jau Tang, and M. H. Shih. Modification of spontaneous emission rates in single colloidal CdSe/ZnS quantum dots by a submicron-sized dielectric disk. *Applied Physics Letters*, 99(5):053116, 2011. ISSN 00036951. doi: 10.1063/1.3622641. URL <http://link.aip.org/link/APPLAB/v99/i5/p053116/s1&Agg=doi>.
- [94] Y Xu, JS Vuckovic, RK Lee, and OJ Painter. Finite-difference time-domain calculation of spontaneous emission lifetime in a microcavity. *JOSA B*, 16(3), 1999. URL <http://www.opticsinfobase.org/abstract.cfm?&id=35669>.
- [95] P Nedel, X Letartre, and C Seassal. Design and investigation of surface addressable photonic crystal cavity confined band edge modes for quantum photonic devices. *Optics express*, 19(6):5014–5025, 2011. URL <http://www.opticsinfobase.org/abstract.cfm?URI=oe-19-6-5014>.
- [96] A. M. Zaitsev. *Optical Properties of Diamond: A Data Handbook*. Springer, 2001.
- [97] Gordon Davies. Properties and Growth of Diamond (E M I S Datareviews Series). *Institution of Electrical Engineers*,, 1980.
- [98] Jörg Wrachtrup and Fedor Jelezko. Processing quantum information in diamond. *Journal of Physics: Condensed Matter*, 18(21):S807–S824, May 2006. ISSN 0953-8984. doi: 10.1088/0953-8984/18/21/S08. URL <http://stacks.iop.org/0953-8984/18/i=21/a=S08?key=crossref.3ebf978682f06b8bfab48217febea4e1>.
- [99] Jason M Smith, Fabio Grazioso, Brian R Patton, Philip R Dolan, Matthew L Markham, and Daniel J Twitchen. Optical properties of a single-colour centre in diamond with a green zero-phonon line. *New Journal of Physics*, 13(4):045005, April 2011. ISSN 1367-2630. doi: 10.1088/1367-2630/13/4/045005. URL <http://stacks.iop.org/1367-2630/13/i=4/a=045005?key=crossref.e54e5b36cbfe91341e5dfb5abbd45426>.

- [100] Chunlang Wang, Christian Kurtsiefer, Harald Weinfurter, and Bernd Burchard. Single photon emission from SiV centres in diamond produced by ion implantation. *Journal of Physics B: Atomic, Molecular and Optical Physics*, 39(1):37–41, January 2006. ISSN 0953-4075. doi: 10.1088/0953-4075/39/1/005. URL <http://stacks.iop.org/0953-4075/39/i=1/a=005?key=crossref.95838f4866b2b386f81cec0cae48c797>.
- [101] T Gaebel, I Popa, a Gruber, M Domhan, F Jelezko, and J Wrachtrup. Stable single-photon source in the near infrared. *New Journal of Physics*, 6:98–98, July 2004. ISSN 1367-2630. doi: 10.1088/1367-2630/6/1/098. URL <http://stacks.iop.org/1367-2630/6/i=1/a=098?key=crossref.c22c6711b1c99f09b470c1b95fb132c0>.
- [102] Elke Neu, David Steinmetz, Janine Riedrich-Möller, Stefan Gsell, Martin Fischer, Matthias Schreck, and Christoph Becher. Single photon emission from silicon-vacancy colour centres in chemical vapour deposition nano-diamonds on iridium. *New Journal of Physics*, 13(2):025012, February 2011. ISSN 1367-2630. doi: 10.1088/1367-2630/13/2/025012. URL <http://stacks.iop.org/1367-2630/13/i=2/a=025012?key=crossref.0265718449d162fd8b5c4479487e12b2>.
- [103] J. R. Rabeau, Y. L. Chin, S. Prawer, F. Jelezko, T. Gaebel, and J. Wrachtrup. Fabrication of single nickel-nitrogen defects in diamond by chemical vapor deposition. *Applied Physics Letters*, 86(13):131926, 2005. ISSN 00036951. doi: 10.1063/1.1896088. URL <http://link.aip.org/link/APPLAB/v86/i13/p131926/s1&Agg=doi>.
- [104] I. Aharonovich, S. Castelletto, D. a. Simpson, a. D. Greentree, and S. Prawer. Photophysics of chromium-related diamond single-photon emitters. *Physical Review A*, 81(4):1–7, April 2010. ISSN 1050-2947. doi: 10.1103/PhysRevA.81.043813. URL <http://link.aps.org/doi/10.1103/PhysRevA.81.043813>.
- [105] Igor Aharonovich, Stefania Castelletto, Brett C. Johnson, Jeffrey C. McCallum, David a. Simpson, Andrew D. Greentree, and Steven Prawer. Chromium single-photon emitters in diamond fabricated by ion implantation. *Physical Review B*, 81(12):1–4, March 2010. ISSN 1098-0121. doi: 10.1103/PhysRevB.81.121201. URL <http://link.aps.org/doi/10.1103/PhysRevB.81.121201>.
- [106] D. a. Simpson, E. Ampem-Lassen, B. C. Gibson, S. Trpkovski, F. M. Hossain, S. T. Huntington, a. D. Greentree, L. C. L. Hollenberg, and S. Prawer. A highly efficient two level diamond based single photon source. *Applied Physics Letters*, 94(20):203107, 2009. ISSN 00036951. doi: 10.1063/1.3141450. URL <http://link.aip.org/link/APPLAB/v94/i20/p203107/s1&Agg=doi>.

- [107] T Müller, I Aharonovich, L Lombez, Y Alaverdyan, a N Vamivakas, S Castelletto, F Jelezko, J Wrachtrup, S Praver, and M Atatüre. Wide-range electrical tunability of single-photon emission from chromium-based colour centres in diamond. *New Journal of Physics*, 13(7):075001, July 2011. ISSN 1367-2630. doi: 10.1088/1367-2630/13/7/075001. URL <http://stacks.iop.org/1367-2630/13/i=7/a=075001?key=crossref.456a341ca53a73ac532ff56e1206b84f>.
- [108] CD Clark and CA Norris. Photoluminescence associated with the 1.473, 1.944 and 2-498 eV centres in diamond. *J. Phys. C: Solid St. Phys*, 4, 1971. URL <http://iopscience.iop.org/0022-3719/4/14/036/pdf>.
- [109] G. Davies and MF Hamer. Optical studies of the 1.945 eV vibronic band in diamond. *Proceedings of the Royal Society of London. A. Mathematical and Physical Sciences*, 348(1653):285, 1976. URL <http://rspa.royalsocietypublishing.org/content/348/1653/285.short>.
- [110] a Lenef and Sc Rand. Electronic structure of the N-V center in diamond: Theory. *Physical review. B, Condensed matter*, 53(20):13441–13455, May 1996. ISSN 0163-1829. URL <http://www.ncbi.nlm.nih.gov/pubmed/9983089>.
- [111] a Lenef, Sw Brown, Da Redman, Sc Rand, J Shigley, and E Fritsch. Electronic structure of the N-V center in diamond: Experiments. *Physical review. B, Condensed matter*, 53(20):13427–13440, May 1996. ISSN 0163-1829. URL <http://www.ncbi.nlm.nih.gov/pubmed/9983088>.
- [112] N B Manson, X F He, and P T Fisk. Raman heterodyne detected electron-nuclear-double-resonance measurements of the nitrogen-vacancy center in diamond. *Optics letters*, 15(19):1094–6, October 1990. ISSN 0146-9592. URL <http://www.ncbi.nlm.nih.gov/pubmed/19771008>.
- [113] I Hiromitsu and J Westra. Cross-relaxation dynamics of the NV center in diamond as studied via optically detected microwave recovery transients. *Physical Review B*, 46(17):600–612, 1992. URL http://prb.aps.org/abstract/PRB/v46/i17/p10600_1.
- [114] Keith Holliday, Neil B Manson, Max Glasbeek, and Eric van Oort. Optical hole-bleaching by level anti-crossing and cross relaxation in the NV centre in diamond. *Journal of Physics: Condens. Matter*, 1:7093–7102, 1989. URL <http://iopscience.iop.org/0953-8984/1/39/021>.
- [115] D. Redman, S. Brown, and S. C. Rand. Origin of persistent hole burning of NV centers in diamond. *Journal of the Optical Society of America B*, 9(5):768,

- May 1992. ISSN 0740-3224. doi: 10.1364/JOSAB.9.000768. URL <http://www.opticsinfobase.org/abstract.cfm?URI=josab-9-5-768>.
- [116] N. Manson, J. Harrison, and M. Sellars. Nitrogen-vacancy center in diamond: Model of the electronic structure and associated dynamics. *Physical Review B*, 74(10):1–11, September 2006. ISSN 1098-0121. doi: 10.1103/PhysRevB.74.104303. URL <http://link.aps.org/doi/10.1103/PhysRevB.74.104303>.
- [117] Adam Gali, Maria Fyta, and Efthimios Kaxiras. Ab initio supercell calculations on nitrogen-vacancy center in diamond: Electronic structure and hyperfine tensors. *Physical Review B*, 77(15):1–12, April 2008. ISSN 1098-0121. doi: 10.1103/PhysRevB.77.155206. URL <http://link.aps.org/doi/10.1103/PhysRevB.77.155206>.
- [118] J. Larsson and P. Delaney. Electronic structure of the nitrogen-vacancy center in diamond from first-principles theory. *Physical Review B*, 77(16):1–8, April 2008. ISSN 1098-0121. doi: 10.1103/PhysRevB.77.165201. URL <http://link.aps.org/doi/10.1103/PhysRevB.77.165201>.
- [119] F. Jelezko, T. Gaebel, I. Popa, a. Gruber, and J. Wrachtrup. Observation of Coherent Oscillations in a Single Electron Spin. *Physical Review Letters*, 92(7):1–4, February 2004. ISSN 0031-9007. doi: 10.1103/PhysRevLett.92.076401. URL <http://link.aps.org/doi/10.1103/PhysRevLett.92.076401>.
- [120] A Gruber, A Dra, C Tietz, L Fleury, J Wrachtrup, and C Von Borczyskowski. Scanning Confocal Optical Microscopy and Magnetic Resonance on Single Defect Centers. *Science*, 276(27 June):2012–2014, 1997.
- [121] C Kurtsiefer, S Mayer, P Zarda, and H Weinfurter. Stable solid-state source of single photons. *Physical review letters*, 85(2):290–3, July 2000. ISSN 1079-7114. URL <http://www.ncbi.nlm.nih.gov/pubmed/10991265>.
- [122] Alexios Beveratos, Rosa Brouri, Thierry Gacoin, Jean-Philippe Poizat, and Philippe Grangier. Nonclassical radiation from diamond nanocrystals. *Physical Review A*, 64(6):2–5, November 2001. ISSN 1050-2947. doi: 10.1103/PhysRevA.64.061802. URL <http://link.aps.org/doi/10.1103/PhysRevA.64.061802>.
- [123] Charles Santori, Philippe Tamarat, Philipp Neumann, Jörg Wrachtrup, David Fattal, Raymond Beausoleil, James Rabeau, Paolo Olivero, Andrew Greentree, Steven Praver, Fedor Jelezko, and Philip Hemmer. Coherent Population Trapping of Single Spins in Diamond under Optical Excitation. *Physical Review Letters*, 97(24):1–4, December 2006. ISSN 0031-9007. doi: 10.1103/PhysRevLett.97.247401. URL <http://link.aps.org/doi/10.1103/PhysRevLett.97.247401>.

- [124] Richard P. Feynman. Simulating physics with computers. *International Journal of Theoretical Physics*, 21(6-7):467–488, June 1982. ISSN 0020-7748. doi: 10.1007/BF02650179. URL <http://www.springerlink.com/index/10.1007/BF02650179>.
- [125] A.S Holevo. Some estimates for information quantity transmitted by quantum communication channel. *Probl. Inform. Transm.*, 9(3):3–11, 1973.
- [126] R. P. Poplavskii. Thermodynamical models of information processing. *Usp.Fiz.Nauk*, 115(3):465–501, 1975.
- [127] R.S. Ingarden. Quantum information theory. *Reports in Mathematical Physics*, 10:43–72, 1976.
- [128] Yuri Manin. Computable and uncomputable (in Russian). *Sovetskoye Radio*, 1980.
- [129] M V Gurudev Dutt, L Childress, L Jiang, E Togan, J Maze, F Jelezko, a S Zibrov, P R Hemmer, and M D Lukin. Quantum register based on individual electronic and nuclear spin qubits in diamond. *Science (New York, N.Y.)*, 316(5829):1312–6, June 2007. ISSN 1095-9203. doi: 10.1126/science.1139831. URL <http://www.ncbi.nlm.nih.gov/pubmed/17540898>.
- [130] L Childress, M V Gurudev Dutt, J M Taylor, a S Zibrov, F Jelezko, J Wrachtrup, P R Hemmer, and M D Lukin. Coherent dynamics of coupled electron and nuclear spin qubits in diamond. *Science (New York, N.Y.)*, 314(5797):281–5, October 2006. ISSN 1095-9203. doi: 10.1126/science.1131871. URL <http://www.ncbi.nlm.nih.gov/pubmed/16973839>.
- [131] Sean Barrett and Pieter Kok. Efficient high-fidelity quantum computation using matter qubits and linear optics. *Physical Review A*, 71(6):2–5, June 2005. ISSN 1050-2947. doi: 10.1103/PhysRevA.71.060310. URL <http://link.aps.org/doi/10.1103/PhysRevA.71.060310>.
- [132] Pieter Kok and Brendon W Lovett. Pieter Kok and Brendon W. Lovett. *Nature*, 444(November):2006–2006, 2006.
- [133] S. C. Benjamin, B. W. Lovett, and J. M. Smith. Prospects for measurement-based quantum computing with solid state spins. *Laser and Photonic Reviews*, 3(6): 5–24, 2009.
- [134] Y. Lim, A. Beige, and L. Kwok. Repeat-Until-Success Linear Optics Distributed Quantum Computing. *Physical Review Letters*, 95(3):1–4, July 2005. ISSN 0031-9007. doi: 10.1103/PhysRevLett.95.030505. URL <http://link.aps.org/doi/10.1103/PhysRevLett.95.030505>.

- [135] A Young, C Y Hu, L Marseglia, J P Harrison, J L O'Brien, and J G Rarity. Cavity enhanced spin measurement of the ground state spin of an NV center in diamond. *New Journal of Physics*, 11(1):013007, January 2009. ISSN 1367-2630. doi: 10.1088/1367-2630/11/1/013007. URL <http://stacks.iop.org/1367-2630/11/i=1/a=013007?key=crossref.a3e1ed945240d1b401a910a40dca1414>.
- [136] C. Su, A. D. Greentree, and L. C. L. Hollenberg. Towards a picosecond transform-limited nitrogen-vacancy based single photon source. *Optics express*, 16(9):6240–50, April 2008. ISSN 1094-4087. URL <http://www.ncbi.nlm.nih.gov/pubmed/18545327>.
- [137] A. Greentree, J. Salzman, S. Prawer, and L. Hollenberg. Quantum gate for Q switching in monolithic photonic-band-gap cavities containing two-level atoms. *Physical Review A*, 73(1):1–6, January 2006. ISSN 1050-2947. doi: 10.1103/PhysRevA.73.013818. URL <http://link.aps.org/doi/10.1103/PhysRevA.73.013818>.
- [138] Young-Shin Park, Andrew K Cook, and Hailin Wang. Cavity QED with diamond nanocrystals and silica microspheres. *Nano letters*, 6(9):2075–9, September 2006. ISSN 1530-6984. doi: 10.1021/nl061342r. URL <http://www.ncbi.nlm.nih.gov/pubmed/16968028>.
- [139] Stefan Schietinger and Oliver Benson. Coupling single NV-centres to high-Q whispering gallery modes of a preselected frequency-matched microresonator. *Journal of Physics B: Atomic, Molecular and Optical Physics*, 42(11):114001, June 2009. ISSN 0953-4075. doi: 10.1088/0953-4075/42/11/114001. URL <http://stacks.iop.org/0953-4075/42/i=11/a=114001?key=crossref.2f950c3d980974c12c3da147b8199262>.
- [140] C. F. Wang, Y-S. Choi, J. C. Lee, E. L. Hu, J. Yang, and J. E. Butler. Observation of whispering gallery modes in nanocrystalline diamond microdisks. *Applied Physics Letters*, 90(8):081110, 2007. ISSN 00036951. doi: 10.1063/1.2709626. URL <http://link.aip.org/link/APPLAB/v90/i8/p081110/s1&Agg=doi>.
- [141] C. F. Wang, R. Hanson, D. D. Awschalom, E. L. Hu, T. Feygelson, J. Yang, and J. E. Butler. Fabrication and characterization of two-dimensional photonic crystal microcavities in nanocrystalline diamond. *Applied Physics Letters*, 91(20):201112, 2007. ISSN 00036951. doi: 10.1063/1.2813023. URL <http://link.aip.org/link/APPLAB/v91/i20/p201112/s1&Agg=doi>.
- [142] Snjezana Tomljenovic-Hanic, C Martijn de Sterke, and M J Steel. Design of high-Q cavities in photonic crystal slab heterostructures by air-holes infiltration. *Optics*

- express*, 14(25):12451–6, December 2006. ISSN 1094-4087. URL <http://www.ncbi.nlm.nih.gov/pubmed/19529678>.
- [143] S Tomljenovic-Hanic, M J Steel, C Martijn de Sterke, and J Salzman. Diamond based photonic crystal microcavities. *Optics express*, 14(8):3556–62, April 2006. ISSN 1094-4087. URL <http://www.ncbi.nlm.nih.gov/pubmed/19516502>.
- [144] M V Gurudev Dutt, L Childress, L Jiang, E Togan, J Maze, F Jelezko, a S Zibrov, P R Hemmer, and M D Lukin. Quantum register based on individual electronic and nuclear spin qubits in diamond. *Science (New York, N.Y.)*, 316(5829):1312–6, June 2007. ISSN 1095-9203. doi: 10.1126/science.1139831. URL <http://www.ncbi.nlm.nih.gov/pubmed/17540898>.
- [145] P Neumann, N Mizuochi, F Rempp, P Hemmer, H Watanabe, S Yamasaki, V Jacques, T Gaebel, F Jelezko, and J Wrachtrup. Multipartite entanglement among single spins in diamond. *Science (New York, N.Y.)*, 320(5881):1326–9, June 2008. ISSN 1095-9203. doi: 10.1126/science.1157233. URL <http://www.ncbi.nlm.nih.gov/pubmed/18535240>.
- [146] Philipp Neumann, Johannes Beck, Matthias Steiner, Florian Rempp, Helmut Fedder, Philip R Hemmer, Jörg Wrachtrup, and Fedor Jelezko. Single-shot readout of a single nuclear spin. *Science (New York, N.Y.)*, 329(5991):542–4, July 2010. ISSN 1095-9203. doi: 10.1126/science.1189075. URL <http://www.ncbi.nlm.nih.gov/pubmed/20595582>.
- [147] G. D. Fuchs, G. Burkard, P. V. Klimov, and D. D. Awschalom. A quantum memory intrinsic to single nitrogenvacancy centres in diamond. *Nature Physics*, 7(10):789–793, June 2011. ISSN 1745-2473. doi: 10.1038/nphys2026. URL <http://www.nature.com/doi/10.1038/nphys2026>.
- [148] G. Waldherr, P. Neumann, S. Huelga, F. Jelezko, and J. Wrachtrup. Violation of a Temporal Bell Inequality for Single Spins in a Diamond Defect Center. *Physical Review Letters*, 107(9):12–15, August 2011. ISSN 0031-9007. doi: 10.1103/PhysRevLett.107.090401. URL <http://link.aps.org/doi/10.1103/PhysRevLett.107.090401>.
- [149] Zhi-Hui Wang, G. de Lange, D. Ristè, R. Hanson, and V. Dobrovitski. Comparison of dynamical decoupling protocols for a nitrogen-vacancy center in diamond. *Physical Review B*, 85(15):57–61, April 2012. ISSN 1098-0121. doi: 10.1103/PhysRevB.85.155204. URL <http://link.aps.org/doi/10.1103/PhysRevB.85.155204>.

- [150] Gijs de Lange, Toeno van der Sar, Machiel Blok, Zhi-Hui Wang, Viatcheslav Dobrovitski, and Ronald Hanson. Controlling the quantum dynamics of a mesoscopic spin bath in diamond. *Scientific reports*, 2:382, January 2012. ISSN 2045-2322. doi: 10.1038/srep00382. URL <http://www.pubmedcentral.nih.gov/articlerender.fcgi?artid=3336181&tool=pmcentrez&rendertype=abstract>.
- [151] Wolfgang Pfaff, TH Taminiau, and Lucio Robledo. Demonstration of entanglement-by-measurement of solid state qubits. *Arxiv preprint arXiv: ...*, 11:1–6, 2012. URL <http://arxiv.org/abs/1206.2031>.
- [152] Lucio Robledo, Lilian Childress, Hannes Bernien, Bas Hensen, Paul F a Alkemade, and Ronald Hanson. High-fidelity projective read-out of a solid-state spin quantum register. *Nature*, 477(7366):574–8, September 2011. ISSN 1476-4687. doi: 10.1038/nature10401. URL <http://www.ncbi.nlm.nih.gov/pubmed/21937989>.
- [153] J. P. Hadden, J. P. Harrison, a. C. Stanley-Clarke, L. Marseglia, Y.-L. D. Ho, B. R. Patton, J. L. OBrien, and J. G. Rarity. Strongly enhanced photon collection from diamond defect centers under microfabricated integrated solid immersion lenses. *Applied Physics Letters*, 97(24):241901, 2010. ISSN 00036951. doi: 10.1063/1.3519847. URL <http://link.aip.org/link/APPLAB/v97/i24/p241901/s1&Agg=doi>.
- [154] Fabio Grazioso, Brian R Patton, and Jason M Smith. A high stability beam-scanning confocal optical microscope for low temperature operation. *The Review of scientific instruments*, 81(9):093705, September 2010. ISSN 1089-7623. doi: 10.1063/1.3484140. URL <http://www.ncbi.nlm.nih.gov/pubmed/20886985>.
- [155] Gopalakrishnan Balasubramanian, Philipp Neumann, Daniel Twitchen, Matthew Markham, Roman Kolesov, Norikazu Mizuochi, Junichi Isoya, Jocelyn Achard, Johannes Beck, Julia Tessler, Vincent Jacques, Philip R Hemmer, Fedor Jelezko, and Jörg Wrachtrup. Ultralong spin coherence time in isotopically engineered diamond. *Nature materials*, 8(5):383–7, May 2009. ISSN 1476-1122. doi: 10.1038/nmat2420. URL <http://www.ncbi.nlm.nih.gov/pubmed/19349970>.